Master Thesis of Science

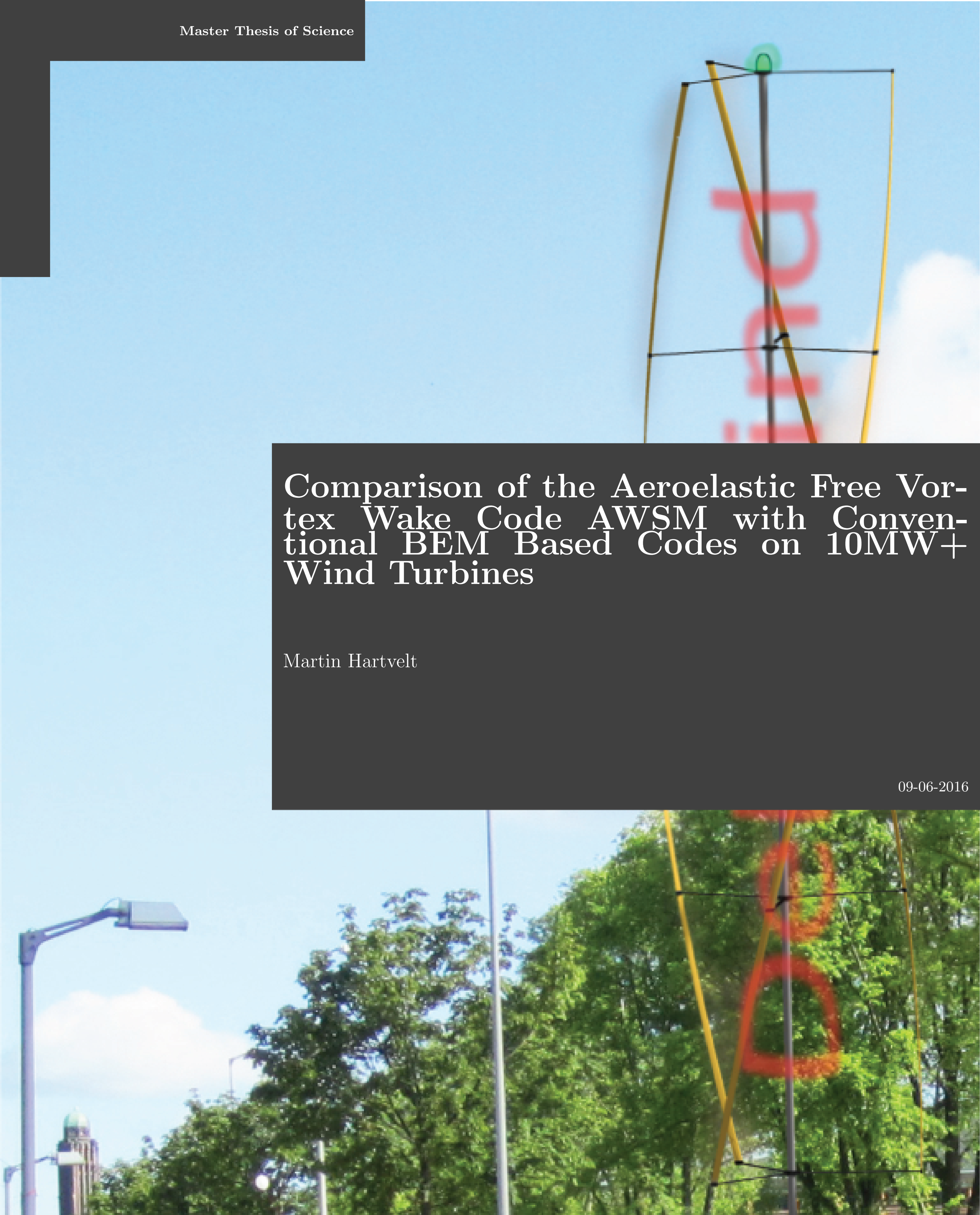

Comparison of the Aeroelastic Free Vortex Wake Code AWSM with Conventional BEM Based Codes on 10MW+ Wind Turbines

Martin Hartvelt

09-06-2016

EWEM TU Delft DTU Carl von Ossietzky Universität Oldenburg NTNU European Commission Erasmus Mundus

European Wind Energy Master - EWEM- Rotor Design Track

Comparison of the Aeroelastic Free Vortex Wake Code AWSM with Conventional BEM Based Codes on 10MW+ Wind Turbines

Master of Science Thesis

For obtaining the degree of Master of Science in Engineering Wind Energy at Technical University of Denmark and in Aerospace Engineering at Delft University of Technology.

Martin Hartvelt

09-06-2016

European Wind Energy Master - EWEM
ECN - Energy Research Centre of the Netherlands

European Wind Energy Master - EWEM
Of
Rotor Design Track

The undersigned hereby certify that they have read and recommend to the European Wind Energy Master - EWEM for acceptance a thesis entitled **"Comparison of the Aeroelastic Free Vortex Wake Code AWSM with Conventional BEM Based Codes on 10MW+ Wind Turbines "** by **Martin Hartvelt** in partial fulfillment of the requirements for the degree of **Master of Science**.

Dated: 09-06-2016

Chairman: ______________________
prof.dr.ir. G.J.W. van Bussel of Delft University of Technology

Supervisor: ______________________
dr.ir. R. de Breuker of Delft University of Technology

Supervisor: ______________________
prof.dr.ir. H.A. Madsen of Technical University of Denmark

Supervisor: ______________________
dr.ir. K. Boorsma of Energy Research Centre of the Netherlands

Acknowledgements

I would like to start by thanking some of the people who have helped and guided me in the process of my writing my Master's thesis. First, I would like to thank Koen Boorsma, my supervisor at ECN, for all the guidance and support, which has greatly contributed to the results of this research. Next, I would like to thank Helge Aagaard Madsen and Roeland de Breuker for their advice and guidance in the process, even though in times this was difficult due to the long distance. I would also like to thank all the people at ECN, who have been very willing to help out in every way possible. It has been a very rewarding experience to work with and learn from you.

On a personal note, I would like to thank my friends, my family and especially my girlfriend, who has learned a lot about the Blade Element Momentum theory and the AVATAR project in the past few months.

Thanks a lot,

Martin Hartvelt

Summary

The current practice in aerodynamic design and load analysis of wind turbines is to use codes based on the Blade Element Momentum theory (BEM). These models are computationally very efficient but are limited in the physical representation of certain flow phenomena, such as yawed flow, dynamic inflow and root/tip flow, for which engineering corrections are applied. For large wind turbines with a capacity of 10MW or higher, these models have not yet been validated. In order to develop or enhance aerodynamic and aeroelastic models for large wind turbines, the AVATAR project is started in November 2013, where BEM models are compared with higher fidelity models. One of these higher fidelity models is the aeroelastic free vortex wake code AWSM, which is compared to a BEM model in this thesis for a set of dynamic load cases, as specified in the AVATAR project.

The BEM and AWSM code have been coupled to the same structural dynamics model Phatas, which makes sure the structural dynamics of a wind turbine is solved exactly the same. The aerodynamics of the global flow are solved fundamentally different: AWSM calculates three-dimensional effects intrinsically by bound vorticity on the blades and shed and trailed vorticity in the wake, whereas the BEM model requires engineering corrections for three-dimensional effects.

This research has compared the results for BEM and AWSM on five different load cases on two 10MW reference wind turbines. Results from these test cases have also been compared to external BEM, vortex wake and CFD codes, as well as an additional validation case with experimental data from the New MEXICO experiment to assess dynamic inflow. This wide variety of test cases and comparison has resulted in an extended insight in the application of AWSM for analysis of dynamic load cases. Furthermore, the engineering correction models in BEM have been compared to the results from AWSM, which has led to the identification of discrepancies between the models, which could serve as an input to develop new or enhance the existing engineering models.

For complex flow situations, such as a wind turbine in half wake, extreme wind shear transient or turbulent inflow, large differences in the load variation are observed, which have been found to originate from the modeling of the local induction factor. It is found that AWSM calculates a much more varying induction factor compared to BEM, resulting in large differences in fatigue loads of the blade and tower moments. This uncertainty of the blade and tower loads might lead to over-designed blades and support structures, which could have a large impact on the cost of wind energy, which is an important driver for the further development of the wind energy market.

With this study it has been shown that AWSM can be used as an aeroelastic tool to assess the loads on wind turbines. Due to the relatively high CPU usage compared to BEM models, AWSM is less suited as a design tool for fast iterations, although the model can be used to compliment BEM models in load analysis and can be used to validate or tune engineering correction models.

Contents

List of Figures

List of Tables

Chapter 1

Introduction

In this thesis the aeroelastic free vortex wake code AWSM will be compared with conventional aerodynamic models to analyze large (10MW+) wind turbines for various test cases. In this introduction, the motivation and objective of this research will first be discussed. Second, the research questions will be described, followed by the methodology to find answers to these research questions. Finally, an outline of the thesis report will be presented.

1.1 Motivation and Objective

In recent years there has been a trend towards increasing the size of wind turbines, especially for offshore applications. This trend is a result of the effort to increase the market share of wind energy and decrease the levelized Cost of Energy (CoE), which results in the development of large wind farms in the range of 500MW. In order to reach this high power production, it is expected that the size of wind turbines will increase in the near future. In Fig. 1.1, the average capacity of offshore wind turbines is shown between 1991 and 2015. From this figure, it can be seen that the average capacity of an offshore wind turbine has increased significantly over the past 25 years.

In the UpWind research project, the up-scaling towards 20MW turbines is considered, from which it is found that future wind turbines could lead to rotor diameters around 250m [10]. With the increased rotor size of the next generation wind turbines, compressibility effects, Reynolds number effects as well as laminar-turbulent transition and separation effects become more pronounced. Due to these effects, the design of future 10 to 20MW wind turbines will violate validity limits of current wind turbine analysis tools, which are based on Blade Element Momentum (BEM) theory. In order to develop or enhance aerodynamic and aeroelastic models for large (10MW+) wind turbine analysis, the AVATAR (AdVanced Aerodynamic Tools for lArge Rotors) project is started in November 2013 [11]. The AVATAR project is started by an EERA (European Energy Research Alliance) consortium of 11 research institutes and 2 industry partners. As part of this project, aeroelastic codes are developed and validated against high fidelity models.

One of the research institutes involved in the AVATAR project is the Energy Research Center of the Netherlands (ECN), which is participating with two aerodynamic models: a conventional BEM model and a higher fidelity lifting line free vortex wake model (AWSM) [4]. These aerodynamic models are coupled to the structural dynamics solver Phatas, creating an aeroelastic code. The coupling between the aerodynamic and structural model is done by Knowledge Centre Wind Turbine, Materials and Construction (WMC). The higher fidelity model AWSM is able to intrinsically

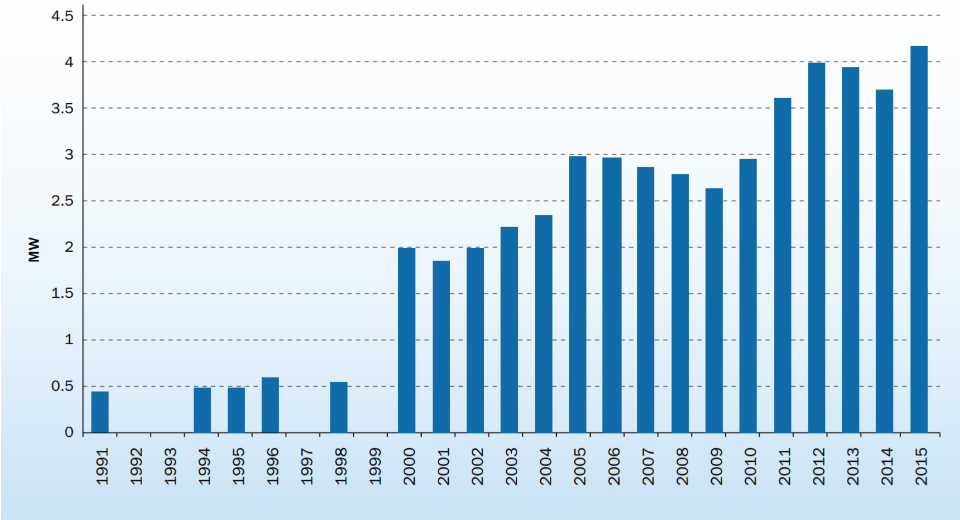

Figure 1.1: *Average offshore wind turbine rated capacity, from [1]*

model three dimensional effects through vorticity, whereas BEM models use engineering models to account for effects like finite number of blades, oblique inflow, turbulent wake and dynamic inflow [9].

In this thesis, the application of AWSM in dynamic load case simulations of large wind turbines will be analyzed by assessing the aeroelastic load cases as defined in Work Package (WP) 4 of the AVATAR project, as well as some additional studies in the application of vortex wake codes and a validation case with experimental results from the New MEXICO experiment. With this research the added value of vortex wake codes for future wind turbine analysis tools can be assessed. The application of AWSM in dynamic load case simulations could lead to new insights in rotor aerodynamics and could help to improve engineering models in BEM codes or replace existing models. This should lead to less uncertainties in the design of modern wind turbines, resulting in a more optimal design and hence a reduction in the CoE. The research objective of this thesis is therefore defined as:

- **Compare the aeroelastic capabilities of the free vortex wake code AWSM with conventional BEM based models, to be used in integral design codes for the next generation of large wind turbines (up to 20MW).**

This will be done by testing the performance of the aeroelastic free vortex wake code AWSM, which is based on non-linear lifting line theory, coupled to the structural dynamics solver Phatas, on different load cases as specified in WP4 of the AVATAR project. The results will be compared to an aeroelastic BEM code based on the same structural code (i.e. only the aerodynamics module of the code is changed). Additionally, the results will be compared with data obtained from other BEM codes and higher fidelity models within the AVATAR project.

1.2 Research Questions

In Section 1.1, the motivation for the research in more advanced aeroelastic tools is described, from which it was made clear that more advanced aeroelastic simulation tools are required for wind turbine analysis and design. The main research questions to be answered in this thesis in order to achieve the research objective is:

- **What is the added value of the aeroelastic free vortex wake code AWSM, coupled to the structural dynamics solver Phatas, over conventional BEM based codes as an integral part of design codes for the next generation of large wind turbines?**

In this research questions the added value could refer to a higher accuracy obtained for certain operational conditions, more detailed information on certain flow phenomena to be used to tune and validate engineering models in current BEM codes or by replacing or complementing BEM codes as a design tool for the next generation wind turbines. From this main research question, four research questions are formulated which are again divided into sub-questions. These research questions are stated below.

1. **How does the numerical stability, accuracy and computation time of AWSM depend on its input parameters?**
   (a) which parameters influence the numerical stability, accuracy and computational time?
   (b) how do these parameters influence numerical stability, accuracy and computational time?
   (c) which recommendations can be made regarding the input parameters which influence numerical stability, accuracy and computation time?
2. **What is the validity of the aeroelastic free vortex wake code AWSM?**
   (a) how does the accuracy of the model compare to BEM codes within the AVATAR project?
   (b) how does the accuracy of the model compare to higher fidelity models within the AVATAR project?
3. **How can the aeroelastic free vortex wake code AWSM be improved?**
   (a) what are the limitations of AWSM?
   (b) how can these limitation be overcome?
4. **What is the added value of AWSM in the current field of wind turbine simulation tools?**
   (a) to what extent could AWSM be used to replace current wind turbine simulation tools?
   (b) to what extent could AWSM be used to investigate certain effects to improve engineering models for BEM codes?

1.3 Methodology

The aim of this research is to analyze the performance and added value of the coupled aeroelastic free vortex wake code AWSM. This will be done by using PhatasAero to analyze two 10MW reference turbines within the AVATAR project. These turbines are the INNWIND [12] and AVATAR turbine [13]. In this section the methodology to achieve the research objective will be discussed.

During this research the lifting line free vortex wake code AWSM will be tested for its performance in analyzing aeroelastic behavior of large wind turbines by running dynamic load case simulations on two 10MW reference wind turbines. In order to compare AWSM with BEM, some of the load cases as specified in WP4 of the AVATAR project will be run and the results from BEM and AWSM from PhatasAero will be compared. In order to make sure only the influence of the aerodynamic model is compared, the structural model for both BEM and AWSM will be the same. In this way there will be no influence due to different modeling of the structural dynamics. Furthermore, the results will also be compared with data from other models, which will be provided by other participants in the project (BEM and vortex models). It should be noted that these results are obtained with other structural models.

Besides running the load cases as specified in the AVATAR project, some additional simulations will be run to get a better insight in the differences between BEM and AWSM and to determine the optimal settings for AWSM. Finally, also an additional validation case is performed to compare the response to dynamic inflow. This test case is validated with results from the New MEXICO project for the response to a pitch step.

1.4 Thesis Outline

The structure of this report is as follows. In Chapter 2, the theory behind the different aerodynamic models will be described. In Chapter 3, an overview is given of the past research projects that have been conducted with the purpose of developing wind turbine simulation tools. The findings from these research projects are important to understand the current state and challenges of state-of-the-art aeroelastic models. Chapter 4 describes the implementation of BEM and AWSM. This chapter will give an overview of the differences in modeling, as well as the advantages and shortcomings of both models. In Chapter 5, the computational set-up of the various load cases is described, for which the results are presented in Chapter 6. The conclusions from this thesis are presented in Chapter 7. Finally, the recommendations for future research will be discussed in Chapter 8.

Chapter 2

Aerodynamic Models

In order to develop or enhance aerodynamic and aeroelastic models for large wind turbine analysis, it is important to get an overview of the available options as well as their advantages and limitations. In the PhD thesis of Schepers [2], a general overview is given of the different wind turbine simulation tools, categorized on computational time and the amount of physics which is used in the model as can be seen in Fig. 2.1. From this figure, it can be seen that BEM requires the least amount of calculation time, although the physics involved in the model are limited. AWSM is a model that uses a more physical representation of the global flow, although the CPU time is also higher, which is one of the main drawbacks for this model. The focus in this thesis is on BEM and free vortex wake models, since these are the two models that will be used for the comparison of the coupled aeroelastic code PhatasAero.

Furthermore, higher fidelity Computational Fluid Dynamics (CFD) models are also used in wind energy. One class of CFD models that is commonly used in wind energy are Reynolds Averaged Navier-Stokes (RANS) models. These models require large CPU time, as is indicated in Fig. 2.1, which makes the use of RANS models unsuitable for the industrial application of aeroelastic analysis or design, for which many simulations are required and quick results are key to reduce the time of each design iteration. However, these models are able to give a more detailed representation of the flow phenomena involved in rotor aerodynamics. An overview of these three type of aerodynamic simulation tools is given in the following sections.

2.1 Blade Element Momentum Models

In order to design and certify a wind turbine, a large number of simulations has to be carried out. Over the past few decades, BEM codes have proven to be very computational efficient while still be able to accurately simulate aerodynamic and aeroelastic effects on wind turbines. With the current computer capacity, higher fidelity models like vortex wake codes and CFD codes are considered to be too computational expensive to run an extensive amount of simulations and completely replace BEM codes [14].

BEM models are based on the coupling of the momentum theory with the blade element theory, which describes the two-dimensional aerodynamics of a blade section. This theory was first introduced by Glauert in 1935, but this method has been extended over the past eighty years. There are a lot of simplifications in the BEM model, which reduces the accuracy. The theory is based on

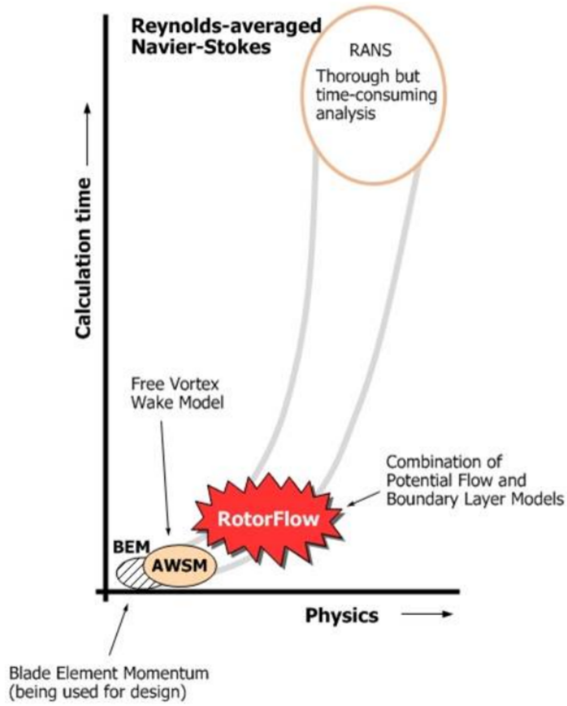

Figure 2.1: *Classification of aerodynamic models, from [2]*

an actuator disk concept with a stream-tube, where the flow through the rotor is assumed to be uniform and the flow over the sections of the blade is assumed to be independent. Furthermore, effects like compressibility, viscosity and turbulence are neglected in this model. In order to make BEM models more accurate, some engineering models have been added, which have mainly been derived empirically [8].

From a comparison with higher fidelity models, it is found that most of these engineering models can still be improved [2]. From a study by Sant, it is found that improvement should be made for the airfoil data and the engineering models for skewed wake effects in yaw [14]. In his work he has compared BEM codes to free vortex wake codes and CFD codes in order to improve some of the engineering models and to get a better understanding of the limitation of BEM models. It is found that in cases of a large variation of the loads over the radial position of the blade, i.e due to aerodynamic devices, vortex wake codes can significantly increase the accuracy, since BEM codes model blade sections as independent annuli.

Research in improving these engineering models have found that for cases with yawed flow, fast pitching or rotor speed variations, root and tip flow and dynamic inflow, it is recommended to look into higher fidelity codes, like free vortex wake codes [2].

2.2 Vortex Wake Models

As was shown in Fig. 2.1, free vortex wake codes take more physical effects into account compared to BEM codes, but are also more computationally expensive. As was stated in the previous section, vortex wake codes become particularly interesting in cases of complex geometry (due to aerodynamic devices), yawed flow, fast pitching or rotor speed variations, root and tip flow and dynamic inflow.

In Katz [3], it is described that the basics of lifting line vortex wake codes can be deducted from

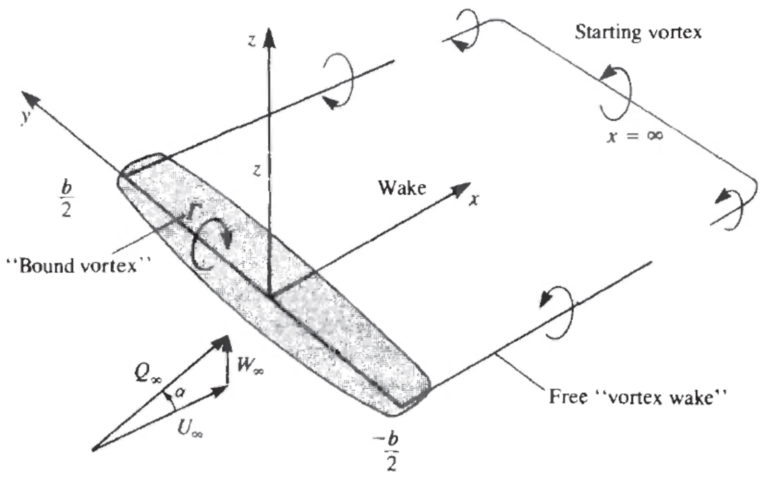

Figure 2.2: *Far-field horseshoe model of a finite wing, from [3].*

a horseshoe model of a finite wing, as can be seen in Fig. 2.2. In this model the lifting properties or a wing are approximated by a lifting line. This model has a constant bound vorticity at its quarter chord line, where the vorticity of the wing is lumped. The vortex will be closed by the starting vortex far downstream, which influence can be neglected. Prandtl has expanded this model to a large number of horseshoe vortices, which creates a lifting line model. This model allows to capture three-dimensional flow effects, since a vortex will influence the flow field in three dimensions. At every time-step, new vortex rings are shed in the wake and will form a vortex lattice. The wake is convected in time by the local wind speed and induced velocities due to the vortex points in the wake.

Another way to model vorticity is by a panel method or lifting surface method. These methods are more complex, since they calculate the vorticity distribution over the chord by respectively vorticity volumes and vortex sheets. One example is the aeroelastic free wake panel method code GENUVP, which has already been used in research and provides valuable information for validation and comparison of BEM models [15].

It has been found that there are many different ways to apply vortex theory to create aerodynamic models. A study on vortex methods in aeronautics shows that vortex wake codes can also be combined with CFD, which allows for a more detailed description on boundary layer corrections and compressibility [16]. In this paper it is stated that vortex methods have been used since the 1970's in aeronautics. In the theoretical background it is explained that Helmholtz's decomposition states that any velocity field can be split up in an irrotational (solid boundaries) and rotational part (wake). The concept of generalized vorticity is formulated by Dirac function, where a point Dirac resembles a point vortex, which leads to the singular behavior of a vortex point, since the induced velocity will go to infinity as the vortex point is approached. In current models, this singularity is solved by a cut-off function.

It is also possible to have a hybrid version between a BEM code and a lifting line vortex wake code, as is described by Pirrung [15]. In his work, he describes a coupled code HAWC2-NW, where the flow in the near wake is modeled by vorticity and the flow in the far wake is modeled by BEM theory. In his study a conventional BEM code, a hybrid code and a panel method are compared for the aerodynamic response to a pitch step and to blade vibrations. It is found that this coupled code shows a significant increase in accuracy compared to the BEM model in unsteady simulations, whereas the computational time is only slightly increased.

2.3 Reynolds Averaged Navier-Stokes Models

As was shown in Fig. 2.1, the most advanced aerodynamic models commonly used in wind energy aerodynamics are RANS models. For these models, the Navier-Stokes (N-S) equations are solved, which describes the motion of Newtonian fluids (such as water and air), as is shown in Eq. 2.1 [17].

$$\rho(\frac{\partial u_i}{\partial t} + u_j \frac{\partial u_i}{\partial x_j}) = \rho g_i + \frac{\partial \sigma_{ij}}{\partial x_j} \tag{2.1}$$

where ρ is the fluid density, u_i is the fluid velocity, x_i are the Cartesian coordinates, g_i is the volume force (gravity) and σ_{ij} is the stress on the fluid, give by:

$$\sigma_{ij} = -p\delta_{ij} + \mu(\frac{\partial u_i}{\partial x_j} + \frac{\partial u_j}{\partial x_i}) \tag{2.2}$$

where p is the pressure, δ_{ij} is the Kronecker delta and μ is the dynamic viscosity.

For RANS models, the N-S equation is averaged over time, resulting into a mean and a fluctuation part, according to Reynolds decomposition (e.g. $u_i = \overline{u_i} + u_i'$). This new equation is known as the Reynolds equation and an additional term is added to the equation, namely $-\rho\overline{u_i'u_j'}$. This additional term is the Reynolds stress, which only occurs in turbulent flows and consists of six components.

There exist four equations for the mean flow: the continuity equation and three equations of motion (Reynolds equation in three directions). For laminar flows, there are four unknowns (p and three components of u_i), which results in a closed system. However, for turbulent flows there are six additional unknowns, being the six components of the Reynolds stress. This problem is known as the closure problem of turbulence. In order to close the system, additional equations are required. These equations are obtained by turbulence modeling through so-called turbulence models, such as:

- Algebraic models. These models are the simplest models and express the Reynolds stress as the product of the turbulent viscosity μ_t and the mean strain rate $\frac{d\overline{u}}{dy}$. In these models μ_t is usually computed as function of the mixing length.
- Turbulence-energy equation models. These models are similar to the algebraic models, although μ_t is computed by the turbulent kinetic energy, $k = \frac{1}{2}(\overline{u_i'u_i'})$.

Besides these RANS models, also simulation models exist, which calculate the turbulence process directly and do not have a closure problem. An example is the Direct Numerical Simulation (DNS), where the N-S and continuity equation are directly computed. However, these models required a large amount of CPU time, especially for high Reynolds number flows. Another simulation model is the Large Eddy Simulation (LES), where the large scale motion of the air is computed and the small scale motion is modeled, resulting in a large decrease in CPU time compared to DNS.

CFD models can also be combined with engineering-type models. An example is EllipSys3D, in which an implementation is made where the RANS equations are solved for the global flow and an actuator disc or actuator line model is used to represent the rotor [18]. In this way, the boundary layer of the blades does not have to be resolved and the computational resources can be devoted to solving the dynamics of flow structures. The blades are represented by body forces without solving the boundary layer, which is done by airfoil polars similar to BEM models.

Chapter 3

Reference Research Projects

In this chapter, an overview is given of several European research projects, which have a similar purpose as the AVATAR project. For some of these projects, ECN has participated with the aeroelastic code Phatas, as well as the standalone version of AWSM (i.e. only the aerodynamics module). The results from these reference research projects give valuable insight in the development of aerodynamic and aeroelastic simulation tools, as well as the capabilities and limitations of BEM and vortex wake codes. The AVATAR project is described in Section 3.8. Since this project is already started in November 2013, the first results from this project will be discussed as well.

3.1 Annexlyse Project

The first project that will be discussed is the Annexlyse project, which took place from 1991 to 2001. This project is one of the many research projects from the International Energy Association (IEA). In this project, a thorough analysis of the aerodynamic field measurements is carried out on data obtained from IEA Task 14 and 18. In this project, full scale aerodynamic measurement campaigns have been performed in seven different facilities. A comparison between the data obtained and ECN's aeroelastic BEM code Phatas have been performed in order to improve the model [19]. The most important results of this study were that large difference were found in the tangential force, especially for the outboard part of the blade. Also, an underprediction of the normal forces was found at high wind speeds, whereas an overprediction was observed near the tip section. Since more than one rotor has been used for the validation and improvement of the models, a more general validation of the aerodyamic models was possible, where certain trends and dependencies on certain model parameters could be confirmed, investigated and/or discovered. After applying the suggested improvements in the lift, drag and tip modeling, Phatas showed a better agreement with the data obtained from the Annexlyse project [20].

3.2 HAWT Project

The second project that is investigated is IEA Task 20, the Horizontal Axis Wind Turbine Aerodynamics (HAWT) project. In this project the measurements from a rotor in the NASA-Ames wind tunnel are analyzed. Since the measurements are taken in a large wind tunnel, the loads have been measured at different radial positions, which allows to investigate yaw effects. During this project, Phatas and the standalone version of AWSM have been compared, where it is found that AWSM is able to capture a radial dependency in the azimuthal variation of induced velocities and the loads agree better with the data than with the BEM model. At higher tunnel speeds, it is found that the results from both models agree poorer, which is expected to be due to dynamic stall effects [21]. A more detailed investigation of the calculations and comparison with respect to the rotational effects have been described by Lindenburg [22]. In this report it is found that the rotational effects near the root are very large, which is expected to be due to the high local solidity of the blade. The location of the root and tip vortex is also found to be an important input for the simulations, although it should be noted that the location of the root vortex can change location with loading.

3.3 MEXICO Project

The last IEA project that has been investigated is IEA Task 29, which is also know as the Model Experiments in Controlled Conditions (MEXICO) project. The aim of this project is to improve and better understand aerodynamic simulation models. Measurements have been performed in the Low-speed Facility (LLF) of the German-Dutch Wind Tunnels (DNW). A large amount of measurements have been performed and codes of different complexity (BEM, vortex wake and CFD) have been compared with data from the experiments in this project. It is found there there is an uncertainty in modeling of the rotor performance of $\approx 10 - 20\%$ and for dynamic loads the uncertainty is even 30%. It is concluded that the differences are caused by the unsteady environment (i.e. yaw, tilt and deformations) [23].

In this project, also Particle Image Velocimetry (PIV) measurements have been performed in order to visualize the flow in the near wake. These measurements have been compared with calculation from the standalone version of AWSM, since this code is able to calculate the velocity of the wake points. From this comparison a very good agreement between the experiment and the numerical predictions was found, both in axial and yawed flow conditions [24].

Additionally, a comparison is done between the standalone BEM code and the AWSM code of ECN (i.e. not coupled to a structural dynamics solver). This comparison is done with data from the IEA Task 20 and 29 for axial and yawed flow and data from a real flexible 2.5MW wind turbine with a sudden pitch step. It is found that for axial flow both models agree well with the measurements. However, for the yawed flow case, the sectional loads were better observed by AWSM than for the BEM model.

3.4 VISCEL Project

Another research project, which is focused on aeroelastic stability investigations is the VISCEL project, part II [26]. In this project different CFD codes have been used to identify the underlying physics of aeroelastic stability in order to develop and validate engineering-type aeroelastic models, both for the flap/lead-lag (stall flutter) instability as well as for the flap/torsion (classical flutter) instability. It is found that classical flutter can be observed by looking at the pitch angle of a blade section. Since this instability lies in the linear part of the polar curve, the models were able to capture the flutter point well, where it was found that relative flexible blades were harder to model. For stall flutter, it was more challenging to model the exact dynamics of the instability, since this instability occurs in the stall region.

3.5 UpWind Project

In the UpWind project, BEM codes have been compared with more advanced model results (vortex wake codes and CFD codes). In this project, the effects of sheared and dynamic flow and ground effects have been investigated. It is found that for sheared flow, large differences are found in the tangential force for the BEM models, where vortex wake codes show a better agreement with the results from the CFD models. It is found that the rotor aerodynamics is influenced by the presence of shear by a varying induction over the blade, a variation of the angle of attack for blade sections and tilted wake due to a higher velocity at the top of the rotor plane [27].

3.6 Dan-Aero Project

In the DAN-AERO project [28], the aerodynamic data is gathered from two different multi-megawatt wind turbines, which makes this data interesting for testing aeroelastic codes, since the blade of these large wind turbines are more flexible than the blades that are used in the MEXICO project and in the NASA-Ames wind tunnel as described before. Unfortunately, no results in terms of comparison of the data to aeroelastic models for this project are publicly available. For a follow-up study or any similar validation study in wind turbine aerodynamics, it might be interesting to try to et access to this data set for validation purposes.

3.7 New MEXICO Project

The New MEXICO project is the successor of the MEXICO project, as described in Section 3.3. The goal of this project is to solve the outstanding research questions from the MEXICO project, as well as validate and compliment the first MEXICO measurement campaign.

From the MEXICO project is was found that there was an overestimation of the blade loads and wake velocity by CFD and vortex wake models compared to the measurements. Since the loads are coupled through the conservation of mass and momentum, an increased load would results in an increased induction and a lower wake velocity. Since CFD and vortex wake models obey the conservation laws, the results from the experiments violate these laws. The reason for this discrepancy is one of the main reasons for the follow-up measurement [29].

In the New MEXICO project, a new measurement campaign has been performed in the LLF wind tunnel of DNW, which is the largest wind tunnel in Europe [30]. During the two-week test campaign in 2014, a large variation of tests have been performed, including axial and yawed flow, dynamic inflow, parked conditions, pitch misalignment, acoustics, flow visualization, roughness effects and effect of aerodynamic devices. This wide variety of experiments is very useful for comparison and validation of BEM and vortex wake codes, as well as the development of engineering correction models.

A full description of this experiment, including the description of the wind turbine model, wind tunnel setup, test matrix, data acquisition and instrumentation can be found in [31]. One set of experiments that are performed during the New MEXICO measurement campaign are dynamic inflow experiments with a step in the rotor speed or pitch angle in axial and yawed inflow conditions. The case with a pitch step in axial inflow conditions will be used as a validation case is this thesis.

3.8 AVATAR Project

Most of the test cases that will be run to compare BEM and AWSM for this thesis will be done within the AVATAR project. For the AVATAR project, two reference turbine are analyzed. The first turbine is the 10MW reference turbine from the INNWIND project. A second turbine, the AVATAR turbine, is designed specifically for this project. The drive behind the new turbine is towards high-speed flows (compressibility) and high Reynolds number flow, since there is still a knowledge gap in this area. The design serves as a test-bench, rather than an optimum design. The main differences are the reduced specific power from 400 to $300W/m^2$ and an increased blade radius from 89 to $102.5m$. Also, the thrust is decreased to keep the bending moment at the tower constant. The rotor speed is kept constant, so that all other systems in the drivetrain can remain the same. This is achieved by designing the turbine to operate at a lower induction, which makes the turbine a so-called low induction turbine [11].

The first results from the AVATAR project are already available from a comparison of the CFD models. From an examination of the rotational effects on the AVATAR turbine, it is found that the lift coefficient at the inner part of the blade is larger compared to 2D airfoil data. At the inner part of the blade, the CFD simulations show delayed separation and a smaller wake size, which is expected to be caused by centrifugal and Coriolis forces (rotational effects) [32]. It should be noted that both BEM and AWSM are not capable of taking these effects into account, since both models use look-up tables for the airfoil polars.

Also, an examination of the steady and unsteady power curve of the 10MW reference turbines with CFD simulations is available. From this comparison it is found that the differences between the steady and unsteady calculations are mainly noticeable near the root section of the blade. It is expected that this difference between the steady and unsteady simulations is caused by flow separation and vortex shedding [33]. It should be noted that AWSM is able to calculate the effects of vortex shedding intrinsically, whereas BEM uses an engineering model to account for the root and tip vortex.

Chapter 4

Code Description

In this section a description of the codes that will be used in this thesis is presented. First, the coupling between the ECN-Aeromodule (ECNAero) and Phatas will be explained, which leads to the aeroelastic code PhatasAero. Next, a description of the two aerodynamic modules in PhatasAero will be presented, as well as a description of the engineering correction models that have been added to the codes. Finally, an overview will be given with the differences between AWSM to the BEM model that is implemented in PhatasAero.

4.1 Coupling ECNAero to Phatas

The aeroelastic code that is used in this thesis is referred to as PhatasAero. In order to model the structural deformation of the blade, the aerodynamic solver ECNAero is coupled to the structural dynamics solver Phatas. Originally, Phatas has an internal BEM code, but for the implementation in PhatasAero this aerodynamic model is being replaced by the aerodynamics module of ECNAero, consisting of a BEM and vortex wake code. This is done as shown in Fig. 4.1. It should be noted that the BEM model in PhatasAero is very similar to the BEM model in Phatas, although small differences are present due to specific implementations.

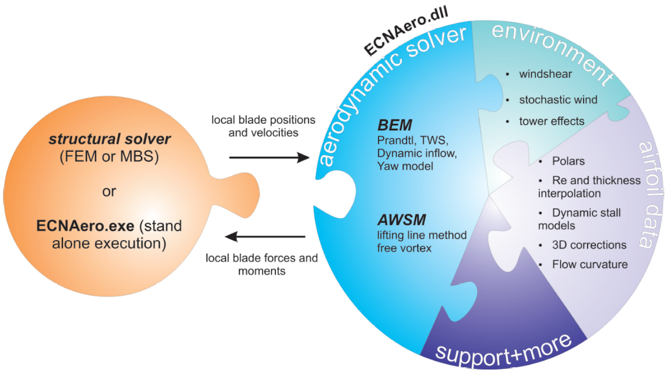

Figure 4.1: *Overview of the program content of the coupling between ECNAero and Phatas, from [4].*

The aerodynamic solver calculates the local forces and moments, which will be send to the structural solver (Phatas), which returns the local blade positions and velocities. A great advantage of this coupling is that ECNAero has an option for both a BEM and a vortex wake model (AWSM). In this way the BEM and AWSM code can be compared with the guarantee that the structural dynamics will be solved in the exact same way. For the scope of this thesis, the structural model inside Phatas will not be covered.

4.2 Description of ECNAero-AWSM

The non-linear lifting line free vortex wake code that will be investigated in this thesis is the Aerodynamic Windturbine Simulation Module (AWSM), developed by ECN [5]. In this model, the vorticity created by a two-dimensional blade section (airfoil) is calculated by a lifting line model, which will be described in Section 4.2.1. As time advances, vortex points with lumbed vorticity are shed in the wake. A description of the wake definition will be presented in Section 4.2.2.

4.2.1 Lifting Line Model

The flowfield around a three-dimensional body (blade) can be represented through a distribution of sources σ and vortices ω, as is shown in Fig. 4.2a. It should be noted that this representation of sources and vortices is equivalent to the flowfield representation of velocity vectors. In AWSM, the effect of thickness or displacement is not taken into account leading to $\sigma = 0$ in the complete flow domain, such that only vorticity effects are modeled.

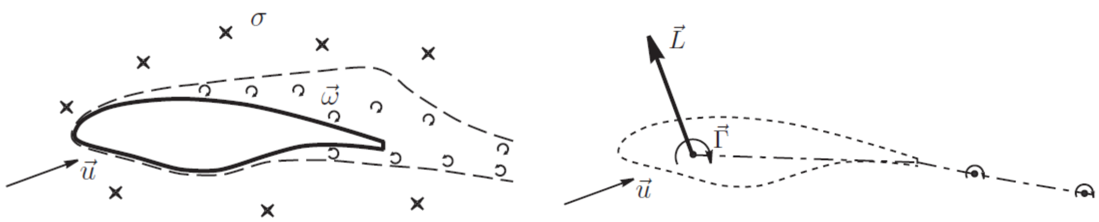

(a) *Distribution of sources and vortices.* (b) *Lifting line.*

Figure 4.2: *Representation of the flowfield model, from [5].*

In AWSM, the vorticity is modeled as a line integral, where vorticity in lumped at the quarter chord point of the airfoil in a blade section, as can be see in Fig. 4.2b. This lifting line method does not take thickness effects into account and it is assumed that lift only acts at the quarter chord position. The elementary force on a blade section is described by the Kutta-Joukowski equation, which relates the bound vorticity Γ (circulation) at the quarter chord position to the lift force per unit length that will act on the blade section, as shown in Eq. 4.1 [34].

$$d\vec{L} = \rho(\vec{u} \times \vec{\Gamma}) = \rho\Gamma(\vec{u} \times d\vec{l}) \tag{4.1}$$

All vortex lines are part of a closed vortex ring, according to Kelvin's circulation theorem, which states that vortex tubes cannot have free ends and have to be closed. The velocity field induced by a vortex is expressed by the Biot-Savart law, which can be expressed analytically by position vectors, starting from the vortex, as shown in Eq. 4.2 [35].

$$\vec{u}_\Gamma(\vec{x}_p) = \frac{\Gamma}{4\pi} \frac{(r1 + r2)(\vec{r_1} \times \vec{r_2})}{r_1 r_2 (r_1 r_2 + \vec{r_1} \cdot \vec{r_2})} \tag{4.2}$$

where $\vec{r_1}$ and $\vec{r_2}$ are the position vectors from the start and end of the vortex line (Γ) to the evaluation points at which the induced velocity is calculated, $\vec{x_p}$, as is shown in Fig. 4.3. In case the evaluation point $\vec{x_p}$ is close to a vortex line, Eq. 4.2 behaves singular. Therefore, a vortex cut-off function is implemented which limits the induced velocity near a vortex line.

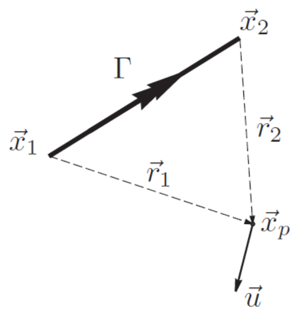

Figure 4.3: *Vortex line geometry, from [5].*

4.2.2 Wake Definition

Different than for BEM codes, with AWSM there is a lot of freedom when it comes to defining the wake, both in wake configuration as well as in wake size. The wake is made out of vortex-lattice nodes, also referred to as wake points, which are shed into the wake every time step. The vortex strength in the wake is evaluated in terms of the circulation Γ, as defined by:

$$\Gamma = \oint \vec{u} \cdot dS \tag{4.3}$$

where $\vec{u}$ is the velocity along the curve dS, which encloses the vortex. In Fig. 4.4, the wake geometry is shown after four time-steps. The position of the first shed vortex is at 25% of the chord downstream, whereas the position of the downstream part of the wake is determined each time-step by convection due to the onset wind velocity and the induced velocity of all bound and trailing vortices.

In AWSM, there are two types of wake points defined, being the fixed and free streamwise wake points. The main difference is that the latter is free to roll up through wake self-influence [25], meaning that the induced velocity of a wake points is calculated by the influence of all other wake points.

In AWSM there are three different wake configurations implemented in terms of how the wake convection is described and for each of these methods there is still some freedom to further define the wake. An illustration of the three concepts is shown in Fig. 4.5. The variable that is used in the software to specify the different options is PRSCRBWAKE.

The first option is to have no wake prescription, this means that the wake convection is only dependent on the induction from the wake points and the onset wind velocity. The first part of the wake behind the rotor consists of free wake points, i.e. the free wake, for which the convection speed is calculated from the influence of all bound and trailing vortices. The second part of the wake is fixed and the convection speed is determine at the free to fixed wake boundary. The amount of fixed wake points is the difference between the total wake points and the free wake points.

The second option is to have the wake convection prescribed as a function of the local blade induction and axial distance from the rotorplane, according to BEM theory. This can be combined

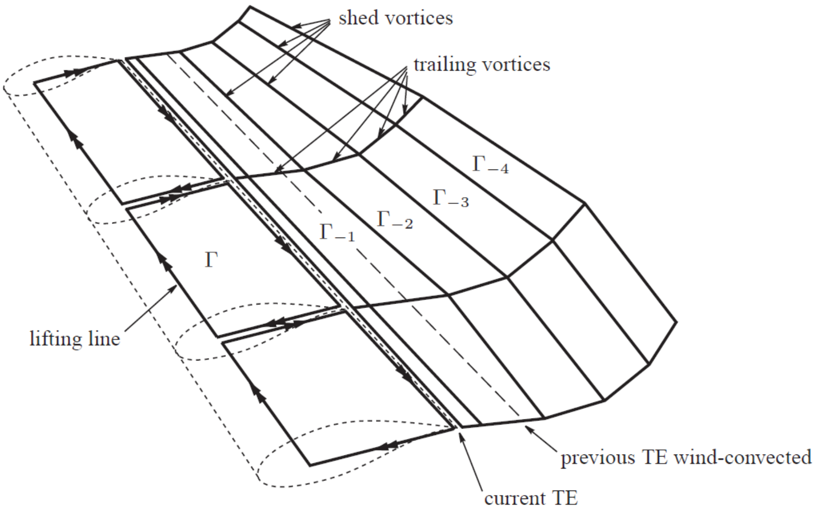

Figure 4.4: *Vortex wake geometry, from [5].*

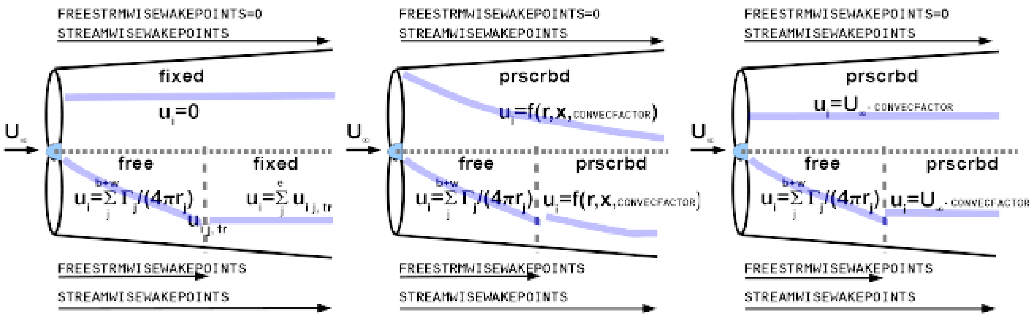

(a) PRSCRBWAKE=0 (b) PRSCRBWAKE=1 (c) PRSCRBWAKE=2

Figure 4.5: *Illustration of the different wake configurations, from [4].*

with a partial free wake, where the first part of the wake consists of free wake points, resulting in a hybrid free-prescribed wake. The value of the induced velocity in the prescribed wake part can be adjusted by a so-called convection factor.

The final option is to have a constant wake convection, where the induction velocity is set as a constant value as a fraction of the inflow velocity. This convection factor is similar to the induction factor and can be obtained by first running a BEM simulation.

4.3 Description of ECNAero-BEM

As introduced in Section 2.1, BEM models are based on the theory of coupling the momentum equation with the local forces from the blade element equation. This theory has been developed over the past eighty years, resulting in many different implementations. An important part of the implementation is on which level the BEM equations are evaluated. For the classical theory, the rotor plane is divided into a set amount of sections, referred to as annuli, as is shown in Fig. 4.6. For each of these annuli, an average induction factor is calculated over the complete rotor revolution (i.e. azimuth averaged). In this way the effect of a varying induction over the blade is included in the model. For each annulus, the axial force F_{ax} can be calculated from momentum conservation using the following relation:

$$F_{ax} = \dot{m}(U_4 - V_w) = \rho V_w^2 2a(1-a)A_r \tag{4.4}$$

where $\dot{m}$ is the mass flow in the streamtube associated with the annulus, V_w and U_4 are the wind velocity far upstream and far downstream, ρ is the density, a is the induction factor and A_r is the cross sectional area of the annulus. The parameter that is unknown to solve this equation is the induction factor, which represents the velocity reduction due to the extraction of energy by the rotor. The induction factor can be found by balancing the momentum conservation equation with the blade element equation by adding up the contribution of each blade in the axial direction. The contribution from each blade in axial direction on an annulus level can be expressed by:

$$dF_{ax} = L\cos\phi dr \tag{4.5}$$

where, L is the lift force, ϕ is the inflow angle in order to make sure the force is acting in axial direction and dr represents the part of the blade in the annulus. Important to note is that the sectional drag does not influence the calculation of the induction factor, since it is argued that the drag only influences the velocity in the wake, which is not considered to be part of the induction factor. By balancing Eq. 4.4 and Eq. 4.5, the induction factor can be calculated iteratively.

For the BEM model implemented in ECNAero, each annuli of the rotor plane is further divided into a separate streamtube for each blade. For each of these sections, a local balance is obtained between the momentum in this streamtube and the forces acting of the blade. From this balance, the induction factor is calculated for each separate blade per annulus. In the equation for the conservation of momentum, the inflow velocity at the blade element is determined and applied to the complete streamtube. In case of a varying inflow velocity, this means that the momentum in each streamtube per annulus is dependent on the inflow velocity for the blade section associated with the streamtube. The convergence criteria implemented in the BEM model of ECNAero is based on the convergence of the mean induction factor over the blades. This mean induction factor is important in the implementation of ECNAero-BEM, since both the yaw and dynamic inflow model are based on the mean induction per annulus. It is important to note that this might lead to a converged solution of the average induction, although the local induction (for each blade) has not reached convergence.

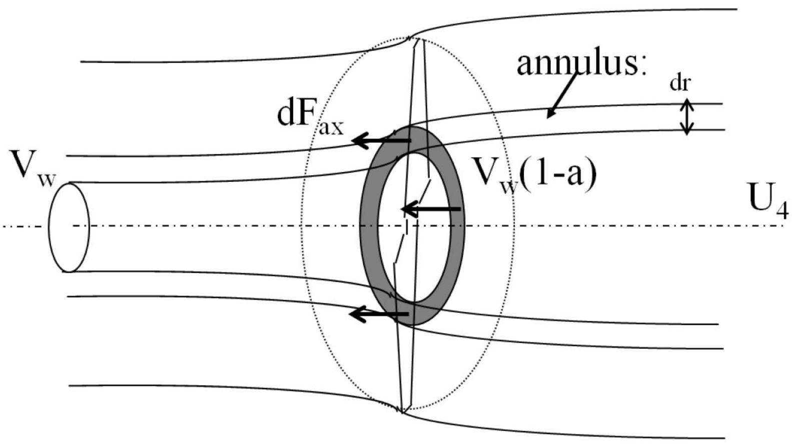

Figure 4.6: *Division of the stream tube in annuli, from [2].*

4.4 Engineering Models

Besides the implementation of the BEM equations, large difference between the many number of BEM models stem from the implementation of the engineering models. In the following sections, the engineering models as implemented in the BEM model of ECNAero will be described. The engineering models associated with stall (Stall Delay and Dynamic Stall) are also implemented in the AWSM code, since AWSM models the local aerodynamic through look-up tables, similar to BEM.

4.4.1 Prandtl Correction

The BEM theory is based on a solid disk, which could be represented by an infinite amount of blades for the rotor. However, since the rotor has a finite number of blades, a vortex is shed in the wake due to the discontinuity of the solid surfaces in the rotor plane. It is found that due to the finite number of blades, a root and tip vortex are present, which decrease the local induction on the blade. This correction was first described by Prandtl and is therefore referred to as the Prandtl correction [36]. The Prandtl tip factor F at the radial position r implemented in ECNAero-BEM is as follows:

$$F = 2/\pi \cdot \arccos(e^{-\pi(R-r)/d}) \tag{4.6}$$

where d is the distance between the trailing vortex sheets and R is the total radius of the blade. A similar equation is used to model the root vortex, where the combined Prandtl factor relates the annulus averaged axial and tangential induction factor to the local induction.

4.4.2 Yaw Model

Since the BEM theory is derived for a rotor plane perpendicular to the wind direction, corrections for the effects of yawed inflow have to be included. The advancing and retreating effects are intrinsically included in the BEM model. However, the effects of a skewed wake have to be included using an engineering model. The skewed wake effects are caused by the trailed tip vortices, which are on average closer to the downwind side of the rotor plane, resulting in a higher value for the axial induced velocity, according to the Biot-Savart law. It should be noted that for yawed flow, the wake skew angle is larger than the yaw angle between the rotor plane and the incoming wind. This means that the wake deflects more than just by the yaw angle, resulting in an increase of the wake skewness effects [37]. The two engineering models for yawed flow that are implemented in ECNAero-BEM will be described below.

Glauert Yaw Model

The first model that is considered is the yaw model developed by Glauert in 1926 [38]. From helicopter aerodynamics, the imbalance of the axial induction velocity due to the skewed wake is expressed as:

$$u_{i,ax} = \overline{u_i} \cdot [1 - K_c f(\frac{r}{R}) sin\phi_r] \tag{4.7}$$

where ϕ_r is the yaw angle. It should be noted that this sinusoidal variation of u_i only includes the influence of the tip vortices and is based on the average rotor induced velocity, $\overline{u_i}$. The value for

K_c is dependent on the wake shape and thus the yaw angle. For the radial dependency f, Glauert proposed a linear relationship:

$$f(\frac{r}{R}) = \frac{r}{R} \tag{4.8}$$

ECN Yaw Model

The second model that will be described is the ECN yaw model, as developed by Schepers in 1999 [39]. The model determines the variation of wake induced axial velocity as function of blade azimuth angle, radial position and yaw angle. The model is derived from and validated with wind tunnel measurements.

The yaw model is based on Equation 4.7, as expressed by Glauert. However, for the ECN yaw model this equation is not based on the average induced velocity, but is applied to each annuli independently. Furthermore, the radial dependency, as well as the yaw angle dependency is modeled differently.

The engineering model for yawed flow is obtained by a second order Fourier fit of measurements taken from experiments of the axial velocity at different radial positions and yaw angles, as function of azimuth angle. The amplitude (A) and phases (ψ) as obtained from the axial velocity are transformed to the A and ψ for u_i and related to $\overline{u_i}$. This results in an expression for positive yaw:

$$u_{i,ax} = \overline{u_i}[1 - A_{1,i}cos(\phi_r - \psi_1) - A_{2,j}cos(2\phi_r - \psi_2)] \tag{4.9}$$

From a comparison with load measurements on actual wind turbines, the values for A and ψ have been refined.

4.4.3 Turbulent Wake State

According to BEM theory, the wake velocity far downstream of the rotor plane is $U = U_\infty(1 - 2a)$. In case $a > 0.5$ (heavily loaded rotor), BEM theory predicts flow reversal in the wake far downstream. In reality, the wake will transform into a so-called turbulent wake state (TWS), where the air from outside is sucked into the streamtube. It is found that for a turbulent wake state, the thrust coefficient C_T does not follow the momentum theory ($C_T = 4a(1 - a)$) [6]. In Fig. 4.7, C_T is shown for as function of the induction factor for various wake states. From this figure, it can be seen that the momentum theory for a turbine is valid for a low induction factor ($0 < a < 0.4$). When the induction is further increased, the turbine will reach a TWS. In Fig. 4.7, it can be seen that form experimental results there is a large uncertainty in C_T.

The TWS equation implemented in the BEM model of ECNAero, the quadratic relationship between the thrust coefficient C_T and a is replaced by a linear relationship tangent to the quadratic line at the specified induction value. The induction value at which the TWS starts can be specified by the user, although the default value is set to 0.38. Despite the large uncertainty in the modeling of the TWS, modern wind turbines are usually not designed for such situations since the power coefficient decreases after $a = 0.33$, whereas the loads continue to increase.

4.4.4 Dynamic Inflow

In case a wind turbine is subjected to changing conditions, i.e. a pitch action, rotational speed variation or wind speed variation, the aerodynamic 'inertia' of the rotor will affect the axial

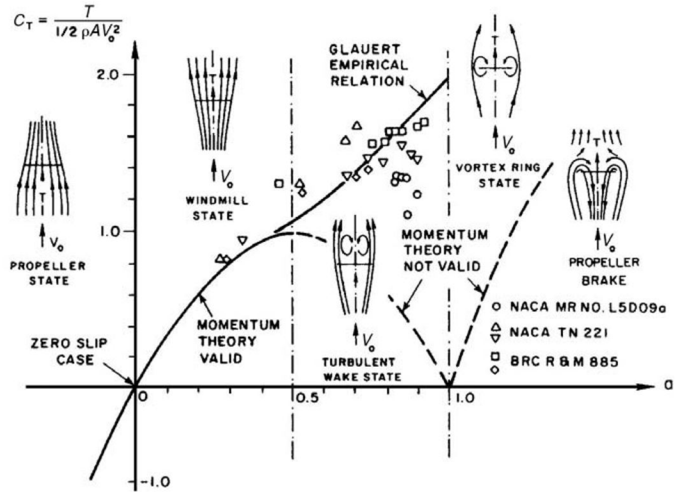

Figure 4.7: *The measured thrust coefficient C_T as a function of the axial induction factor a and the corresponding rotor states, from [6].*

momentum equation. Physically, this can be explained by the fact that the air around the blade has to be accelerated or decelerated, resulting in a lagging induced velocity. In AWSM, this effect is intrinsically modeled by the vorticity in the wake points, as is visualized in Fig. 4.8. In case of dynamic inflow, the vorticity of the wake points will adjust to the new situation, but the vorticity of the 'old' wake points will still affect the calculation of the induced velocity at the blade. This effect of shed vortices results in a sort of damping due to the wake, which results in a decrease of load amplitude.

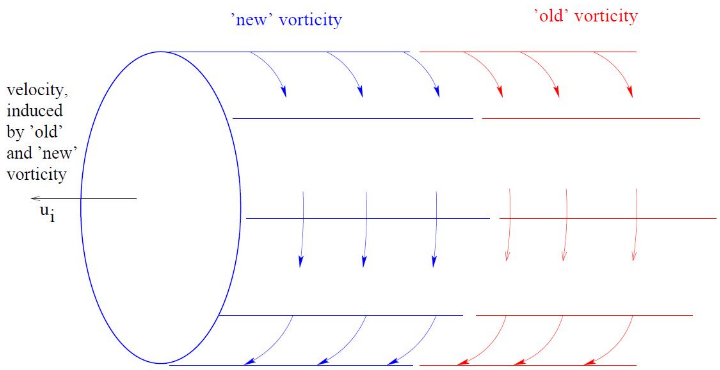

Figure 4.8: *Visualization of the wake due to dynamic inflow, from [2]*

In order to model this so-called lag in induced velocity, a dynamic inflow model is implemented in the BEM model of ECNAero. This dynamic inflow model adds another term to the axial momentum equation described in Eq. 4.4. This additional term is based on a first order time derivative of the induced velocity u_i:

$$\tau du_i/dt + 4u_i(1-u_i) = V_w C_T \tag{4.10}$$

where τ is the time constant, which has a dependency on the radial position [40] and C_T is the axial force or thrust coefficient.

4.4.5 Stall Delay

The stall delay model implemented in ECNAero is a three-dimensional correction model developed by Snel [41]. This model takes the effects of rotation on the airfoil coefficients into account. These airfoil coefficients are obtained from experiments in a two-dimensional environment, where the lift, drag and moment coefficient is determined as function of AoA and stored in look-up tables. These look-up tables are used to determine the sectional forces and moment on a blade section.

It should be noted that both BEM and AWSM use these look-up tables for the airfoil coefficients and the stall delay model implemented in ECNAero is therefore used in both the BEM and AWSM module.

4.4.6 Dynamic Stall Models

Dynamic stall models are implemented in ECNAero to account for the fact that the aerodynamics on a blade section does not respond instantaneously to changing environmental conditions, like turbulent inflow, blade deformation and tower effects. Similar to the stall delay model, the dynamic stall model alters the airfoil coefficients from the static look-up tables. This also implies that the dynamic stall models are used in both BEM and AWSM.

The physical explanation behind dynamic stall is that due to time-dependent pitching, plunging, vertical translation or other movements, the local AoA can increase above stall. With the increasing AoA, a vortex is shed at the leading edge of the airfoil, causing the lift to rapidly increase. When the vortex has passed the airfoil, a large drop of the lift force is followed, which results in cyclic pressure loading (lift hysteresis). The dynamic stall characteristic is important to determine the aerodynamic damping of vibrations in stall, which is important for the ultimate load on the blades. In ECNAero, four different dynamic stall models are implemented, being the first and second order Snel model, the ONERA model and the Beddoes-Leishman model, which will be described below [42]. It should be noted that the implementation of the ONERA and Beddoes-Leishman models in PhatasAero has not yet been fully tested.

Snel Model The default dynamic stall model implemented in ECNAero is developed by Snel [43]. The model describes the evolution of sectional load coefficients as a function of the AoA and time derivatives by means of Ordinary Differential Equations (ODEs). It should be noted that this model is semi-empirical and does not require airfoil specific parameters, which is the case with many dynamic stall models. The model consists of two ODEs; a linear ODE for the forcing terms and a non-linear ODE for the self excited oscillations. The dynamic lift coefficient can be described as the sum of the steady lift coefficient plus the contribution of the Δc_l from the first and second order ODE. In ECNAero, there is the option to choose for either the first or the combined first and second order ODE.

$$c_{l,dyn} = c_{l,steady} + \Delta c_{l1} + \Delta c_{l2} \tag{4.11}$$

The linear ODE is based on the Beddoes Leishman model and determines the Δc_l on the difference between the potential and steady c_l. The non-linear ODE models the high frequency dynamics, which are sustained even if there is no forcing.

ONERA Model The third model is the ONERA model, which also describes the unsteady airfoil behavior by a first order ODE for the inviscid attached flow and a second order ODE for the non-linear viscous effects, associated with stall. It should be noted that this model requires many empirical coefficients for the ODE equations. In case these are not available, the coefficients based on the angle of attack are taken as coefficient for a flat plate and the lift dependent coefficients are taken from a so-called mean airfoil.

Beddoes-Leishman Model This dynamic stall model has an emphasis on the complete physical representation of dynamic stall. The Beddoes-Leishman dynamic stall model consist of four separate modules, being: [44]:

- A model for attached flow for unsteady linear aerodynamic forces.
- A model for separated flow for non-linear forces.
- A dynamic stall onset model.
- A model for vortex induced aerodynamic forces.

The first two sub-models are quit similar to the implementation of the ONERA and Snel models. The onset of leading edge flow separation can be represented by a critical leading edge pressure and associated pressure gradient. The definition of this onset is considered to be the most important aspect of dynamic stall modeling [45]. The last sub-model describes the effect of vortex shedding by defining a so-called vortex lift as the difference between the linearized value of the unsteady circulatory lift and the unsteady non-linear lift. One of the advantages of the Beddoes-Leishman model is that it takes flow separation explicitly into account by means of the vortex lift.

4.5 Differences between BEM and AWSM in PhatasAero

When comparing the application of AWSM in dynamic load case simulations with the conventional BEM code, it is important to know what the fundamental differences are in modeling between BEM and AWSM. In Table 4.1, an overview is given for how BEM and AWSM take certain effects into account. In this overview, a classification is made based on a global or local effect, where local effects refer to effects in the boundary layer and global effects to effects of the complete flow field. Stationary effects are defined as time-independent inflow effects with respect to the complete rotor.

It is interesting to observe that all global effects are covered by AWSM, whereas the local effects are modeled by engineering models. This is the case, since AWSM uses a look-up table for the two-dimensional aerodynamic polars, similar to BEM. With regards to the induction, it is observed that BEM does not take the radial induction into account, which results in wake expansion. Furthermore, the engineering models as described in the previous section are stated here as well.

Table 4.1: *Classification of the aerodynamic situations, adapted from [9].*

Aerodynamic situation	**Classification**	**BEM**	**AWSM**
Axial induction	Global/ stationary	Intrinsic	Intrinsic
Tangential induction	Global/ stationary	Intrinsic	Intrinsic
Radial induction	Global/ stationary	Not included	Intrinsic
Finite number of blades	Global/ stationary	Engineering model	Intrinsic
Oblique inflow	Global/ stationary	Engineering model	Intrinsic
Turbulent wake state	Global/ stationary	Engineering model	Intrinsic
Dynamic inflow	Global/ non-stat.	Engineering model	Intrinsic
Stall delay	Local/ stationary	Engineering model	Engineering model
Dynamic stall	Local/ non-stat.	Engineering model	Engineering model

Chapter 5

Computational Set-up

In order to compare the aeroelastic free vortex wake code AWSM with conventional BEM codes, it is important to use many different test cases in order to see how the codes analyze a wind turbine in different environmental conditions. In this research, two 10MW reference wind turbines are analyzed for a set of test cases, being the INNWIND [12] and the AVATAR turbine [13]. The test cases that are simulated on these turbines include Axial Inflow (Section 5.1), Yawed Inflow (Section 5.2), Half Wake (Section 5.3), Extreme Wind Shear (Section 5.4), Turbulent Inflow (Section 5.5) and Pitch Step (Section 5.6). It should be noted that the last test case is performed on a different turbine, which represents the model used in the New MEXICO experiment, from which experimental data is available for validation.

Each of these cases will be separately described in this chapter, although a more detailed description of each of these test cases can be found in the appendices to this thesis. For the wake settings of the free and prescribed wake configuration, a default wake length of three rotor diameters is taken. For the free wake configuration, the first two rotor diameters are usually filled with free wake points, whereas the the prescribed wake configuration only one rotor revolution of free wake points is used to model the nearby wake dynamics. Deviations from these default wake settings will be described in the test cases.

5.1 Axial Inflow

The first test case that will be considered is a wind turbine in uniform axial inflow without shear. It is expected that for this test case the results from BEM and AWSM give similar results, since the BEM theory is based on axial inflow conditions. The analysis is done on both the INNWIND and AVATAR reference wind turbines. As part of a deliverable for the AVATAR project, already some simulations have been performed with AWSM and BEM under axial inflow. However, these simulations have only been performed at rated wind speed. Furthermore, the AWSM simulations for the AVATAR turbine at rated wind speed experienced convergence problems and have therefore not been completed. In this section the simulations will be performed in the partial load regime with a wind speed of 8 m/s for both the AVATAR and INNWIND turbine. A more detailed description of this test case can be found in Appendix A.

Table 5.1: *Overview of the simulations for axial inflow at* $8m/s$.

#	Turbine	Code	Wake	N_{free}	N_{total}	ω [rpm]	CPU [hr]
1	INN	BEM	-	-	-	6.44	≈ 0.02
2	INN	AWSM	Free	449	674	6.44	119.48
3	INN	AWSM	Prescribed	63	674	6.44	21.01
4	AVA	BEM	-	-	-	6.00	≈ 0.02
5	AVA	AWSM	Free	436	654	6.00	105.54
6	AVA	AWSM	Prescribed	67	654	6.00	20.00

5.1.1 Description of Test Case

The simulation is run for the BEM model, as well as the vortex wake model with a free and prescribed wake configuration. The simulation is run with a time-step of $\Delta t = 0.15s$ and with the controller off. The rotor speed and pitch angle settings are determined by running a BEM simulation with $\Delta t = 0.01s$ and taking the average values over the simulation time. This results in a rotor speed of 6.44 and 6.00 rpm for the INNWIND and AVATAR turbine respectively, as well as a pitch angle of $0°$ for both turbines.

An overview of which simulations that have been run with a straight uniform straight inflow at $8m/s$ is shown in Table 5.1. From the table it can be seen that for the prescribed wake simulation the amount of free wake points is significantly lower, which results in much lower computational time. It can be seen that the difference between the BEM and AWSM prescribed wake simulation is a factor of 10^3 in CPU time. It should be noted that BEM simulations usually take a much smaller time step, resulting in a CPU time of about 10 times higher, although this is still much lower compared to AWSM. Finally, it can be seen that there is a significant difference in CPU time between the free and prescribed wake configuration, due to the free wake points, which significantly increase the CPU time.

5.1.2 Opportunities and Limitations

In this section the opportunities and limitation of this test case are presented. Since the BEM theory is derived for a wind turbine in axial inflow, it is expected that the results from this test case will generate accurate results from the BEM model. Due to the absence of unsteady conditions, engineering models like the root and tip correction and the tower model can be compared between BEM and AWSM.

Some assumptions and simplifications have been used for this simulation in order to keep the CPU time limited and still get a fair comparison between BEM and AWSM. The first limitations of this test case is that the simulations are done without a controller. The effect of a changing rotor speed and pitch angle is therefore not modeled. Furthermore, the assumption is made that the BEM and AWSM model will reach the same steady values for rotor speed and pitch angle in order to compare the two models at the same operational conditions. It is more than likely that the exact values for the rotor speed will be different when calculated with two different models. Additionally, there is the limitation of the large time step, which is chosen in order to limit the CPU time of the simulations. I is shown that a larger time step will result in a different behavior of the codes, although this impact is limited by setting the rotor speed to the steady value of the simulation that was performed with a time step of $0.01s$. For more details on these settings, the reader is referred to Appendix A. Finally, this large time step also filters out high frequency dynamics. However, since this case has a uniform axial inflow these effects are expected to be insignificant.

5.2 Yawed Inflow

The second test case that will be considered is a wind turbine in yawed conditions without shear. The yaw angle is set to 30°, which results in advancing and retreating effects as well as skewed wake effects. Although the advancing and retreating effects are calculated intrinsically for both BEM and AWSM, an engineering model is implemented for BEM codes in order to model the skewed wake effects. AWSM models the skewed wake effects intrinsically by the wake definition. A more detailed description of this test case can be found in Appendix B.

5.2.1 Description of Test Case

The simulations for the yawed inflow case are run with the BEM and vortex wake model, both with a free and prescribed wake configuration. For the BEM model, both the yaw model of ECN and the Glauert yaw model have been used. The analysis is done on both the INNWIND and AVATAR reference wind turbine at a wind speed of $8m/s$. The simulations have been performed with a time-step of $\Delta t = 0.15s$ and with the controller off.

An overview of the simulations that have been run for the extreme yaw case are listed in Table 5.2. It can be seen that the lower amount of free wake points for the prescribed wake configuration results in a much lower CPU time. The prescribed wake configuration results in a reduction in CPU time of about 5 to 6 times.

Interesting to see is that there is also a significant difference in CPU time between the INNWIND and AVATAR turbine, where the INNWIND turbine requires $\approx$ 50% more CPU time. This difference is due to various factors. First, there is the fact that the INNWIND turbine has more blade elements, resulting in more wake points (+10%). Second, there is the fact that the INNWIND turbine has a higher induction, which means that the wake velocity is lower and there are more streamwise wake points required to reach three rotor diameters of wake length. However, this effect is canceled out by the fact that the INNWIND has a lower rotor diameter, which means the wake length of three rotor diameters is smaller compared to the AVATAR turbine. Finally, the most interesting and most contributing difference is that for the INNWIND turbine, more sub-iterations are required on average between the aerodynamics and structural model in PhatasAero. It is found that the INNWIND turbine requires 14.77 sub-iterations on average, whereas the AVATAR turbine only uses 12.62 sub-iterations. Since the aerodynamic module is only called at the first sub-iteration and every sub-iteration larger or equal to 9, the INNWIND turbine requires 38% more calls of the aerodynamic module. This result is similar for the free and prescribed wake configuration.

Table 5.2: *Overview of the simulations for yawed inflow at* $8m/s$.

#	Turbine	Code	Wake	Yaw model	N_{free}	N_{total}	ω [rpm]	CPU [hr]
1	INN	BEM	-	ECN	-	-	6.00	≈ 0.02
2	INN	BEM	-	Glauert	-	-	6.00	≈ 0.02
3	INN	AWSM	Free	-	395	592	6.00	131.55
4	INN	AWSM	Prescribed	-	67	592	6.00	26.75
5	AVA	BEM	-	ECN	-	-	6.82	≈ 0.02
6	AVA	BEM	-	Glauert	-	-	6.82	≈ 0.02
7	AVA	AWSM	Free	-	413	619	6.82	82.23
8	AVA	AWSM	Prescribed	-	59	619	6.82	14.13

5.2.2 Opportunities and Limitations

In this section the opportunities and limitations of this test case will be described. For the yawed inflow case, the effects of the engineering models for oblique inflow can be checked, which models the skewed wake effects. The yaw models that will be compared in this test case are the ECN and Glauert yaw model. Furthermore, the effect of the advancing and retreating blade can be compared as well as the validity of BEM models in yawed inflow in terms of blade and tower loads.

Similar limitations are found for the yawed inflow case as for the straight uniform inflow case, since both test cases deal with a uniform inflow, fixed rotor speed and pitch angle and use the same time-step.

5.3 Half Wake

The third test case that will be considered is a wind turbine in the half wake of another wind turbine at 8 rotor diameters distance. This test case creates a variation in the inflow velocity for different azimuth positions of the blade.

For this test case the INNWIND turbine is tested at a wind speed of $8m/s$, where there is a deficit in the inflow velocity due to a wind turbine at eight rotor diameters upstream. The INNWIND turbine was chosen since this turbine was found to be more challenging than the AVATAR turbine from a modeling point of view, from the results of the axial inflow and yawed inflow test case. The minimum wind speed in the rotor plane with an inflow velocity of $8m/s$ is found to be below $4m/s$, which is lower than the cut-in wind speed of the INNWIND turbine. Therefore, it is expected that there are large variations in the blade loads, depending on the azimuth position of the blade.

5.3.1 Description of Test Case

Similar to the test cases of axial and yawed inflow, a time step of $\Delta t = 0.15s$ is used in order to keep the CPU time of AWSM limited. Since the BEM simulations for the half wake case have already been completed for the AVATAR project deliverable, the operational conditions from this test case have been used for the simulation of AWSM as well. This means that the rotor speed is kept constant at 5.75 rpm and the pitch angle is kept constant at $0°$.

The wind file that is used for this simulation is based on the wake deficit files that have been created with HAWC2 in the AVATAR project. From these deficit files the 3D wind speed vector is calculated in a rectangular grid for each time-step, although it should be noted that the wind speed is constant throughout the simulation. The results from the wind file are shown in Fig. 5.1. In this figure, the rotor center is located at [Y,Z]=[0,119], where the latter is the hub height of the INNWIND turbine in meters. It can be seen that on the right side of the rotor plane, the wind speed is $8m/s$, except for a small area near the center due to wake expansion. This means that the free-stream velocity will be $8m/s$ for azimuth angles between $0°$ and $180°$ for the blade. In the second half of the revolution, the incoming velocity will decrease and increase with a certain value, depending on the radial position, where the largest differences are found in the outer part of the blade.

An overview of the simulations that have been run for the half wake case are listed in Table 5.3. It can be seen that the lower amount of free wake points for the prescribed wake configuration results in a much lower CPU time. The prescribed wake configuration with 70 free wake points results in a reduction in CPU time of about 5 to 6 times, similar to the uniform and yawed inflow case. It can be seen that the prescribed wake configuration with 210 free wake points requires more than twice the CPU time, although it is still only 40% of the time required for the free wake configuration.

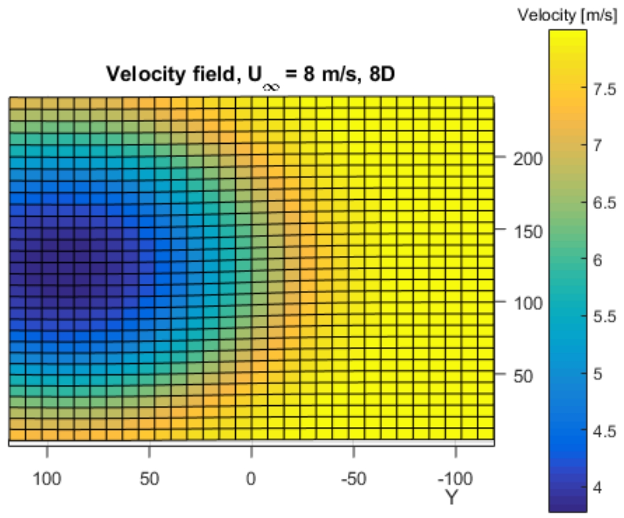

Figure 5.1: *Velocity field for the half wake case.*

Table 5.3: *Overview of the simulations for the half wake case at* $8m/s$.

#	Turbine	Code	Wake	N_{free}	N_{total}	ω [rpm]	CPU [hr]
1	INN	BEM	-	-	-	5.75	≈ 0.02
2	INN	AWSM	Prescribed	70	778	5.75	38.97
3	INN	AWSM	Prescribed	210	778	5.75	86.18
4	INN	AWSM	Free	415	778	5.75	213.18

5.3.2 Opportunities and Limitations

For the half wake test case, the effects of a non-uniform inflow velocity over the rotor plane can be compared between BEM and AWSM. It is interesting to see how BEM and AWSM deal with the varying inflow velocity over the azimuth positions and how this affects the calculation of the loads on the blade and the tower.

Similar limitations have been found for the half wake test case as for the axial and yawed inflow cases. Again, the simulations have been performed with the controller off and a time-step of $\Delta t = 0.15s$. Since the velocity is varying over the rotor plane, it is expected that the absence of the controller might have a larger influence on the results. The assumption is made that the wake deficit files which serve as an input for the wind file are representative for the flowfield in the wake of a wind turbine. Furthermore, due to time considerations, only one turbine has been selected for this test case at one specific distance from the upstream wind turbine.

5.4 Extreme Wind Shear

For this test case, the wind turbine is analyzed when it is subjected to an extreme transient shear, as defined by DLC 1.5 according to IEC61400 Edition 3 [46]. Due to simulation time considerations, only one test case from this DLC is chosen. In this test case, a positive vertical wind shear is considered, meaning that the wind speed increases with height. During the transient, this variation in wind speed over vertical position increases, resulting in a large increase in inflow wind speed for the top part of the rotor plane, whereas the wind speed at the lower part of the rotor plane decreases further.

Similar to the half wake case, the INNWIND turbine is chosen, since this turbine is more challenging from a modeling point of view. The wind speed at hub height is $9.4m/s$ throughout the complete simulation, even when the transient shear occurs. The time period for the transient shear is defined by IEC standard to be 12 seconds. For the rest of the simulation, the wind profile is defined by a vertical exponential wind shear, with a wind shear exponent of 0.2. Finally, the DLC also specifies an uptilt angle of 8°, which means that there is a component in the vertical direction from the inflow velocity. Interesting from this test case is to see how the models cope with the sudden increase and decrease in wind speed and how this affects the calculation of the loads on the blade and in the tower. Furthermore, comparison data is available from the AVATAR project by DTU Wind Energy (BEM) and NTUA (BEM and vortex wake).

5.4.1 Description of Test Case

An overview of the simulations that have been run for the extreme wind shear case are listed in Table 5.4. It can be seen that the lower amount of free wake points for the prescribed wake configuration results in a reduction of CPU time of almost a factor of 7. When comparing the CPU times for the EWS case compared to the half wake case, it can be seen that EWS requires only half the CPU time, which can be explained by the lower simulation time ($140s$ instead of $180s$) and the increased rotor speed and average inflow velocity, which results in the fact that less (free) wake points are required.

Table 5.4: *Overview of the simulations for the extreme wind shear case at* $9.4m/s$.

#	Turbine	Code	Wake	N_{free}	N_{total}	ω [rpm]	CPU [hr]
1	INN	BEM	-	-	-	8.095	≈ 0.02
2	INN	AWSM	Prescribed	50	673	8.095	18.31
3	INN	AWSM	Free	359	673	8.095	123.48

The wind file used for this test case consists of the wind speed vector in a rectangular grid around the rotor plane at each time-step. In the first $120s$, the wake is developed by AWSM and the solution converges to a cyclic behavior. At $120s$, the wind shear hits the turbine. At this point, the blade which is considered is at an azimuth angle of 180°, i.e. in downward position. It is important that the blade is in the same position when the transient shear hits the blades, since the response is found to be very different depending on the azimuth position.

In Fig. 5.2, the velocity field is shown at $t = 120s$, the time-step when the shear is about to hit the turbine, and at $126s$ which is when there is the largest variation of wind speed over height. The center of the rotor is located at [Y,Z]=[0,119], where the latter is the hub height in meters.

As can be seen from Fig. 5.2a, the wind speed at the hub height is $9.4m/s$. Since the blade length of the INNWIND turbine is $89.27m$ (incl. blade root), the lowest point is $\approx 30m$, corresponding to a wind speed of $\approx 6.5m/s$, which is the lowest winds speed that will be achieve by the tip of the blade. Similarly, the highest wind speed at the tip is $\approx 10.5m/s$, resulting in a maximum difference of $\approx 4m/s$ at the tip of the blade.

From the velocity profile at $126s$ in Fig. 5.2b, it can be observed that the difference in inflow velocity is much larger of the rotor plane. It can be seen that the minimum wind speed is $\approx 0m/s$ and increases to $\approx 18m/s$ for the tip of the blade. This means that wind shear during the transient results in a difference in inflow variation of ≈ 4 times the variation compared to the normal shear. Finally, it should be noted that the wind speed is also increasing and decreasing over time during the transient, which makes this test case even more challenging.

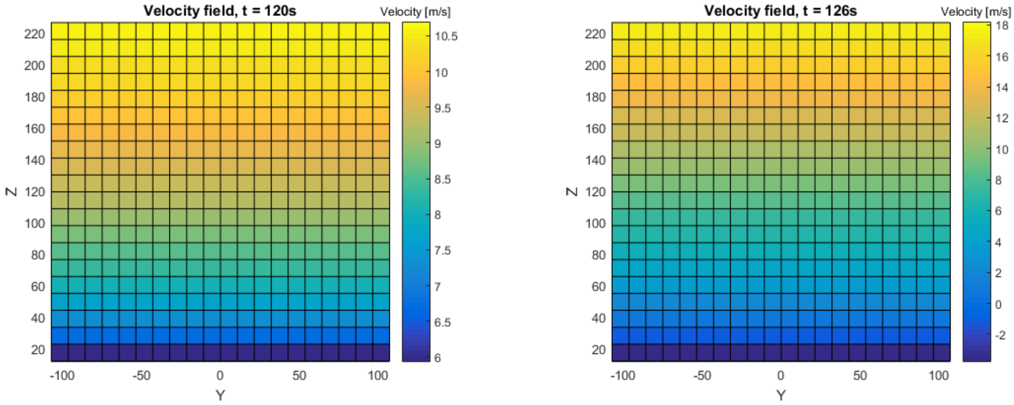

(a) $t = 120s$.

(b) $t = 126s$.

Figure 5.2: *Velocity field for the extreme wind shear case.*

5.4.2 Opportunities and Limitations

For this test case the effects of a non-uniform inflow velocity can be assessed by means of the shear. Furthermore, due to the transient between $t = 120s$ and $t = 126s$, the response to a wind speed variation can be compared, from which the effect of dynamic inflow can be compared. Furthermore, this transient results in a large variation of AoA, which allows for the comparison of dynamic stall in the root section of the blade, where the stall AoA is relatively small. Finally, this test case allows for the cross comparison with other BEM and vortex wake codes form the AVATAR project.

Similar to the previous test cases, the controller is off for comparison reasons. Furthermore, the time-step is kept at $\Delta t = 0.15s$ to keep a reasonable CPU time. Due to time considerations, only the positive vertical shear case is run, where the blade is at an azimuth position of 180°. It would be valuable to compare the results for negative shear and horizontal shear (positive and negative), as well as a different blade orientation at the point of the wind shear transient.

Finally, it should be noted that the other partners in the project have made other assumptions and simplifications, which might lead to differences as well. One major difference is the fact that both DTU Wind Energy and NTUA have the controller on during the simulation, allowing for a different rotor speed and pitch angle.

5.5 Turbulent Inflow

In this test case, a wind turbine is considered in a turbulent inflow field. With this test case, the effect of dynamic inflow can be compared between BEM and AWSM. The simulations have been run with a controller on, from which the effect of a changing rotor speed can be compared as well, which was not done for the previous test cases.

For this test case, the INNWIND turbine is considered, with an average wind speed at hub height of $8m/s$. The incoming wind velocity varies over time during a time-period of $600s$, in order to get a data sample long enough to be used for fatigue analysis. However, due to CPU time considerations, only a part of this time series is analyzed in this research.

5.5.1 Description of Test Case

An overview of the simulation that have been run for the turbulent inflow case can be found in Table 5.5. It can be seen that the time-step has been decreased from $\Delta t = 0.15s$ to $0.10s$ compared to the previous test cases. This has been done in order to capture the high-frequency dynamics, which was found to be important for a turbulent inflow case. With this decreasing time-step, CPU time increases exponentially, due to the increased amount of time-steps and wake points required. Furthermore, the amount of sub-iterations required to converge between the aerodynamic and structural solver is increased to 23.72 on average, which is approximately twice the amount of aerodynamic calls compared to the steady inflow cases. Considering these effects, the total simulation time has been kept limited to $150s$.

Table 5.5: *Overview of the simulations for the turbulent inflow case.*

#	Turbine	Code	Wake	N_{free}	N_{total}	$\Delta t[s]$	$T[s]$	CPU [hr]
1	INN	BEM	-	-	-	0.10	150	≈ 0.03
2	INN	AWSM	Prescribed	92	645	0.10	150	43.43
3	INN	AWSM	Free	645	645	0.10	150	305.65

This test case is part of the AVATAR project. In this test case, a ten-minute time series with a turbulent wind inflow will be analyzed. However, as mentioned before, in this research only the first $150s$ of the simulation will be considered due to CPU considerations. In Fig. 5.3, the wind speed at hub height is compared during this time-period. The wind profile is defined with a reference wind speed of $8m/s$ at hub height and a normal turbulence model, where the Kaimal spectrum is used to create the correct frequency content of the wind speed variations. The Kaimal spectrum is defined as [37]:

$$\frac{nS_u(n)}{\sigma_u^2} = \frac{4nL_{1u}/\overline{U}}{(1 + 6nL_{1u}/\overline{U})^{5/3}} \tag{5.1}$$

where $S_u(n)$ is the autospectral density function for the longitudinal wind component, n is the frequency in Hz, L_{1u} is a length scale and $\overline{U}$ and σ_u^2 are the mean and variance of the wind speed, defined as $8m/s$ and $3.44(m/s)^2$ in this case.

This results in a characteristic turbulence intensity value of 23.2% in axial direction at hub height, which is in accordance with IEC 61400-1, Edition 3 for a wind turbine with turbulence class A [46]. Besides the turbulent inflow, also wind shear is included with a power law exponent of 0.2 and an uptilt angle of 8°.

The results from the turbulent wind file is shown in Fig. 5.3. The time-period that is used for the analysis is between $100s$ and $150s$. During this time-period, the incoming wind velocity at hub height is found to vary between $U_{hub} = 5.55m/s$ and $8.72m/s$. From an analysis of the statistics of the 10-minute wind file it is confirmed that $\overline{U}$ and the turbulence intensity are $8m/s$ and 23.2% respectively.

The exact turbulent wind file for this test case has not been determined yet, since the deadline for this test case is set to November 2016. Therefore, a comparison between the results from other partners is not yet possible. The wind profile that is used in this study is a preliminary wind profile, although it can still be used to analyze the influence of a turbulent inflow and agrees with the rules from IEC 61400-1, Edition 3.

5.5.2 Opportunities and Limitations

The turbulence test case can be used to get a better insight in the effects of a varying inflow velocity over time. Different than for the extreme wind shear case, the inflow velocity in the turbulence

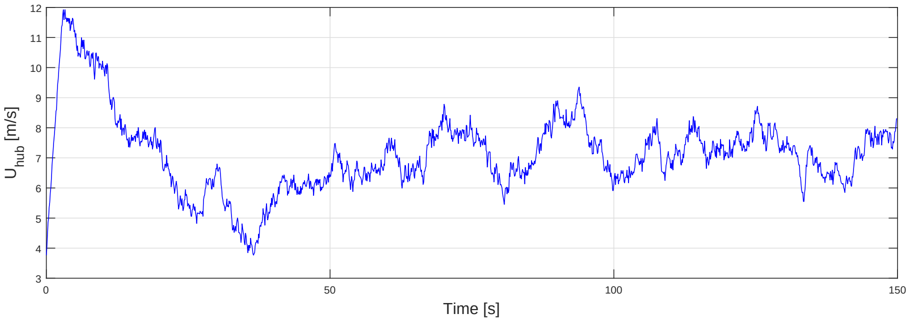

Figure 5.3: *Velocity at hub height during for the turbulence test case.*

test case is varying continuously, which allows for a proper analysis of the fatigue loads. Besides the fatigue analysis, also effects like dynamic inflow and dynamic stall behavior can be compared between BEM and AWSM.

Different from the previous test cases, the turbulent inflow case is run with the controller on, which results in more realistic conditions for the turbulence test case. In order to be able to compare the results from BEM and AWSM, the exact same rotor speed settings have been prescribed, which were determined from an initial BEM simulation.

Since this test case is still in progress for the AVATAR project, a comparison with results from external partners is not yet possible. However, it should be mentioned that the results from this study will be compared with the results from the other partners in the AVATAR project, which might lead to additional insight in the modeling of a turbulent inflow between BEM and vortex wake models.

Due to the varying inflow velocity, it was found that a smaller time-step has to be used in order to capture the higher frequency dynamics of the turbulent inflow. In combination with the increasing amount of sub-iterations to converge between ECNAero and Phatas, the CPU has increased enormously compared to steady case simulations with a time-step of $\Delta t = 0.15s$. Therefore, the simulation has only been run for the first $150s$ instead of the full ten-minute period. Finally, it should be mentioned that for this test case the implementation of parallel computing has first been tested, which results in a decrease of CPU time of a factor 4.

5.6 Pitch Step

The last test case that is considered in this thesis is the pitch step case. For this test case, the response to a pitch step will be compared between BEM and AWSM. With this comparison, the difference in response to a dynamic inflow can be assessed. Due to the availability of validation data from the New MEXICO experiment (See Section 3.7), this test case will be designed to reproduce the pitch step experiments in the New MEXICO project, which allows for a validation of the results.

5.6.1 Description of Test Case

The pitch step experiment in the New MEXICO project consists of runs at three different tip speed ratios ($\lambda \approx 5.4, 6.6, 10$), for two different rotor speeds ($\omega = 325, 425rpm$) and various yaw angles (Yaw $= 0°, 15°, 30°$). This results in a total of 18 unique pitch step experiments. For each of these experiments, the pitch angle is changed from $-2.3°$ to $5°$ and back to $-2.3°$ during a $15s$ run.

For this comparison, only the experiments in axial inflow conditions are considered. The run for $\lambda = 6.6$ is considered the optimal design condition of the rotor ($a \approx 0.33$), which results in the fact that the experiments at a higher λ will result in a turbulent wake state, whereas the experiment at a lower λ will result in a low induction case, since the same pitch angles are used during the run. It is found that the experiments at a low tip speed ratio result in an overshoot of the aerodynamic forces, from which the response to the dynamic inflow can be well assessed. However, for these cases the induction is close to $a = 0.5$, resulting in a turbulent wake state, which might trigger additional differences between BEM and AWSM. Therefore, also runs at $\lambda = 6.6$ are considered to assess the difference in the response to a pitch step case between BEM and AWSM. The test matrix of the runs that are considered for the validation can be found in Table 5.6.

Table 5.6: *Test matrix of experiments from the New MEXICO campaign used for validation.*

Run	$Q_\infty[Pa]$	$\rho_\infty[kg/m^3]$	$V_\infty[m/s]$	$T_\infty[K]$	$\omega[rpm]$	$\lambda[-]$	$P_\infty[Pa]$	$P_{t,\infty}[Pa]$
1146	60.1	1.20877	9.97	293.3	425.1	10.045	102271	102331
1147	139.4	1.20846	15.19	293.4	425.1	6.594	102267	102407
1152	35.6	1.20677	7.68	293.8	324.9	9.963	102274	102310
1153	80.8	1.20703	11.57	293.7	324.9	6.614	102277	102357

From the simulations with AWSM it was found that the prescribed wake configuration was not sufficient to accurately model the wake dynamics of the pitch step case for the high induction cases. Therefore, only the free wake configuration of AWSM has been used to generate data for the pitch step case. The time-step that has been used in the simulations is chosen to result in an azimuth angle of 10° per time-step. This results in a time-step of $\Delta t = 0.00393s$ and $\Delta t = 0.00510s$ for a rotor speed of 425 rpm and 325 rpm respectively. The full pitch action from $-2.3°$ to 5° was found to last approximately $1s$ for all cases, which means that for the case with the low rotor speed, there was a faster relative pitch action, when considering the change in pitch angle over a revolution.

The combination of the free wake configuration and the small time-step results in a very large CPU time for the simulations with AWSM. Since the rotor that is used in the experiment is a rather stiff model, it was chosen to run the simulations without the structural dynamics model and therefore only model the aerodynamic effects. For a more detailed study, also the effects of the structural dynamics should be included. For the free wake configuration a total wake length of two rotor diameters is chosen. This results in a CPU time of $38hr$ for the simulations with $\Delta t = 0.00393s$ and $28hr$ for the simulations with $\Delta t = 0.00510$.

5.6.2 Rotor Model and Measurement Equipment

A full description of the wind tunnel model that has been used for the experiment has been published by Technion in [47] and [48]. The rotor that is used in the experiment is a three bladed rotor with a diameter of $4.5m$. The model is equipped with 148 pressure sensors, which are used to determine the pressure distribution around the airfoil at five different locations on the blade, as can be seen in Fig. 5.4. Due to blade structural and PCB spatial constraints, the sensors have been distributed over the three blades. The calibration of the pressure sensors and the removal of faulty pressures sensors is described in [31] and [7] and is considered to be out the scope for this investigation.

In order to reproduce the experiment, the pitch angle has to be known throughout the complete simulation. Since the data from the pitch step experiment has not yet been processed, the data from the pitch angle sensor has not been calibrated, as can be seen in Fig. 5.5a. In the experiment description, it is mentioned that the pitch angle is set to $-2.3°$ at the start of the simulation and increases until 5° during the first pitch action. By setting the mean value of the pitch signal before the pitch step to $-2.3°$ and the mean value of the pitch signal after the first pitch step to 5°, the

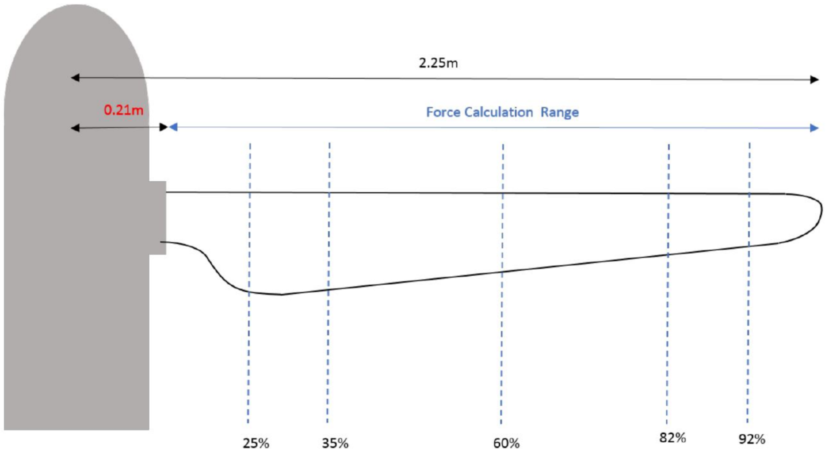

Figure 5.4: *Location of the pressure sensors on the New MEXICO rotor, from [7].*

complete pitch angle history can be calculated by a linear interpolation method. This calibration results in a pitch signal as shown in Fig. 5.5b. It should be noted that the results in this figure are averaged over 90 time-step to filter the fluctuations in the sensor.

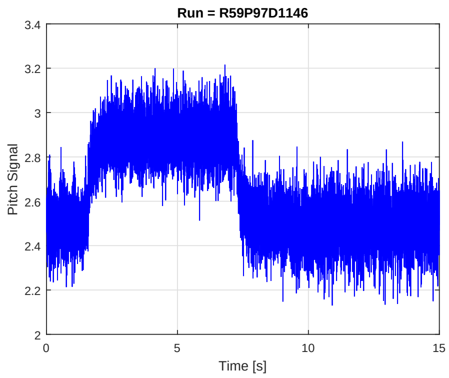

(a) *Raw data.*

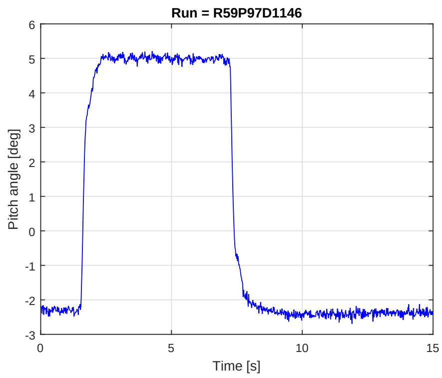

(b) *Calibrated data.*

Figure 5.5: *Pitch angle signal for run 1146 of the New MEXICO experiment.*

5.6.3 Opportunities and Limitations

The pitch step case is a unique test case to compare the results between BEM and AWSM, since validation data is available from the New MEXICO experiment. With this experiment, the response to a dynamic inflow can be compared between BEM and AWSM, since the pitch action results in a large difference of the environmental conditions over time. From research into the validity of BEM and vortex wake codes, it is found that vortex wake codes have an advantage over BEM models for fast pitching actions [2], which are occurring on state-of-the-art wind turbines. It is expected that the inclusion of the wake dynamics will act as a damper to the pitch step case and will show a larger influence of the pitch step on the wake dynamics for AWSM, whereas the results from BEM are expected to return faster to steady state condition.

The main disadvantage of this test case is that the structural dynamics is not taken into account in the simulations. However, due to the high stiffness of the wind tunnel model, it is expected that structural deformations will have a small effect on the results. Furthermore, there will always be differences between the wind tunnel conditions and the reproduced conditions in the simulations with BEM and AWSM, for example in the calibration of the pressure data or pitch angle signal. Finally, there is the size of the wind tunnel model, which is many times smaller compared to the full-size rotors. Despite the high rotational velocity of the wind tunnel model, the Reynolds number is still smaller compared the 10MW reference wind turbines used in the other test cases.

Chapter 6

Results

In this chapter the results from the various test cases will be presented. The test cases that have been considered are the Axial Inflow (Section 6.1), Yawed Inflow (Section 6.2), Half Wake (Section 6.3), Extreme Wind Shear (Section 6.4), Turbulent Inflow (Section 6.5) and Pitch Step (Section 6.6) test case. For each of these test cases, the results are presented to show the the most important differences between BEM and AWSM, as well as a more in-depth description of certain flow phenomena associated with the test cases. For some cases, the results of BEM and AWSM have also been compared to results from other models in the AVATAR project (Axial Inflow and Extreme Wind Shear) or validation data from the New MEXICO project (Pitch Step).

6.1 Axial Inflow

In this section, the results from the axial inflow test case will be presented. First the results will be presented in terms of the mean and standard deviation values of the output parameters in the statistics section. Next, the Damage Equivalent Load (DEQL) will be compared for the blade and tower moments. Then, the most important observations from this test case will be presented, being the modeling of the trailed vortices and the tower effect. Furthermore, the results from additional simulations for the axial inflow test case will be presented. The section will conclude with a summary of the most important findings.

In order to distinguish the results between the different simulation tools in the tables, each code is numbered, as indicated in Table. 6.1.

Table 6.1: *Labeling of the codes for the axial inflow case.*

Number	Code	Turbine
1	ECNAero-BEM	INNWIND
2	ECNAero-AWSM-Prscrb	INNWIND
3	ECNAero-AWSM	INNWIND
4	ECNAero-BEM	AVATAR
5	ECNAero-AWSM-Prscrb	AVATAR
6	ECNAero-AWSM	AVATAR

6.1.1 Statistics

Mean Values

In Table 6.2, an overview of the mean values for the output parameters is presented for the various codes. In this table, the results are presented for blade sectional parameters (induced velocity, angle of attack and normal force) at two radial positions, blade loads (root bending moments), rotor performance (power and axial force) and tower loads (bottom bending moments).

From this table it can be observed that there is a good agreement between the results of BEM and AWSM for the blade sectional parameters in terms of mean values over a rotor revolution. Maximum differences are found to be 7% for $u_{i,ax}$ and 6% for AoA. Furthermore, a better agreement is obtained for the AVATAR turbine, which is expected to be due to the lower operational region in terms of AoA. An interesting observation is that the normal force in the mid-section of the blade is larger when computed with AWSM, a result that has been observed more often when comparing BEM to AWSM.

For the blade root bending moments, an excellent agreement is obtained. For M_y, the maximum differences are 1.5% for the INNWIND turbine and 0.4% for the AVATAR turbine. Also, the rotor performance shows a good agreement, with maximum 4% difference in power and 2% in F_{ax}. Again, the AVATAR turbine shows a better agreement compared to the INNWIND turbine.

For the tower loads, a good agreement is found in M_x and M_y. However, large differences are obtained for the tower M_z for the INNWIND turbine, where AWSM calculates the M_z to be almost twice as high compared to BEM.

Table 6.2: *Mean values of output parameters for the INNWIND and AVATAR turbine in axial inflow.*

Parameter	Unit	Location	1	2	3	4	5	6
$u_{i,ax}$	m/s	$r/R = 0.5$	2.501	2.393	2.335	1.705	1.629	1.631
AoA	deg	$r/R = 0.5$	5.878	6.121	6.220	3.626	3.769	3.766
F_n	N/m	$r/R = 0.5$	3283	3390	3429	2936	3016	3015
$u_{i,ax}$	m/s	$r/R = 0.95$	2.784	2.957	2.898	1.541	1.518	1.520
AoA	deg	$r/R = 0.95$	7.403	7.196	7.253	1.623	1.571	1.570
F_n	N/m	$r/R = 0.95$	4759	4639	4665	3572	3450	3449
blade M_x	kNm	$r = 0m$	1674	1713	1749	2094	2088	2087
blade M_y	kNm	$r = 0m$	16251	16377	16493	17762	17693	17689
blade M_z	kNm	$r = 0m$	63.63	63.77	64.84	-51.65	-52.08	-52.11
P	MW	full rotor	3.658	3.741	3.805	4.242	4.224	4.221
F_{ax}	kN	full rotor	766.2	774.3	779.9	735.8	732.7	732.5
tower M_x	kNm	bottom	5448	5463	5562	6961	6853	6853
tower M_y	kNm	bottom	89464	90255	90962	90137	89530	89498
tower M_z	kNm	bottom	-192.5	-352.8	-351.4	-699.3	-717.8	-717.3

Standard Deviation Values

In Table 6.3, the standard deviation values for the output parameters are shown. The table is built up identical to Table 6.2. When comparing the results for the blade sectional parameters, it is observed that BEM calculates a higher fluctuation in the mid-section, especially for the induced velocity (max. +106%) and normal force (max. +76%). Near the tip of the blade, these differences become much smaller. Interesting to see is that these observations are similar for both turbines.

For the blade loads, a good agreement is observed for M_x and M_z, whereas the results for M_y show a difference of 16% between BEM and AWSM for both turbines. Interesting to see is that the results from AWSM show the largest standard deviations. For the rotor performance BEM shows the largest standard deviations, with +37% for power and +50% for F_{ax}.

Finally, the tower loads show a large spread in terms of standard deviation, especially for the INNWIND turbine. This could have a large impact on the equivalent fatigue load of the tower.

Table 6.3: *Standard deviation values of output parameters for the INNWIND and AVATAR turbine in axial inflow.*

	Unit	Location	1	2	3	4	5	6
$u_{i,ax}$	m/s	$r/R = 0.5$	0.064	0.039	0.036	0.068	0.033	0.033
AoA	deg	$r/R = 0.5$	0.225	0.227	0.226	0.235	0.210	0.208
F_n	N/m	$r/R = 0.5$	64.40	36.58	38.90	53.68	31.01	31.08
$u_{i,ax}$	m/s	$r/R = 0.95$	0.104	0.119	0.111	0.083	0.062	0.062
AoA	deg	$r/R = 0.95$	0.223	0.247	0.241	0.169	0.169	0.168
F_n	N/m	$r/R = 0.95$	49.98	47.06	45.68	50.91	51.34	50.96
blade M_x	kNm	$r = 0m$	7648	7639	7639	10208	10212	10212
blade M_y	kNm	$r = 0m$	345.3	399.2	392.5	375.9	435.5	434.8
blade M_z	kNm	$r = 0m$	48.38	48.09	47.79	45.62	44.60	44.58
P	kW	full rotor	33.87	25.85	27.45	45.76	33.29	33.33
F_{ax}	kN	full rotor	4.106	2.746	2.883	5.187	3.523	3.530
tower M_x	kNm	bottom	107.4	120.0	177.7	388.1	343.4	423.0
tower M_y	kNm	bottom	252.8	191.6	191.8	239.6	204.0	207.8
tower M_z	kNm	bottom	107.1	46.74	47.28	119.3	67.93	67.82

6.1.2 Damage Equivalent Loads

In the previous section it was found that there is a generally good agreement between BEM and AWSM in terms of mean value, although there are some larger differences found in terms of standard deviation. In order to quantify the difference in mean and fluctuating values into one load, the 1Hz damage equivalent load (DEQL) is calculated. This DEQL is defined as the 1Hz harmonic constant load range that causes the same amount of damage over the examined time period. The DEQL is calculated as follows:

$$DEQL = \left(\frac{\sum_{b=1}^{N_{bins}} N_{cycl}(b) \cdot L(b)^m}{N_{cycl,1Hz}} \right)^{1/m} \tag{6.1}$$

where N_{bins} specifies the amount of bins, N_{cycl} and L define the number of cycles and the corresponding loading in each bin, m is the fatigue exponent and $N_{cycl,1Hz}$ defines the amount of 1Hz cycles in the time period. The DEQL has been calculated for the last two full rotor revolutions for the blade and tower moments, which is $\approx 20s$ depending on the rotor speed. The results for the DEQL for the blade and tower moments are shown in Table 6.4. It should be noted that m is taken as 11 for the blade (glass-fiber) and 4 for the tower (steel), which is a common value for these materials [8].

From the table, it can be observed that there is a very large DEQL for the blade M_x, which can be explained by the gravity loading, which results in a very large cyclic load with a 1P frequency. Since the gravity effect is similar for all codes, there is a good agreement found. For the blade M_y, AWSM calculates a value of 15% and 22% higher for the INNWIND and AVATAR turbine respectively, whereas the agreement for the blade M_z is much better (max 5%).

For the tower DEQLs, larger differences have been observed between BEM and AWSM. For the tower M_x, the free wake configuration of AWSM calculates a 60% higher value for the INNWIND turbine, whereas for the AVATAR turbine the largest differences are observed between the two wake configuration of AWSM (25%), where the result from BEM falls in between. For the tower M_y and M_z, BEM calculates a larger DEQL for both turbines. Maximum differences between BEM and AWSM are 40% for M_y and 90% for M_z, both for the INNWIND turbine.

Table 6.4: *Damage equivalent loads of output parameters for the INNWIND and AVATAR turbine in axial inflow.*

	Unit	Location	1	2	3	4	5	6
blade M_x	kNm	$r = 0m$	16514	17517	17525	21689	21688	21687
blade M_y	kNm	$r = 0m$	860.1	985.4	978.1	926.3	1084	1134
blade M_z	kNm	$r = 0m$	104.3	110.2	109.3	96.96	95.10	95.11
tower M_x	kNm	bottom	250.4	288.7	399.9	876.2	780.8	971.8
tower M_y	kNm	bottom	598.6	420.6	475.6	595.0	518.2	543.8
tower M_z	kNm	bottom	244.1	127.3	128.5	286.5	181.7	181.5

6.1.3 Modeling of Trailed Vortices

In this section the modeling of the trailed vortices is compared between BEM and AWSM. As was explained in Section 4.4.1, the BEM model in ECNAero takes the effect of a root and tip vortex into account through the Prandtl correction. The BEM model only models the root and tip vortex, which is found to result in differences with AWSM, which also takes the effect of vortices in the mid-section of the blade into account. In this section, both the root and tip vortices, as well as the effect of a non-uniform distribution of circulation is discussed.

Root and Tip Vortices

For a wind turbine in axial inflow the effect of the root and tip vortex can be separately examined, without the effect of e.g. yawed or dynamic inflow. In Fig. 6.1, the azimuth averaged AoA and $u_{i,ax}$ are shown as function of radial position for the INNWIND and AVATAR turbine.

The effect of the root and tip vortex can be well observed for the INNWIND turbine, since this turbine operates at a higher induction, resulting in a stronger vortex compared to the AVATAR turbine. The effect is noticeable in both the BEM and AWSM results. It can be seen that AWSM calculates a lower AoA and a higher $u_{i,ax}$ at the root and tip of the blade. This means that BEM underestimates the strength of the root and tip vortex for the INNWIND turbine. Differences in AoA are $\approx 5°$ in the root section and $\approx 0.5°$ in the tip section. It should be noted that the modeling of the tip vortex is much more important, due to the higher contribution to the overall turbine performance and load generation.

For the AVATAR turbine, the effect of the root and tip vortex is much smaller and there is a better agreement between BEM and AWSM for the AoA and $u_{i,ax}$. From Figs. 6.1a and 6.1d, it can be seen that BEM overestimates the effect of the root and tip vortex, which results in differences in AoA of $\approx 3°$ near the root and $\approx 0.3°$ at the tip of the blade.

Effect of Non-Uniform Distribution of Circulation

As was mentioned before, BEM only models the root and tip vortices by means of the Prandtl correction. With this model, it is assumed that there are no trailed vortices in the mid-section of the blade due to a non-uniform distribution of circulation. However, it is found that this assumption results in differences between BEM and AWSM. It is expected that the non-uniform distribution of circulation in the blade results might contribute to the differences in the normal

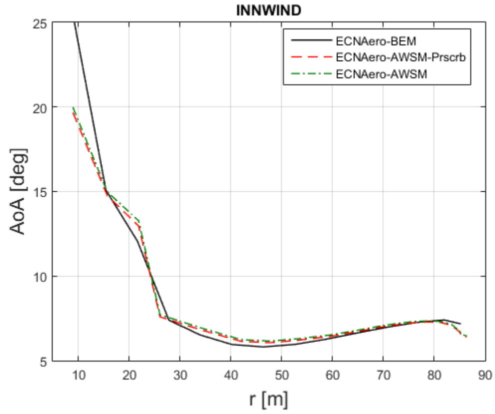

(a) *Angle of attack, INNWIND turbine.*

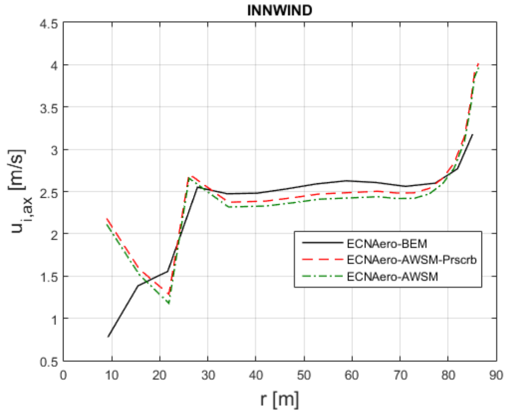

(b) *Axial induced velocity, INNWIND turbine.*

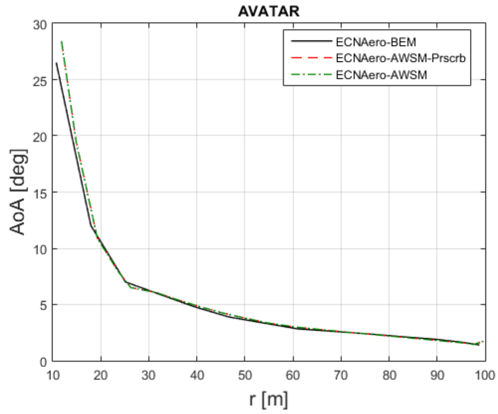

(c) *Angle of attack, AVATAR turbine.*

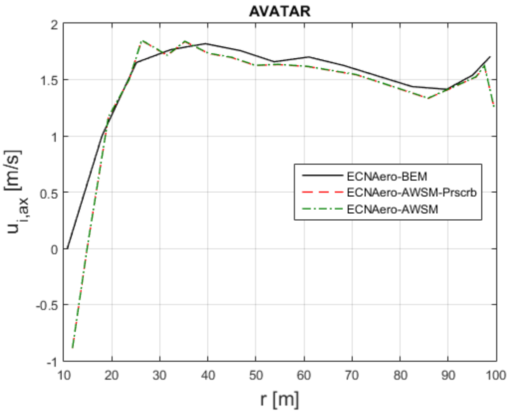

(d) *Axial induced velocity, AVATAR turbine.*

Figure 6.1: *Evaluation of the tip loss correction for the INNWIND and AVATAR turbine in axial inflow.*

force over the blade for the INNWIND turbine, as is shown in Fig. 6.2. In this figure it can be seen that AWSM overestimates the normal force. This effect is known to occur on high induction rotors, such as the INNWIND turbine. The effect of a longer wake length, increased blade discretization, longer simulation time and smaller time-step has not been found to reduce this difference in normal force between BEM and AWSM. By increasing the pitch angle, this difference in normal force is found to reduce, although it should be noted that the induction of the rotor also reduces.

In order to investigate what would happen if the circulation is constant over the blade, the twist distribution of the INNWIND turbine has been altered in order to create a more constant distribution of circulation. Since it was found that the induction factor of the complete rotor plays an important role in the agreement of the normal force in the mid-section of the blade, it was made sure the induction factor remains similar for the adjusted twist distribution. In order to do so, the twist is decreased in the tip-section of the blade, resulting in a larger AoA and larger Γ, whereas the opposite is done in the mid-section of the blade. This results in the fact that Γ is reduced in the mid-section and increased in the tip-section, as can be seen in Fig. 6.3a.

The result of the normal force distribution for the adjusted twist distribution are shown in Fig. 6.3b. From this figure it can be found that there is a much better agreement between the results of BEM and the prescribed wake configuration of AWSM. However, for this adjusted twist distribution, the results from the free wake configuration of AWSM show a slightly higher F_n in the mid-section of the blade compared to the prescribed wake configuration. A similar behavior has been found when inspecting the adjusted twist distribution at other pitch angles.

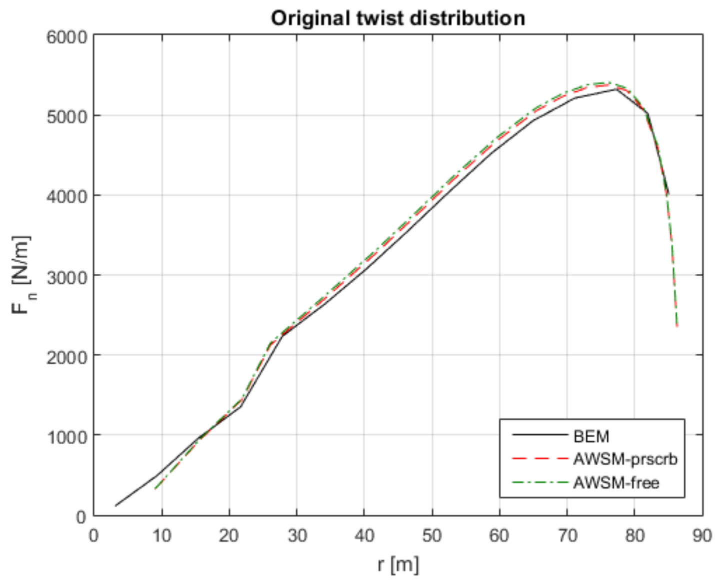

Figure 6.2: *Normal force distribution over the radius for the INNWIND turbine in axial inflow.*

Comparison to EllipSys3D

As part of the AVATAR project, comparison data from higher fidelity models has been made available [49]. For the INNWIND turbine in axial flow conditions, results for the normal force curve have been provided with the RANS model EllipSys3D [18]. The simulations with EllipSys3D have been run with a fine common grid (CGF), for both a free transition (Tran) and a fully turbulent simulation (Turb).

In Fig. 6.4a, the results from ECNAero and EllipSys3D have been compared for the normal force curve. From this figure, it can be seen that there are large differences in the root section, where the RANS models tend to calculate a larger F_n. Furthermore, it can be seen that there is a good agreement between the free transition and fully turbulent simulation with EllipSys3D in the mid-section of the blade between $40m$ and $60m$. In Fig. 6.4b, the mid-section of the blade is enlarged in order to be able to compare the results from ECNAero and EllipSys3D. From this figure, it can be seen that there is a good agreement between AWSM and the results from EllipSys3D.

However, it should be noted that both BEM and AWSM make use of airfoil polars, whereas EllipSys3D calculates the sectional lift and drag of the blade by solving the RANS equations. The accuracy of the lift and drag polar is expected to be in the same order as the difference between BEM and AWSM in the mid-section of the blade. Furthermore, it is found that the difference between various CFD models are found to be larger than the difference between BEM and AWSM [49]. Due to this uncertainty in both CFD models as well as the airfoil polars, no conclusions can be drawn on whether BEM or AWSM calculates the correct normal force in the mid-section of the blade. A good option would be to compare the results to an actuator line or disc model, where the global flow is modeled by RANS equations and airfoil polars are used to model the local blade aerodynamics. Unfortunately, the actuator line model in EllipSys3D has not been used to assess the INNWIND turbine, although this would give valuable comparison data.

6.1.4 Modeling of Tower Effect

When the blade is passing the tower, the wind field is locally influenced, which results in a reduction of the induced velocity. In order to compare the tower effect for BEM and AWSM, $u_{i,ax}$

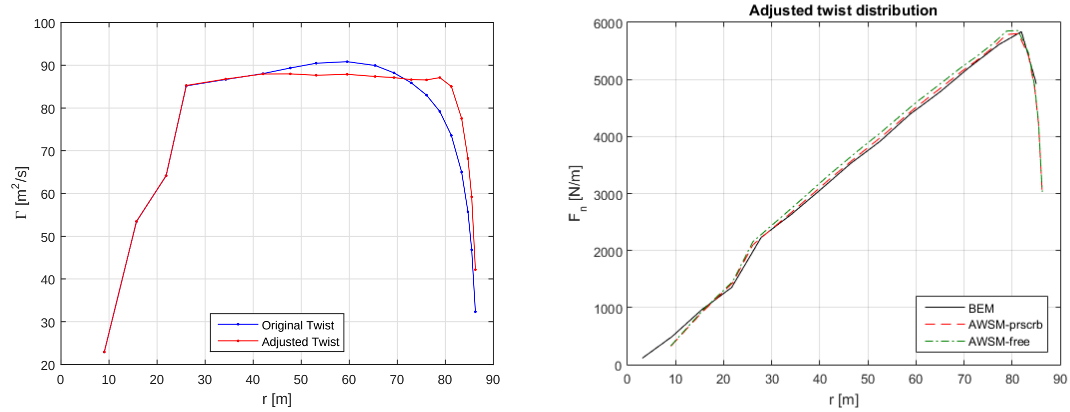

(a) *Comparison of the circulation over the blade.* (b) *Adjusted distribution of normal force.*

Figure 6.3: *Results for the study on normal force.*

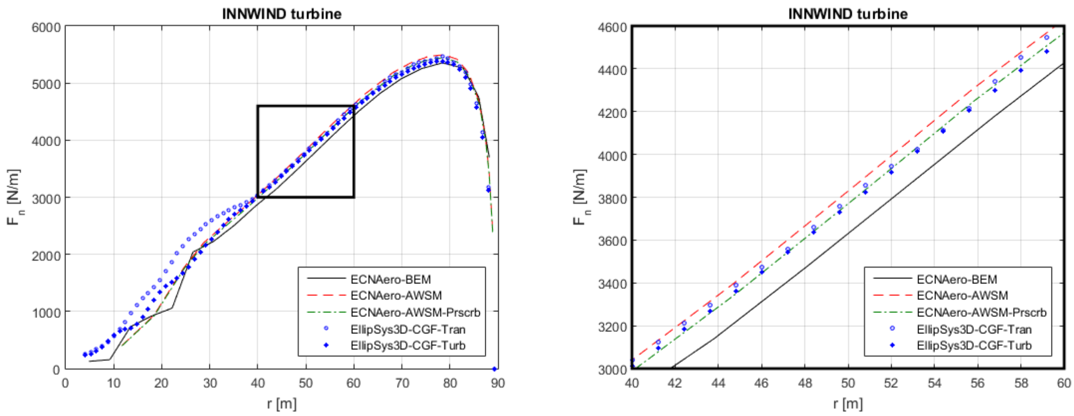

(a) *Full blade.* (b) *Mid-section of the blade.*

Figure 6.4: *Comparison of the normal force curve between ECNAero and EllipSys3D.*

and F_n are compared for the INNWIND and AVATAR turbine as function of azimuth position to assess the difference in the local induced velocity and the effect on the local aerodynamic loads.

In Fig. 6.5, $u_{i,ax}$ is shown as function of azimuth position at $r/R = 95\%$. From this figure, it can be observed that BEM calculates a much larger decrease of $u_{i,ax}$ due to the tower compared to AWSM for both turbines. It should be noted that this observation is made at all radial positions. In Fig. 6.6, F_n is shown as function of the azimuth angle for the INNWIND and AVATAR turbine in the tip-section of the blade. From this figure, it can be seen that there is much better agreement in terms of the load variation due to the tower passage for both turbines. However, it can be observed that the effect of the tower on F_n seems to be slightly larger for BEM compared to AWSM.

Since the same model is used in BEM and AWSM to assess the tower effects, it is possible that the observed differences are caused by the implementation in PhatasAero. However, it should be noted that this analysis is done with a rather coarse time-step, where the results are calculated every 6° azimuth angle. For a more detailed investigation, it is suggested to decrease the time-step and compare the results in more detail near the azimuth angles where the blade passes the tower.

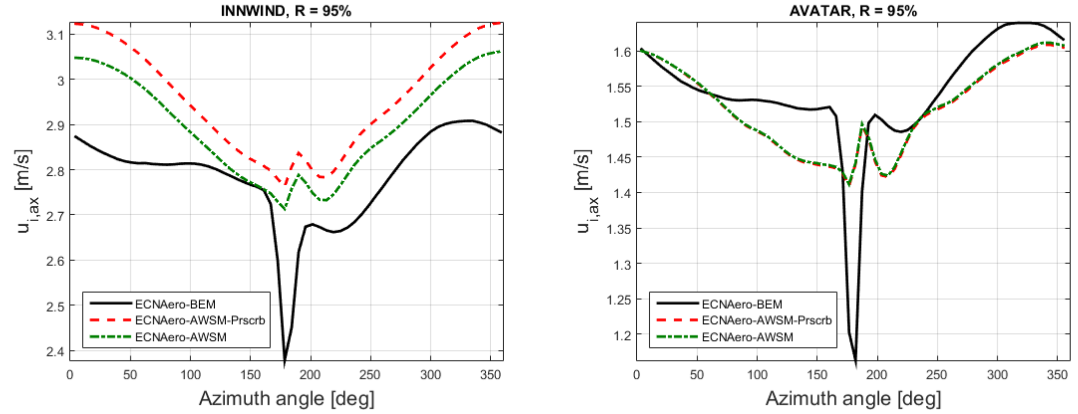

(a) *INNWIND turbine.* (b) *AVATAR turbine.*

Figure 6.5: *Axial induced velocity vs. azimuth position for the INNWIND and AVATAR turbine in axial inflow.*

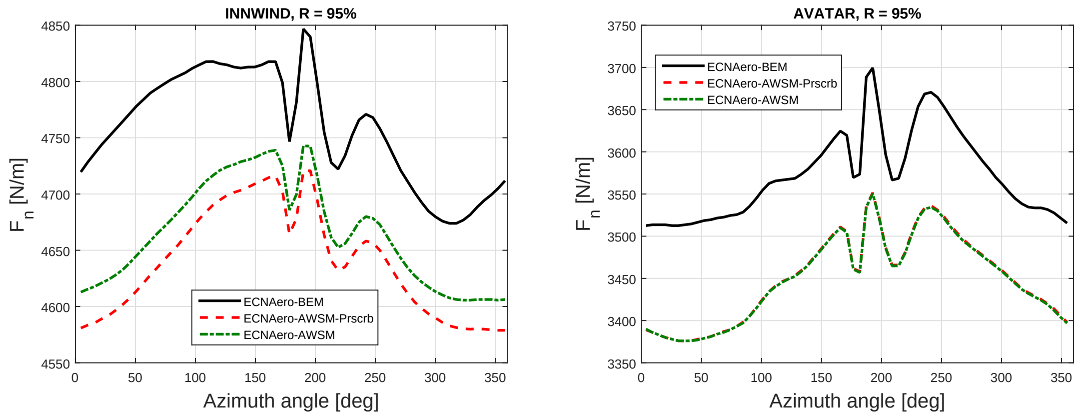

(a) *INNWIND turbine.* (b) *AVATAR turbine.*

Figure 6.6: *Sectional normal force vs. azimuth position for the INNWIND and AVATAR turbine in axial inflow.*

6.1.5 Convergence Analysis

From simulations for the AVATAR turbine in axial inflow at rated wind speed ($U_\infty = 10.75 m/s$, a convergence problem has occurred. Since the coupling between ECNAero and Phatas has only been completed in the beginning of 2015, there are still some issues in the software that could be improved.

Since PhatasAero is an aeroelastic code, the solution has to converge every time-step between the results in ECNAero and Phatas. In case the blade deformations are large, it is found to be more difficult to convergence the solution. Since the AVATAR turbine is designed as a relatively flexible blade, large flapwise blade deformations occur in rated wind speed conditions. From an investigation on the evolution of the circulation during a time-step, it is found that the circulation between the sub-iterations is fluctuating with an amplitude that is higher than the convergence criteria implemented in AWSM (10^{-5}), as is shown in Fig. 6.7.

During an investigation in the convergence issues with PhatasAero, it was found that the convergence criteria is based on the rated torque. However, since the rated torque is not an input to the code, this has been solved by calculating the rated torque by dividing the rated power by the rated rotor speed. However, changing either the rotor power or rated rotor speed has found to influence the simulation more than just the convergence criteria between the aerodynamics solver in ECNAero and the structural dynamics solver in Phatas. Therefore, an additional parameter has been added for the rated torque to the updated version of PhatasAero. By slightly increasing the rated torque, it is found that most of the convergence problems in PhatasAero have been solved and that CPU time has been reduced by a factor up to 10 for cases where convergence problem occurred. It should be mentioned that changing the convergence criteria might also lead to small difference in the final solution.

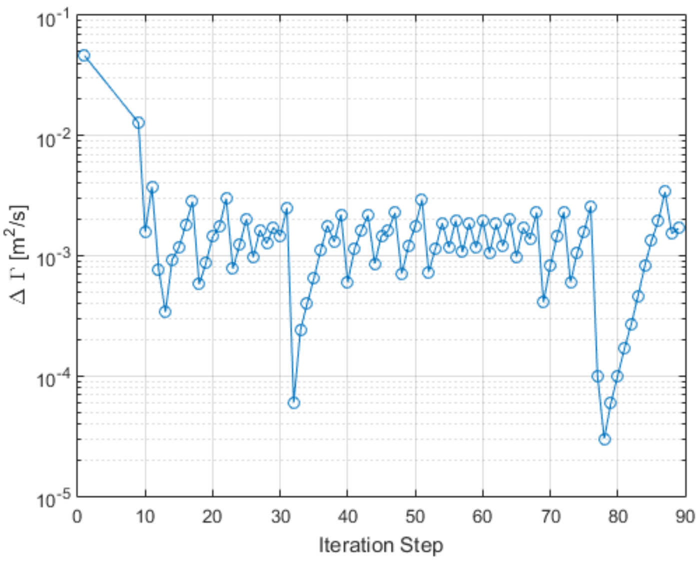

Figure 6.7: *Difference of circulation between sub-iteration steps at $r = 49.8m$ for the AVATAR turbine in rated wind speed conditions.*

6.1.6 Analysis

In this section, the main results form the axial inflow test case will be described. In general, a good agreement has been obtained for the mean and standard deviation value of most output parameters between BEM and AWSM for the INNWIND and AVATAR turbine. This results in a good agreement for the DEQL of the blade and tower loads, although large differences are obtained for the tower M_z as is shown in Table 6.4. The main observations are summarized below:

- For the local aerodynamics, a good agreement has been found between BEM and AWSM, with maximum differences in the order of $\approx 5\%$. A better agreement has been observed for the AVATAR turbine, which is expected to be due to the lower operating range for AoA. AWSM is found to calculate a higher normal force in the mid-section for the INNWIND turbine, whereas the agreement is found to be better in the tip-section, as is shown in Fig. 6.2. For the standard deviation, larger differences have been found between BEM and AWSM, especially in the mid-section, where BEM calculates a higher fluctuation $\approx +100\%$. At the tip of the blade, the differences reduce to max 30%.

- For the blade loads and rotor performance a good agreement has been obtained for the mean values (max 5% difference), whereas larger differences are obtained for standard deviation ($\approx 16\%$ for blade loads and $40 - 50\%$ for rotor performance).

- The tower M_x and M_y show a good agreement in terms of mean and fluctuating values, whereas M_z shows differences of more than 100% in both the mean and standard deviation for the INNWIND turbine. For the DEQL, a good agreement has been found for the blade loads, with maximum differences of 20% between BEM and AWSM for M_y. For the tower M_x, a large difference has been found between the free and prescribed wake configuration ($\approx 25\%$), where the result from BEM falls in between. The difference between the two wake configurations is caused by the fact that the free wake configuration calculates a slightly higher peak value of M_x for each revolution, which might be caused by differences in the wake velocity in lateral direction. For the tower M_y and M_z, BEM calculates a much higher DEQL of 40% and 90% higher respectively. The large relative difference for M_z is expected to be caused by the fact that the absolute value of M_z is small in axial inflow. Small differences in the calculation of M_z will lead to large relative differences.

- It has been found that there is a reasonable agreement for the modeling of the root and tip vortices. For the INNWIND turbine, BEM underestimates the effect of the tip and root vortices, resulting in an AoA of $5°$ higher at the root and $0.5°$ higher at the tip. For the AVATAR turbine, the opposite behavior is found, although the differences are smaller.

- It has been found that absence of modeling trailed vortices due to non-uniform distribution of circulation in the mid-section of the blade might lead to differences in normal force over the blade, especially for high induction rotors. From an adjusted twist distribution of the INNWIND turbine, it was found that with a more constant distribution of circulation, there is a better agreement with the prescribed wake configuration with BEM, although the free wake configuration of AWSM shows a similar difference in normal force with BEM. From a comparison to EllipSys3D, it has been found that there is a good agreement with the results from AWSM in the mid-section of the blade for F_n. However, due to the uncertainty in the airfoil polars, no conclusions can be drawn from this case. An actuator disc or line model would results in a better comparison, since the same airfoil polars can be used. Furthermore, the correction model for the root and tip loss correction might be extended to include the effect of trailed vortices in the mid-section of the blade.

- It has been found that BEM calculates a much larger influence of the tower on $u_{i,ax}$ compared to AWSM, which leads to a larger variation in loads and rotor performance when the blade is passing the tower.

- A good agreement has been obtained between the prescribed and free wake configuration of AWSM. This means that for normal operational conditions, the prescribed wake configuration might be a good trade-off between CPU-time and accuracy, where the CPU time is reduced by a factor of 5-6.

- For the coupling between AWSM and the structural model of Phatas, it has been found that the solution seems to fluctuate around a certain circulation value, which results in the fact that the solution does not converge. This behavior is found for the AVATAR turbine in rated wind speed conditions, where the large flapwise blade deformations are expected to enhance converge problems. For such cases, it might be an option to implement an under-relaxation factor to enhance converge.

6.2 Yawed Inflow

In this section, the results for the INNWIND and AVATAR turbine with a yaw misalignment of 30° at $8m/s$ will be presented. For this study, two different yaw models have been compared with the results from AWSM, being the ECN yaw model and the Glauert yaw model. The results will be presented for the mean, standard deviation and DEQL of certain output parameters. Furthermore, some of the observations from the test case will be discussed. Finally, the main observations from this test case are summarized in the analysis section.

In order to distinguish the results between the different simulation tools in the tables, each code is numbered, as indicated in Table. 6.5.

Table 6.5: *Labeling of the codes for the yawed inflow case.*

Number	Code	Turbine
1	ECNAero-BEM	INNWIND
2	ECNAero-BEM-Glauert	INNWIND
3	ECNAero-AWSM-Prscrb	INNWIND
4	ECNAero-AWSM	INNWIND
5	ECNAero-BEM	AVATAR
6	ECNAero-BEM-Glauert	AVATAR
7	ECNAero-AWSM-Prscrb	AVATAR
8	ECNAero-AWSM	AVATAR

6.2.1 Statistics

Mean Values

An overview of the mean values of certain output parameters can be found in Table 6.6. When looking at $u_{i,ax}$, an excellent agreement is obtained in terms of mean value at the mid- and tip-section of the blade. Largest differences are obtained for the INNWIND turbine, especially at $r/R = 95\%$, where AWSM calculates a larger induced velocity. For the AoA, also a good agreement is obtained, where the largest differences are found near the tip, where BEM calculates an AoA of $\approx 0.3°$ larger. For the normal force, a good agreement is found as well, where BEM is found to calculate a slightly higher value near the tip, $\approx 5\%$ more for both turbines.

For the blade loads, a good agreement is found in mean values, with maximum differences of 4% for M_x, M_y and M_z between all codes for both turbines. For the rotor performance, maximum differences are found to be 2% and 4% for the INNWIND and AVATAR turbine respectively, whereas this is only 0.5% and 1.5% for F_{ax}.

Finally, the results for the tower loads also show an excellent agreement for the mean values of M_x and M_y, with maximum differences of 6% and 2%. However, for the tower M_z, the differences are found to be more than 100% between the codes, where the largest differences are obtained between the two yaw models of BEM.

Standard Deviation Values

In Table 6.7, the results are presented in terms of standard deviation values. Large differences are found in terms of $u_{i,ax}$, which are caused by the different modeling of the skewed wake effects, which will be elaborated upon in the next section. For the AoA a generally good agreement is found, although large differences are observed for the normal force, especially in the mid-section of the blade, where BEM calculates ≈ 2 times the standard deviation compared to AWSM. The

Table 6.6: *Mean values of output parameters for the INNWIND and AVATAR turbine in yawed inflow.*

Parameter	Unit	Location	1	2	3	4	5	6	7	8
$u_{i,ax}$	m/s	$r/R = 0.5$	1.826	1.828	1.849	1.822	1.292	1.292	1.291	1.282
AoA	deg	$r/R = 0.5$	5.951	5.947	5.948	5.998	1.426	1.426	1.439	1.450
F_n	N/m	$r/R = 0.5$	2825	2830	2851	2868	2432	2435	2461	2468
$u_{i,ax}$	m/s	$r/R = 0.95$	2.153	2.155	2.456	2.428	1.223	1.225	1.272	1.266
AoA	deg	$r/R = 0.95$	7.414	7.424	7.101	7.129	0.083	0.088	0.000	0.005
F_n	N/m	$r/R = 0.95$	4130	4132	3984	3995	3245	3247	3092	3010
blade M_x	kNm	$r = 0m$	1451	1455	1428	1443	1241	1246	1197	1202
blade M_y	kNm	$r = 0m$	14227	14239	14162	14212	16189	16209	15977	16002
blade M_z	kNm	$r = 0m$	53.53	55.47	53.36	53.85	-91.69	-90.65	-91.47	-91.34
P	MW	full rotor	2.943	2.952	2.897	2.926	3.103	3.112	2.993	3.004
F_{ax}	kN	full rotor	660.1	661.2	658.3	661.1	638.6	639.5	629.2	630.5
tower M_x	kNm	bottom	6459	6169	6444	6491	6928	6687	6538	6550
tower M_y	kNm	bottom	74088	74067	74476	74809	77088	77053	75857	76019
tower M_z	kNm	bottom	-142.0	-123.5	-119.9	-115.1	-797.1	-2196	-1820	-1820

differences are caused in the downwind part of the rotor plane, which indicates the influence of the skewed wake.

For the blade loads, an excellent agreement is found for M_x and M_y, whereas large differences are found in M_y. For the INNWIND turbine, the results from BEM with both yaw models show a larger standard deviation of M_y $(15 - 30\%)$, compared to AWSM. For the AVATAR turbine, the BEM model with ECN's yaw model shows a lower value (37%), whereas the Glauert model shows a larger value (23%) compared to AWSM. For the rotor performance, it is found that the standard deviation of both F_{ax} and P are overestimated by BEM by about 50%. This is mainly caused by the large dip due to the tower effects.

For the tower loads, it is found that there is generally good agreement for the standard deviation values. Interesting to see is that the Glauert model seems to predict a much lower value for M_x and M_z for the INNWIND turbine and M_y and M_z for the AVATAR turbine, whereas the results from ECN's yaw model seem to agree better. The largest differences are found in the tower M_z, especially for the AVATAR turbine.

Table 6.7: *Standard deviation values of output parameters for the INNWIND and AVATAR turbine in yawed inflow.*

Parameter	Unit	Location	1	2	3	4	5	6	7	8
$u_{i,ax}$	m/s	$r/R = 0.5$	0.108	0.259	0.164	0.156	0.075	0.223	0.090	0.090
AoA	deg	$r/R = 0.5$	1.122	1.032	1.083	1.090	0.721	0.704	0.620	0.620
F_n	N/m	$r/R = 0.5$	239.8	249.3	144.4	147.8	115.2	120.5	53.45	53.27
$u_{i,ax}$	m/s	$r/R = 0.95$	0.218	0.298	0.545	0.524	0.157	0.213	0.309	0.307
AoA	deg	$r/R = 0.95$	0.561	0.671	0.827	0.810	0.387	0.439	0.480	0.478
F_n	N/m	$r/R = 0.95$	282.4	293.6	302.6	298.8	220.1	263.1	312.9	311.8
blade M_x	kNm	$r = 0m$	7619	7470	7474	7481	10214	10084	10130	10130
blade M_y	kNm	$r = 0m$	1225	1389	1066	1066	526.8	1024	830.9	832.0
blade M_z	kNm	$r = 0m$	56.59	50.87	52.07	52.14	46.06	48.56	45.98	45.53
P	kW	full rotor	38.99	36.32	25.80	26.49	45.83	46.72	31.58	31.84
F_{ax}	kN	full rotor	5.706	5.092	3.596	3.698	7.471	7.234	4.845	4.875
tower M_x	kNm	bottom	237.1	101.9	228.6	248.6	330.8	327.7	267.0	339.7
tower M_y	kNm	bottom	565.5	596.5	557.9	506.2	545.0	240.3	199.7	199.4
tower M_z	kNm	bottom	278.1	162.9	213.6	211.0	385.0	205.4	169.9	167.4

6.2.2 Damage Equivalent Loads

In order to quantify the differences in mean and standard deviation between BEM and AWSM, the DEQL of the blade and tower moments are calculated, as defined in Section 6.1.2. The DEQL of the blade and tower moments are shown in Table 6.8. Since the blade M_x is mainly caused by the gravity effect, differences are less than 2%. For the blade M_y, both BEM results show a large value for the INNWIND turbine, whereas the models seem to contradict for the AVATAR turbine. Interesting to see is that the Glauert model calculates an 87% higher M_y for the AVATAR turbine compared to ECN's yaw model, where the results from AWSM are in between. For the blade M_z a reasonable agreement is found with differences up to 10%.

For the tower M_x it is interesting to see that for the INNWIND turbine, the Glauert model calculates approximately half the value compared to both ECN's yaw model and AWSM. For the AVATAR turbine, the largest differences are obtained between the two wake configurations of

AWSM (30%), whereas the results from both BEM models seem to agree well with the free wake configuration. For the tower M_y, it is interesting to see that ECN's yaw model calculates a twice as high value compared to the Glauert yaw model and AWSM. The tower M_z also shows large differences, where ECN's yaw model calculates the highest value for both turbines. Differences are found to be maximum 62% for the INNWIND and even 132% for the AVATAR turbine.

Table 6.8: *Damage equivalent load of output parameters for the INNWIND and AVATAR turbine in yawed inflow.*

Parameter	Unit	Location	1	2	3	4	5	6	7	8
blade M_x	kNm	$r = 0m$	17379	17054	17070	17084	23329	23039	23166	23165
blade M_y	kNm	$r = 0m$	2938	3212	2456	2444	1323	2473	2014	2018
blade M_z	kNm	$r = 0m$	128.2	117.0	118.3	118.5	106.1	111.5	104.9	105.0
tower M_x	kNm	bottom	550.1	256.5	512.6	562.1	612.1	653.6	466.6	610.7
tower M_y	kNm	bottom	1269	1285	1181	1063	1271	655.9	532.7	534.2
tower M_z	kNm	bottom	596.5	369.1	463.3	487.9	836.0	475.7	364.9	359.8

6.2.3 Modeling of Yaw Effects

It is found that two important effects occur in yawed inflow, being the advancing and retreating effect and the skewed wake effect. In this section, the different modeling approaches of the yaw effects in PhatasAero will be compared.

Advancing and Retreating Effect

The advancing and retreating effect occurs due to the fact that the yawed inflow has a wind velocity component in the rotor plane. This velocity component is in the same direction as the blade rotational velocity in case the blade is upward position, whereas the opposite is true when the blade is in downward position. This effect will either decrease (upward position) or increase (downward position) the relative velocity of the velocity component in the rotor plane, hence the advancing and retreating effect. From a previous research in this effect, it was observed that this effect is dominant in case of a low local speed ratio, since the lateral inflow velocity is large compared to the rotational velocity [9]. Therefore, this effect is investigated in the mid-section of the blade.

The implementation of this effect can be checked by looking at the AoA in the mid-section of the blade over the azimuth position in Fig. 6.8b. From this figure a cosine distribution of the AoA is found. When the blade is in upward position (azimuth = 0°), the lateral inflow velocity is in opposite direction of the rotational speed, resulting in a relatively higher axial inflow velocity compared to the rotating part, resulting in a higher AoA. The opposite is found when the blade is in downwind position (azimuth = 180°). From the figure, a good agreement is found for this effect between all codes for both turbines. The largest differences are obtained at azimuth angles of 90° and 270°, which is caused by the skewed wake.

Skewed Wake Effect

The second effects is the skewed wake effect, which is caused by the fact that the trailed tip vortices are on average closer to the downwind part of the rotor plane (azimuth $\approx$ 90°), compared to the upwind part of the rotor plane. According to the law of Biot-Savart (Eq. 4.2), this results in an increase in induced velocity. This effect is the strongest near the tip of the blade, where the distance to the tip vortex is the smallest.

In Fig. 6.9, $u_{i,ax}$ is plotted as function of azimuth angle at $r/R = 95\%$. From this figure the effect of the skewed wake is clearly visible in the results from AWSM, whereas it is observed that the BEM models seem to calculate a much smaller effect of the skewed wake. It is interesting to

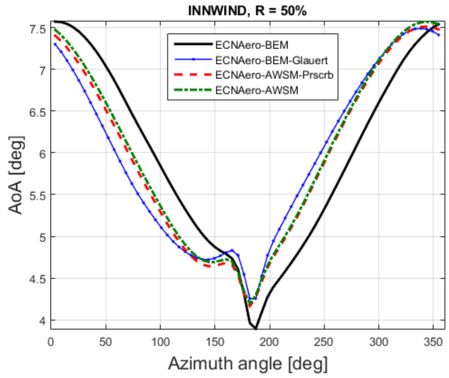

(a) *INNWIND turbine.*

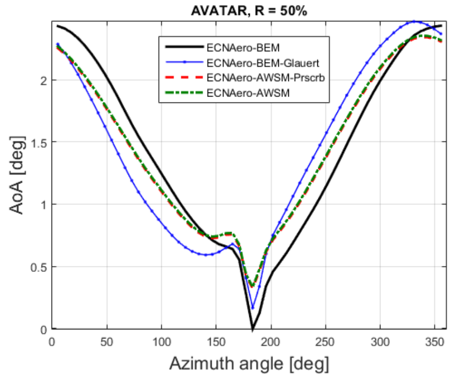

(b) *AVATAR turbine.*

Figure 6.8: *Angle of attack vs. azimuth positions at radial position of* 50% *of blade length.*

see that the results in the upwind part of the rotor plane match much better compared to the downwind part of the rotor plane. Furthermore, it seems that the Glauert model takes this effect better into account compared to ECN's yaw model, although it should be noted that it is found that the opposite is true in the root section of the blade. Finally, it is observed that the effect of the tower on the induced velocity is much larger for BEM compared to AWSM, which was also found for the axial inflow case.

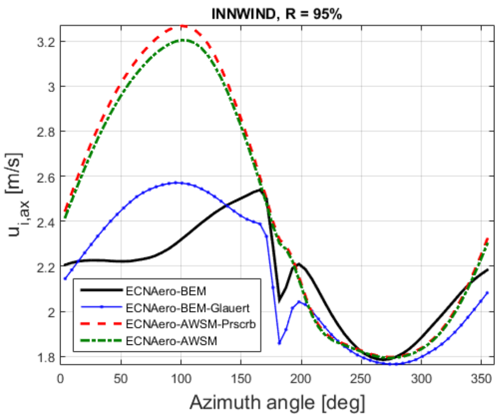

(a) *INNWIND turbine.*

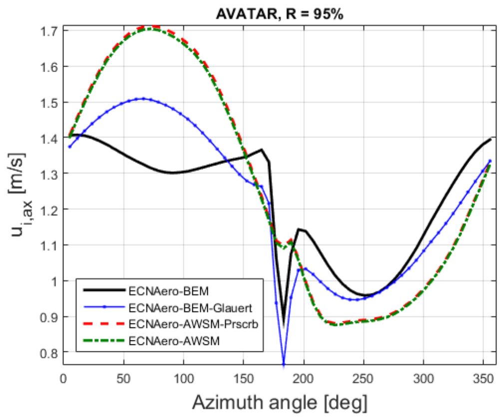

(b) *AVATAR turbine.*

Figure 6.9: *Axial induced velocity at* $r/R = 95\%$ *as function of azimuth angle for the INNWIND and AVATAR turbine in yawed inflow.*

6.2.4 Analysis

From this test case, a few interesting observations have been made.

- A generally good agreement is obtained when looking at the mean values of the output parameters on blade sectional level, blade loads, rotor performance and tower loads. Large differences have only been found for the tower M_z, which was also found for the axial inflow case.
- For the standard deviation values, large differences in blade sectional output parameters are caused by the different modeling techniques of the skewed wake effect. For the blade loads,

this results in large differences in the fluctuating part of the blade M_y, as well as for F_{ax} and P (up to 50%). For the tower loads, differences of more than 100% have been found for M_x, M_y and M_z on either the INNWIND or AVATAR turbine.

- Significant differences are found in the DEQL of the blade loads, especially for the blade M_y between the two yaw models for the AVATAR turbine (87%). Also the tower loads show a large scatter in DEQL, with the largest differences usually obtained between the ECN and Glauert yaw model of more than 100%.

- Large differences in $u_{i,ax}$ are obtained between BEM and AWSM, especially when the blade is in the downwind part of the rotor plane, where the blade is on average closer to the trailed tip vortices compared to the upwind part of the rotor plane. This skewed wake effect results in an increase in induced velocity for azimuth angles between 0° and 180°. It is found that the Glauert yaw model better models this effect near the tip of the blade, whereas ECN's yaw model has a better agreement in the root section. The effects are intrinsically modeled in AWSM.

- The advancing and retreating effect is modeled the same by BEM and AWSM, by a vector summation of the wind velocity. This leads to a good agreement between BEM and AWSM, as is shown in Fig. 6.8.

6.3 Half Wake

In this section, the results from the half wake case are presented. The simulations are only performed for the INNWIND turbine, since it was found that for this turbine the largest differences were obtained between BEM and AWSM and is therefore the most interesting to analyze from a modeling point of view. The results from BEM are compared to the free and prescribed wake configuration of AWSM. It should be noted that for the prescribed wake configuration, the results are taken from the case with 3 rotor revolutions of free wake points, as described in the computational set-up. The results in this section are presented as mean and standard deviation values, as well as the DEQL of the blade and tower moments. Next, the modeling of non-uniform inflow is compared between BEM and AWSM. Finally, the most interesting observations from this test case are summarized. Interesting in this test case is to see how BEM and AWSM cope with the changing incoming wind speed over the rotor plane. The numbering of the codes is similar to the axial inflow case for the INNWIND turbine, as indicated in Table. 6.1.

6.3.1 Statistics

Mean Values

The results for the half wake case in terms of mean values is shown in Table 6.9 for the BEM code, as well as for AWSM with the free and prescribed wake configuration. It can be observed that although the amount of free wake points for the prescribed wake configuration is increased, there are still significant differences with the free wake configuration. Hence, the results from BEM will be mainly compared to the free wake configuration, which is expected to better capture the wake effects.

When inspecting the blade sectional aerodynamics, it can be seen that there is a rather large difference found in the mid-section of the blade, where $u_{i,ax}$ is found to be 23% lower and the AoA is 0.9° higher for AWSM. This results in an increase of $\approx$ 15% in normal force for AWSM compared to BEM. Near the tip of the blade, these differences are much smaller.

For the blade moments, it can be found that AWSM calculates a larger mean value around all three axis. The differences for the blade M_x, M_y and M_z are 10%, 5% and 50% respectively. For the rotor performance, AWSM also calculates a larger mean value, with 10% and 6% for the power and F_{ax} respectively.

Despite the relatively larger differences found in the rotor aerodynamics for the half wake case, a reasonable agreement has been found for the tower M_x and M_y, with differences of only 4% and 7% respectively. For the tower M_z, BEM calculates a 40% higher value. It should be noted that for the straight uniform inflow and yawed inflow case, also large differences have been found for the tower M_z.

Standard Deviation Values

The standard deviation values of the output parameters for the half wake case are shown in Table 6.10. A very interesting observation that can be made is that the standard deviation of $u_{i,ax}$ is about 9 times higher for AWSM as it is for BEM in the mid-section of the blade. It is expected that this is caused by the convergence criteria for the BEM equations, which is based on the convergence of the mean induction for each blade rather than the convergence of each blade separately. Since the incoming wind speed changes over the azimuth position, this effect becomes more pronounced in the half wake case. This effect will be elaborated upon in Section 6.3.3. It can be seen that this effect is less dominant in the tip section of the blade, where $u_{i,ax}$ is also influenced by the tip loss correction. The effect of the non-uniform inflow velocity is better

Table 6.9: Mean values of output parameters for the INNWIND turbine in half wake.

Parameter	Unit	Location	1	2	3
$u_{i,ax}$	m/s	$r/R = 0.5$	2.228	1.960	1.809
AoA	deg	$r/R = 0.5$	4.023	4.616	4.908
F_n	N/m	$r/R = 0.5$	2012	2248	2340
$u_{i,ax}$	m/s	$r/R = 0.95$	2.486	2.685	2.495
AoA	deg	$r/R = 0.95$	6.735	6.642	6.844
F_n	N/m	$r/R = 0.95$	3673	3506	3579
blade M_x	kNm	$r = 0m$	1094	1122	1202
blade M_y	kNm	$r = 0m$	11869	12134	12431
blade M_z	kNm	$r = 0m$	19.85	26.94	30.26
P	MW	full rotor	1.826	1.858	2.002
F_{ax}	kN	full rotor	526.2	540.0	557.2
tower M_x	kNm	bottom	3451	3078	3325
tower M_y	kNm	bottom	59649	61545	63647
tower M_z	kNm	bottom	5140	3660	3641

captured by BEM for the AoA, since the local velocity is used to determine the local AoA on each blade section. BEM is found to calculate a larger variation in AoA and normal force compared to the results of AWSM of $50 - 60\%$ in the mid-section and 30% in the tip section of the blade.

For the blade loads, it is found that BEM calculates a larger variation compared to AWSM for all three blade moments. Largest differences are found for the blade M_y, where BEM calculates a 33% larger standard deviation, compared to AWSM. For the standard deviation of the power a reasonable agreement has been found between BEM and AWSM, whereas the variation in F_{ax} is found to be 60% higher for BEM. This is caused by the larger effect of the tower on F_{ax}, as well as a larger load variation due to the more constant $u_{i,ax}$ for BEM.

For the standard deviation of the tower loads, it is found that BEM calculates a larger variation. Differences are $\approx 30\%$ for the moments around all three axis of the tower.

Table 6.10: Standard deviation values of output parameters for the INNWIND turbine in half wake.

Parameter	Unit	Location	1	2	3
$u_{i,ax}$	m/s	$r/R = 0.5$	0.050	0.468	0.458
AoA	deg	$r/R = 0.5$	2.405	1.510	1.523
F_n	N/m	$r/R = 0.5$	770.5	501.9	508.7
$u_{i,ax}$	m/s	$r/R = 0.95$	0.238	0.279	0.291
AoA	deg	$r/R = 0.95$	1.744	1.403	1.386
F_n	N/m	$r/R = 0.95$	688.2	523.8	517.3
blade M_x	kNm	$r = 0m$	8245	8107	8123
blade M_y	kNm	$r = 0m$	2631	1976	1979
blade M_z	kNm	$r = 0m$	95.63	87.04	86.19
P	kW	full rotor	14.67	17.27	16.25
F_{ax}	kN	full rotor	3.363	1.801	2.057
tower M_x	kNm	bottom	991.8	733.5	778.3
tower M_y	kNm	bottom	5531	3965	4177
tower M_z	kNm	bottom	853.2	646.1	670.2

6.3.2 Damage Equivalent Loads

The damage equivalent loads are calculated for the half wake case, as described in 6.1.2. Again, the last two rotor revolutions of the simulation have been used to calculate the DEQL of the blade and tower moments. The results are shown in Table 6.11. From this table a few interesting observations can be made.

First of all, it can be seen that there is a reasonable agreement for the blade M_x and M_z, which is expected since these loads are mainly influenced by the gravity force. For the blade M_y, it can be found that BEM calculates a 37% higher DEQL compared to AWSM. This difference is mainly caused by the differences in load variation calculation between BEM and AWSM. For the tower loads, BEM is found to calculate a higher DEQL for the moments around all three axis of the tower. The differences are found to be 29%, 37% and 24% for the M_x, M_y and M_z respectively.

For a wind turbine that is designed for a wind farm, the differences in DEQL could prove to be very important. When assessing the fatigue life of the blades and the tower, the results from BEM will result in a significantly lower life time compared to AWSM. This uncertainty will result in large safety factors, which will result in over-designed structures and increase turbine cost.

Table 6.11: *Damage equivalent loads of output parameters for the INNWIND turbine in half wake.*

Parameter	Unit	Location	1	2	3
blade M_x	kNm	$r = 0m$	18661	18333	18370
blade M_y	kNm	$r = 0m$	6054	4385	4411
blade M_z	kNm	$r = 0m$	218.4	198.4	196.6
tower M_x	kNm	bottom	2026	1494	1576
tower M_y	kNm	bottom	11359	7870	8295
tower M_z	kNm	bottom	1802	1400	1448

6.3.3 Modeling of Non-Uniform Inflow

In this section the effect of the modeling of the non-uniform inflow by BEM and AWSM will be discussed.

Effect on Axial Induced Velocity

The BEM model in ECNAero divides each annulus into a streamtube for every blade, where the local axial loads balance the momentum equation for the streamtube and the momentum is determined by the incoming velocity at the blade section. The solution is converged when the residue of the mean induction factor between two iterations is below a certain threshold. AWSM calculates the $u_{i,ax}$ at every time-step for the current azimuth angle by the influence of the vorticity of the bound and trailed vortices. This difference in modeling results in a large difference for $u_{i,ax}$ between BEM and AWSM. As was shown in Table 6.10, a factor of 9 difference in standard deviation was found at $r/R = 50\%$. In Fig. 6.10a, $u_{i,ax}$ is shown as function of azimuth angle for the mid-section of the blade. From this figure, it can be seen that there is an almost constant $u_{i,ax}$ during a rotor revolution for BEM, except when the blade passes the tower. For the results from AWSM, a large variation in $u_{i,ax}$ is found, where the induced velocity is approximately half when the blade is completely in the wake, i.e. at an azimuth angle of 270°. Furthermore, it can be observed that there is a larger effect of the tower on $u_{i,ax}$ for BEM than there is for AWSM.

At the tip section of the blade, the $u_{i,ax}$ is also influenced by the tip loss correction and hence the induced velocity changes more over time. It can be seen that there is a better agreement between BEM and AWSM in general, although the different wake configuration begin to deviate more.

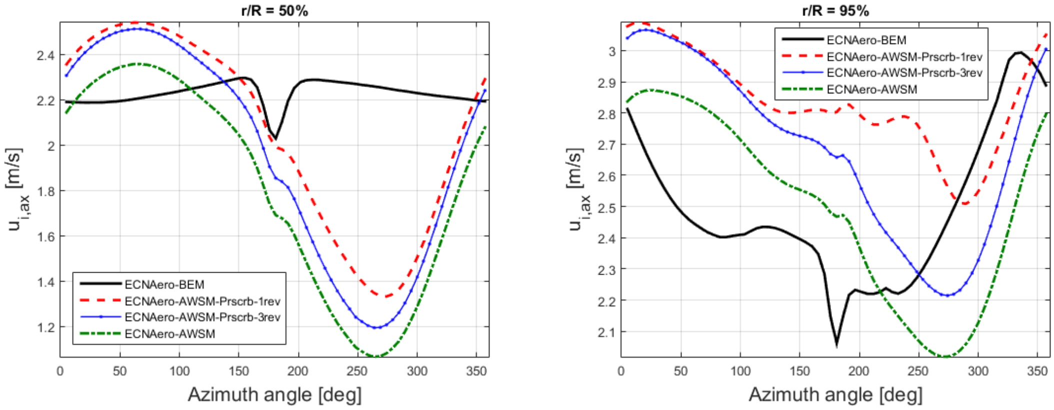

(a) $r/R = 50\%$. (b) $r/R = 95\%$.

Figure 6.10: *Axial induced velocity vs. azimuth angle for the INNWIND turbine in half wake.*

Effect on Angle of Attack

The local inflow velocity is taken into account for the calculation of the AoA, which was not the case for $u_{i,ax}$. Therefore, a much better agreement is found for the AoA in the mid-section of the blade between BEM and AWSM. In Fig. 6.11a, it can be seen that BEM calculates a lower AoA when the blade is in the wake (azimuth $= 270°$) compared to AWSM, which is a direct result of the higher induction for BEM in this part of the rotor plane. At $r/R = 95\%$, there is a better agreement between BEM and AWSM, although it can still be observed that BEM calculates a larger variation of AoA over the rotor revolution.

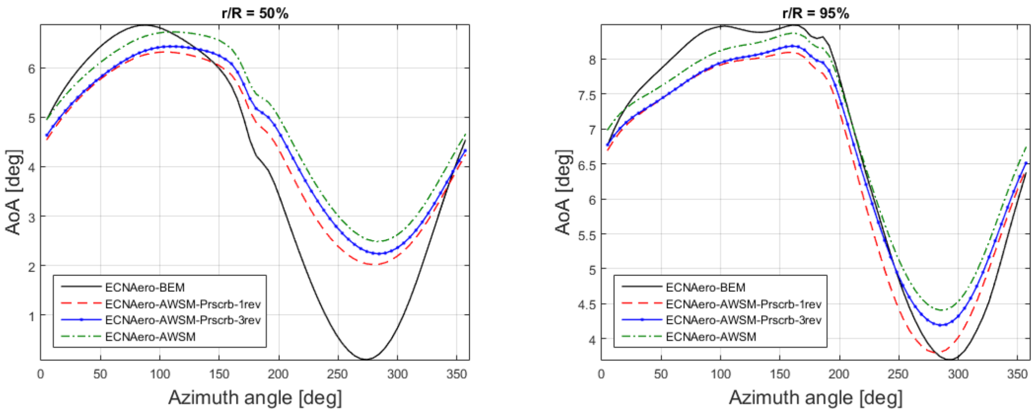

(a) $r/R = 50\%$. (b) $r/R = 95\%$.

Figure 6.11: *Angle of attack vs. azimuth angle for the INNWIND turbine in half wake.*

The larger variation of AoA for BEM can be explained by looking at the definition of the velocities for a rotating airfoil in Fig. 6.12. From this figure, the following relation can be deducted for the flow angle ϕ, which is equal to the AoA for this case, since the pitch angle $\theta = 0$.

$$\tan\phi = \frac{(1-a)V_0}{(1+a')\omega r} \tag{6.2}$$

During a rotor revolution for the rotor in a partial wake, the local incoming velocity V_0 decreases when the blade enters the part of the rotor plane that is in the wake and increases when the blade

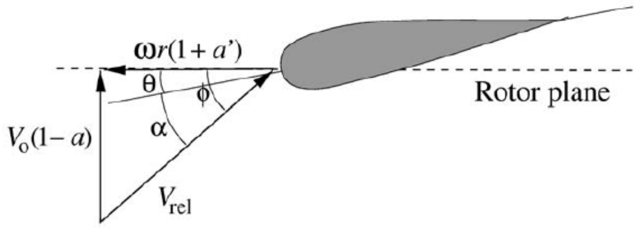

Figure 6.12: *Definition of the velocities on a rotating airfoil, from [8].*

leaves the section of the rotor plane that is in the wake. However, the local rotational velocity ωr remains constant. As was shown in Fig. 6.10, AWSM shows a larger fluctuation of $u_{i,ax}$. The increase in $u_{i,ax}$ is coincides with an increased V_0. From Eq. 6.2, it is shown that an increased $u_{i,ax}$ or a will reduce AoA, whereas the opposite is true for the influence of V_0. This means that the effect of the variation of $u_{i,ax}$ and V_0 have an opposite influence on AoA. Since BEM does not model this variation in $u_{i,ax}$ due to the variation of V_0, a larger variation of AoA is obtained during a revolution. This increased variation of AoA also causes an increase in the variation of blade loads, as was already observed in Table 6.11.

Effect on Flapwise Blade Moment

From Table 6.11, it was found that the DEQL was calculated to be 37% higher for the blade M_y with BEM compared to AWSM. In order to find out where these differences come from, the blade M_y is compared as function of azimuth position in Fig. 6.13.

From this figure, it can be seen that there is a reasonable agreement between BEM and AWSM when the blade is not in the wake, i.e. azimuth angle between 0° and 180°. For the second half part of the rotor revolution, when the blade is in the wake, BEM calculates a lower blade M_y compared to AWSM, which is a result of the lower AoA and indirectly of the higher induced velocity. This creates a larger load amplitude, resulting in a DEQL of 37% higher for BEM compared to AWSM.

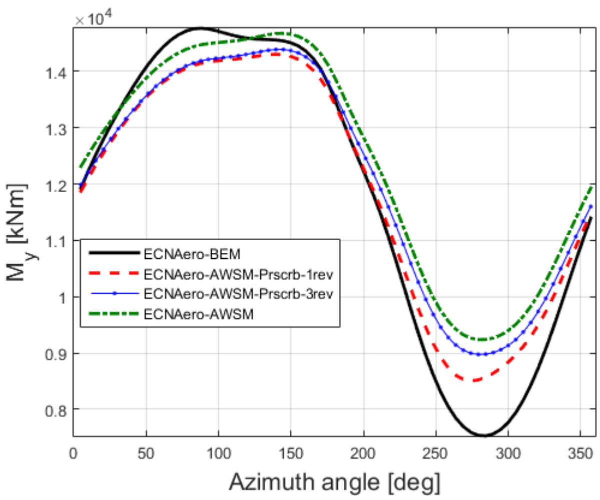

Figure 6.13: *Flapwise blade root bending moment vs. azimuth angle for the INNWIND turbine in half wake.*

6.3.4 Analysis

In this section, the results from the half wake test case will be discussed. In this test case, the effect of a non-uniform inflow can be compared between BEM and AWSM. The main observations are summarized below:

- For the local blade aerodynamics, large differences have been found in $u_{i,ax}$ and AoA in terms of mean and standard deviation values between BEM and AWSM. This is expected to be due to the convergence criteria implemented in BEM, which is based on the convergence of the mean induction factor per annulus, rather than a convergence for each blade. This might result in filtering some of the variations in $u_{i,ax}$. This leads to large differences when the blade is in the wake, where AWSM calculates only 50% of the $u_{i,ax}$ calculated by BEM. This results in an increased variation in AoA for BEM, leading to larger load fluctuations in the blade, as found from the DEQL values in Table 6.11.
- AWSM is found to calculate a large mean value for the normal force in the mid-section of the blade. The differences are found to be 16% large for AWSM with a free wake configuration compared to BEM. In the tip section of the blade, the differences between the local blade aerodynamics become smaller.
- For the blade loads, it is found that AWSM calculates a larger mean value, whereas BEM calculates a larger fluctuation during a rotor revolution. When comparing the DEQL of the blade moments, it is found that BEM calculates a larger DEQL for all blade moments, where the largest differences are obtained for the blade M_y (37%).
- It is found that BEM calculates a larger fluctuation in tower loads compared to AWSM. This leads to a DEQL of $\approx$ 30% more for the tower M_x, M_y and M_z. This would mean that for a wind turbine in a wind farm, where a wind turbine operates a significant amount of the time in a wake, the life-time would be estimates to be much smaller when the analysis is done with BEM compared to AWSM.

6.4 Extreme Wind Shear

In this section, the results from the extreme wind shear case are presented. Similar to the half wake case, the simulation have only been run for the INNWIND turbine with BEM and AWSM, for which two wake configurations have been applied. The focus for this test case is how the different codes cope with the calculation of the response to a sudden increase in wind shear, which leads to a local variation in wind speed. First, the modeling of the wind shear transient is investigated by comparing the induced velocity and AoA between BEM and AWSM. Then, the dynamic stall effects are compared between BEM and AWSM, which happens to occur mainly in the root section of the blade. Besides the comparison between the models of ECNAero, also a comparison is done between ECNAero with hGAST and HAWC2. First, the DEQL of the blade and tower loads will be compared in order to quantify the differences between BEM, AWSM and the external codes. Next, the local blade aerodynamics are compared for $u_{i,ax}$ and AoA, followed by a comparison of the blade M_y and F_{ax}. Finally, also the dynamic stall behavior is compared between all models.

In order to distinguish the results between the different simulation tools in the tables, each code is numbered, as indicated in Tables 6.12.

Table 6.12: *Labeling of the codes for the extreme wind shear case.*

Number	Code	Turbine
1	ECNAero-BEM	INNWIND
2	ECNAero-AWSM-Prscrb	INNWIND
3	ECNAero-AWSM	INNWIND
4	hGAST-BEM	INNWIND
5	hGAST-vortex	INNWIND
6	HAWC2-BEM	INNWIND

6.4.1 Modeling of Wind Shear Transient

In this section, the effects of the response to the wind shear transient are compared for BEM and AWSM. In Fig. 6.14, $u_{i,ax}$ is plotted as function of time in the mid-section and tip of the blade. In the mid-section of the blade, it can be observed that BEM does not seem to calculate a significant response to the transient, whereas AWSM shows a large variation. This could be caused by the convergence criteria in BEM, which is based on the convergence of the mean induction rather than the local induction for each blade. In the tip section, a large increase in $u_{i,ax}$ is observed around $t = 7s$ for AWSM, which is not observed by BEM. This is caused by the fact that the local wind speed is reduced close to zero in the lower part of the rotor plane at $t = 7s$, which is when the blade is in downward position. This results in an accumulation of vortex points behind the blade, which increases $u_{i,ax}$. As can be seen from Fig. 6.14, this effect is not modeled by BEM.

For the AoA, a much better agreement has been obtained between BEM and AWSM, as can be seen in Fig. 6.15. It can be seen that BEM calculates a large increase in AoA as a response to the transient compared to AWSM. In the tip section of the blade, it can be observed that AWSM calculates a lower AoA at $t = 7s$, which is caused by higher $u_{i,ax}$ due to the accumulation of vortex points.

The larger variation of AoA during the transient for BEM can be explained by the fact that BEM does not model the variation of $u_{i,ax}$ as function of azimuth angle, as was found in Section 6.3.3. This increased variation in AoA causes an increase in the variation of the blade loads, which will be elaborated upon in Section 6.4.3.

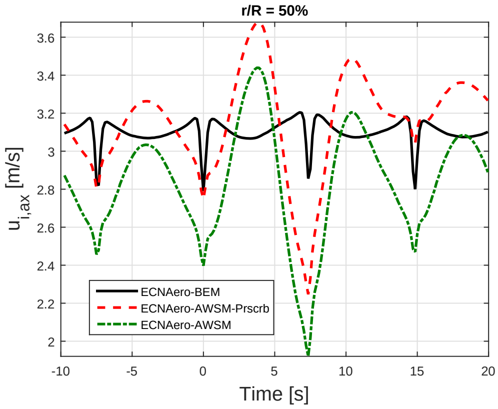

(a) $r/R = 50\%$.

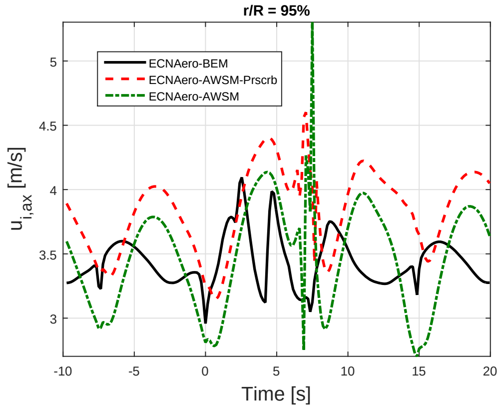

(b) $r/R = 95\%$.

Figure 6.14: *Axial induced velocity as function of time for the INNWIND turbine during the wind shear transient.*

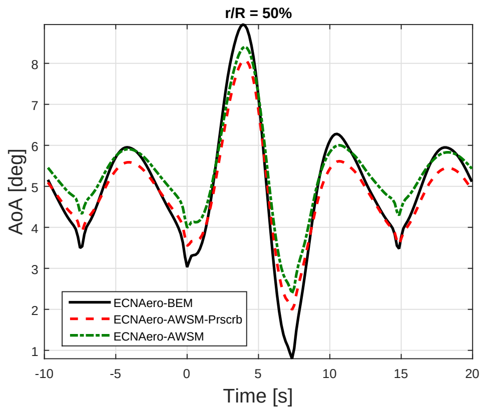

(a) $r/R = 50\%$.

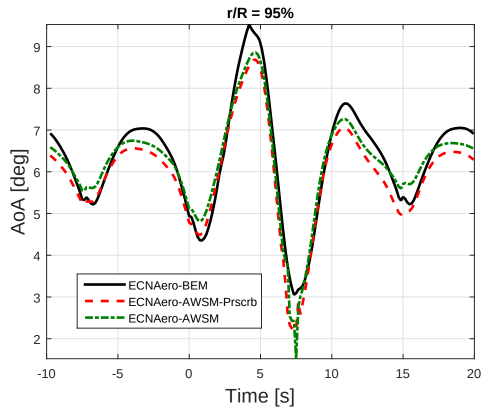

(b) $r/R = 95\%$.

Figure 6.15: *Angle of attack as function of time for the INNWIND turbine during the wind shear transient.*

6.4.2 Modeling of Dynamic Stall

In this section the effect of dynamic stall is investigated and how BEM and AWSM models this effect. The physical explanation behind dynamic stall is that the AoA is increased above stall, resulting in a vortex being shed at the leading edge and causing a rapid increase in lift. After a short time, this vortex has passed the airfoil and the lift decreases again. The dynamic stall model used in this test case is the first order Snel model, as described in Section 4.4.6. This dynamic stall model adds an additional dynamic contribution to the steady lift coefficient at a certain AoA and is dependent on the time history of the AoA.

Dynamic stall occurs mainly in the root section of the blade for the extreme wind shear case, since the airfoils used in the root section have a high thickness ratio, which results in a much lower stall AoA. In Fig. 6.16, the lift polar is shown for the FFA airfoils used in the INNWIND turbine, where the last 3 digits stand for the thickness ratio. An overview of the airfoil and for which section of the blade they are used can be found in Table 6.13. For the first 9.69m of the blade, a cylinder is used with a constant c_l of 0 and a constant c_d of 0.6. It should be noted that the stall AoA is an approximation, since the airfoil data is presented in steps of 2°.

Table 6.13: Overview of airfoil data for the INNWIND turbine.

Start $[m]$	Airfoil	AoA_{stall}
9.69	FFA-W3-600	-
15.96	FFA-W3-480	6
20.74	FFA-W3-360	12
28.62	FFA-W3-301	14
40.81	FFA-W3-241	16

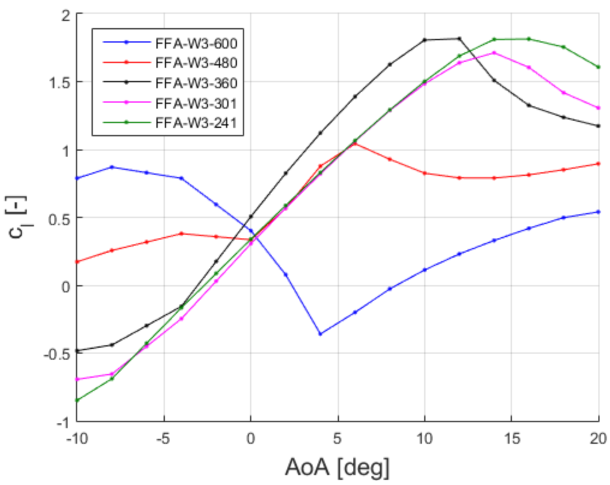

Figure 6.16: Lift polar of FFA airfoils used in the INNWIND turbine.

In order to compare the dynamic stall effect between BEM and AWSM, c_l is plotted as function of AoA during the full transient at $r/R = 24\%$ and 50% in Fig. 6.17. Since the exact evaluation points along the blade are different for BEM and AWSM, a location is chosen where the steady lift slope is similar, which is found to be at $r/R = 24\%$. At this location, there is the transition between the FFA-W3-480 and FFA-W3-360 airfoil.

From Table 6.13, it can be seen that the FFA-W3-480 has a stall AoA of 6°. Due to this low stall AoA, the blade section will be in stalled conditions for most of the time and dynamic stall effects will occur. In Fig. 6.17a, c_l is plotted as function of AoA during the 12s transient. From this figure, it can be seen that there is a significant difference in the dynamic stall behavior between BEM and AWSM in the root section of the blade. This is expected to be the case, since AWSM models the interaction between blade elements through the vorticity, whereas BEM calculates independent blade elements. Since the root section suffers from severe dynamic stall behavior due to the low stall AoA and AWSM models the interaction between the blade elements, the dynamic stall effects are expected to influence the aerodynamic for a longer blade section from the root.

In the mid-section of the blade, the FFA-W3-241 airfoil is used, which has a stall AoA of 16°. As can be seen in Fig. 6.17b, the mid-section of the blade does not exceed the stall AoA, although there are still small differences in c_l found for the same AoA. This can be explained by the fact that the dynamic stall model of Snel adds a dynamic stall term to the steady c_l based on the difference between the steady and potential lift, which has a $c_l - AoA$ slope of 2π. Since there exist a difference in steady and potential c_l before stall, small differences in c_l will occur, as were found in Fig. 6.17b. Again, it is found that the variation in c_l for the same AoA is the largest for BEM, which is expected to be caused by the larger fluctuation of AoA during a rotor revolution.

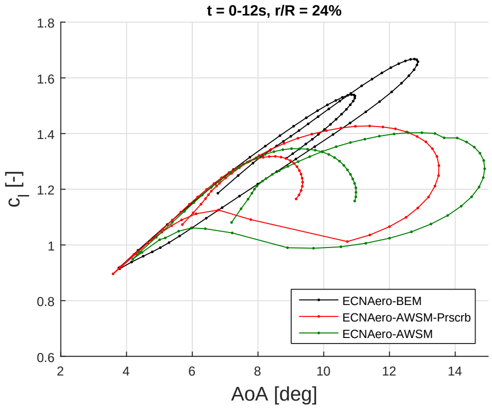

(a) $r/R = 24\%$.

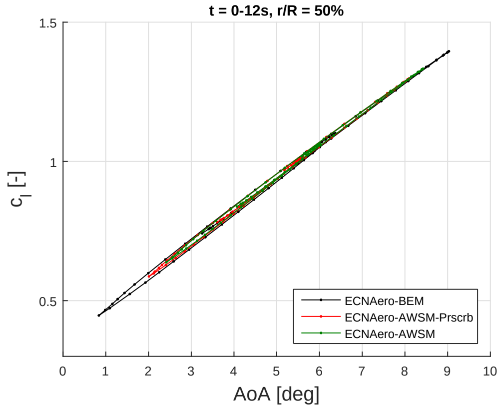

(b) $r/R = 50\%$.

Figure 6.17: *Lift coefficient vs. angle of attack during the wind shear transient for the INNWIND turbine.*

6.4.3 Cross Comparison with External Codes

In this section, the results are compared between PhatasAero, hGAST and HAWC2. The comparison will be done for the blade and tower DEQL, the local blade aerodynamics, the blade loads, the rotor performance and the dynamic stall effect. It should be noted that the simulation from hGAST and HAWC2 have been run with the controller on, which results in a changing rotor speed. Therefore, this comparison will focus on the trends rather than the quantification of the results.

Damage Equivalent Loads

In order to compare the fatigue loads for the extreme wind shear case for the various codes, the DEQL has been calculated for the blade and tower moments, as is introduced in Section 6.1.2. It should be noted that the DEQL is calculated only for the time period of the transient, i.e. for $12s$. The DEQL of the blade and tower moments are shown in Table 6.14.

From this table it can be seen that there is a good agreement for the blade M_x between the results of PhatasAero and hGAST, although the results form HAWC2 shows a 10% lower value. This might be caused by the fact that HAWC2 uses a much smaller time step ($\Delta t = 0.02s$) compared to ECNAero ($\Delta t = 0.15s$) and hGAST ($\Delta t \approx 0.09s$). For the blade M_y, it can be seen that ECNAero-BEM calculates a 17% larger value compared to AWSM. Interesting to see is that the results from ECNAero-BEM agree well with the results from HAWC2 and the vortex model of hGAST, whereas the results from AWSM agree better with the results from the BEM model of hGAST. A similar observation is made for the blade M_z, with differences up to 20%.

For the tower M_x, it can be seen that ECNAero-BEM again calculates a larger DEQL compared to AWSM. It can be seen that the three BEM codes (ECNAero, hGAST and HAWC2) are in good agreement, whereas the same holds for the three vortex wake models. For the tower M_y, the largest differences are obtained. It can be found that ECNAero-BEM calculates a 17% larger DEQL compared to AWSM, whereas the results from hGAST and HAWC2 show a much lower value. The DEQL of the tower M_y from HAWC2 is only 30% of the DEQL from ECNAero-BEM. For the tower M_z, a much better agreement is found, with a maximum difference of 12% between the BEM and vortex wake model of hGAST.

Table 6.14: *Damage equivalent loads of output parameters for the INNWIND turbine in extreme wind shear.*

Parameter	Unit	Location	1	2	3	4	5	6
blade M_x	kNm	$r = 0m$	18589	18312	18331	18058	18400	16397
blade M_y	kNm	$r = 0m$	13663	12011	11652	11507	13766	13682
blade M_z	kNm	$r = 0m$	165.8	148.7	142.4	133.0	159.5	161.0
tower M_x	kNm	bottom	5982	4767	4934	6842	5325	6169
tower M_y	kNm	bottom	12507	10639	10692	7441	8999	3790
tower M_z	kNm	bottom	3073	3118	3132	3259	2906	3104

Local Blade Aerodynamics

The results for $u_{i,ax}$ are shown in Fig. 6.18. It should be noted that the results from the vortex wake code of hGAST did not contain induced velocity data and is therefore not shown in the comparison. In the mid-section of the blade, a good agreement is obtained between the BEM model of PhatasAero and hGAST. It can be seen that the results from HAWC2 show a larger influence of the transient compared to the other BEM models. Again, this can be caused by the convergence criteria of BEM, which is based on the mean induction and might average the variations per blade. Furthermore, it can be observed that the tower effect on $u_{i,ax}$ is much smaller from the two external BEM codes compared to PhatasAero-BEM. In the tip section of the blade, it can be oberved that the BEM models from hGAST and HAWC2 both capture the large increase in $u_{i,ax}$ due to the low incoming velocity during the transient, as is also observed from AWSM. This effect is not captured by the BEM model of PhatasAero.

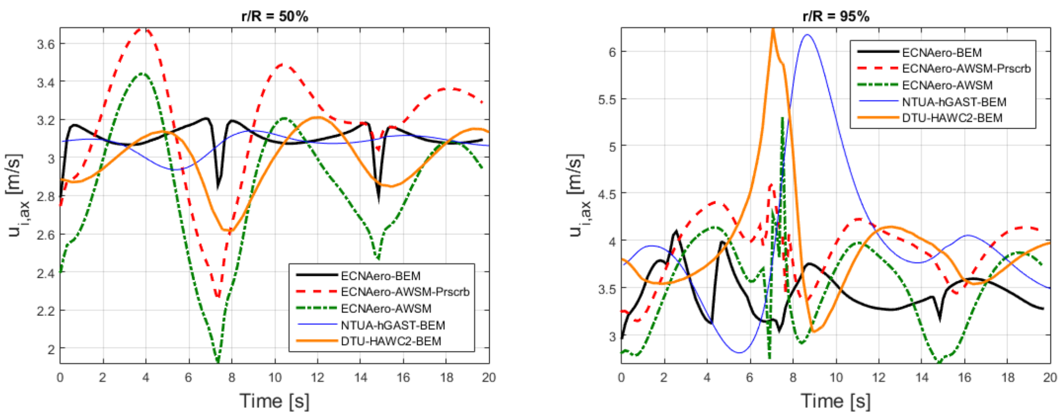

(a) $r/R = 50\%$. (b) $r/R = 95\%$.

Figure 6.18: *Axial induced velocity vs. time during the wind shear transient for the INNWIND turbine.*

A comparison of the AoA is shown in Fig. 6.19. From this figure, it can be observed that there is a reasonable agreement in terms of the response to the transient. It can be observed that HAWC2 seems to calculate the largest variation in AoA, especially near the tip of the blade. However, it should be kept in mind that some of the differences in AoA are caused by a different rotor speed between the models, as is shown in Fig. 6.20. From this figure it can be seen that the implemented controller for HAWC2 and hGAST increases the rotor speed and consequently adjusts to the transient. The simulations for ECNAero have been without a controller, which results in a constant rotor speed during the transient.

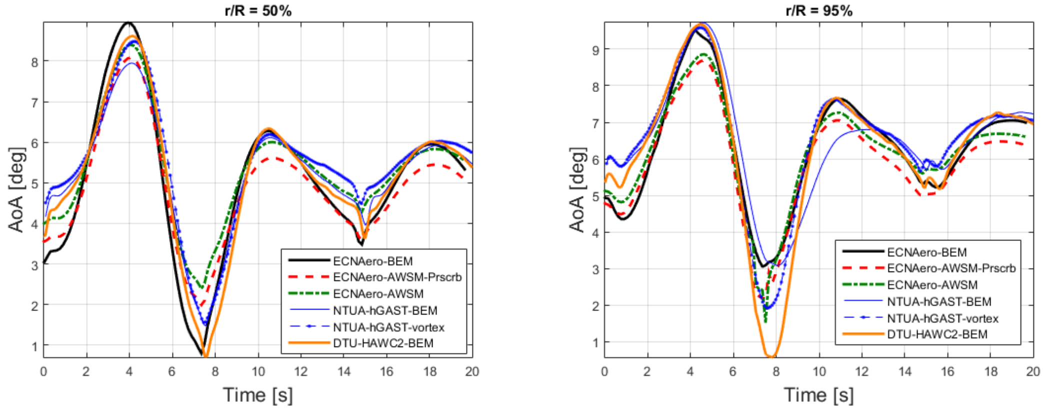

(a) $r/R = 50\%$.

(b) $r/R = 95\%$.

Figure 6.19: *Angle of attack vs. time during the wind shear transient for the INNWIND turbine.*

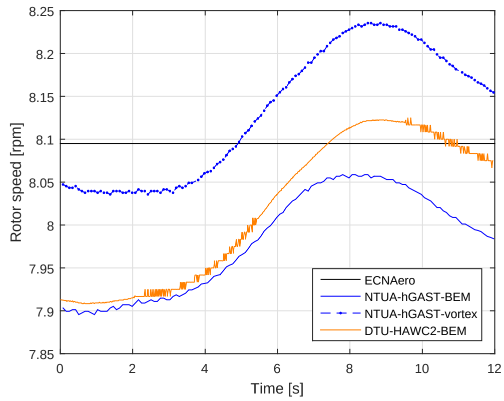

Figure 6.20: *Comparison of the rotor speed during the wind shear transient for the INNWIND turbine.*

Blade Loads

For the comparison of the blade loads, the flapwise blade root bending moment is compared, since this is loading is mainly caused by the aerodynamic forces rather than gravity forces. In Fig. 6.21, the blade M_y is shown as function of time during the transient. It can be seen that there is a good agreement for the response to the wind shear transient between the codes for M_y. It can be seen that the largest fluctuations are found for the BEM models of ECNAero and HAWC2 and the vortex wake model of hGAST. These large fluctuations also result in a larger DEQL of the blade M_y, as was found in Table 6.14. Furthermore, the good agreement between AWSM and the BEM model of hGAST can be explained from the lower fluctuations found in the blade M_y.

Interesting to note is that the results between the BEM and vortex wake model of hGAST seem to contradict the behavior of the BEM and vortex wake model in ECNAero. From the results of hGAST, it seems that the vortex wake model calculates the largest fluctuations and hence largest DEQLs compared to BEM, whereas the opposite is found for ECNAero. It should be noted that there are fundamental differences between the two vortex wake models, where the model in hGAST uses a panel code and AWSM uses a lifting line method. Furthermore, operational differences, as well as different engineering models makes it hard to find the root of the differences.

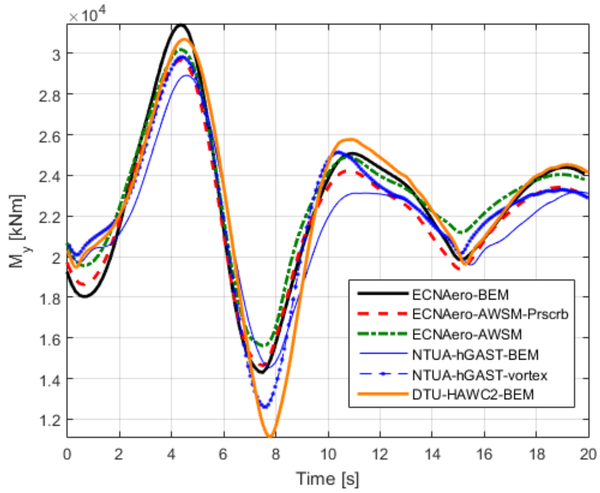

Figure 6.21: *Flapwise blade root bending moment vs. time during the wind shear transient for the INNWIND turbine.*

Rotor Performance

When comparing the rotor performance between the various codes, an interesting difference is observed for F_{ax}, as is shown in Fig. 6.22. From the results obtained by PhatasAero, it can be observed that F_{ax} decreases for the first $3s$ of the transient, then F_{ax} increases between $t = 3s$ and $t = 9s$ and finally F_{ax} decreases again until the end of the transient at $t = 12s$. The increase of F_{ax} during the transient is found to be $\approx 10\%$ for the results from PhatasAero, where the largest increase is found for the BEM model.

From the results of hGAST, this increase in F_{ax} during the transient is hardly noticeable, with an increase of $\approx 1\%$. For the results from HAWC2, the increase of F_{ax} is found to be $\approx 3\%$. It is expected that this large difference in response of F_{ax} is the reason for the difference found in the DEQL of the tower M_y, which is the fore-aft moment. This moment is mainly caused by F_{ax} multiplied by the hub height.

A large part of difference in the response of F_{ax} to the transient could be explained by the rotor speed, which is shown in Fig. 6.20. It is expected that the adjusted rotor speed limits the increase of F_{ax} during the transient. Since the different codes have used different controllers, the effect of dynamic inflow cannot be assessed properly.

Dynamic Stall Effect

In this section the dynamic stall effect is compared between the codes. The data that is available from the external codes for the comparison is only presented at $r/R = 25\%, 50\%, 70\%$ and 95%. The most interesting location to investigate dynamic stall effects is near the root. However, at $r/R = 24\%$ the airfoil changes from FFA-W3-480 to FFA-W3-360, which results in an increase in c_l for the same AoA and an increase stall AoA. Furthermore, the AoA is obtained by the interpolation between two blade elements, which means that it is likely that the blade elements used for the interpolation have different airfoils.

Keeping this in mind, c_l is plotted against AoA in Fig. 6.23 for $r/R = 50\%$ and 95%. For the mid-section of the blade, it can be seen that there are large differences found between the codes, even though dynamic stall effects are not expected to be large in this section of the blade. It can be seen that the results from HAWC2 show a small range of AoA during the transient of $\approx 2.5°$,

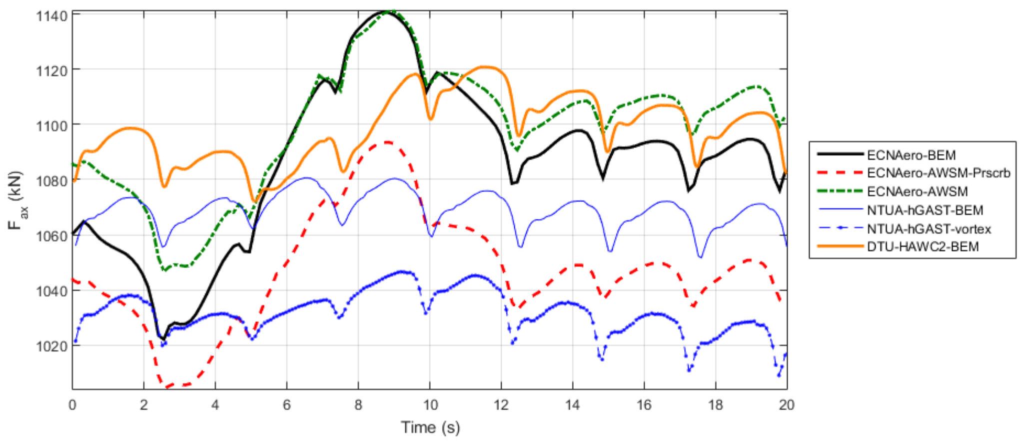

Figure 6.22: *Axial force vs. time during the wind shear transient for the INNWIND turbine.*

whereas ECNAero-BEM calculates a range of $\approx 8°$. All other models are in good agreement and are in a range of $5°$ to $6°$. The maximum variation of c_l for the same AoA is found to be only 0.07 at AoA $= 4°$. Interesting to observe is that the results from hGAST seem to fluctuate around a different lift polar, from which it can be assumed that hGAST uses either a different lift polar or applies a different correct such as a 3D correction for rotational airfoils.

Near the tip of the blade, it can be seen that there are hardly any dynamic stall effects present. Again, it can be seen that HAWC2 shows a rather small variation of AoA during the transient. Despite this small variation in AoA, there is still a significant variation in c_l compared to the results from ECNAero-BEM and AWSM. This is expected to be due to the dynamic stall model in HAWC2, which is a modified version of the Beddoes-Leishmann model, which models both the effects from shed vorticity from the trailing edge and the effects of stall separation lag caused by an in-stationary trailing edge separation point, whereas the Snel model does not model the effects of shed vorticity. Again, it can be seen that the results from hGAST show a lower steady c_l.

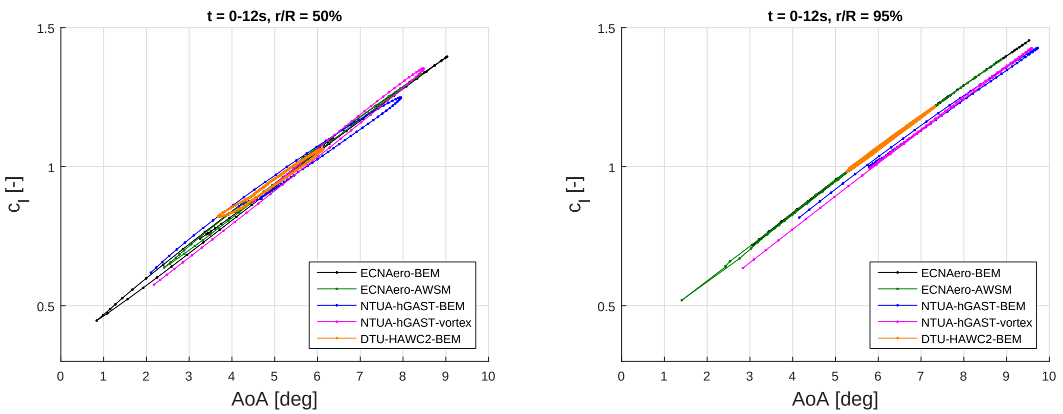

(a) $r/R = 50\%$.

(b) $r/R = 95\%$.

Figure 6.23: *Lift coefficient vs. angle of attack during the wind shear transient for the INNWIND turbine.*

6.4.4 Analysis

In this section, the main observations from the extreme wind shear case will be presented. The wind shear transient allows to investigate the effect of wind shear (transient), as well as dynamic stall, although it should be noted that this only occurs in the root section of the blade. Furthermore, this test case allows for a comparison with the two external BEM models (hGAST and HAWC2) and a vortex wake model (hGAST). The main observations are summarized below:

- From a comparison of the local blade aerodynamics, it is found that the BEM model in ECNAero calculates an almost constant $u_{i,ax}$. This could be explained by the fact that the convergence criteria in BEM is based on the mean induction factor per annulus rather than a local induction factor per blade. This is different compared to AWSM, where the influence of the azimuth location on $u_{i,ax}$ is modeled intrinsically. The lower variation of $u_{i,ax}$ results in a larger variation of AoA, caused by the variation of inflow velocity. This increased variation of AoA results in a larger blade load amplitude, resulting in a DEQL of the blade M_y and M_z of 20% larger for BEM compared to AWSM.

- From a comparison of the local blade aerodynamics to the results from the external codes, it is found that the BEM models of HAWC2 and hGAST both calculate an increase of $u_{i,ax}$ due to the transient at $t = 7s$, which was also found for AWSM. This effect was not modeled in the BEM model of PhatasAero. It is found that there is a good agreement found between the codes for AoA during the transient.

- For the DEQL of the tower M_x and M_y, BEM is found to calculate a larger value compared to AWSM (+20%), whereas a good agreement is found in M_z (2% difference).

- In general, a reasonable agreement has been found for the DEQL of the blade and tower moments between the codes during the wind shear transient, except for the tower M_y. The large variation in DEQL for the tower M_y is expected to be caused by the differences found in the response of F_{ax}, which in turn are expected to be due the implementation of the controller for hGAST and HAWC2, where the simulations with ECNAero are run without a controller.

- It is found that in the root section of the blade, significant dynamic stall effects occur. Since BEM and AWSM use the same dynamic stall behavior, a similar observation of the evolution of c_l is expected during the transient. However, due to the dependency between the blade elements in AWSM, the dynamic stall effects in the root section influences a larger section of the blade. In the mid-section of the blade, dynamic stall effects are also present, although the effect is much smaller and there is a very good agreement between BEM and AWSM. From a comparison to the external codes, significant differences are obtained in the mid-section, which is expected to be due the different dynamic stall models and the calculation of the AoA. In the tip-section of the blade, a good agreement has been obtained between the models, although the results from hGAST seem to use a different steady lift curve.

6.5 Turbulent Inflow

In this section the results from the turbulence case will be presented, as described in Section 5.5. In this test case, the INNWIND turbine will be analyzed in a turbulent inflow and the results from BEM and AWSM will be compared. Due to CPU considerations, only the first $150s$ of the turbulent wind file are used, which does not fully represent the statistics of the ten-minute turbulent inflow. With this test case, the differences of modeling a turbulent inflow between BEM and AWSM can be compared. This will be done by comparing the DEQL of the blade and tower moments, a frequency analysis on the axial induced velocity, angle of attack and flapwise blade moment, a comparison of various dynamic stall models, the effects of dynamic inflow on the rotor performance, a comparison of the wake configuration of AWSM and finally the effect of changing the evaluation location for the angle of attack.

6.5.1 Damage Equivalent Loads

In this section the results between BEM and AWSM are compared in terms of the DEQL of the blade and tower moments. The DEQL has been calculated as described in Section 6.1.2, for a $50s$ time period. Due to the varying wind velocity, the fatigue loads are expected to be much larger than for a steady inflow. The inclusion of turbulence, which is a well known phenomena in real life wind conditions, makes the analysis of the DEQL for the turbulent inflow much more relevant.

In Table 6.15, the DEQL of the blade and tower moments are listed for BEM and AWSM. From this table, it can be seen that there is a good agreement for the blade M_x and M_z, which is expected since the DEQL of these blade moments is mainly determined by gravitational loading. For the blade M_y, it can be seen that BEM calculates a 26% and 32% higher DEQL compared to the prescribed and free wake configuration of AWSM. This difference is caused by the larger load amplitude that is calculated in BEM, as can be seen in Fig. 6.24. This increased fatigue load is a result of the lower fluctuations in the axial induced velocity by BEM, which results in a larger fluctuation in AoA, which in turn results in larger blade load fluctuations. When comparing the DEQL of the turbulent inflow to the steady axial inflow case as listed in Table 6.4, it can be seen that the results from the turbulent inflow case show 9.64 times higher DEQL of the blade DEQL for BEM, indicating that indeed the varying inflow velocity has a major impact on the fatigue loads. When comparing the results between the steady and turbulent inflow case for AWSM, it is found that the DEQL is only 6-7 times higher.

Table 6.15: *Damage equivalent loads of output parameters for the INNWIND turbine in turbulent inflow.*

Parameter	Unit	Location	BEM	AWSM -Prscrb	AWSM
blade M_x	kNm	$r = 0m$	17958	17756	17746
blade M_y	kNm	$r = 0m$	8287	6592	6291
blade M_z	kNm	$r = 0m$	169.8	164.1	158.8
tower M_x	kNm	bottom	26493	23051	24033
tower M_y	kNm	bottom	44343	43206	43166
tower M_z	kNm	bottom	9155	8087	8001

When comparing the DEQL of the tower moments between BEM and AWSM, it can be seen that there is a good agreement for the INNWIND turbine in a turbulent inflow. It is found that BEM calculates a 15% higher DEQL for the tower M_x and M_z, whereas the differences for the tower M_y are less than 3%. Again, a good agreement in found between the results from the free and prescribed wake configuration of AWSM.

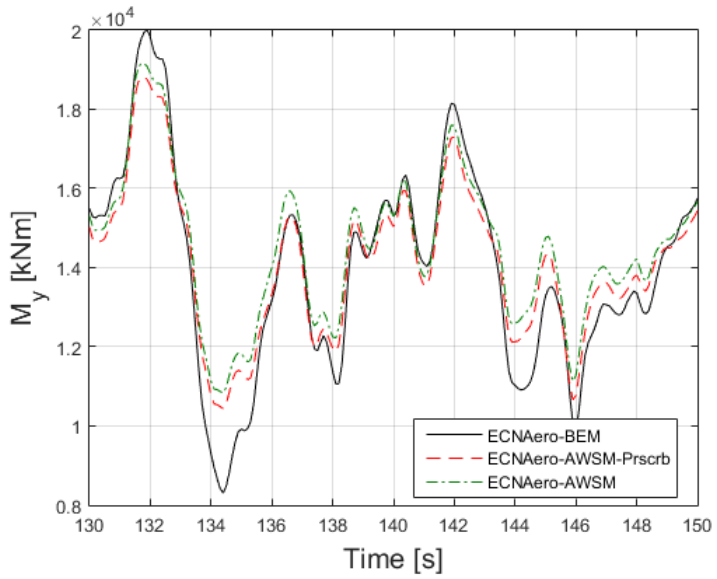

Figure 6.24: *Comparison of the flapwise blade root bending moment for the INNWIND turbine in a turbulent inflow.*

6.5.2 Frequency Domain Analysis

From a comparison of the axial induced velocity and angle of attack between BEM and AWSM in the time-domain, it was found that the results from BEM show a rather constant $u_{i,ax}$, which results in a more fluctuating AoA, as can be seen in Fig. 6.25. It should be noted that this behavior is most dominant in the mid-section of the blade, where the effect of the trailed root and tip vortices as well as the skewed wake effects are not affecting the results by engineering corrections.

This increased variation in AoA leads to larger fluctuations in normal and tangential force over the complete blade length, which results in larger blade load amplitudes and thus fatigue loads. In the following sections, $u_{i,ax}$, AoA and the blade M_y will be compared in the frequency domain. This will be done by means of the comparison of the PSD to inspect the distribution of the energy over the frequency spectrum in order to get a better understanding of where the differences between BEM and AWSM occur.

Axial Induced Velocity

As can be observed in Fig. 6.25a, the axial induced velocity in the mid-section of the blade is rather constant for BEM, whereas AWSM shows large fluctuations over time, following the incoming wind velocity. These fluctuations result in a larger energy for BEM over the complete range of frequencies that are considered, as can be seen in Fig. 6.26a. Interesting to observe is that AWSM shows a large increase in energy near the 1P, 2P and 3P frequency, which corresponds to a frequency of approximately $0.1Hz$, $0.2Hz$ and $0.3Hz$. This confirms that there is a strong cyclic influence on the axial induced velocity found from the results of AWSM. However, this influence of the rotor frequency is much less visible in the results from BEM, although a small peak is observed near the 1P frequency.

Near the tip of the blade, it can be seen that there is a much better agreement in the PSD of $u_{i,ax}$ between BEM and AWSM. It can be seen that both BEM and AWSM accurately capture the influence of the 1P and 2P frequency, where there is also a slightly influence of the 3P frequency

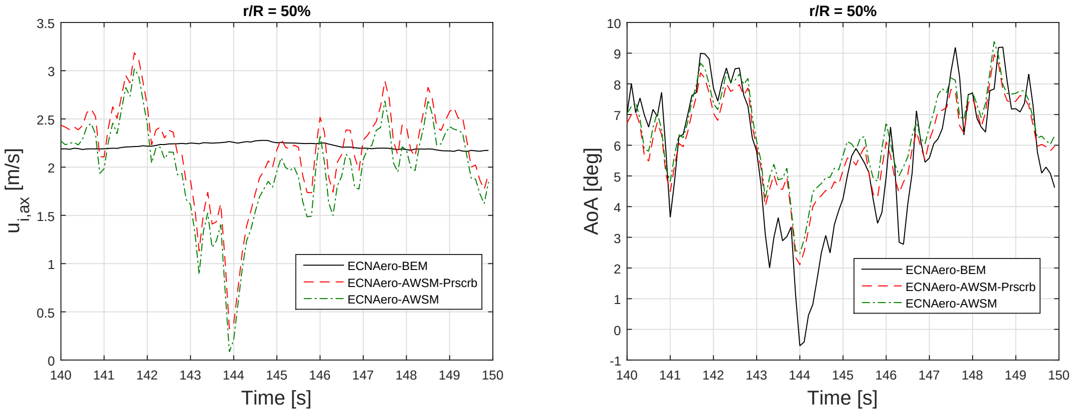

(a) *Axial induced velocity.* (b) *Angle of attack.*

Figure 6.25: *Comparison of the local blade aerodynamics at $r/R = 50\%$ for the INNWIND turbine in a turbulent inflow.*

noticeable. However, it should be noted that the energy at the 1P frequency is still significantly higher for the results from AWSM, which are confirmed by the higher standard deviation that is found in this section of the blade for $u_{i,ax}$. Interesting to observe is that for there are significant differences between the free and prescribed wake configuration of AWSM for $u_{i,ax}$, especially in the tip-section of the blade. These differences are caused by a difference in the mean value rather than the fluctuating part, as will be discussed later.

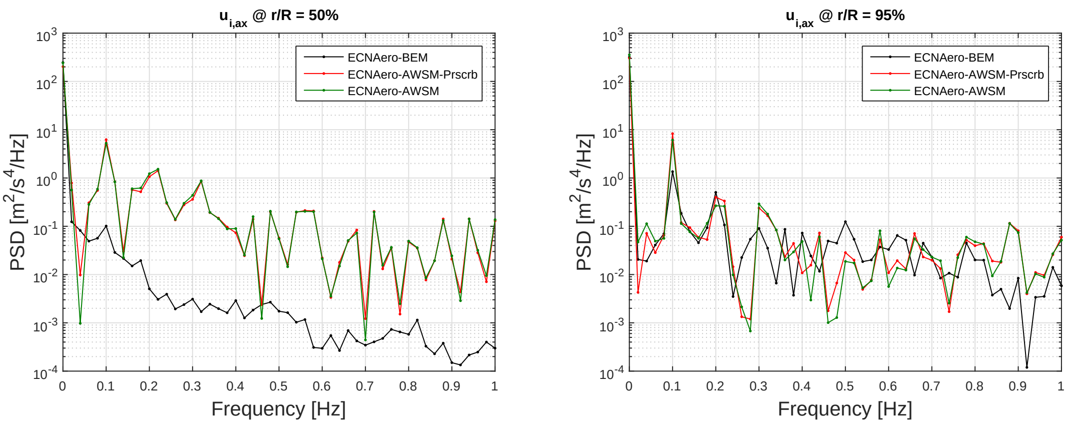

(a) $r/R = 50\%$. (b) $r/R = 95\%$.

Figure 6.26: *Comparison of the power spectral density of the axial induced velocity.*

Angle of Attack

From the time-domain analysis of the AoA in the mid-section of the blade in Fig. 6.25b it was shown that there is a much better agreement for the AoA between BEM and AWSM than for $u_{i,ax}$. However, it can be observed that BEM shows a larger variation of AoA over time, a result that was also found for the half wake and extreme wind shear test cases.

In Fig. 6.27, the PSD of AoA is compared between BEM and AWSM for the mid- and tip-section of the blade. From this comparison it becomes clear that BEM shows a larger energy over the complete frequency range in the mid-section of the blade, although there is a much better agreement compared to the PSD of $u_{i,ax}$, especially for the agreement in the energy peak at the rotor frequency. This confirms that the influence of the 1P frequency on the AoA is well modeled in BEM. A very good agreement has been obtained between the two wake configurations of AWSM for the PSD of AoA.

At the tip-section of the blade, it can be observed that there is a much better agreement of the PSD between BEM and AWSM, although it can be observed that BEM shows a slightly higher energy at the 1P frequency. From the comparison of the PSD for AoA is becomes clear that BEM indeed models a higher fluctuation of AoA over time, which is expected to result in the increased fatigue loads for the flapwise blade moment.

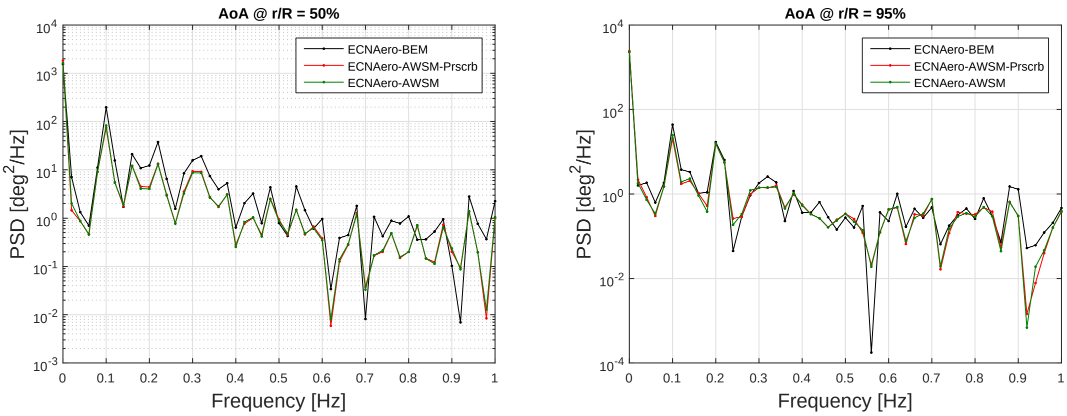

(a) $r/R = 50\%$.　(b) $r/R = 95\%$.

Figure 6.27: *Comparison of the power spectral density of the angle of attack.*

Flapwise Blade Root Bending Moment

In Section 6.5.1, it was already shown that BEM seems to calculate a larger load amplitude for the blade M_y, resulting in a larger fatigue load, which is confirmed by comparing the DEQL between BEM and AWSM. In order to further investigate this difference, the PSD of the blade M_y is compared in Fig. 6.28. From this figure, it becomes clear that BEM calculates a larger energy peak for the 1P, 2P and 3P frequency, which is a results of the larger load amplitude. For higher frequencies, there is a better agreement between BEM and AWSM, although the energy is much lower here and therefore has a smaller impact on the fatigue load.

It should be note that due to the varying rotor speed in the simulation, the 2P and 3P frequencies have a larger frequency spread. This results in the fact that the peak for the 1P frequency is more narrow compared to the peak for the 2P and 3P frequency. This means that the higher multiples of the rotor frequencies will overlap, which is the reason why the higher frequencies do not show any peaks and are therefore less interesting to investigate.

6.5.3 Comparison of Various Dynamic Stall Models

The default option for the dynamic stall model during simulations for this test case is the first order Snel model. However, in ECNAero also the second order Snel model, the Beddoes-Leishman model and the ONERA model are implemented, as is explained in Section 4.4.6. It should be noted that the implementation of these additional models is not fully validated in PhatasAero. In order to inspect the differences between these dynamic stall models, additional simulations have been run with ECNAero-BEM for the second order Snel model (Snel2), the Beddoes-Leishman

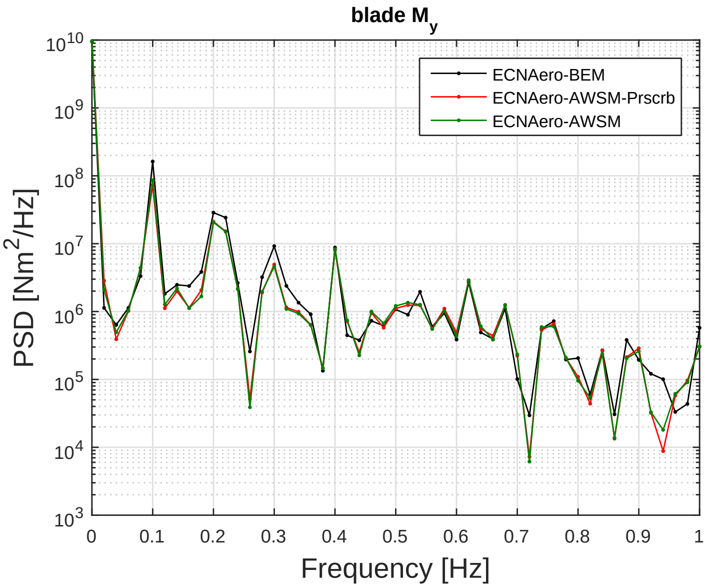

Figure 6.28: *Comparison of the power spectral density of the blade M_y.*

model and the ONERA model. All other settings for the simulations have been kept similar, as described in Section 5.5. The results from the prescribed wake configuration of AWSM have been added for reference in this comparison, where it should be noted that an excellent agreement is found between the free and prescribed wake configuration for the dynamic stall modeling. The results from AWSM are obtained with the default first order Snel model.

The dynamic stall behavior is analyzed for the time-period between $133s$ and $136s$. For this period, it is found that there is a large increase in wind speed, which results in useful data to compare the various dynamic stall models, as can be seen in Fig. 6.29a. For this time-period, the lift coefficient at $r/R = 60\%$ is plotted as function of the angle of attack in Fig. 6.29b. In this section of the blade, the FFA-W3-241 airfoil is used, for which the lift polar has been added to the plot for reference. From the c_l-α plot for the simulations with the various dynamic stall models, an interesting observation can be made. It can be seen that the results from the Beddoes-Leishman model show the largest difference from the steady lift, whereas the results from the Snel1 and Snel2 are almost identical. The results from the ONERA model are similar to the results from the Snel models, although a slightly higher variation from the steady airfoil data is observed.

In order to get a better understanding of the effect of the dynamic stall models on the variation of the aerodynamic coefficients, the difference in lift (Δc_l) and drag (Δc_d) coefficient due to the dynamic stall models is compared. For the comparison, Δc_l is defined as the difference between the simulated c_l and the steady c_l of the airfoil for each AoA in the time-period between $133s$ and $136s$ as shown in Fig. 6.29a. The definition of Δc_d is defined similar to Δc_l.

$$\Delta c_l = c_{l,sim} - c_{l,airfoil} \tag{6.3}$$

In Fig. 6.30a, Δc_l is shown as function of time for the various dynamic stall models. From this figure, it can be seen that indeed the results from the Beddoes-Leishman model show the largest variation in lift over time. Furthermore, it can be seen that there is a reasonable agreement between the ONERA and Snel models, although the ONERA model seems to result in a larger variation of Δc_l. Interesting to observe is that the BEM model with Snel1 calculates a larger Δc_l compared to AWSM, although the same dynamic stall model is implemented. This is expected to be caused by the fact that BEM calculates a larger variation of AoA over time, resulting in a

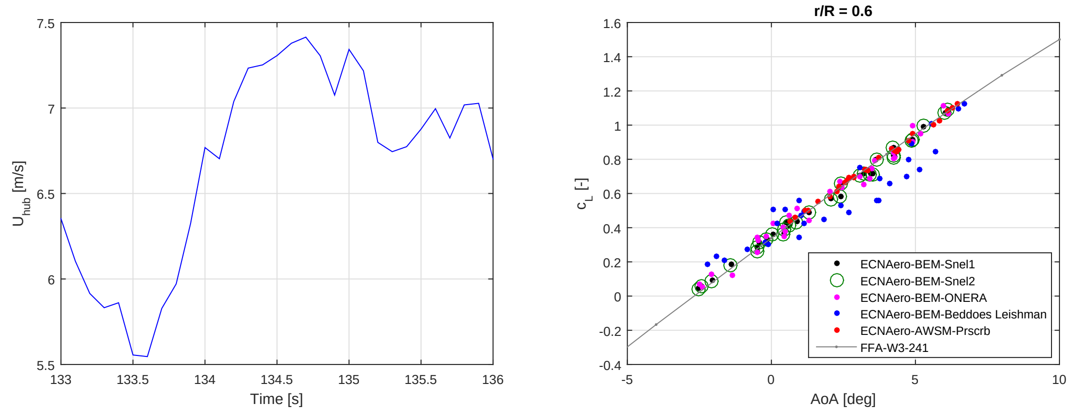

(a) *Wind speed.* (b) c_l-α *curve.*

Figure 6.29: *Comparison of the c_l-α curve during a turbulent inflow.*

more active dynamic stall behavior, since the Snel model is also dependent on the time-history of AoA. When comparing Δc_d in Fig. 6.30b, it can be seen that there is a relatively large fluctuation for the Beddoes-Leishman model, whereas all other models show a negligible Δc_d. This can be explained by the fact that both the Snel and ONERA model only apply a modification to c_l, whereas the Beddoes-Leishman model applies a modification to both c_l and c_d. The variation of drag for the other models is expected to be caused by numerical interpolation of the AoA and blade element locations.

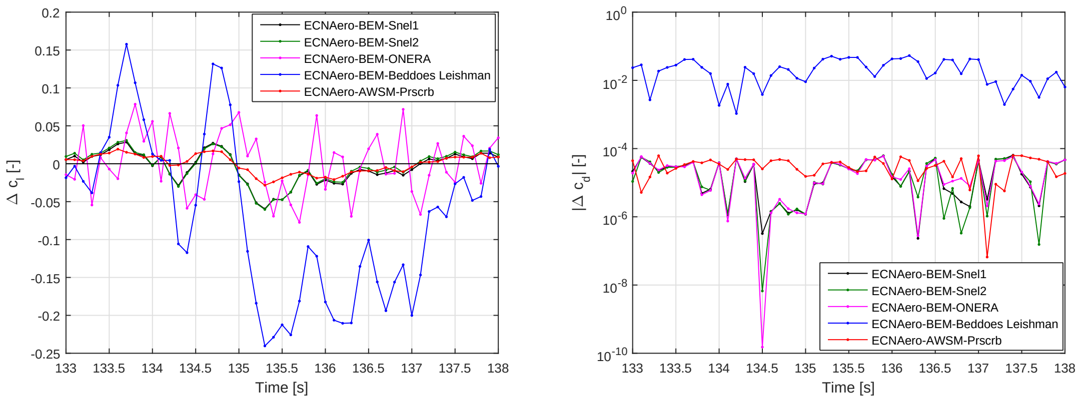

(a) Δc_l. (b) Δc_d.

Figure 6.30: *Comparison of Δc_l and Δc_d for various dynamic stall models during a turbulent inflow.*

In order to inspect how the various dynamic stall models affect the calculations of the aerodynamic loads on the turbine, the DEQL of the blade and tower moments is compared in Fig. 6.31. Due to stability problems in the root section of the blade for the Beddoes-Leishman model, the first $20m$ of the blade is not modeled for the BEM simulation with the Beddoes-Leishman dynamic stall model. However, the root section of the blade has a small contribution to the complete blade loads. From the figure, it can be observe that there is a good agreement between the models, especially between the ONERA and Snel models. The results from the Beddoes-Leishman model show the largest offset from the other models, which is expected to be caused by the inclusion of the influence of the dynamic stall model on c_d, where the other dynamic stall models only affect c_l. This leads to large variations in the tangential force, resulting in large differences in the blade

M_z and tower M_x. The reason that the blade M_x does not seem to be influenced, can be explained by the fact that the DEQL for the blade M_x is mainly determined by the gravity loading.

Furthermore, the Beddoes-Leishman model explicitly models the effect of flow separation by means of the vortex lift due to shed vortices. The differences in aerodynamic lift directly influences the blade M_y. From Fig. 6.31, it can be seen that there is a better agreement between the Beddoes-Leishman model and the results from AWSM, indicating that the inclusion of the shed vortices leads to a better agreement between BEM and AWSM.

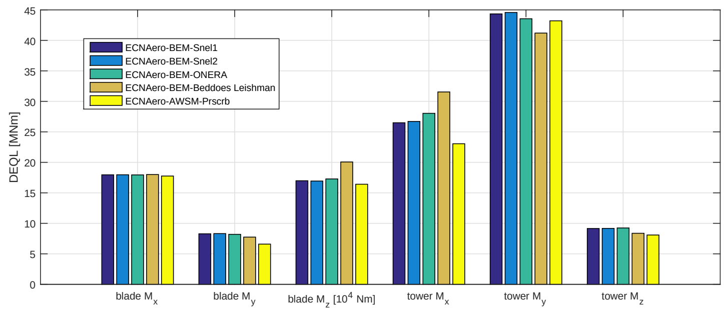

Figure 6.31: *Comparison of the DEQL for the blade and tower moments for various dynamic stall models during a turbulent inflow.*

6.5.4 Modeling of Dynamic Inflow

In this section the effect of the dynamic inflow is investigated. As explained in Section 4.4.4, the dynamic inflow model implemented in the BEM model of ECNAero adds an additional term to the axial momentum equation to correct for the rotor inertia. In order to investigate the effect of this dynamic inflow model, an additional BEM simulation has been run for the turbulent inflow case with the dynamic inflow model turned off.

In Fig. 6.32a, F_{ax} is compared for the BEM model with and without the dynamic inflow model and the results from AWSM. When comparing the results between the four models, it can be seen that AWSM seems to calculate the smallest variation of F_{ax} for both wake configurations. Furthermore, it can be seen that the implementation of the dynamic inflow model seems to restrains some of the peaks in F_{ax}, resulting in a better agreement between BEM and AWSM. When comparing the standard deviation for F_{ax} during a $50s$ time-period, it is found that the standard deviation is reduced from $41.34kN$ to $39.03kN$ with the implementation of the dynamic inflow model, which is closer to the $32.70kN$ and $31.44kN$ that were found from the free and prescribed wake configuration of AWSM.

When comparing the power in Fig. 6.32b, the same observation can be made as for F_{ax}. The implementation of the dynamic inflow model reduces the standard deviation of the power for the same time-period from $439.2kW$ to $400.8kW$. This makes the results from the BEM simulation with the dynamic inflow model agree better with the results from AWSM, for which a standard deviation of $360.9kW$ and $333.2kW$ is found for the free and prescribed wake configuration of AWSM.

Interesting to observe is that there are significant differences in the mean value of F_{ax} and P between the two wake configurations of AWSM. This is caused by a difference in the mean value of $u_{i,ax}$, which will be elaborated upon in the following section.

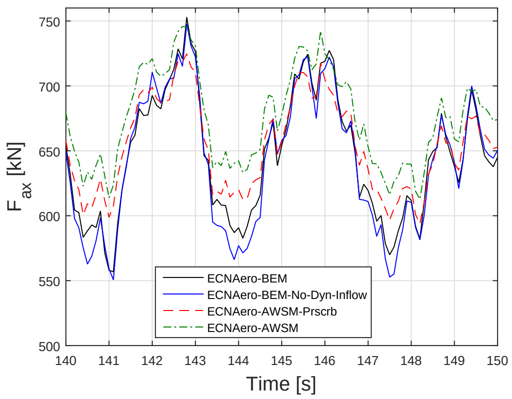

(a) *Axial Force.*

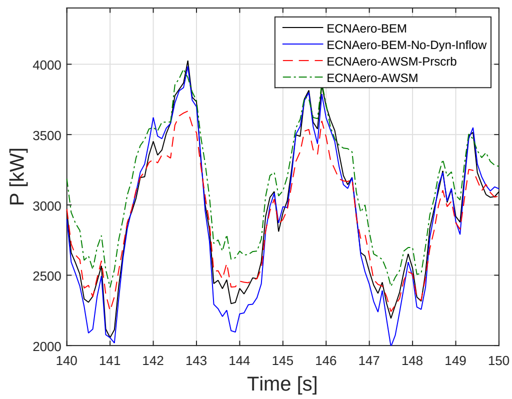

(b) *Power.*

Figure 6.32: *Comparison of the rotor performance for the INNWIND turbine in a turbulent inflow.*

6.5.5 Differences Wake Configuration AWSM

As was found from the comparison of the blade and tower DEQL, the frequency domain analysis of $u_{i,ax}$ and the rotor performance, there is a significant difference between the free and prescribed wake configuration of AWSM for the turbulence test case.

In order to get a better insight in the differences between the free and prescribed wake configuration of AWSM, the mean and standard deviation values of $u_{i,ax}$ are calculated along the blade for every 5% of the blade between 20% and 95% span. In Fig. 6.33, the results are shown for the complete time-period between $100s$ and $150s$. It can be seen that the free wake configuration of AWSM calculates a significantly lower mean $u_{i,ax}$ over the complete blade length compared to the prescribed wake configuration. Furthermore, it can be seen that there is an excellent agreement between the results from BEM and the prescribed wake configuration of AWSM. This might be explained by the fact that the velocity in the wake for the prescribed wake configuration is based on BEM theory.

When inspecting the standard deviation values of $u_{i,ax}$, it can be seen that there is an excellent agreement between the two wake configurations, whereas BEM is found to calculate a much lower variation in time. This is the reason why there is such a much better agreement between the DEQL of the blade and tower for AWSM compared to BEM, despite the differences in the mean values.

Since the induced velocity and the AoA have a direct geometrical relationship through the so-called velocity triangle, it is found that there is a good agreement between BEM and the prescribed wake configuration in terms of the mean values of AoA in the mid-section of the blade, whereas the free wake configuration of AWSM calculates a significantly higher mean AoA. For the standard deviation values, an excellent agreement between the two wake configuration of AWSM is found, where BEM calculates a much higher variation, resulting in large load variations and consequently fatigue loads.

The differences in $u_{i,ax}$ between the wake configurations of AWSM result in a different wake velocity. Since a lower induced velocity results in a higher wake velocity, it is expected that the axial wake length is longer for the free wake configuration. In Fig. 6.34a, the axial wake length is shown for the two wake configurations. In this figure, the mean distance traveled by the wake points is plotted as function of the time since they were shed into the wake. From this figure it can be seen that the free wake indeed shows a larger wake length.

In Fig. 6.34b, the mean wake velocity in axial direction V_x is plotted as function of the radial position on the blade from which they were shed. From this figure, it can be seen that the

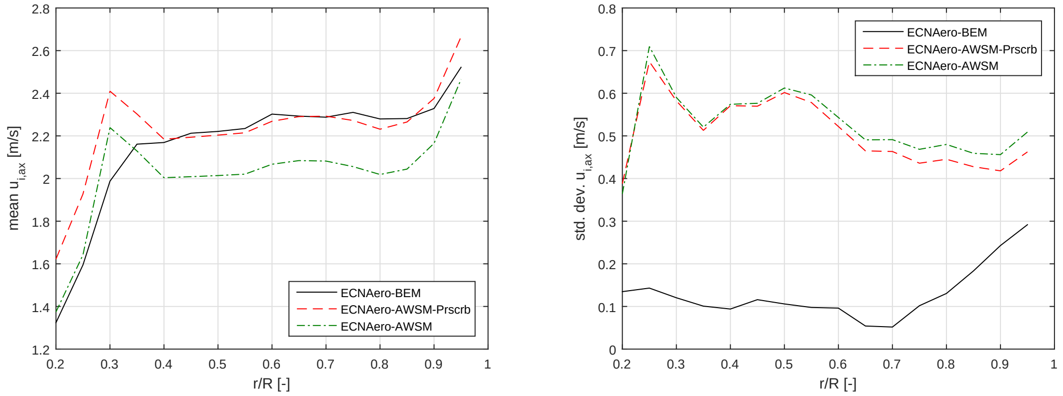

(a) *Mean values.* (b) *Standard deviation values.*

Figure 6.33: *Statistics of the axial induced velocity for the INNWIND turbine in a turbulent inflow.*

difference in wake velocity occurs for all wake points along the blade, although it can be observed that the differences are smallest near the tip of the blade.

When comparing the results for the aerodynamic power of the rotor, it is found that prescribe wake configuration calculates a mean power of $2,789kW$, whereas the results from the free wake configuration results in a mean power of $3,001kW$, which is 7.6% higher. Due to large difference in aerodynamic power, the difference between the two wake configuration should be further investigated. The results from the BEM model results in a mean power of $2,910kW$, which is in between the results from the two wake configurations.

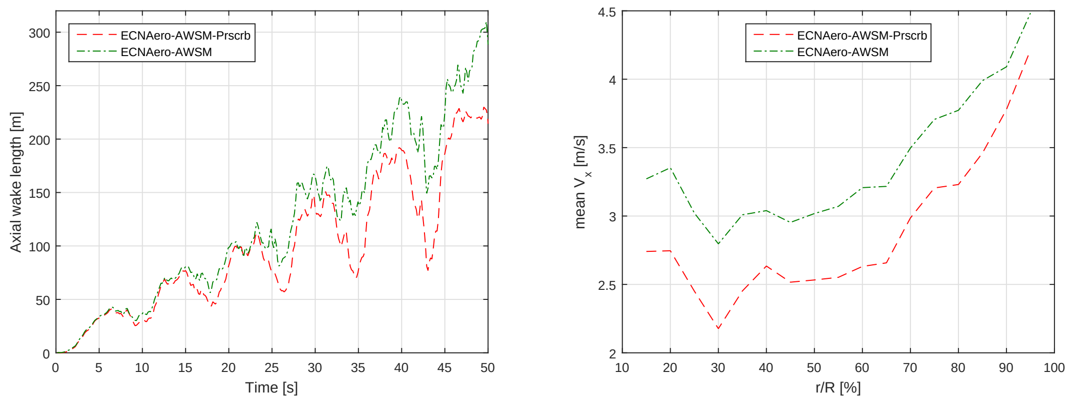

(a) *Axial wake distance.* (b) *Mean axial wake velocity.*

Figure 6.34: *Comparison of the axial wake length for AWSM.*

6.5.6 Evaluation Location of AoA

A large part of the uncertainty of BEM and vortex wake models stem from the modeling of the local aerodynamics through two-dimensional airfoil polars, which are usually obtained from experiments or CFD simulations on 2D airfoils in steady conditions. A stall delay model is implemented for both BEM and AWSM to correct the airfoil coefficients for rotational effects, such as the Coriolis effect and centrifugal forces in a rotating boundary layer, as discussed in Section 4.4.5.

Through thin airfoil theory it is shown that for an airfoil with a uniform camber line in fully laminar flow, the strength of the circulation is such that the flow at the three-quarter chord location is in the same direction as the camber line [22]. For this reason, the BEM model in ECNAero evaluates the angle of attack at the three-quarter chord location, instead of the quarter chord location, which is done in many BEM models. In order to evaluate the effect of the evaluation location of the AoA, the turbulence test case is run for BEM with the evaluation location shifted to the quarter chord location. Due to the unsteady inflow, the flow field around the blade will be curved with respect to the airfoil, which makes this test case an interesting test case to compare the differences of the evaluation location for AoA.

In Fig. 6.35, the mean and standard deviation value of the AoA is plotted as function of the radial position for the last 50s of the turbulent wind file. The results are show for the BEM model with the evaluation location set to the quarter chord location (`c14`) and the three-quarter chord location (`c34`). Furthermore, the results form the prescribed wake configuration of AWSM are added as reference. From this figure, it can be seen that `c14` shows a slightly higher mean value of the AoA from the root section up until approximately 60% of the blade. Furthermore, `c14` also shows a larger variation from the root section up until 45% blade span. For the outer part of the blade, there are hardly differences observed between the two evaluation locations for the AoA.

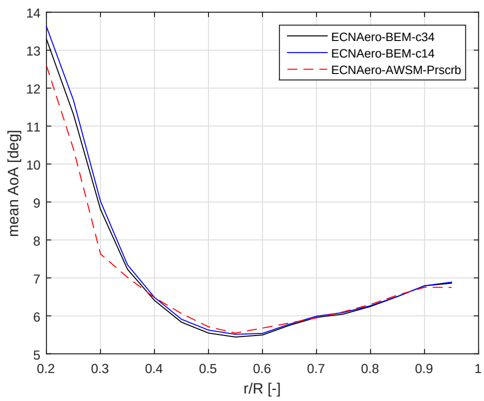

(a) *Mean values.*

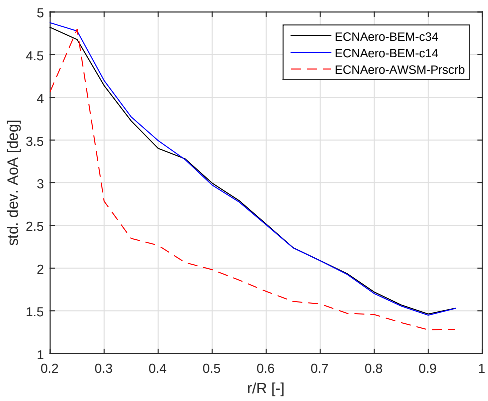

(b) *Standard deviation values.*

Figure 6.35: *Comparison of the angle of attack for varying evaluation locations for the AoA.*

The effect of the evaluation location for AoA on $u_{i,ax}$ is shown in Fig. 6.36. From this figure, it can be seen that `c14` shows a slightly higher mean $u_{i,ax}$ in the mid-section of the blade, whereas a similar value is obtained in the root- and tip-section of the blade. For the standard deviation values of $u_{i,ax}$ only small differences are found between the results from the varying evaluation location of the AoA.

From the analysis of the AoA and $u_{i,ax}$, only small differences are found between `c14` and `c34`. Interesting to note is that the higher $u_{i,ax}$ and AoA for `c14` have an opposite effect on the lift force, which should results in a good agreement of the loads on the rotor. From a comparison of the DEQL of the blade moments for the 50s period, it is found that `c14` calculates a 1.8% higher M_y and a 0.3% and 0.1% lower M_x and M_z. From these findings it could be concluded that there is only a small difference between the evaluation locations of AoA in case of a turbulent inflow from a normal turbulence model. It should be noted that in case of a gust, the differences might be much larger, although these differences usually last for a short time-period.

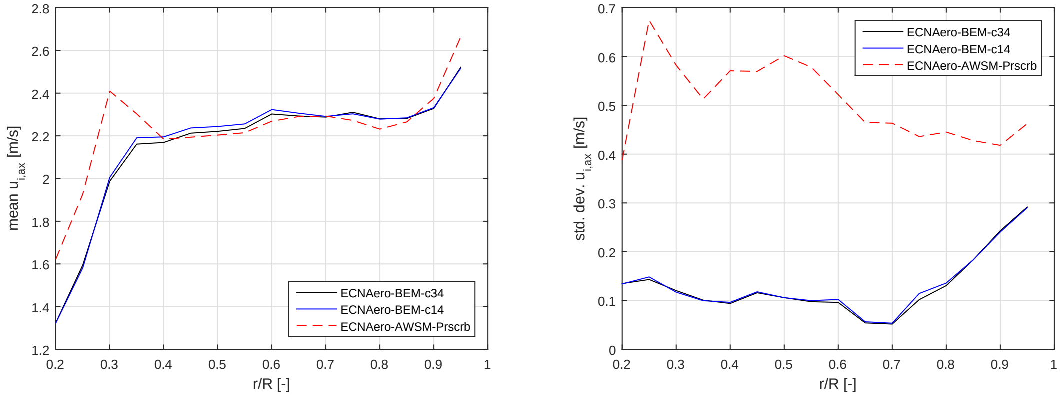

(a) *Mean values.* (b) *Standard deviation values.*

Figure 6.36: *Comparison of the axial induced velocity for varying evaluation locations for the AoA.*

6.5.7 Analysis

In this section, the main observations for the turbulence test case are presented. For this test case, the effect of a varying inflow velocity can be compared between BEM and AWSM, which gives a good platform to compare the calculation of the fatigue loads between the two models. This turbulent inflow field also allows for a proper comparison of the energy distribution in the power spectral density of the local blade aerodynamic and blade loads, to see how BEM and AWSM calculate the distribution of energy over certain frequencies. Furthermore, the effect of the dynamic inflow and various dynamic stall models have been investigated, as well as a comparison between the wake configurations implemented in AWSM. Finally, also the evaluation location of the AoA is varied for BEM. The main observations are summarized below:

- Similar to the results from the half wake and extreme wind shear case, it was found that BEM calculates a rather constant induced velocity in case of a turbulent inflow, whereas AWSM calculates a much more fluctuating induced velocity. It is found that this results in an increased variation of AoA for BEM, which in turn results in an increased load variation. From a comparison of the DEQL for the flapwise blade moment, it was found that BEM calculates a 26% and 32% higher fatigue load compared to the prescribed and free wake configuration of AWSM. From the comparison of the DEQL for all blade and tower moments around their three axis, it was found that BEM calculates a larger fatigue load compared to AWSM.

- From a frequency domain analysis of the induced velocity in the mid-section of the blade, it was found that the influence of the 1P frequency is hardly visible in the power spectral density plot for BEM, whereas the results from AWSM show a large energy peak near the 1P frequency, as well as the 2P and 3P frequency. Near the tip of the blade, the influence of the rotor frequency is better visible from the BEM results, although this is expected to be due to the influence of the engineering models like the yaw and the tip loss correction model. For the AoA and blade M_y, a much better agreement is found between BEM and AWSM for the PSD, although it should be noted that BEM calculates a larger energy over the complete frequency range due to the larger amplitude of the load variations.

- The effect of the dynamic stall models has been investigated by running the BEM model with four different dynamic stall models, being the first and second order Snel model, the ONERA model and the Beddoes-Leishman model. It has been found that there is an excellent agreement between the two Snel models, indicating that there is a negligible influence of the high frequency dynamics for this test case. From the comparison of the models, it has been found that the ONERA model agrees well with the Snel models, although it results in a slightly higher variation of Δc_l. The Beddoes-Leishman model is found to show the largest variation in Δc_l. Furthermore, the Beddoes-Leishman model also influences the c_d, an effect that is not taken into account in the other models. This leads to larger tangential force variations, resulting in an increased DEQL of the blade M_z and tower M_z. Finally, it was found that the Beddoes-Leishman model agrees better with the results from AWSM for the DEQL of the blade M_y. This might be caused by the inclusion of the effect of shed vortices, which is only modeled by the Beddoes-Leishman model and intrinsically in AWSM.

- The dynamic inflow model is assessed by comparing F_{ax} and P for simulations with BEM with and without the dynamic inflow model and comparing the results to AWSM. It is found that there is a generally good agreement between the results of BEM and AWSM and that the dynamic inflow model indeed reduces some of the peaks, which are suppressed by the inertia of the rotor, which is modeled in BEM by the dynamic inflow model.

- For the turbulent inflow case it was foud that there is a significant difference between the free and prescribed wake configuration of AWSM. It is found that the free wake configuration calculates a lower mean induction, which is found both in the local blade aerodynamics and in the longer wake length. This lower $u_{i,ax}$ for the free wake configuration results in a higher mean AoA. It is found that there is a good agreement between the prescribed wake configuration of AWSM and the results from BEM in terms of the induction. This is expected to be the case, since the wake velocity for the prescribed wake configuration is based on BEM theory. However, there is still a good agreement in terms of the fluctuating part of the local aerodynamic between the two wake configuration of AWSM, which leads to a good agreement in the DEQL of the blade and tower moments. The effect of this difference between the wake configurations of AWSM leads to a 7.6% higher power for the free wake configuration, whereas the results from BEM seem to fall in between.

- Finally, the evaluation location for the AoA is compared. Due to the turbulent inflow, the incoming wind field is curved with respect to the airfoil, which results in a different AoA depending on the evaluation location along the chord. Besides the default location of three-quarter chord (`c34`), also the quarter chord (`c14`) location is tested for the BEM model. It is found that `c14` results in a slightly higher mean $u_{i,ax}$ and AoA from the root until approximately 60% of the blade. However, it is found that this difference does not significantly affect the loads on the blade and tower.

6.6 Pitch Step

The results from the pitch step case will be described in this section. First, the processing of the pressure data will be covered, from which the normal and tangential force are calculated. In the following sections, the results from the normal force and tangential force comparison will be compared between BEM, AWSM and the experiment. From the distribution of the normal and tangential force, the blade root bending moments in edgewise and flapwise direction are calculated and compared for BEM, AWSM and the experiment, from which the effect of dynamic inflow on the blade loads can be compared. Next, the results from the free and prescribed wake configuration of AWSM are compared, which is found to give large differences in case of a turbulent wake state. Finally, the main observations from this test case are summarized. Additional results from the pitch step case can be found in Appendix F.

6.6.1 Processing Pressure Data

In order to compare results between ECNAero and the experiment, the pressure data has to be converted into aerodynamic forces in terms of F_n and F_t. In order to do so, first the full pressure distribution around the airfoils at the five blade stations has to be determined. Since no pressure sensors are located at the trailing edge of the blades, the pressure at this location is determined by linearly extrapolating the pressure by assuming a constant pressure gradient near the trailing edge. The pressure gradient is calculated from the two pressure sensors closest to the trailing edge for the upper and lower side of the blade. By determining the pressure at the trailing edge from both the upper and lower side of the blade, the pressure at the trailing is assumed to be the average of these two values. From an inspection of the pressure distribution around the airfoil at $r/R = 92\%$ for run 1146, it can be seen that this results in a reasonable pressure distribution.

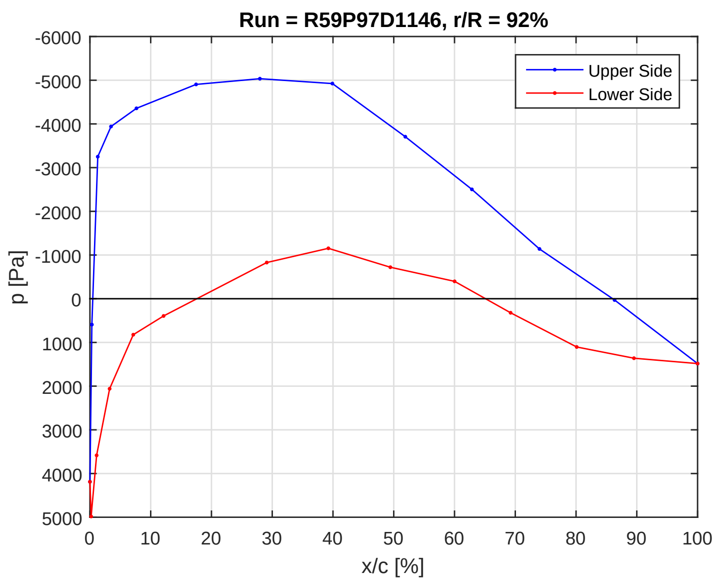

Figure 6.37: *Pressure distribution around the airfoil at* $r/R = 92\%$.

The aerodynamic forces in normal and tangential direction have been calculated by integrating the pressure distribution over the airfoil, by means of the trapezoidal rule:

$$F_n = \sum_{i=1}^{N_1-1} \frac{P_{i+1} + P_i}{2}(x_{i+1} - x_i) \tag{6.4}$$

$$F_t = \sum_{i=1}^{N_1-1} \frac{P_{i+1}+P_i}{2}(y_{i+1}-y_i) \tag{6.5}$$

In these equations, the locations of the pressure sensors are ordered from the trailing edge to the leading edge (upper side), back to the trailing edge (lower side), where N_1 is the amount of pressure locations and $i = 1$ and $i = N_1$ represent the trailing edge pressure location.

6.6.2 Normal Force Comparison

In this section the results for the normal force will be compared between BEM, AWSM and the experimental data. It was found that Run 1146 showed the largest overshoot in aerodynamic forces and is therefore considered the most interesting experiment to assess the dynamic inflow. In Fig. 6.38, F_n is shown as function of time for the complete test run at 25%, 60% and 92% blade span in order to get a good overview of the response over the complete blade.

It can be seen that during the experiment, there are two pitch actions. During the first pitch action, the pitch angle (θ) is increased from $-2.3°$ to $5°$, which results in a lower F_n. During the second pitch step, the opposite pitch step is conducted, after which F_n is found to return to its steady value for a pitch angle of $-2.3°$. From this figure, it can be seen that there is much better agreement for the steady values of F_n for a pitch angle of $5°$, which is expected to be true since the rotor operates at a low induction and at low AoA.

In the root-section of the blade, it can be seen that there is a good agreement between BEM and AWSM in terms of the steady F_n values, whereas the results from the experiment show a lower steady value. For the results at the mid- and tip-section of the blade, a better agreement has been obtained between the steady values of F_n. From this figure, it can be seen that the results from AWSM seem to take a much longer time to reach a steady value compared to BEM. This can be explained by the fact that AWSM models the wake in terms of vortex points, which will keep an influence on the rotor aerodynamics for as long as the wake is modeled. The total amount of wake points is set to 689, which results in a wake length of almost 20 rotor revolutions. In BEM, the aerodynamics is solved by balancing the momentum equation, where an additional term is added in case of a dynamic inflow. However, the time for which this model effects the aerodynamics is much shorter compared to AWSM.

Since it is found that the distribution of the normal force before and after the pitch step is different between BEM, AWSM and the experimental data, F_n is scaled in order to assess the response to the pitch step. The normal force is scaled according to:

$$\tilde{F_n} = \frac{F_n - F_{n,0}}{F_{n,1}} \tag{6.6}$$

where $F_{n,0}$ is the steady value before the pitch action and $F_{n,1}$ is the steady value after the pitch action. This results in a case where the value of $\tilde{F_n}$ at the start of the pitch action will be equal to 0 and the steady value of $\tilde{F_n}$ after the pitch action will be equal to 1. In this way, it becomes easy to assess the overshoot percentage during the pitch action and to qualitatively compare the response of BEM and AWSM with the experimental data.

In Fig. 6.39, $\tilde{F_n}$ is shown at 25%, 60% and 92% blade span for the pitch action from $5°$ to $-2.3°$. From this figure, a few interesting observations can be made. First of all, it can be seen that the largest overshoot occurs in the root section of the blade ($\approx$ 70% overshoot). At $r/R = 25\%$, it can also be observed that there are large fluctuations of $\tilde{F_n}$ over time with a 1P frequency, which are much smaller for BEM and AWSM. This could be explained by the absence of modeling blade flexibility. Interesting to see is that the results from BEM seem to reach the steady value after

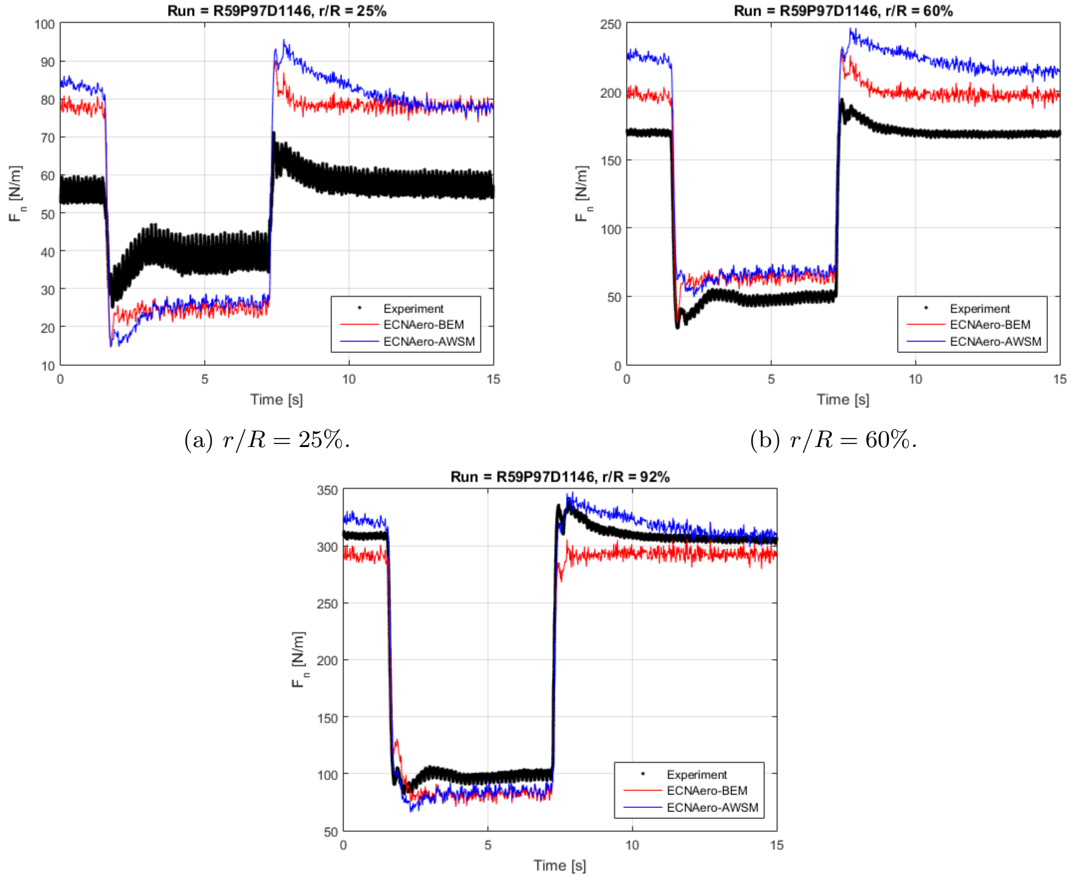

(a) $r/R = 25\%$.

(b) $r/R = 60\%$.

(c) $r/R = 92\%$.

Figure 6.38: *Comparison of the normal force during the pitch step of run 1146.*

approximately $1s$, whereas the results from both AWSM and the experiment have not completely reached the steady value ($\tilde{F_n} = 1$) after $3s$. A reasonable agreement is visible between AWSM and the experiment in terms of the dynamic inflow effect.

In the mid-section of the blade, the overshoot is much smaller (20%) compared to the root-section. At this blade location, it can be seen that there is an excellent agreement between BEM and the experimental data, both in initial overshoot and in terms of time to reach the steady value, which indicates a similar response to dynamic inflow. The results form AWSM seem to require a longer time to reach the steady value. Furthermore, it can be observed that the peak value for AWSM occurs much latter compared to BEM and the experimental data. This could be explained by the fact that the wake still contains wake points with a low vorticity, which results in a lower induction at the blade. When these vortex points convect downstream in the wake, their influence on the blade aerodynamic reduces and vortex points with a higher vorticity are shed in the wake.

In Fig. 6.39c, the response to the pitch action is shown at the tip-section of the blade. From this figure, it can be seen that BEM seems to underpredict the increase of F_n, compared to AWSM and the experimental data. A good agreement is found between AWSM and the experiment in terms of the calculation of the overshoot, although it should be mentioned that AWSM does not accurately capture the first peak of $\tilde{F_n}$. In terms of the time to reach the steady value, it can be seen that BEM requires only a few rotor revolutions to reach the steady value, whereas the results from AWSM requires a much longer time, indicating a lower aerodynamic damping. The experimental results also show a relatively long period to reach the steady value, although it can

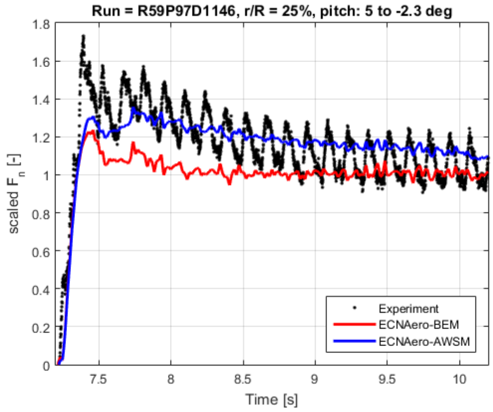

(a) $r/R = 25\%$.

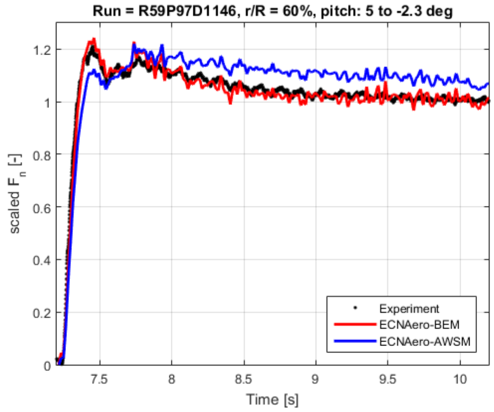

(b) $r/R = 60\%$.

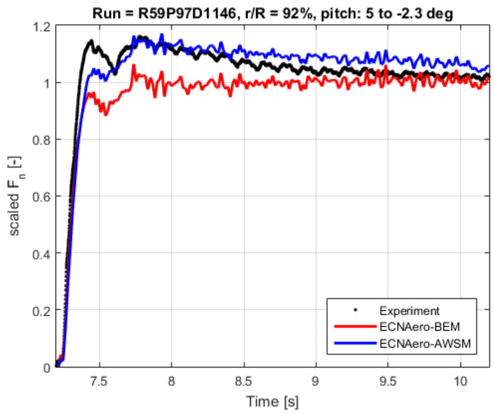

(c) $r/R = 92\%$.

Figure 6.39: *Comparison of the scaled normal force during the pitch step from* 5° *to* -2.3° *of run 1146.*

be observed that the steady value is reached slightly faster compared to AWSM.

6.6.3 Tangential Force Comparison

In this section the results for F_t are compared for experiment Run 1146. In Fig. 6.40, the results are shown at the tip section of the blade for the full time-period for F_t and during the second pitch step for $\tilde{F}_t$. Note that $\tilde{F}_t$ is defined similar to $\tilde{F}_n$, as discussed in the previous section.

From the results of the complete time-series of F_t in Fig. 6.40a, it can be seen that there is a large difference between the two pitch steps. During the first pitch step, the pitch angle is increased, consequently decreasing the AoA and thus the loads. This means that the blade starts to operate more in the linear part of the airfoil curves and at a lower induction. For this pitch action, it can be seen that there is no significant aerodynamic overshoot noticeable. Similar results have been obtained for the other radial positions. For the second pitch step, the pitch angle is decreased, resulting in a higher AoA and thus higher loads and induction. It can be seen that for this pitch action, there is a significant overshoot in F_t, which is interesting to compare the response to dynamic inflow. Again, this behavior is found at all five radial positions.

In Fig. 6.40b, $\tilde{F}_t$ is shown for the second pitch step. From this pitch step, it can be seen that the experimental results show a large overshoot of approximately 30% compared to the steady value. The results from AWSM show an overshoot of close to 20%, whereas BEM hardly shows any overshoot. Furthermore, it can be seen that the results from BEM seem to have reached the steady value ($\tilde{F}_t = 1$) approximately $0.5s$ after the pitch action, whereas the results from AWSM and the experiment show a much longer time-period to reach the steady state ($\approx 3s$). For the other blade locations, a similar observation is made, where there is a reasonable agreement between the overshoot in AWSM with the experiment and the results from BEM show a smaller overshoot. Furthermore, the results from BEM seem to reach the steady value much faster compared to AWSM and the experiment, which can also be found from the results of $\tilde{F}_n$ in Fig. 6.38.

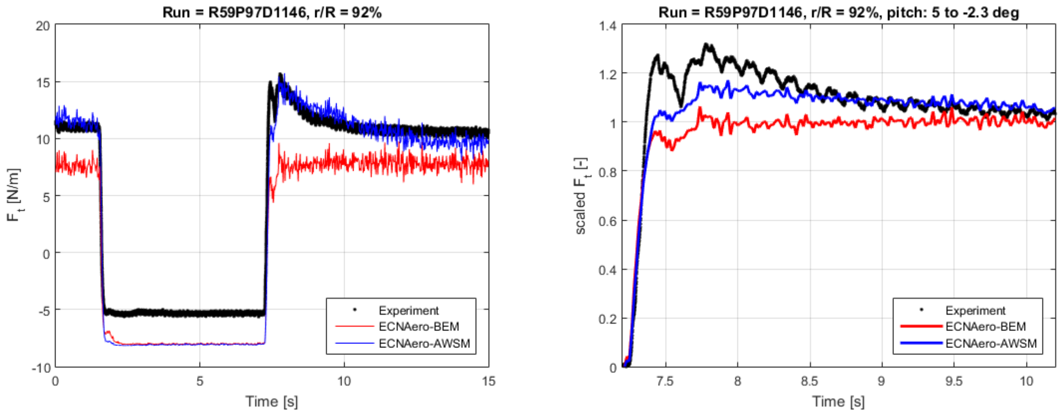

(a) F_t *vs. time.* (b) $5°$ *to* $-2.3°$.

Figure 6.40: *Comparison of the tangential force during the pitch step of run 1146 at* $r/R = 92\%$.

6.6.4 Blade Root Bending Moments

An important part of the validation between BEM, AWSM and the experimental data is to compare the loads on the blades. In order to do a comparison of the complete blade loads, the blade root bending moment in edgewise and flapwise direction is calculated from the distribution of the normal and tangential force at the five locations of the pressure sensors along the blade. Although this leads to a rather coarse distribution of the aerodynamic forces over the blade, the evaluation locations are similar to the experiment, which is important for the comparison.

First, the thrust F_{th} and driving force F_{dr} is calculated, which is defined as the out-of-plane and in-plane force on the blade. In the equations below, the twist angle φ is used to translate F_n and F_t from Equations 6.4 and 6.5 into F_{th} and F_{dr}.

$$F_{th} = F_n \cos(\varphi) - F_t \sin(\varphi) \tag{6.7}$$
$$F_{dr} = F_t \cos(\varphi) + F_n \sin(\varphi) \tag{6.8}$$

The aerodynamic moment on the blade root is calculated by assuming zero force at the blade root ($r = 0m$) and blade tip ($r = 2.04m$) and a linear relation between the evaluation points of F_{th} and F_{dr}. Furthermore, the gravity force is neglected in the calculation of the blade root moments, since this effect is not measured in the experiment.

$$M_x = \sum_{i=1}^{N_2-1} \frac{F_{dr}(i+1) + F_{dr}(i)}{2} \cdot \frac{r(i+1) + r(i)}{2} \cdot (r(i+1) - r(i)) \tag{6.9}$$
$$M_y = \sum_{i=1}^{N_2-1} \frac{F_{th}(i+1) + F_{th}(i)}{2} \cdot \frac{r(i+1) + r(i)}{2} \cdot (r(i+1) - r(i)) \tag{6.10}$$

where N_2 is defined as the locations of the evaluations points plus the blade root and tip.

The results of the blade M_x and M_y are shown in Fig. 6.41 for the complete time-period of the experiment. For the blade M_x, it can be seen that there is a significant relative difference in the loads for the experiment with BEM and AWSM. This can be explained by the fact that there is a large uncertainty found in the modeling of F_n and F_t in the root section of the blade. The uncertainty in the root section has a large influence on M_x, since the there is a large positive twist angle, which results in a large influence of F_n from the root section on M_x, according to Eq. 6.8 and Eq. 6.9. For the first pitch step ($\theta : -2.3° \rightarrow 5°$), it can be seen that there is an overshoot in the loads noticeable for the experimental data, which lasts approximately $1s$. This effect is well capture by AWSM, although the results from BEM seem to reach the steady value for M_x much faster. For the second pitch step ($\theta : 5° \rightarrow -2.3°$), it can be seen that for the experimental data the overshoot in M_x is larger compared to the first step. This behavior is also observed for BEM and AWSM. It can be seen that BEM calculates the effect of the dynamic inflow for a shorter period compared to the experimental data, whereas AWSM takes longer to reach the steady value.

In Fig. 6.41b, the results of M_y are shown. From this figure, it can be seen that there is a good agreement between the BEM and AWSM with the experimental results. During the first and last part of the simulation ($\theta = -2.3°$), the experimental results of M_y are in between the results of BEM and AWSM, although the results from BEM seem to be closer. The experiment shows a higher value of M_y between $2s$ and $7s$ compared to BEM and AWSM, where is an excellent agreement found between BEM and AWSM. An almost identical observation can be made for the results of run 1152, where the rotor speed is decreased in order to get a higher pitch speed per azimuth angle. The plots for the blade M_x and M_y are shown for reference in Appendix F.

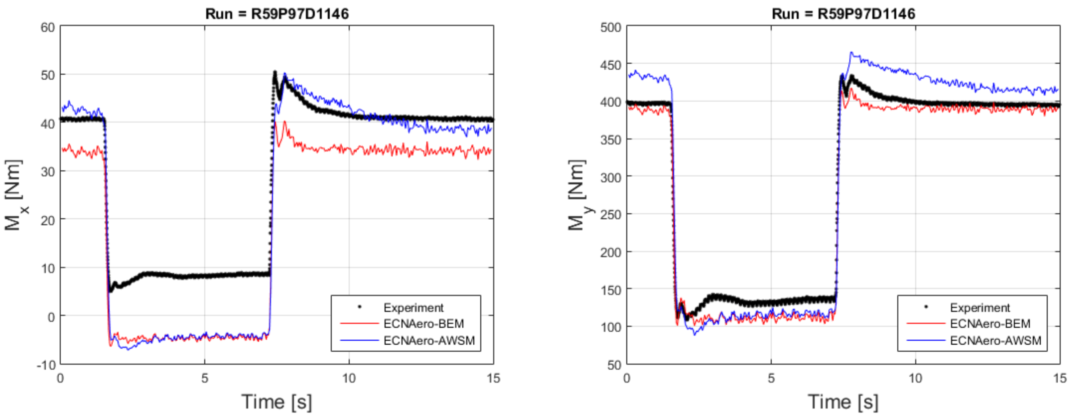

(a) *Edgewise moment.* (b) *Flapwise moment.*

Figure 6.41: *Comparison of the blade root bending moments during the pitch step of run 1146.*

In order to analyze the dynamic inflow effect on the blade loads, the scaled flapwise moment $\tilde{M}_y$ is calculated for both pitch actions, similar to Eq. 6.6. In Fig. 6.41, the results of $\tilde{M}_y$ are shown. From the experimental results, it can be seen that there is an overshoot in M_y of approximately 10% for the first pitch step and 15% for the second pitch step. The results from BEM seem to agree well for calculation of the initial overshoot, although the steady value is reached within $1s$ for both pitch steps. The results from AWSM also seem to agree well with the calculation of the overshoot in M_y and the response seem to match better with the response from the experiment. In terms of the duration of the dynamic inflow effect, is seems that AWSM calculates a longer effect of the dynamic inflow compared to the experiment.

The results for M_x and M_y for the other pitch step experiments are added to Appendix F. From these experiments it is found that for the runs with a lower tip speed ratio, there is no significant overshoot in the aerodynamic loads found. This could be explained by the fact that the rotor

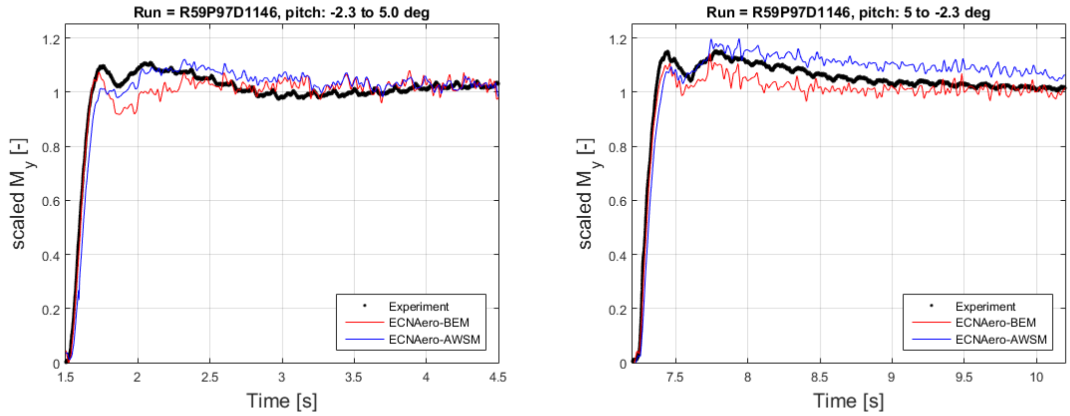

(a) $-2.3°$ *to* $5°$. (b) $5°$ *to* $-2.3°$.

Figure 6.42: *Comparison of the scaled flapwise blade root bending moments during the pitch step of run 1146.*

operates at a lower induction. However, when comparing the response to the pitch step, an excellent agreement is found for the runs at a lower tip speed ratio. Finally, it is observed that changing the rotor speed while keeping the tip speed ratio the same does not significantly influence the results. It is found that the results from run 1146 and 1152, as well as for 1147 and 1153 show an excellent agreement in terms of the dynamic inflow effect. Only the mean value for the loads are different due to the varying effective inflow velocity.

6.6.5 Comparison Wake Configurations AWSM

Similar to most test cases, both the free and prescribed wake configuration of AWSM have been used to calculate the response to the pitch step. For most cases, the two wake configuration give very similar results, where the prescribed wake configuration of AWSM reduces the CPU time by approximately a factor of 5. However, for the pitch step case it is found that the prescribed wake configuration leads to unstable behavior in case of a turbulent wake state. In Fig. 6.43, F_n and F_t are shown for run 1146. From this figure it can be seen that the prescribed wake simulation results in larger fluctuations when the pitch angle is $-2.3°$ and even becomes unstable at $12s$. When the pitch angle is $5°$, there is a good agreement between the free and prescribed wake configuration, since the average induction factor is reduced from 0.5 to 0.1. Since the velocity in the wake for the prescribed wake configuration is based on BEM theory with the mean induction, the velocity will reduce to $0m/s$ in the far wake, which is expected to be the cause of the unstable behavior. From this results, it can be concluded that the current prescribed wake configuration implemented in AWSM is unsuitable for a wind turbine in a turbulent wake state.

6.6.6 Analysis

The main observations from the pitch step case will be discussed in this section. Due to fact that only pressure sensors have been used to validate the differences between BEM and AWSM, only the normal and tangential forces have been compared at various blade stations, as well as the blade M_x and M_y from the distribution of F_n and F_t. However, the results from the various pitch step experiments have lead to valuable findings. The main observations from this test case are summarized below:

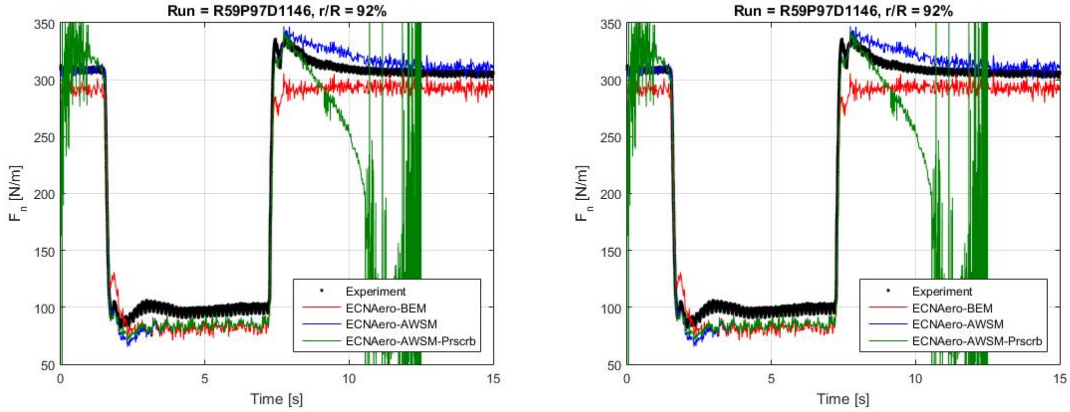

(a) F_n. (b) F_t.

Figure 6.43: *Comparison of the wake configuration during the pitch step of run 1146 at* $r/R = 92\%$.

- From the comparison of F_n and $\tilde{F_n}$, it was found that there is a generally better agreement between AWSM and the experiments in the root- and tip-section of the blade, whereas in the mid-section of the blade the results from BEM seem to agree well with the experiment. This could be explained by the fact that BEM does not intrinsically model the root and tip vortex, leading to larger differences in these sections of the blade. Similar results have been obtained for F_t.

- From a comparison of the blade loads, it is found that the dynamic inflow effect is shorter for BEM compared to AWSM. In general the data from the experiment is in between the results of BEM and AWSM in terms of the time to reach the steady state value. It is expected that this is caused by the influence of the vortex points in the wake, which affect the local blade aerodynamics as long as they are present in the wake. From the experimental data no conclusions have been drawn regarding the time is takes to reach the steady state value, since the results from the experiment seem to fall in between the results from BEM and AWSM.

- From the experimental data it is found that the dynamic inflow effect is more pronounced when the when the pitch angle is adjusted to increase the loading, compared to when the pitch angle is adjusted to reduce the loading. This behavior is also observed from the results of BEM and AWSM.

- It is found that the prescribed wake configuration becomes unstable when the turbine operates in a turbulent wake state. This is expected to be due to the wake velocity, which reduces according to BEM theory. This implies that for an induction factor of 0.5 (which occurs in run 1146), the wake velocity far downstream will be close to $0m/s$, which is expected to results in unphysical behavior in the wake.

- For the experiment runs at a lower tip speed ratio ($\lambda \approx 6.6$), no significant overshoot in the blade loads is observed. This means that dynamic inflow effects are more dominant for rotors operating in high tip speed ratios and/or induction factors. Furthermore, it is found that the results from the runs at the same tip speed ratio but with a different rotor speed showed a very similar response to the dynamic inflow, even though the relative pitch speed per azimuth position is increased by $\approx 20\%$ due to the lower rotor speed.

- For a follow-up study, it is important to also incorporate the blade flexibility. From the experimental results, it can be seen that there is a variation in the loads with a 1P frequency, which indicates the influence of the blade flexibility, as well as the tower effect. Furthermore, the experiments should be repeated with a constant pitch angle (except during the pitch step) in order to assess whether the fluctuations in the rotor speed sensor are physical or that it is due to noise. It is expected that with a more constant pitch angle, the results will reach the steady value faster, which would results in a better agreement between AWSM and the experimental data.

Chapter 7

Conclusion

The main objective of this thesis is to compare the aeroelastic capabilities of the free vortex wake code AWSM with conventional BEM based models on large wind turbines. This has been achieved by running five different load cases on two different 10MW reference wind turbines and comparing the results in terms of mean and standard deviation values of several output parameters, a comparison of the Damage Equivalent Load (DEQL) of blade and tower moments and by comparing the modeling of certain flow phenomena specific to the test case. Furthermore, a pitch step case from the New MEXICO experiment has been simulated with BEM and AWSM, which has been validated with experimental data for this dynamic inflow case. The main conclusions for each of these test cases are described below. Furthermore, the research questions form Section 1.2 will be discussed from which some more general conclusions are drawn regarding the capabilities and limitations of AWSM.

- In case of an axial inflow, a generally good agreement has been found between the results of BEM and AWSM. For the local blade aerodynamics, the largest differences have been found in the root and tip section of the blade, which can be attributed to the modeling of the root and tip vortex, which is done by the Glauert correction for BEM and is calculated intrinsically for AWSM. Furthermore, it has been found that the effect of the tower on the induced velocity seems to be significantly higher for BEM compared to AWSM, resulting in larger dip in local forces when the blade passes the tower. A comparison of $u_{i,ax}$ in the extreme wind shear case has shown that this is probably due to the implementation of the BEM model in ECNAero, since the other BEM and vortex wake models agree better with the results from AWSM.

  Besides the root and tip vortices, it has been shown by AWSM that there also exist trailed vortices in the mid-section of the blade, which is the result of a non-uniform distribution of bound circulation over the blade. This leads to differences between BEM and AWSM, since BEM does not model trailed vortices in the mid-section of the blade. It is expected that this effect might contribute to the difference in the sectional normal force in the mid-section of the blade between BEM and AWSM, which has found to occur on high induction rotors. In order to investigate this difference, the twist distribution of the INNWIND turbine is redesigned to create a more constant vorticity distribution. With the new twist distribution, a much better agreement has been found between BEM and the prescribed wake configuration of AWSM, although the sectional normal force remains higher for AWSM free wake. From a comparison to results from the RANS model EllipSys3D, it has been found that the results from AWSM agree better with the CFD results. However, it should be noted that there is a large uncertainty in the airfoil polars. Therefore, comparison with an actuator disk on line model should lead to better insight, since the global flow is modeled with RANS equations, whereas the local flow is modeled by the same airfoil polars.

- In case of a yawed inflow, two important flow phenomena have been detected, being the advancing and retreating effect and the skewed wake effect. The first effect is calculated intrinsically by both BEM and AWSM and a good agreement has been obtained for this flow phenomena. For the skewed wake effect, the axial induction is increased in the downwind part of the rotor plane, since the trailed tip vortices are on average closer to this side of the rotor plane. This flow phenomena is intrinsically modeled in AWSM, where BEM uses an engineering model. From a comparison of the ECN and Glauert yaw model for BEM, it is found that both yaw models estimate a smaller effect of the skewed wake on $u_{i,ax}$ compared to AWSM. The skewed wake effects are found to be captured better in the tip section of the blade by the Glauert model, whereas ECN's yaw model performs better in the root section, due to the inclusion of the root vortex.

- From the comparison of the axial and yawed inflow cases, it was found that there is a much better agreement between BEM and AWSM for the AVATAR turbine compared to the INNWIND turbine. This is expected to be the case for turbines with a low induction, which operate at a lower AoA range, for which the aerodynamics can be better modeled due to the linear behavior of the aerodynamic polars.

- From the results of the half wake case, it was found that there are large differences in $u_{i,ax}$ over the blade azimuth position, where BEM calculates an almost constant induction and AWSM calculates a large fluctuation over the azimuth locations. The largest differences have been found when the blade is in the wake of an upstream turbine, since the inflow velocity changes rapidly over time. The difference in modeling the induction might be attributed to the convergence criteria of the BEM equations, which is based on the convergence of the mean induction over the blades per annulus, possibly filtering the variation of $u_{i,ax}$. It is found that a varying inflow velocity over the rotor plane results in a larger fluctuation in AoA and a larger blade load amplitude. This increased amplitude results in a larger increase in DEQL of the blade and tower moments for BEM. This effect is also observed for the extreme wind shear and turbulent inflow case, where there is a varying inflow velocity over time and/or azimuth location. It has been found that the DEQL of the blade M_y is 30%, 14% and 26% higher for BEM compared to AWSM for the half wake, extreme wind shear and turbulent inflow test case respectively. This overestimation of the fatigue loads might results in an overdesigned blade, which is less efficient in terms of weight and cost. Concerning that a large amount of future wind turbines will be placed in wind farms, wind turbines are expected to be subjected to wake effects for a significant time during their lifetime.

- From the results of the extreme wind shear case, it was found that there is a reasonable agreement in dynamic stall behavior between BEM and AWSM, which is expected since the same dynamic stall model is implemented. It is found that for AWSM, a larger section of the root is in stalled conditions during the transient. This is expected to be caused by the dependency between the blade elements in AWSM, whereas BEM assumes independent annulli. For the mid-section of the blade a good agreement has been found in the dynamic stall behavior between BEM and AWSM, although the larger variation in AoA results in a more active dynamic stall behavior for BEM. From a comparison to the dynamic stall results from external codes in the AVATAR project with hGAST and HAWC2, it was found that there is a reasonable agreement in the mid-section and tip-section of the blade, although it should be noted that the influence of dynamic stall is limited in this test case.

  In general, a good agreement has been obtained between the results of PhatasAero, hGAST and HAWC2. However, large differences have been found in the response of the rotor F_{ax}

to the wind shear transient, where hGAST and HAWC2 calculate a much smaller variation in F_{ax} compared to ECNAero, for both BEM and AWSM. It is found that this difference in F_{ax} results in large differences in the DEQL of the tower M_y. The DEQL of the tower M_y calculated by HAWC2 is found to be more than 3 time as small compared to the results from ECNAero-BEM. However, the simulations with hGAST and HAWC2 are run with a controller on, resulting in a varying rotor speed, which is expected to limit the load variation.

- The turbulence test case allows for a proper comparison of the results in the frequency domain due to the turbulent inflow velocity and the varying rotor speed. From a frequency domain analysis of $u_{i,ax}$, it has been found that BEM only shows a small influence the 1P frequency, whereas a large peak is obtained for the 1P, 2P and 3P frequency in the PSD for AWSM. This indicates that BEM models a smaller influence of the 1P variation of the induction. Besides the frequency domain analysis, also various dynamic stall models have been tested. It has been found that the first and second order Snel model and the ONERA model only model the dynamic stall effect on c_l, whereas the Beddoes-Leishman model also models the effect on c_d. Furthermore, the Beddoes-Leishman model also models the effect of shed vortices. From a comparison of the DEQL of the blade and tower moments, a reasonable agreement between all dynamic stall models has been found. The results from the Beddoes-Leishman model seem to agree better with AWSM for M_y, which is expected to be due to the inclusion of the shed vortices on the lift. Finally, also the dynamic inflow model has been assessed, which has found to result in a better agreement between BEM and AWSM by limiting the variation in thrust during a turbulent inflow.

  Interesting to observe is that there is a significant difference found between the free and prescribed wake configuration of AWSM, where the free wake configuration calculates a lower mean induction factor over the complete blade, although the variation of the local aerodynamic parameters is similar. This results in very similar fatigue loads, although the mean values differ significantly. This results in the fact that the free wake configuration of AWSM calculates a 7.6% higher mean power compared to the prescribed wake configuration, which is a very large difference considering the only difference is the velocity of the wake points. Finally, also the effect of a varying evaluation location for the AoA for BEM is compared. From this comparison, it is found that shifting the evaluation location from the three-quarter chord location to the quarter chord location only slightly increases the mean $u_{i,ax}$ and AoA, although the variation of these parameters over time is similar. No significant differences in the loads have been observed.

- In the pitch step case, the results from BEM and AWSM are compared to the sectional normal and tangential forces obtained from the New MEXICO experiment, as well as the edgewise and flapwise blade root bending moments. From this validation case, it has been found that the results from BEM tend to reach the steady value after the pitch step much faster compared to AWSM. This can be explained by the fact that the wake in AWSM is made up from vortex points, which are shed in the wake at each time-step. This wake acts as a damper to a varying inflow condition, since the circulation of the vortex points before the pitch step will be present in the wake for a relatively long time-period. From a comparison to the experimental data it was found that there is generally good agreement in the root- and tip-section of the blade, although the results in the mid-section of the blade seem to agree better with BEM. With regard to the dynamic inflow, it was found that the time to reach the new steady value from the experimental results are in between the results from BEM and AWSM. Furthermore, it has been found that the prescribed wake configuration cannot be used in case of a turbulent wake state, since this configuration leads to unstable behavior due to the wake prescribed based on the induction factor. Also, it is found that dynamic inflow effect occur mainly at high tip speed ratios for the New MEXICO rotor ($\lambda \approx 10$). The experiments at the design tip speed ratio ($\lambda \approx 6.6$) do not show a significant overshoot in the aerodynamic loads. Finally, it is found that reducing the rotor speed to increase the pitch speed relative to the rotor speed does not significantly affect the dynamic inflow effect.

- For the numerical stability, accuracy and computational time of AWSM, it is found that there a few parameters which are important. It has been found that the time-step is an important parameter for both stability, accuracy and CPU time. Generally, the maximum time-step for a simulation should not exceed 10° of azimuth angle per time-step. However, for a turbulent inflow case the time-step should be set smaller to capture the high frequency dynamics. It is found that a reduction of the time-step in AWSM exponentially increases the CPU time, since more time-steps are required and more wake points are required in order to fully model the wake. The blade discretization has been found to be an important parameter as well to increase the accuracy of the solution, especially near the root and the tip of the blade. However, it should be kept in mind that the blade points should not be too close, since this might lead to unstable behavior due to the singular behavior of the Biot-Savart equation for the induced velocity.

- Regarding the general validity of AWSM compared to BEM, it can be concluded that both models seem to be comparable for axial inflow conditions. This is an important result, since the BEM theory is developed for a wind turbine in axial inflow. The largest differences that have been observed between BEM and AWSM are caused by flow phenomena that are not intrinsically modeled in BEM, like trailed vortices, yawed inflow, wind shear, half wake and dynamic inflow. From a comparison to the results from HAWC2 (BEM) and hGAST (BEM and vortex wake), it is found that there is a generally good agreement with PhatasAero. Furthermore, the experimental results from the New MEXICO experiment confirm that AWSM seems to calculate a better response to a pitch step in most cases, when assessing the dynamic inflow.

- The largest limitation of AWSM is the required CPU time. For the CPU time of the simulations, it was found that BEM is in the order of $10^3 - 10^4$ times faster compared to the free wake configuration of AWSM. It was found that the prescribed wake configuration in AWSM reduces the CPU time by $\approx 80\%$. However, it is found that the prescribed wake configuration does not always work properly for a wind turbine with a turbulent wake state. Furthermore, a recent software upgrade to allow parallel computing, resulted in a reduction of CPU time by a factor of 4 on average. Due to this relatively large CPU requirement, dynamic load case simulations are limited to a relatively course time-step ($\approx \Delta t = 0.1s$). However, with the recent developments in the code it has been shown that AWSM can be used for the analysis of aeroelastic load cases.

- With respect to the application of AWSM, it has been shown that AWSM can be used as a tool to inspect flow phenomena to create results to adjust and tune engineering models, like the root and tip flow correction, oblique inflow model, dynamic inflow model or even the algorithm to calculate the local induction. Besides the implementation as a research tool, with current CPU capacity, AWSM can also be used to replace or complement BEM model for load case analysis in the near future. Especially for the next generation large wind turbines, the addition of a higher fidelity aeroelastic design tool might significantly increase the efficiency of wind turbines and reduce the cost of wind energy, especially for more complex blade designs or wind turbines in a farm, where flow phenomena like half wake and increased turbulence situations are present due to the interaction between the turbines.

Chapter 8

Recommendations

The research in the aeroelastic capabilities of AWSM and the comparison with BEM has led to some interesting observations, for which additional research might lead to more insight and significant improvements in the accuracy of future aeroelatic wind turbine analysis tools. In this chapter the recommendations for future research are described.

First, an overview is presented of the various flow phenomena and a recommendation on which model to use for which application. The application is divided into:

- Design. This requires fast iterations and thus a low CPU effort is very important.
- Load analysis. A full load analysis requires many simulations for long time-period to get a valid representation of the loads that occur on a wind turbine during its 20-year lifetime. However, accuracy is also very important.
- Research. For research purposes, the main requirement is to accurately capture the physics of the flow around a wind turbine and the force applied on the blades and tower.

In Table 8.1, the results are shown for various flow phenomena, where the results from the pitch step case are used to give a recommendation on both the dynamic inflow and turbulent wake state conditions. It can be seen that for design purposes, BEM models are still the best way to go with current computing possibilities and the CPU usage of AWSM. However, for load analysis the prescribed wake configuration of AWSM can be used to do a full aeroelastic load analysis, although

Table 8.1: *Recommendation of application of BEM and AWSM in various environmental conditions. Rated for Design (D), Load analysis (L) and Research (R).*

Case	BEM	AWSM-Prscrb	AWSM
Axial Inflow (steady)	D, L	R	R
Yawed Inflow (steady)	D, L	L, R	R
Half Wake	D, L	L	R
Extreme Wind Shear	D, L	L	R
Turbulent Inflow	D, L	L	R
Dynamic Inflow	D, L	L, R	R
Turbulent Wake State	D, L	-	L, R

the CPU time will be in the order a few days for a 10-minute time-series. For research purposes, the free wake configuration of AWSM would be the ideal option for most cases, since it gives a more physical representation of the global flow, especially in the wake. Interesting to note is that for a steady inflow (axial and yawed inflow), the agreement between the two wake configuration is very good and a prescribed wake configuration should suffice as well. For a turbulent wake state, it is found that the prescribed wake configuration is unstable and cannot be used. Finally, it should be mentioned that for fast iterations in the design process, the standalone version of AWSM is also an option and requires approximately 5% of the CPU time of the aeroelastic model. The downside is that flexibility effects are not taken into account, similar to the results from the pitch step test case.

Recommendation for future research are described below:

- From the comparison between BEM and AWSM it has been found that there are large differences in the fundamental approach for the calculation of the induced velocity. Large differences in $u_{i,ax}$ are found for a varying inflow velocity. A high variation in $u_{i,ax}$ is found with AWSM, whereas BEM calculates a more constant value. This lower variation of $u_{i,ax}$ for BEM has found to result in an increased variation of AoA and consequently in a larger load amplitude and thus fatigue loads. Further research is required to investigate which option would results in the most accurate calculation of the local induction for BEM models. An option to investigate would be to solve the BEM equations at multiple azimuth locations for each annulus, rather than an option where the induction is calculated separately for each blade by balancing the momentum equation for a streamtube per blade based on the inflow velocity at the blade azimuth position. Also the convergence criteria could be reconsidered, which is currently based on the mean induction. However, this mean induction is important in the implementation of ECNAero-BEM, since the yaw and dynamic inflow model are based on this parameter.

- From the analysis of the flow phenomena associated with a yawed inflow condition, it was found that BEM estimates a smaller effect of the skewed wake compared to AWSM for both the ECN and Glauert yaw model. Since the wind velocity changes direction constantly in time and wind turbines cannot react instantaneously to direction changes, wind turbines are expected to operate in yawed conditions for a significant amount of time during their lifetime. In order to improve the yawed inflow models, the results from AWSM can be used to tune these engineering models to make them more accurate. Furthermore, these engineering models as well as the results from AWSM should be validated with higher fidelity models or experimental data. In the New MEXICO experiment PIV measurements have been taken at various axial and radial locations for a wind turbine in yawed conditions, which could be used to validate the wake velocity and consequently the axial induced velocity over the blade.

- For highly loaded rotors, it is found that AWSM calculates a larger sectional normal force compared to BEM. This effect might be caused by the trailed vortices in the mid-section of the blade, due to the non-uniform distribution of the bound circulation. In order to validate which model calculates the correct sectional normal force in the mid-section of the blade, the results could be compared to an actuator line or acuator disc model. Such a high fidelity model solves the global flow through the RANS equations, whereas the local flow is modeled by airfoil polars. An option would be to add a correction for the trailed vortices in the mid-section of the blade and investigate the effect of such a correction.

- As part of the pitch step case, it would be interesting to further investigate the differences in dynamic inflow. From an initial comparison it has been found that BEM seems to reach the steady state much faster compared to AWSM, where the effect of the pitch step is observed for a much longer time-period. The dynamic inflow can also be assessed by a rotational speed variation, which is also tested in the New MEXICO experiment. Furthermore, these simulations should be repeated with the blade flexibility included to see if the same variation in loads can be observed and to assess whether these variations are caused by blade deflection or other phenomena. Finally, the simulations with BEM and AWSM should also be run with a constant pitch angle (except at the pitch step). The results from these simulations could be used to assess whether the variation in pitch angle from the sensor is physical or due to noise. With a constant pitch angle, it is expected that the blade loads will reach a steady state value faster, which would result in a better agreement between AWSM and the experimental results.

- During the coarse of the investigation, it has become clear that an important aspect of the comparison of wind turbine analysis tools is validation. In order to validate the models, data from either higher fidelity CFD models or wind tunnel experiments could help to asses the validity of the models, which should allow for an interesting comparison and useful validation data. In the AVATAR project, a lot of comparison data is available to compare the models. Furthermore, the results from the New MEXICO experiment have shown to provide valuable insight and many experiments have not yet been used for validation.

- For most of the test cases in this report, it has been found that the prescribed wake configuration of AWSM gives a good trade-off in terms of accuracy and computational time. However, for a turbulent inflow it is found that the free wake configuration leads to a lower mean induction factor, resulting in a 7.6% higher power compared to the prescribed wake configuration. In order to validate the wake velocity for the various wake configurations of AWSM, PIV measurements from the New MEXICO experiments can be used. Furthermore, it is found that the prescribed wake configuration becomes unstable when the induction is too high and a turbulent wake state has been reached. A further investigation in the effect of a turbulent wake state might lead to a more accurate definition of the prescribed wake formulation.

- In order to get a better understanding of the possibilities of the frequency and damping characteristics of AWSM, it would be valuable to do a stability analysis with AWSM and compare the results to BEM. An example of a test case that could be used for this purpose is the flutter test case, which is also part of the AVATAR project, which has the additional benefit that comparison data is available. Furthermore, the calculation of the blade modes could be compared.

- In order to make AWSM more suitable for the application of the analysis of (dynamic) load cases, the required CPU time has to decrease significantly. It has been found that a prescribed wake configuration reduces the CPU time by a factor of 5 and a recent development of parallel computing reduces the CPU time by another factor of 4. In order to further decrease the CPU time of AWSM, the vortex wake points could be clustered and shed every few time-steps to reduce the amount of wake points, although care should be taken with the trade-off between the accuracy and the calculation time.

- A rather recent development in wind energy is to apply aerodynamic devices to the blades (e.g. vortex generators, spoilers and flaps). It would be interesting to investigate the differences in modeling of aerodynamic devices between BEM and AWSM. Differences are expected, since BEM models the rotor as a set of independent annuli, whereas AWSM calculates the influence of each blade element by the vorticity. Such an investigation is part of the AVATAR project, which would make data from external codes available for comparison.

- Due to time considerations, the current test cases have been run at one wind speed in the partial load regime only. In order to get more insight in the differences between BEM and AWSM, it would be interesting to see what happens at other wind speeds. Since the induction of the rotor above the rated wind speed reduces, it is expected that there is a better agreement between BEM and AWSM, as was also found for the AVATAR turbine.

References

[1] G. Corbetta, A. Ho, and A. Mbistrova, "The european offshore wind industry–key trends and statistics 2015," 2016.

[2] J. Schepers, *Engineering models in wind energy aerodynamics: Development, implementation and analysis using dedicated aerodynamic measurements.* PhD thesis, TU Delft, Delft University of Technology, 2012.

[3] J. Katz and A. Plotkin, *Low-speed aerodynamics*, vol. 13. Cambridge University Press, 2001.

[4] K. Boorsma and F. Grasso, *ECN Aero-Module: User's manual.* Energy Research Centre of the Netherlands, ECN, 213 ed., 2015.

[5] A. Van Garrel, *Development of a wind turbine aerodynamics simulation module.* Citeseer, 2003.

[6] D. M. Eggleston and F. Stoddard, "Wind turbine engineering design," 1987.

[7] E. Parra, "Data reduction and analysis of new mexico experiment," tech. rep., ECN-Wind-Memo-2015-189, ECN, February 2016.

[8] M. Hansen, *Aerodynamics of wind turbines.* Routledge, 2008.

[9] S. Hauptmann, M. Bülk, L. Schön, S. Erbslöh, K. Boorsma, F. Grasso, M. Kühn, and P. Cheng, "Comparison of the lifting-line free vortex wake method and the blade-element-momentum theory regarding the simulated loads of multi-mw wind turbines," in *Journal of Physics: Conference Series*, vol. 555, p. 012050, IOP Publishing, 2014.

[10] G. Sieros, P. Chaviaropoulos, J. Sørensen, B. Bulder, and P. Jamieson, "Upscaling wind turbines: theoretical and practical aspects and their impact on the cost of energy," *Wind Energy*, vol. 15, no. 1, pp. 3–17, 2012.

[11] J. Schepers, O. Ceyhan, F. Savenije, M. Stettner, H. Kooijman, P. Chaviarapoulos, G. Sieros, C. S. Ferreira, N. Sørensen, M. Wächter, *et al.*, "Avatar: Advanced aerodynamic tools for large rotors," in *33rd ASME Wind Energy Symposium.*

[12] C. Bak, F. Zahle, R. Bitsche, T. Kim, A. Yde, L. C. Henriksen, A. Natarajan, and M. Hansen, "Description of the dtu 10 mw reference wind turbine," *DTU Wind Energy Report-I-0092*, 2013.

[13] A. I. Ruiz, H. A. Madsen, D. R. V. DTU, A. Croce, L. Sartori, M. S. Lunghini, M. Reijerkerk, H.-J. Kooijman, and M. S. GE, “Avatar deliverable d1. 3 comparison of the innwind and avatar research wind turbines,” 2015.

[14] T. Sant, *Improving BEM-based aerodynamic models in wind turbine design codes*. PhD thesis, TU Delft, Delft University of Technology, 2007.

[15] G. Pirrung, *Fast Trailed Vorticity Modeling for Wind Turbine Aerodynamics and its Influence on Aeroelastic Stability*. PhD thesis, Technical University of Denmark, 2014.

[16] S. Voutsinas, “Vortex methods in aeronautics: how to make things work,” *International Journal of Computational Fluid Dynamics*, vol. 20, no. 1, pp. 3–18, 2006.

[17] B. M. Sumer, “Lecture notes on turbulence,” 2013.

[18] S. Ivanell, R. Mikkelsen, and D. Henningson, “Validation of methods using ellipsys3d,” 2008.

[19] C. Lindenburg, *PHATAS User’s Manual*. Energy Research Centre of the Netherlands, ECN, 2006.

[20] J. Schepers and R. van Rooij, “Final report of the annexlyse project,” 2005.

[21] J. Schepers, “Iea annex xx: Comparison between calculations and measurements on a wind turbine in yaw in the nasa-ames wind tunnel,” tech. rep., Tech. Rep. No. ECN-E-07-072, 2008.

[22] C. Lindenburg, “Investigation into rotor blade aerodynamics,” *ECN Report: ECN-C-03-025*, 2003.

[23] J. Schepers, K. Boorsma, T. Cho, S. Gomez-Iradi, P. Schaffarczyk, A. Jeromin, W. Shen, T. Lutz, K. Meister, B. Stoevesandt, *et al.*, “Final report of iea task 29, mexnext (phase 1): Analysis of mexico wind tunnel measurements,” *Wind Energy*, vol. 2014, p. 2013, 2015.

[24] F. Grasso and A. van Garrel, “Near wake simulation of mexico rotor in axial and yawed flow conditions with lifting line free wake code,” in *Wake Conference*, 2011.

[25] K. Boorsma, F. Grasso, and J. Holierhoek, “Enhanced approach for simulation of aerodynamic loads,” *EWEA Offshore*, 2011.

[26] P. Chaviaropoulos, N. Soerensen, M. Hansen, I. Nikolaou, K. Aggelis, J. Johansen, M. Gaunaa, T. Hambraus, H. von Geyr, C. Hirsch, *et al.*, “Viscous and aeroelastic effects on wind turbine blades. the viscel project. part ii: Aeroelastic stability investigations,” *Wind Energy*, vol. 6, no. 4, pp. 387–403, 2003.

[27] H. Madsen, V. Riziotis, F. Zahle, M. Hansen, H. Snel, F. Grasso, T. Larsen, E. Politis, and F. Rasmussen, “Blade element momentum modeling of inflow with shear in comparison with advanced model results,” *Wind Energy*, vol. 15, no. 1, pp. 63–81, 2012.

[28] H. Madsen, C. Bak, U. Paulsen, M. Gaunaa, N. Sørensen, P. Fuglsang, J. Romblad, N. Olsen, P. Enevoldsen, J. Laursen, *et al.*, “The dan-aero mw experiments,” in *Conference Proceedings48th AIAA Aerospace Sciences Meeting Including The New Horizons Forum and Aerospace Exposition*, 2010.

[29] K. Boorsma and J. Schepers, “New mexico experiment: Preliminary overview with initial validation,” 2014.

[30] “Large low-speed facility.” www.dnw.aero/wind-tunnels/llf. Accessed: 07-04-2016.

[31] K. Boorsma and J. Schepers, “Description of experimental setup: New mexico experiment,” tech. rep., ECN-X-15-093-v1, ECN, August 2015.

[32] G. Bangga, T. Lutz, and E. Krämer, "An examination of rotational effects on large wind turbine blades," in *11th EAWE PhD Seminar, Stuttgart, Germany*, 2015.

[33] E. Jost, T. Lutz, and E. Krämer, "Steady and unsteady cfd power curve simulations of generic 10 mw turbines," 2015.

[34] P. G. Saffman, *Vortex dynamics*. Cambridge university press, 1992.

[35] W. Phillips and D. Snyder, "Modern adaptation of prandtl's classic lifting-line theory," *Journal of Aircraft*, vol. 37, no. 4, pp. 662–670, 2000.

[36] L. Prandtl and A. Betz, *Vier Abhandlungen zur Hydrodynamik und Aerodynamik...: mit einer Literaturübersicht als Anhang*. Kaiser Wilhelm-Instituts für Strömungsforschung, 1927.

[37] T. Burton, D. Sharpe, N. Jenkins, and E. Bossanyi, *Wind energy handbook*. John Wiley & Sons, 2001.

[38] H. Glauert, A. R. Committee, *et al.*, *A general theory of the autogyro*, vol. 1111. HM Stationery Office, 1926.

[39] J. Schepers, *An engineering model for yawed conditions, developed on the basis of wind tunnel measurements*. Netherlands Energy Research Foundation ECN, 1998.

[40] H. Snel, J. Schepers, and S. E. C. Nederland, *Joint investigation of dynamic inflow effects and implementation of an engineering method*. Netherlands Energy Research Foundation ECN, 1995.

[41] B. Montgomerie, *Three-dimensional effects in stall*. Netherlands Energy Research Foundation ECN, 1997.

[42] J. Holierhoek, J. De Vaal, A. Van Zuijlen, and H. Bijl, "Comparing different dynamic stall models," *Wind Energy*, vol. 16, no. 1, pp. 139–158, 2013.

[43] H. Snel, "Heuristic modelling of dynamic stall characteristics," in *EWEC-conference-*, pp. 429–433, Bookshop for Scientific Publications, 1997.

[44] J. G. Leishman, "Challenges in modeling the unsteady aerodynamics of wind turbines," in *ASME 2002 Wind Energy Symposium*, pp. 141–167, American Society of Mechanical Engineers, 2002.

[45] S. Gupta and J. G. Leishman, "Dynamic stall modelling of the s809 aerofoil and comparison with experiments," *Wind Energy*, vol. 9, no. 6, pp. 521–547, 2006.

[46] I. 61400-1, "Wind turbine generator systems, part 1 safety requirements: Edition 3," tech. rep., Tech. Rep. No. IEC-61400-1:2005(E), 2005.

[47] A. Rosen, A. Wolf, D. B. Shmuel, and G. Omri, "Part 1. the mexico project wind turbine model," 2011.

[48] A. Rosen, A. Wolf, D. B. Shmuel, and G. Omri, "Part 2. the mexico project wind turbine model," 2011.

[49] N. N. Sorensen, M. O. Hansen, N. R. Garcia, L. Florentie, and K. Boorsma, "Power curve predictions," tech. rep., AVATAR, June 2014.

[50] F. Meng, "Comparison of models with respect to loads analysis in extreme shear and half wake of the innwind.eu and avatar rwts," tech. rep., AVATAR, December 2015.

Appendix A

Axial Inflow

A.1 Case Set-Up

For aeroelastic simulations of wind turbines with BEM codes usually a time step in the order of $\Delta t \approx 0.01s$ is taken, which results in CPU times in the order of ten minutes for one load case. However, the same simulations with AWSM would require much more CPU time (in the order of several weeks or more), since for every time-step and sub-iteration the circulation at every point in the wake has to calculated. The amount of vortex wake points is determined by the amount of blade elements (usually around 20) multiplied the amount of streamwise wake points (usually up to 1,000) and the amount of blades. This leads to a total number of up to 60,000 wake points, which have to be evaluated at very sub-iteration for each time-step. Currently, time steps that are used for aeroelastic simulations with AWSM are in the order of $\Delta t \approx 0.1s$. When the time-step is decreased, the amount of wake point in the wake will increase, resulting in a large increase of CPU time. For the simulations at rated wind speed for the AVATAR project a time step of $0.15s$ was used, which will be used for the simulations at partial load as well.

With the increasing time step, dynamic effects with a higher frequency will be filtered out. In order to show how this increasing time step affects the simulations, a BEM simulation is run with Phatas with a time-step of $0.01s$ and $0.15s$ with the controller on. For the simulation with a time-step of $0.15s$ the controller was updated to cope with the the lower update rate. In Fig. A.1 it can be seen that the two runs give different values for rotor speed and therefore also for flapwise blade root bending moment M_y and shaft torque. The pitch angle is zero for both cases during the complete simulation. The simplification is made to keep the rotor speed constant and run the simulation again with a time step of $0.15s$ without controller. In Fig. A.1, it can be seen that for this case the results are closer to those from the controller with the smaller time step. From the blade M_y it can be seen that the simulation is out of phase due to small differences in rotor speed. Finally, it can be seen that the shaft torque shows large oscillations. It is expected that the variations in rotor speed reduce the oscillations, which is not possible in case the controller is off.

A.1.1 Wake Settings AWSM

After the operational conditions are determined, the description of the wake that will be used for the simulations with AWSM will be presented. For this case a prescribed (hybrid) and a free wake

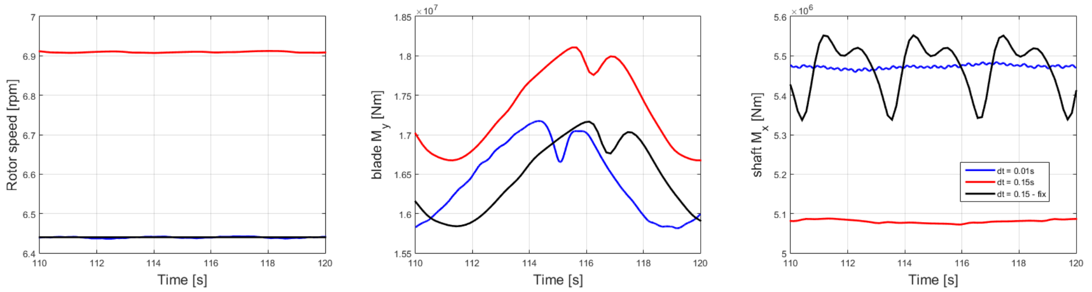

Figure A.1: *Comparison of output variables for the INNWIND turbine with different time-step settings.*

formulation will be used. In order to make sure enough vortex points are shed into the wake, a total wake length of three rotor diameters is used. The amount of streamwise wake points is determined using Eq. A.1.

$$N_{total} = \frac{3 \cdot D}{U_\infty (1-a)\Delta t} \tag{A.1}$$

The flow right behind the wind turbine slows down by the induction factor a, which is a value that is obtained from the simulation itself. Therefore, the simulation with the BEM code will be conducted first in order to determine a and consequently determine the amount of wake points for the simulation with the vortex wake code. The results from this simulation with Phatas can be found in Fig. A.2. From this figure it can be seen that induction is found to be around $a = 0.33$. It should be noted that this value is just taken as the average of four points along the blade. A more accurate value of the induction can be obtained by integrating the induction over the blade and taking into account that induction over the outer part of the blade has more influence due to the increased swept area. Since the induction is not constant over the rotor plane, it is argued that this method is accurate enough to reach a wake length of approximately three rotor diameters.

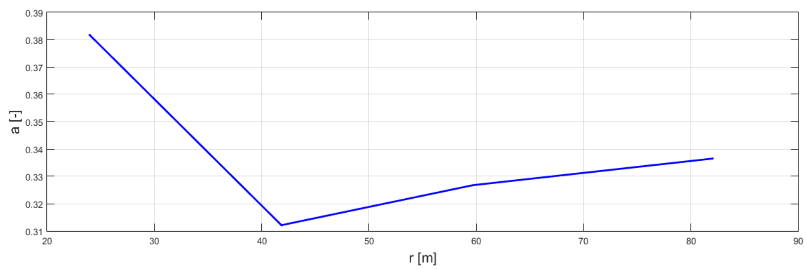

Figure A.2: *Induction factor as function of radial position for the INNWIND turbine in axial inflow.*

The free wake convection in AWSM is determined by the amount of free wake points. For this simulation this is set to 2 rotor diameters. The amount of free wake points is found by using Eq. A.1 and replace the factor 3 by 2 (i.e. take 2/3 of the total amount of wake points). Additionally, also a hybrid free-prescribed wake formulation is used to reduce the CPU time of the simulations. For this case, only one rotor revolution of free wake points is used as a free convection, whereas the rest of the wake is prescribed. The amount of free wake points in order to have one rotor revolution of wake points is found in Eq. A.2.

$$N_{free} = \frac{60}{\Delta t \cdot \omega} \tag{A.2}$$

In order to visualize the difference between the two wake configurations that will be used in this case, the wake of the INNWIND turbine at $t = 120s$ is shown for the prescribed and free wake formulation in Fig. A.3. When comparing the wake results form the two configurations it can be seen that the wake is almost identical for the first rotor revolution behind the turbine, which is expected since the first part of the wake is calculated in a similar matter. When the wake progresses in space it can be seen that the free wake configuration becomes more chaotic due to the interaction between the vortex points. However, the prescribed wake configuration seems to remain a similar shape when it is convected downstream, which is also expected since the induced velocity of this wake is prescribed. From the prescribed wake configuration it can be observed that the distance between a full revolution of wake points becomes smaller away from the rotor plane, indicating the reduction of wind speed in the wake from $U_\infty(1-a)$ to $U_\infty(1-2a)$. From the free wake configuration this behavior is more difficult to observe, although it can be seen that the total length of the wake is slightly smaller, indicating a higher induction. Finally, it can be observed that the minimum and maximum circulation of the wake points is similar for the two wake configurations, indicating that the circulation that is calculated in the wake points falls in the same range.

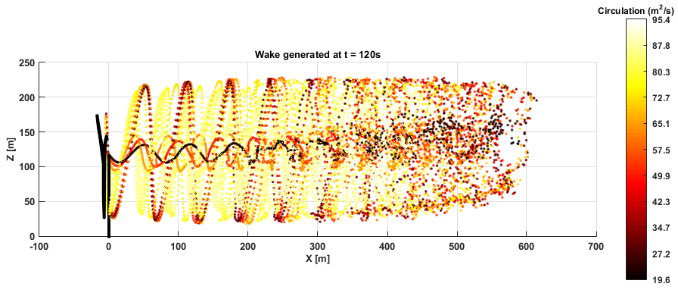

(a) *Free wake.*

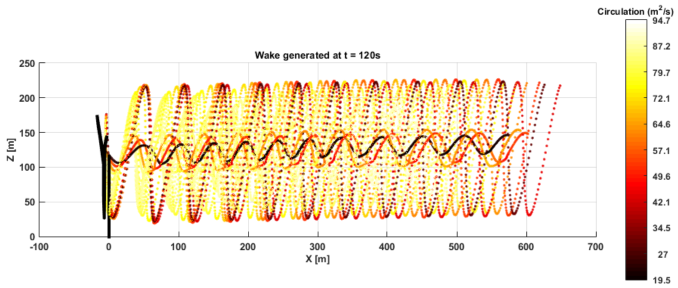

(b) *Prescribed wake.*

Figure A.3: *Visualization of the wake at $t = 120s$ for the INNWIND turbine.*

A.1.2 Computational Set-up

The most important part of the settings for the computational set-up are shown in Section 5.1.1. More information about the computational set-up can be found in Table A.1. In this table the settings are shown that are similar for the six simulations that are described in Table 5.3. It can be seen that all the degrees of freedom for the blade are taken into account, i.e. torsion, flap and edge-wise direction. Furthermore, it can be seen that the generator runs at constant speed and the controller and pitch actions are turned off.

Table A.1: Overview of simulation settings for axial inflow.

Case	Axial inflow
Solver	Phatas-Aero
Subiteration settings	3 (Aerodynamic call at 1 and ≥ 9)
Simulation time (s)	120
Time step (s)	0.15
Blade torsion	ON
Flapping flag	ON
Lagging flag	ON
Dynamic stall	Snel (1st order)
Gearbox support	OFF
Controller	OFF
Generator model	Constant speed
Pitch flag	OFF
Shaft torsion	OFF
Pitch angles (deg)	0.0
Wind speed (m/s)	8
Wind ramp	0.3 (starts at 30%)

A.2 Comparison of the Results

In this section the results from the axial inflow test case will be presented. In the following subsections, different output parameters will be analyzed and the results between BEM and AWSM will be compared. In the figures, the INNWIND turbine is indicated by the solid line, whereas the AVATAR turbine is indicated by the dashed line.

A.2.1 Axial Induced Velocity

The axial induced velocity $u_{i,ax}$ has been checked at different azimuth positions (0°, 90°, 180° and 270°) as a function of radial position for both the INNWIND and AVATAR turbine in Fig. A.4. It can be seen that the AVATAR turbine operates at a much lower induction for the complete blade length, which is expected sine the AVATAR turbine is a so-called low induction turbine. The results obtained from AWSM prescribed and free wake configuration are in good agreement with each other over the whole blade length and for all azimuth positions, especially for the AVATAR turbine.

For the INNWIND turbine, the differences between BEM and AWSM are large at the root and tip section of the blade, which is expected since the BEM code uses an engineering model for root and tip flow based on empirical data, whereas AWSM is capable of calculating the flow in the root and tip section intrinsically from vorticity. Differences in $u_{i,ax}$ at the tip are in the order of 25%, whereas the differences in the root section are even larger. These results have been confirmed at all four azimuth positions, as is shown in Fig. A.4. For the AVATAR turbine is can be seen that the differences near the tip are much smaller, indicating a better fit between the codes, which could be explained by the fact that the low induction AVATAR turbine operates at much lower angles of attack, where the aerodynamics can be better predicted.

For the mid-section of the blade, it is found that at 360° azimuth position (blade pointing upwards) the results from BEM and AWSM are relatively accurate, which can be seen in Fig. A.4a. However, the results at 180° azimuth (blade pointing downwards) are off by $\approx 10\%$, which is expected to be due to the influence of the tower on the induced velocity. A final observation that can be made is that BEM estimates a higher induction factor over the mid-section of the blade for all cases except at 180°.

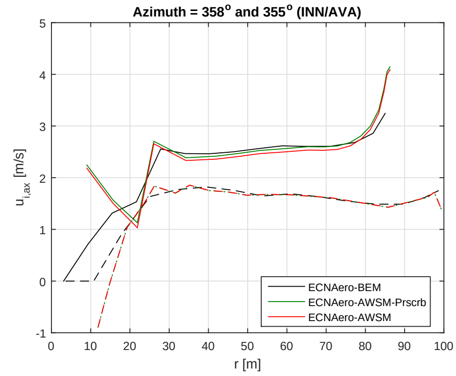

(a) *Azimuth* $\approx 360°$.

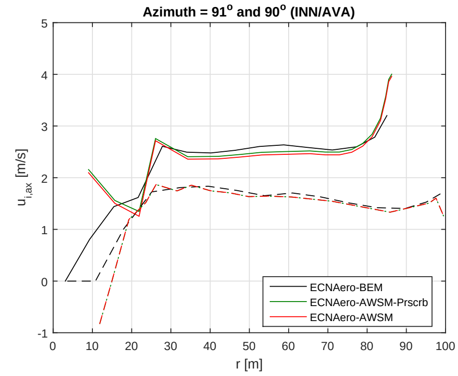

(b) *Azimuth* $\approx 90°$.

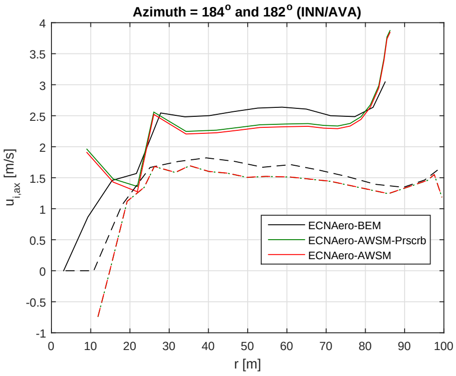

(c) *Azimuth* $\approx 180°$.

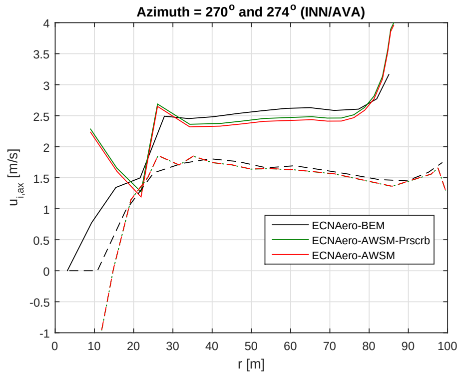

(d) *Azimuth* $\approx 270°$.

Figure A.4: *Axial induced velocity over the blade at different azimuth positions for the INNWIND (solid line) and AVATAR (dashed line) turbine.*

A.2.2 Angle of Attack

Similar to the axial induction factor, the AoA is also checked at different azimuth positions for both the INNWIND and AVATAR turbine in Fig. A.5. As expected, it can be observed that the AVATAR turbine operates at a much lower AoA, especially near the tip section of the blade. It can be seen that at the tip section of the INNWIND turbine, there is difference in AoA of $\approx 1°$. Again, it is found that the largest difference occur at an azimuth position of 180° in the mid-section of the blade for both turbines.

There is an excellent agreement found between the two wake configurations of AWSM, showing only minor differences in AoA. In the root section of the blade the differences between BEM and AWSM are much larger, which could be explained by the fact that the airfoils in this section have a low lift coefficient and are thus very sensitive to influence of other sections of the blade, which is not taken into account in BEM codes (independent annuli). However, the root section of the blade does not influence the total performance and loads of the turbine too much, due to the this low lift coefficient and small distance from the rotor center.

Similar results have been obtained from an analysis of the lift coefficient. The lift coefficient is obtained from a look-up table, which is the same for BEM and AWSM and explains why the behavior of the lift coefficient is similar to that of the AoA.

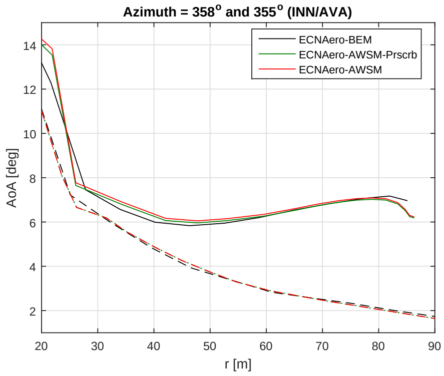

(a) *Azimuth* $\approx 360°$.

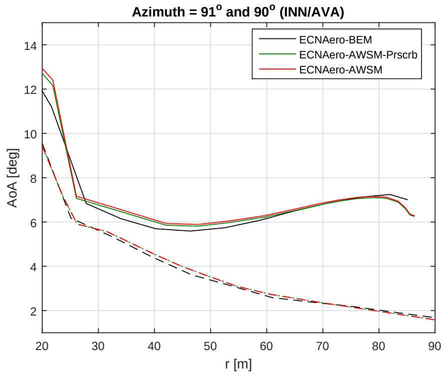

(b) *Azimuth* $\approx 90°$.

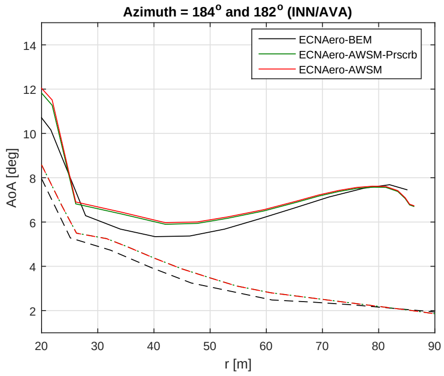

(c) *Azimuth* $\approx 180°$.

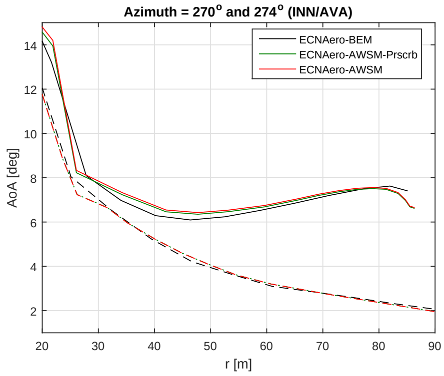

(d) *Azimuth* $\approx 270°$.

Figure A.5: *Angle of attack over the blade at different azimuth positions for the INNWIND (solid line) and AVATAR (dashed line) turbine.*

A.2.3 Normal Force

The sectional normal force that is generated by the blades is again dependent on the AoA. From the AoA, the lift and drag coefficient are obtained by a look-up table, which determines the normal force coefficient (i.e. coefficient of force perpendicular to the chord). The look-up table for the lift and drag coefficient at the same for BEM and AWSM. Since the blade is twisted along radial length, the direction of the normal force is also changing over the blade, relative to the rotor plane.

From Fig. A.6, it can be seen normal force per unit length shows a very good agreement between the two wake configurations of AWSM for all cases. At an azimuth angle of 180° it can be seen that AWSM calculates a much higher value for the normal force for the INNWIND turbine, which is also visible for the other azimuth angles in a smaller amount. For the AVATAR turbine, also significant differences are found between BEM and AWSM, however BEM seems to give a larger value for the normal force. In general, a good agreement is found for the trend of the normal force over the blade.

A.2.4 Tangential Force

The sectional tangential force is the force perpendicular to the normal force (i.e. the force along the chord). The tangential force is important for generation of the torque and consequently the power of the turbine. In Fig. A.7, it can be seen that the tangential force in the root section is negative for the AVATAR turbine, which can be explained by the large AoA, where the drag

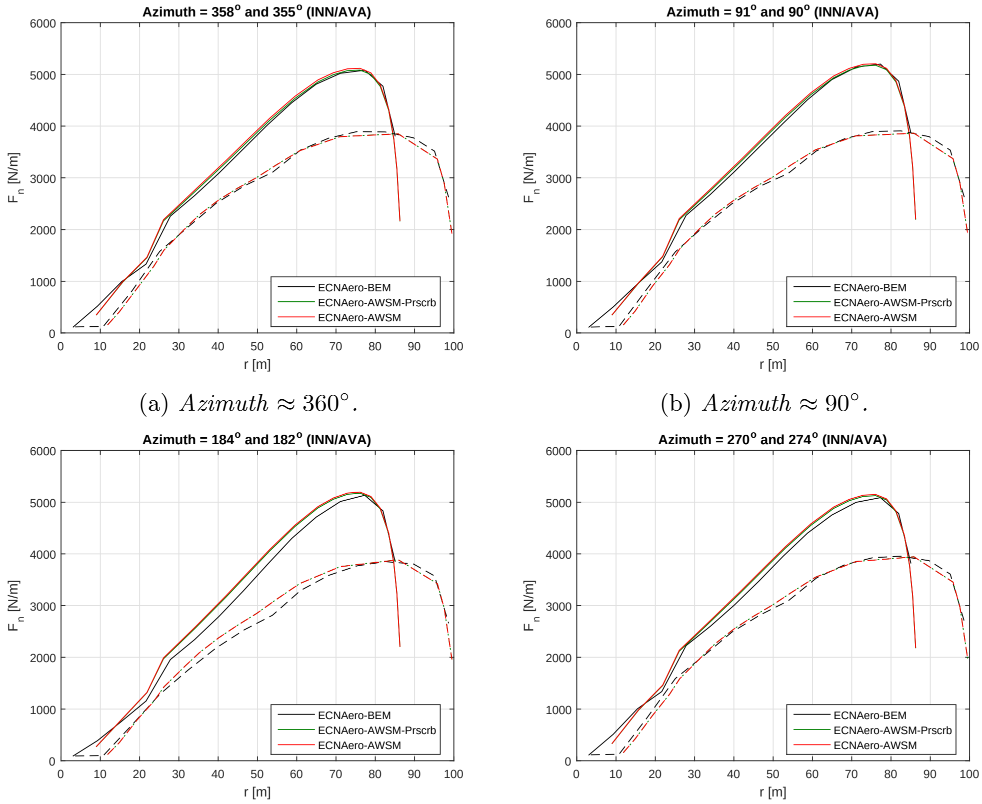

(a) *Azimuth* $\approx 360°$.

(b) *Azimuth* $\approx 90°$.

(c) *Azimuth* $\approx 180°$.

(d) *Azimuth* $\approx 270°$.

Figure A.6: *Normal force over the blade at different azimuth positions for the INNWIND (solid line) and AVATAR (dashed line) turbine.*

is very large compared to the lift. The difference between BEM and AWSM is large in the root section, which can be explained by the large AoA in this section.

It can be seen that there is a very good agreement between BEM and AWSM for the AVATAR turbine. Again, at an azimuth angle of 180°, the largest differences are found. For the INNWIND turbine some larger differences are found. For F_t, also some differences are found between the two wake configurations of AWSM, although the differences are relatively small.

A.2.5 Blade Root Bending Moment

Now that some of the parameters on the blade sectional level have been investigated, the loads on the complete blade will be investigated, starting with the blade root bending moment. In this section the blade M_x, M_y and M_z at the root will be analyzed.

Edgewise The first blade load that is discussed in the blade M_x, which is the moment that causes the blade to deflect in edgewise direction (i.e. in the rotor plane). In Fig. A.8a, the M_x is plotted against the azimuth angle for a full rotation for both turbines. This blade load is caused mainly by the gravity force, which is acting as a sinusoidal variation over the azimuth positions. From this figure it can be seen that there is an excellent agreement between the codes for the complete rotation and for both turbines.

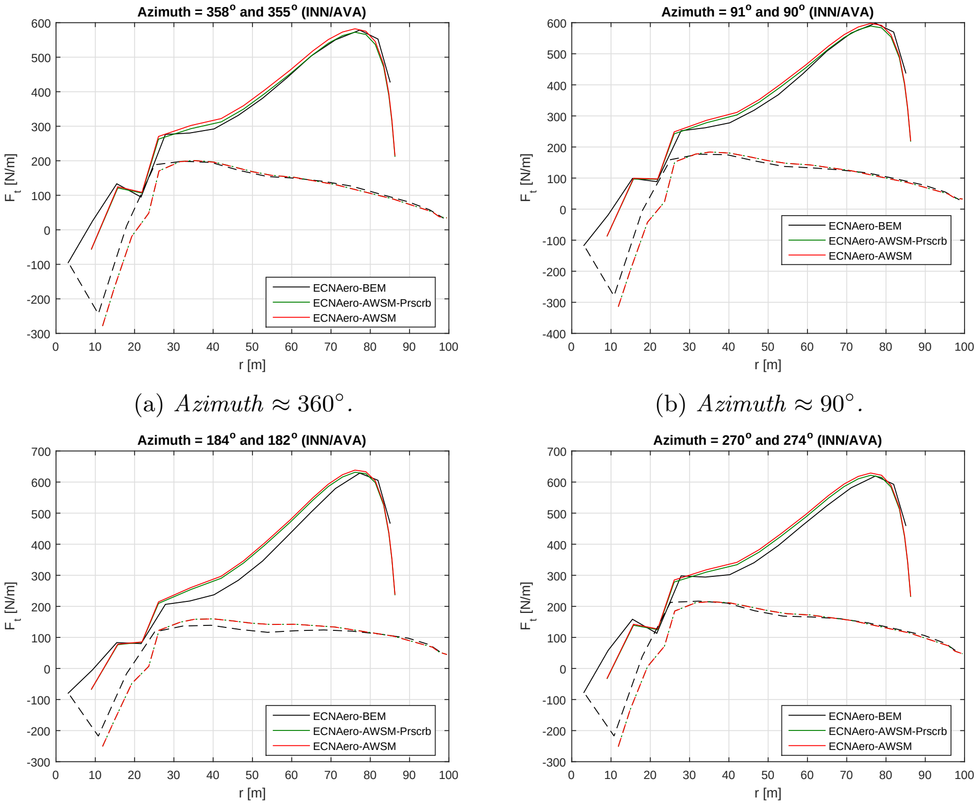

(a) *Azimuth* $\approx 360°$.

(b) *Azimuth* $\approx 90°$.

(c) *Azimuth* $\approx 180°$.

(d) *Azimuth* $\approx 270°$.

Figure A.7: *Tangential force over the blade at different azimuth positions for the INNWIND (solid line) and AVATAR (dashed line) turbine.*

Flapwise The second blade load that will be discussed is the blade M_y, which is the moment that causes the blade to deflect in flapwise direction (i.e. out of the rotor plane). This load is important when considering the clearance between the deflected blade and the tower. In Fig. A.8b, M_y is plotted against the azimuth angle for a full rotation for both turbines.

It can be seen that there is a good agreement between the two wake configurations of AWSM for the AVATAR turbine, although the free wake simulations shows a higher M_y for the INNWIND turbine over the complete rotor revolution ($\approx 1\%$). The agreement with the BEM results is fair for the AVATAR turbine, although it can be observed that BEM predicts a larger dip due to the tower passage. For the INNWIND turbine, the results between BEM and AWSM show much larger differences.

Torsional The last blade load that is discussed is the blade M_z, which is the moment that causes the blade to twist. In Fig. A.8c, M_z is plotted against the azimuth angle for a full rotation for both turbines.

It can be seen that the behavior of M_z is opposite for the INNWIND and AVATAR turbine. In order to understand how this is possible, it is important to note how M_z is created. First of all, there is the influence of the moment coefficient of the airfoils, which creates negative (nose down) moment for both turbines and is relatively constant over the rotor revolution. Secondly, there is the influence of the normal force due to the offset between the pitch axis and the quarter chord location. It is found that this influence creates a positive (nose up) moment on the blade. Again, this influence is rather constant over the rotor revolution. Furthermore, there is the influence of

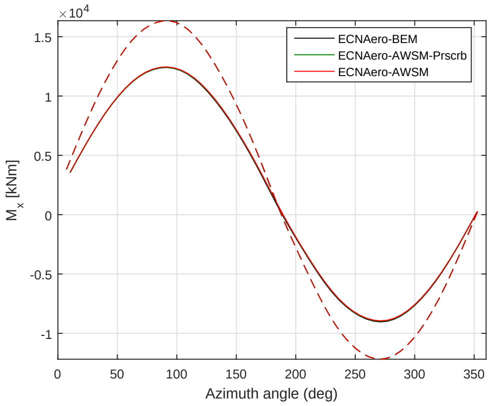

(a) M_x.

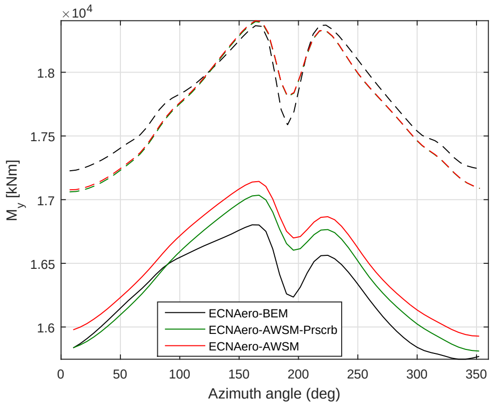

(b) M_y.

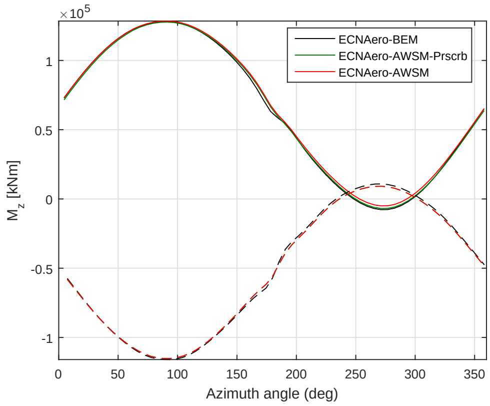

(c) M_z.

Figure A.8: *Blade root bending moment as a function of azimuth angle for the INNWIND (solid line) and AVATAR (dashed line) turbine.*

the tangential force and the offset in blade flapwise direction. Finally, this blade flapwise deflection will also generate a torsional moment due to the gravity force. Since the blade deformation is cyclic, this also explain the cyclic behavior of M_z. The different shape of M_z over the azimuth positions can be explained by the fact that the INNWIND turbine has pre-bend in the opposite direction of the flapwise blade deformation, resulting in a torsional moment in the other direction, as can be seen in Fig. A.8c.

In terms of the comparison between BEM and AWSM, the results seem to match well for the complete range of azimuth angles for both turbines.

A.2.6 Blade Tip Deflection

The blade tip deflection is an important variable when considering tower clearance. The AVATAR turbine is designed to be relatively flexible and the blades are also longer and thus it is expected that this will result in larger blade tip deflections. In Fig. A.9, the blade deflection at 95% of the blade length is shown. As expected, it can be seen that the AVATAR turbine shows much larger deflections at the same wind speed (i.e. $8m/s$).

When comparing the results from the different codes, a good agreement can be observed, both in shape as well as in absolute value. This was also expected, since the blade M_y showed a good agreement and the same structural model is used for both aeroelastic codes. For the INNWIND turbine it can be observed that the results from the two AWSM simulations have an identical shape over the full rotation with a slight difference in absolute value, whereas the BEM results show a slightly different shape of the displacement over the rotor revolution. The results from the two wake configurations of AWSM on the AVATAR turbine show an excellent agreement, although it can be observed that BEM obtains slightly higher deflections over the complete rotor revolution.

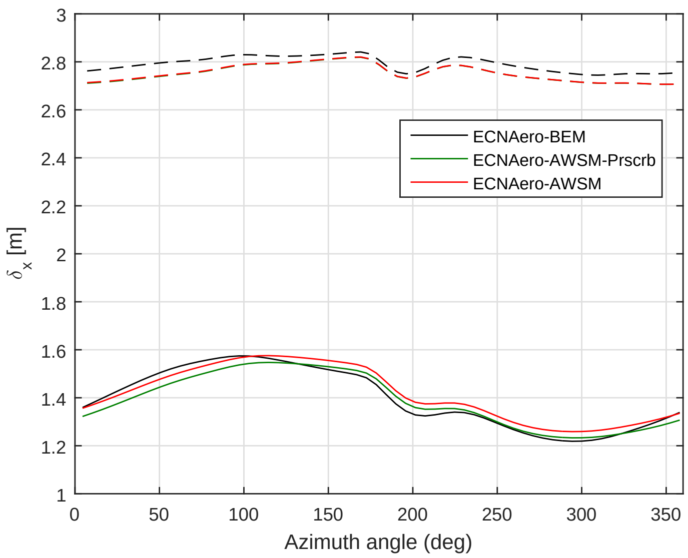

Figure A.9: *Blade tip deflection as a function of azimuth angle for the INNWIND (solid line) and AVATAR (dashed line) turbine.*

A.2.7 Rotor Performance

In this section the total performance of the rotor is compared between BEM and AWSM by means of the axial force F_{ax} and aerodynamic power P.

Axial Force The axial force or thrust of a wind turbine determines how much force is acting on the complete wind turbine in axial direction. This force is equal to the force that slows down the wind and consequently extracts the energy from the flow. The axial force is therefore an important measure of the complete rotor performance. In Fig. A.10, the axial force for both turbines is shown as a function of time. The last $20s$ of the simulation are taken, since this is the time period in which the solution has converged.

The first thing that can be observed is that the axial force on the INNWIND turbine is larger than on the AVATAR turbine, although the latter has larger blades and the wind conditions are similar. This can be explained by the low induction design of the AVATAR turbine, where the turbine operates at lower AoA, where the drag is also lower. In this way the turbine can operate more efficiently at the cost of an increase blade length.

When comparing the codes it can be seen that the results match reasonably well for the AVATAR turbine, whereas the results for the INNWIND turbine show significant differences between the three codes that have been used. The dips in the thrust are caused by the tower passage (i.e. three times per revolution). It can be seen that the dip in axial force due to the tower passage is larger for the BEM result than for the AWSM results.

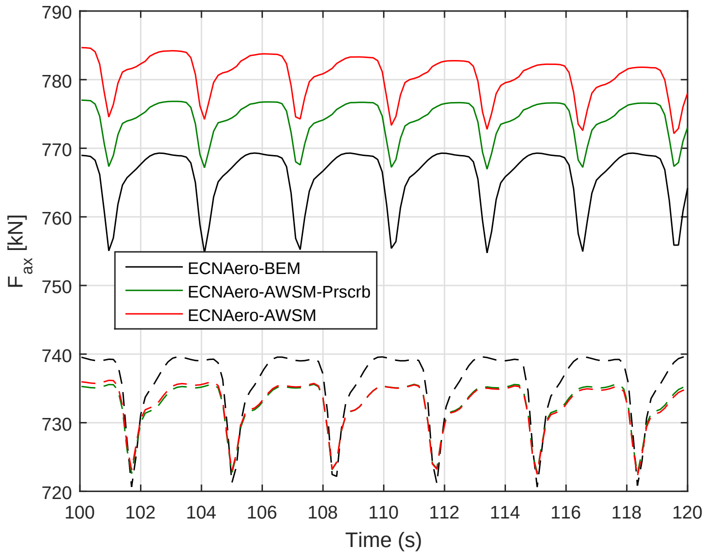

Figure A.10: *Axial force as a function of time for the INNWIND (solid line) and AVATAR (dashed line) turbine.*

Power The actual power of a wind turbine is one of the most important global parameter when designing a wind turbine. It should be noted that this is the aerodynamic power and no losses have been taken into account. The power is produced by the torque of the three blades multiplied by the rotor speed. Since the rotor speed is constant in these simulations, the torque and the power follow the exact same pattern. In Fig. A.11, the power is shown as a function of time for both turbines. Again, the dip in the power is caused by the tower passage of the blades. Although it was found that AVATAR turbine has a lower thrust, the power level is significantly higher at $8m/s$, confirming the working principle of the low induction turbine.

When comparing the results from the different codes it can be seen that there is a good agreement between BEM and AWSM for the AVATAR turbine. For the INNWIND turbine, the differences between the codes is much larger. Interesting to see is that for the power there is also a significant difference between the two wake configurations of AWSM. This could be due to the fact that for high induction turbines, AWSM takes longer to fully converge. It can be seen that the results at $t = 120s$ seem to be closer to each other than the results at $t = 100s$.

A.2.8 Tower Bottom Bending Moment

The last parameters that will be compared are the tower bottom bending moments around the three axis of the tower, M_x, M_y and M_z. These tower moments are affected by the calculation of many different parameters on the complete turbine and it is expected that the errors in these parameters are accumulated. In Fig. A.12, the tower moments are shown as a function of time for both turbines.

The calculation of the tower M_x is mainly affected by the gravity force and the rotor torque. Since the gravity force is the same for BEM and AWSM and a good agreement has been found for the aerodynamic power (and thus torque), it is expected that there is good agreement between BEM and AWSM. In Fig. A.12a, it can be seen that there is indeed a good agreement in the tower M_x. It can be seen that the free wake configuration of AWSM shows a slightly higher mean value for the INNWIND turbine, which agrees with the results that this model shows a larger power and

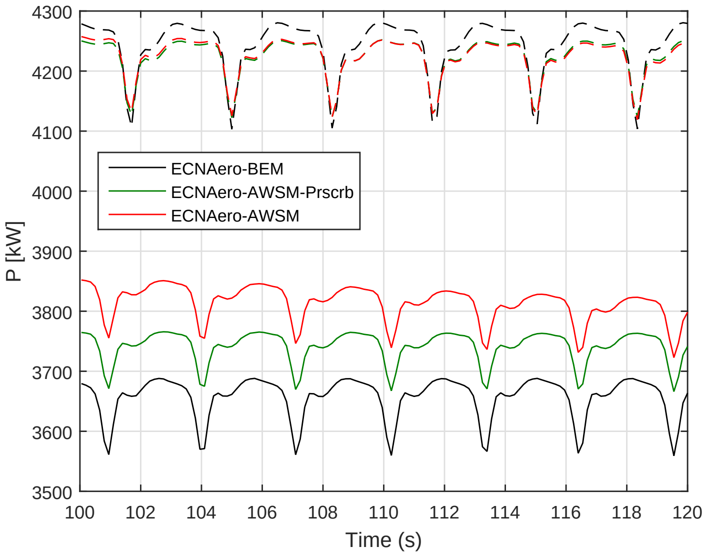

Figure A.11: *Power as a function of time for the INNWIND (solid line) and AVATAR (dashed line) turbine.*

thus also a larger torque. Furthermore, it can be seen that the AVATAR turbine shows a larger mean value of M_x, which can be explained by the larger blade mass.

The tower M_y is mainly determined by the calculation of F_{ax}. In Fig. A.12b, the tower M_y is shown as function of time. From this figure, it can be seen that there is a good agreement between the models, which is expected since a good agreement was found for the rotor F_{ax}.

In Fig. A.12c, the tower M_z is shown. It can be seen that M_z is much higher for the AVATAR turbine, which could be due to the larger blade length causing a higher yawing moment on the tower. When comparing the codes it can be seen that the results for the AVATAR turbine match reasonably well, although there are clear differences in the shape of M_z over time and the differences between the codes could reach up to 20%. However, for the INNWIND turbine, the differences for the absolute values are much higher. Interesting though, the results between the free and prescribed wake are almost identical for both turbines. Considering there are significant differences found in axial force and power it is surprising that M_z shows such a good agreement.

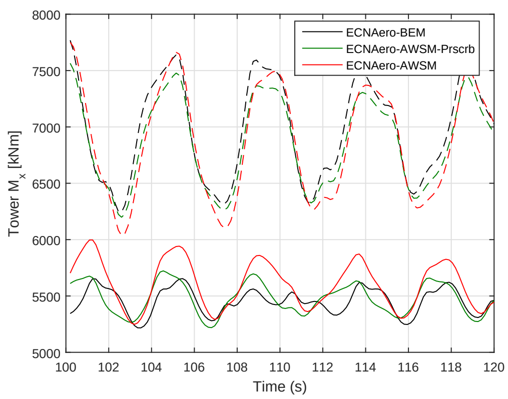

(a) *Edgewise.*

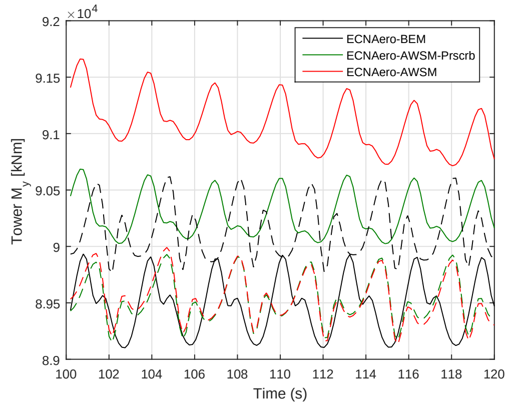

(b) *Flapwise.*

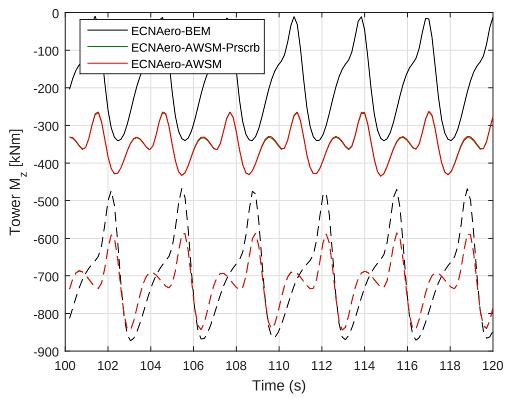

(c) *Torsional.*

Figure A.12: *Tower bottom bending moment as a function of time for the INNWIND (solid line) and AVATAR (dashed line) turbine.*

Appendix B

Yawed Inflow

B.1 Case Set-Up

Similar to the case with axial inflow, a time step of $\Delta t = 0.15s$ is used for the case with yawed inflow. In order to see how the increasing time step influences the modeling of the turbine, first a simulation with BEM (ECN yaw model) is run with a controller and a time step of $\Delta t = 0.01s$ and $0.15s$. In Fig. B.1, it can be seen that the large time step will result in a higher rotor speed. Consequently, also the blade flapwise moment and shaft M_x are different with an increasing time step. Therefore, similar to the case with axial inflow, the simplification is made to keep the rotor speed constant and run the simulation without a controller. In Fig. B.1, it can be seen that the rotor speed, as well as the blade M_y and shaft M_x, show a much better agreement with the results from the simulation with the controller on and a time step of $0.01s$. The phase difference is caused by the fact that one simulation has a changing rotor speed, whereas the other simulation have a fixed rotor speed.

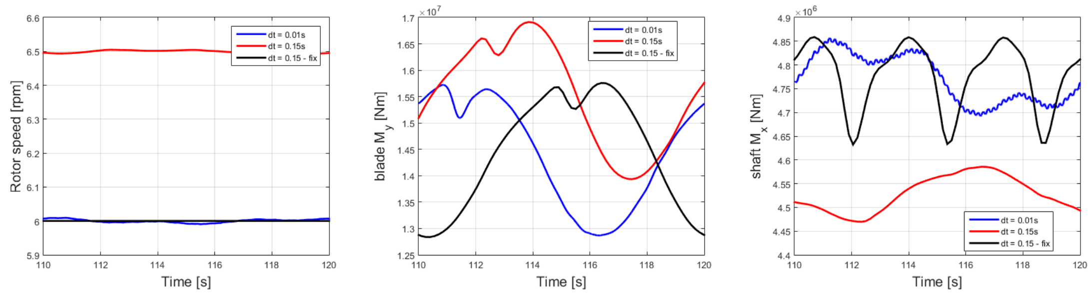

Figure B.1: *Comparison of output variables for the INNWIND turbine with different time-step settings.*

B.1.1 Wake Settings AWSM

For this test case a free wake simulation and a prescribed (hybrid) wake configuration will be used. The prescribe wake configuration is used to reduce CPU time, but still be able to accurately calculate the near wake effects.

The total wake length is set to three rotor diameters, as was found to be long enough for the solution to not significantly change anymore. The total amount of streamwise wake points is determined by the wake length, time step and average convection speed right behind the rotor speed, i.e. $U = U_\infty(1 - \overline{a})$. The amount of streamwise wake points is the same for both wake configurations of AWSM.

For the free wake configuration, the first two rotor diameters of wake length is filled with free wake points (i.e. 2/3 of the complete wake). For the remaining part of the wake, the induced velocity is constant, as is described in Fig. 4.5 (PRSCRBWAKE = 0). For the prescribed wake configuration, only the first rotor revolution of the wake is simulated by free wake points, which is about 20% of the free wake configuration. For the remaining part of the wake, the wake velocity is reduced according to BEM theory.

In Fig. B.2, the top view of the wake is shown for the two wake configurations of AWSM. It can be seen that the wake of the prescribed wake configuration is very similar to the free wake, although there is a large reduction in CPU time for the prescribed wake configuration.

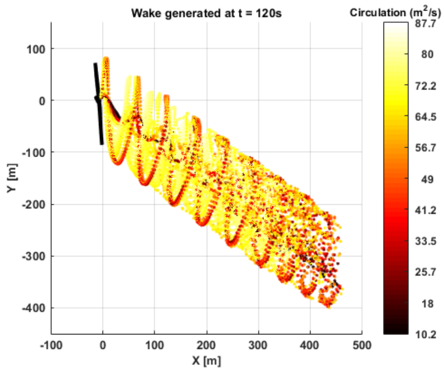

(a) *Free wake.*

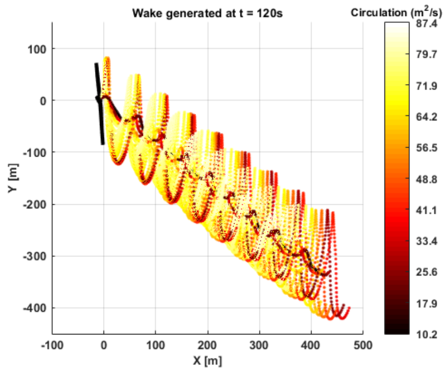

(b) *Prescribed wake.*

Figure B.2: *Top view of the wake at $t = 120s$ for the INNWIND turbine.*

B.1.2 Computational Set-up

The most important settings for the computational set-up for the yawed inflow case are already shown in Section 5.2.1. More details of the computational set-up can be found in Table B.1. Important to note is that all degrees of freedom for the blade are taken into account. Furthermore, the generator runs at constant speed and the controller and pitch actions are turned off. The dynamic stall model that is implemented for the calculations is the Snel model, first order. However, it is expected that this is only used for the root section of the blade, where the angles of attack are above stall.

Table B.1: *Overview of simulation settings for yawed inflow.*

Case	Extreme Yaw
Solver	Phatas-Aero
Subiteration settings	3 (Aerodynamic call at 1 and $\geq$ 9)
Simulation time (s)	120
Time step (s)	0.15
Blade torsion	ON
Flapping flag	ON
Lagging flag	ON
Dynamic stall	Snel (1st order)
Gearbox support	OFF
Controller	OFF
Generator model	Constant speed
Pitch flag	OFF
Shaft torsion	OFF
Pitch angles (deg)	0.0
Wind speed (m/s)	8
Wind ramp	0.3 (starts at 30%)

B.2 Comparison of the Results

In this section the results from BEM and AWSM will be compared for the INNWIND and AVATAR turbine. The BEM code has been run with two different yaw models, being the ECN and Glauert yaw model.

Firstly, some local blade parameters will be compared: local induction, angle of attack and normal and tangential force. Secondly, the loads on the blade will be assessed with a comparison of the flapwise, edgewise and torsional root bending moment, as well as the blade deformation near the tip. Then, the performance of the turbine is compared with the axial force and power produced by the rotor and finally the loads on the tower structure are compared.

For this test case, it is interesting to see how well the yaw models that are implemented in BEM are compared to the results with AWSM, where the skewed effects are taken into account intrinsically. The advancing and retreating effects due to oblique inflow is included in both models by a vector summation of the wind speed.

B.2.1 Angle of Attack

In order to compare the effects of yawed inflow, the local aerodynamic parameters are inspected as function of radial position and as function of azimuth angle at different radial position.

The angle of attack is averaged over a full revolution and plotted as function of blade radial position in Fig. B.3. The first 20 meters of the blade are disregarded, in order to enhance the differences that are found in the mid-section and tip of the blade, where the AoA does not change too much.

It can be seen that there is a very good agreement in AoA between BEM and AWSM for both turbines when the values are averaged over a full rotor revolution. For the INNWIND turbine, AWSM calculates a lower AoA in the tip region ($\approx 0.2°$ lower). For the mid-section of the blade, the differences are found to be less than $0.1°$. For the AVATAR turbine, the differences are even smaller. Again, AWSM calculates an AoA in the tip region of $\approx 0.1\%$ lower compared to BEM, except for the point closest to the blade tip.

However, it should be noted that some significant differences are observed when the AoA is plotted against radial position at a fixed azimuth position, especially at 90° and 270° azimuth positions. When averaging the results over a full revolution, these differences seem to cancel out.

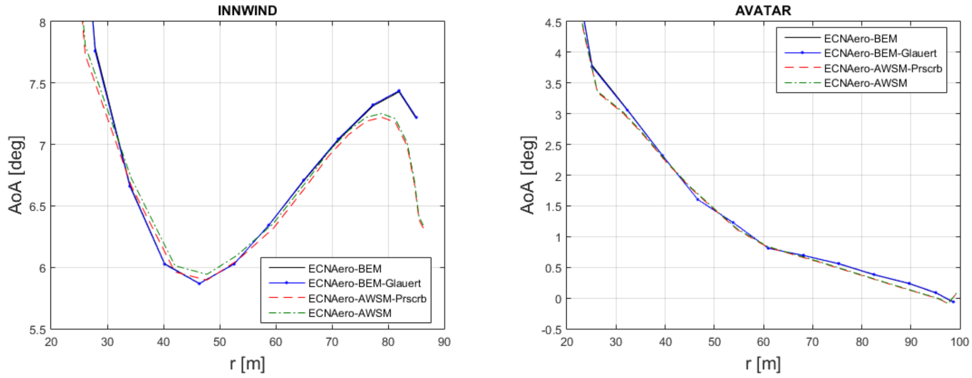

(a) *INNWIND turbine.* (b) *AVATAR turbine.*

Figure B.3: *Azimuth average AoA vs. radial position for the INNWIND and AVATAR turbine.*

In Fig. B.4, the AoA is plotted against azimuth position in the mid-section of the blade. At the mid-section of the blade, the local speed ratio is low, for which is has been found that the advancing and retreating effects are dominant over the wake skewness effects, since the lateral inflow velocity is large compared to the local rotational velocity [39]. The results match the expectations for the advancing and retreating effect, leading to a larger AoA when the blade is pointing upwards and a smaller AoA when the blade is pointing downwards.

From this figure it can be found that there is a reasonable agreement between the results of AWSM and BEM for both turbines, with a maximum difference in AoA of less than 1°. This reasonable agreement between BEM and AWSM is expected, since the advancing and retreating effects are dominant in this case and the effects are calculated intrinsically for both AWSM and BEM.

Interesting to see is that the largest differences are obtained between the two yaw models of BEM, rather than between BEM and AWSM. This indicates that the selected yaw model has a large impact on the calculation of AoA. Also, it can be observed that the differences occur at azimuth positions around 90° and 270°, indicating that the differences are most likely caused by the skewed wake effects.

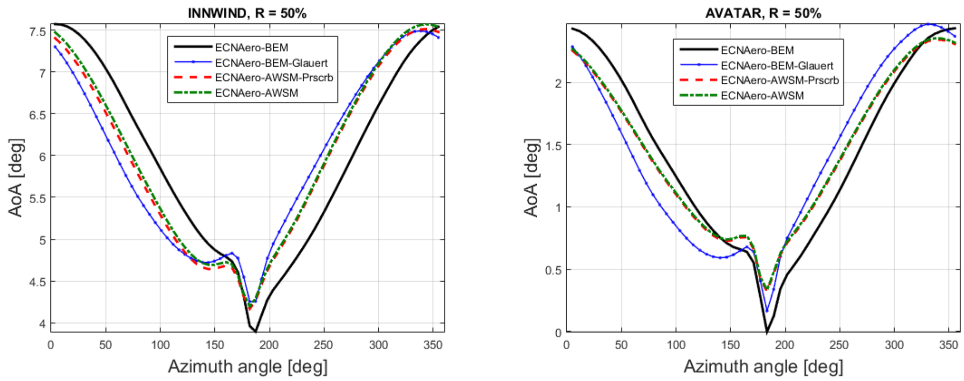

(a) *INNWIND turbine.* (b) *AVATAR turbine.*

Figure B.4: *Angle of attack vs. azimuth position at radial position of* 50% *of blade length.*

At the tip of the blade, the local speed ratio is larger, which results in a more pronounced influence of the wake skewness effect (or rather a smaller effect of advancing and retreating), which should be visible at azimuth angles around 90 and 270°. In Fig. B.5, the AoA is plotted against the azimuth angle in the tip region of the blade. As is expected, the differences become larger at 90°, whereas there seems to be a reasonable agreement at 270°. Considering that the trailed tip vortices are closer to the rotor plane in case of an azimuth position of 90°, it is not surprising that the differences between AWSM and BEM are largest at this azimuth position. It can be observed that the Glauert yaw model seems to calculate a larger effect due the skewed wake on both sides of the rotor plane, compared to ECN's yaw model.

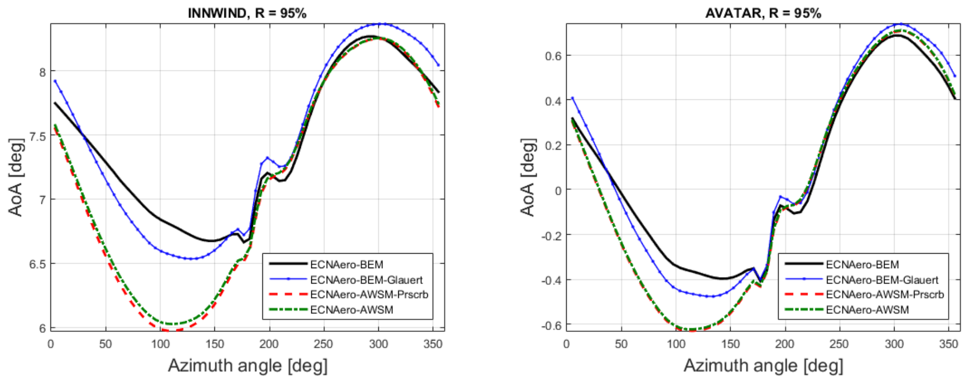

(a) *INNWIND turbine.* (b) *AVATAR turbine.*

Figure B.5: *Angle of attack vs. azimuth position at radial position of* 95% *of blade length.*

B.2.2 Axial Induction Factor

The azimuth averaged axial induction factor plotted as a function of radial position in Fig. B.6. From this figure, it can be observed that there is a very good agreement between BEM and AWSM, especially in the mid-section of the blade. The largest differences are found in the root and tip section of the blade and are expected to be due to the fact that BEM uses a engineering correction for the root and tip vortex, whereas AWSM calculates this effect intrinsically. The agreement between the free and prescribed wake as well as between the two yaw models are excellent for both turbines.

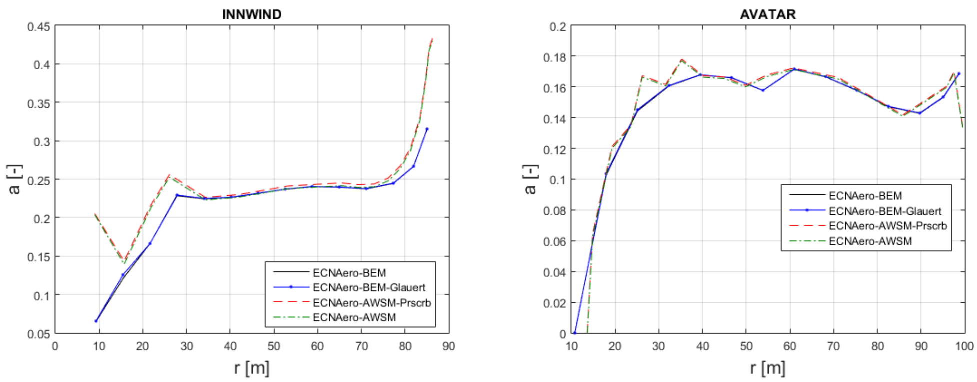

(a) *INNWIND turbine.* (b) *AVATAR turbine.*

Figure B.6: *Azimuth averaged axial induction factor vs. radial position for the INNWIND and AVATAR turbine.*

The axial induction factor is plotted as a function of azimuth position at a radial position of 25% of the blade span in Fig. B.7. Although the root section of the blade does not significantly contribute to the generation of loads, it is interesting to see how the two yaw models calculate the influence of the root vortex. The Glauert model calculates the axial induced velocity as a sinusoidal variation around an average induced velocity, where only the tip vortices are taken into account. From Fig. B.7a, it can be seen that the induction factor stays rather constant over the rotor revolution for the Glauert model, except when the blade passes the tower. The ECN yaw model seems to calculate much larger influence of the skewed wake, although this is still lower compared to the results found by AWSM. For the AVATAR turbine it is hard to make any strong statements, since the results from neither of the two yaw models seem to follow the behavior of the results found by AWSM.

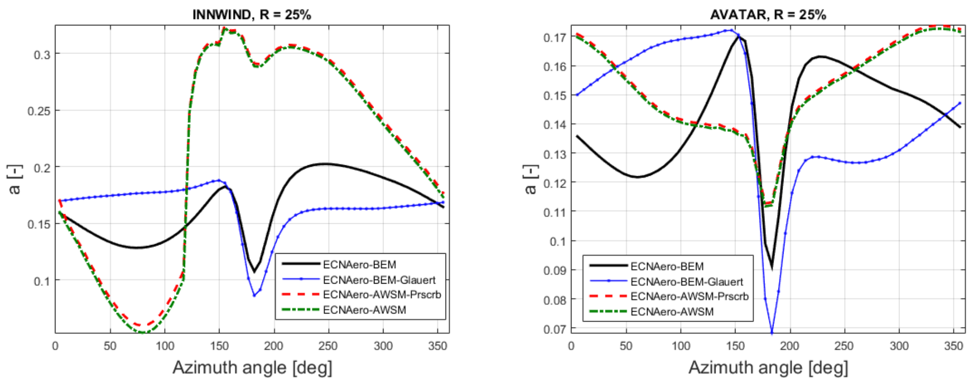

(a) *INNWIND turbine.* (b) *AVATAR turbine.*

Figure B.7: *Induction factor vs. azimuth position at radial position of* 25% *of blade length.*

The axial induction factor is plotted as a function of azimuth position at a radial position of 50% of the blade span in Fig. B.8. From this figure, large differences are found between AWSM and BEM. Most pronounced is the different shape of the induction over the azimuth positions. The largest differences are found at 90° and 270°, from which it can be assumed that the differences are caused by the different implementation of the skewed wake effects. The incoherent shape of the induction over azimuth position for the different codes can be explained by the fact that the advancing and retreating effect plays an important role in the mid-part of the blade, which also changes the induction over azimuth positions. It should be noted that the maximum difference in induction is only ≈ 0.05 for the INNWIND turbine and ≈ 0.04 for the AVATAR turbine.

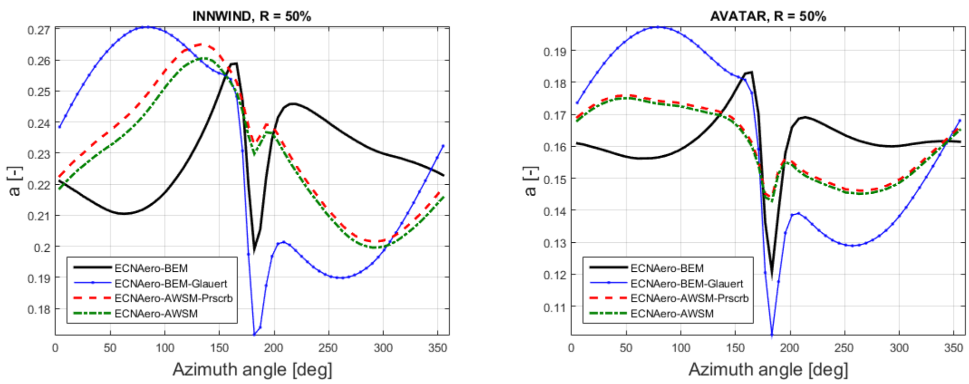

(a) *INNWIND turbine.* (b) *AVATAR turbine.*

Figure B.8: *Induction factor vs. azimuth position at radial position of* 50% *of blade length.*

In Fig. B.9, the axial induction is plotted at the tip of the blade as a function of azimuth position. It can be seen that the difference between AWSM and BEM is in order of 30% for the INNWIND turbine at the downstream part of the rotor plane ($\approx 90°$), where the trailed tip vortices of the skewed wake are closer to the rotor plane and consequently increase the induction factor in this part of the rotor plane. This difference is more than twice as big compared to the results at the mid-section of the blade. It can be observed that the Glauert model seem to capture this increase in induction in the downstream part of the rotor plane better. On the other hand, the results at the upstream part of the rotor plane ($\approx 270°$) seem to match very well. The same observations can be made for the AVATAR turbine, although the differences are found to be smaller than for the INNWIND turbine.

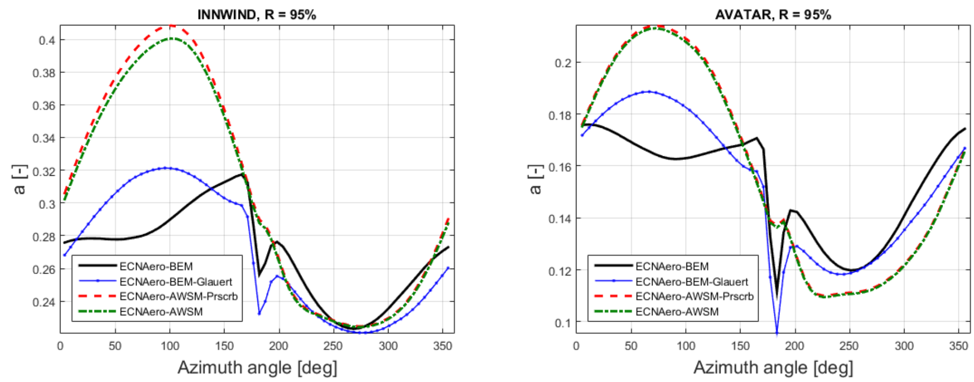

(a) *INNWIND turbine.* (b) *AVATAR turbine.*

Figure B.9: *Induction factor vs. azimuth position at radial position of* 95% *of blade length.*

B.2.3 Normal Force

The azimuth averaged normal force per unit length is shown as a function of radial position in Fig. B.10. From this figure it can be seen that there is an excellent agreement in normal force for both turbines. Small differences in the order of a few percent are observed for the AVATAR turbine in the tip region of the blade.

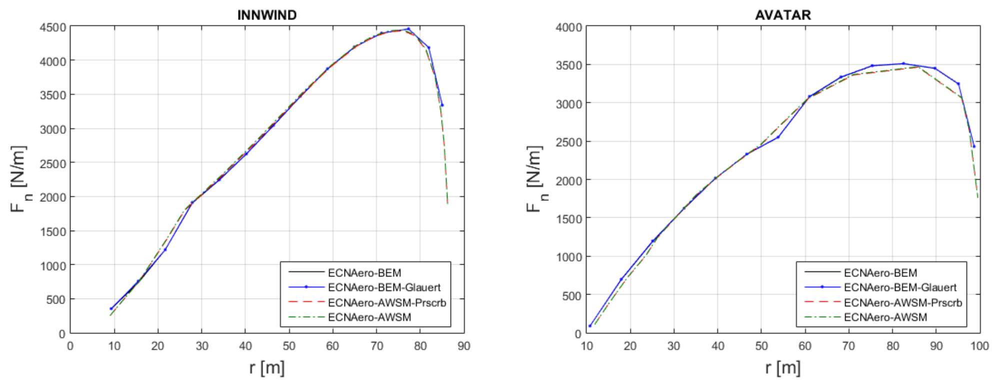

(a) *INNWIND turbine.* (b) *AVATAR turbine.*

Figure B.10: *Azimuth average normal force vs. radial position for the INNWIND and AVATAR turbine.*

In Fig. B.11, the normal force at the mid-section of the blade is plotted against azimuth angle for both turbines. Interesting to see is that there is a large difference between the variation of the normal force over a full revolution between the INNWIND and AVATAR turbine, which could be explained by the fact that the AVATAR turbine operates at much lower AoA and that the AoA changes less during a rotor revolution, resulting in a different behavior of the normal force.

When comparing the differences between the two yaw models of BEM, it can be seen that the ECN yaw model calculates a larger normal force in the downstream part of the rotor plane and a lower normal force in the downstream part of the rotor plane compared to the results from AWSM, whereas the opposite is true for the Glauert model. This observation can be made for both turbines.

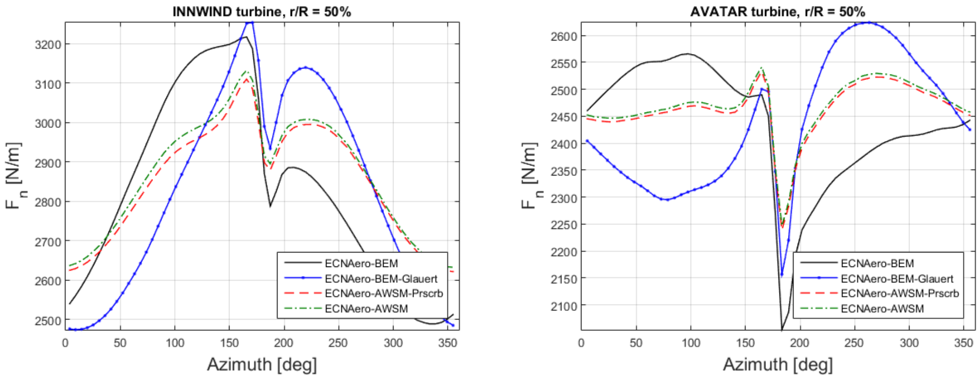

(a) *INNWIND turbine.* (b) *AVATAR turbine.*

Figure B.11: *Normal force vs. azimuth position at radial position of* 50% *of blade length.*

In Fig. B.12, the normal force at the tip of the blade is plotted as a function of azimuth angle for both turbines. As was found from the analysis of the AoA and axial induction, the differences between AWSM and BEM are mainly found in the first half of the revolution (i.e. azimuth angle: $0° - 180°$.) As can be seen in the figure, the same is true when comparing the results for the normal force.

When looking at the results for the AVATAR turbine in Fig. B.12b, it can be observed that the BEM codes calculate a larger normal force in the downstream part of the rotor plane compared to AWSM. For the upstream part of the rotor plane, the agreement between the codes seems to be much better. When comparing the two yaw models, it can be observed that ECN's model calculates a larger normal force for the downstream part of the rotor plane, whereas the opposite is true for the upstream part of the rotor plane.

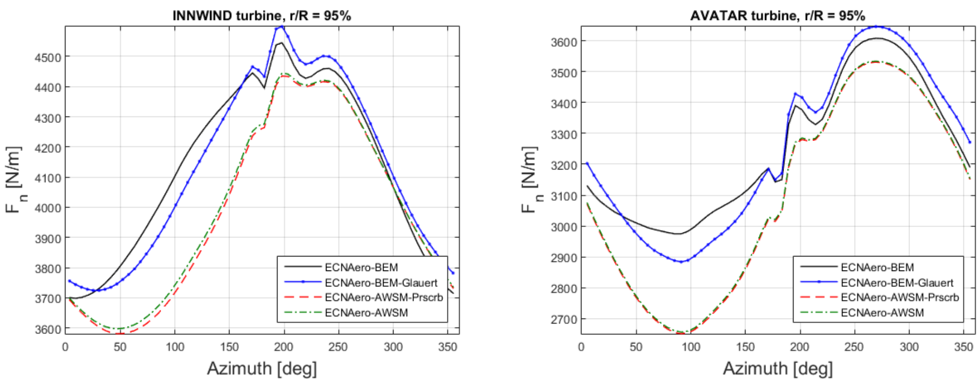

(a) *INNWIND turbine.* (b) *AVATAR turbine.*

Figure B.12: *Normal force vs. azimuth position at radial position of* 95% *of blade length.*

B.2.4 Tangential Force

In Fig. B.13, the azimuth averaged tangential force is plotted against the radial position. Similar to the comparison of the normal force, an excellent agreement has been found between the different codes, especially in the mid-section of the blade.

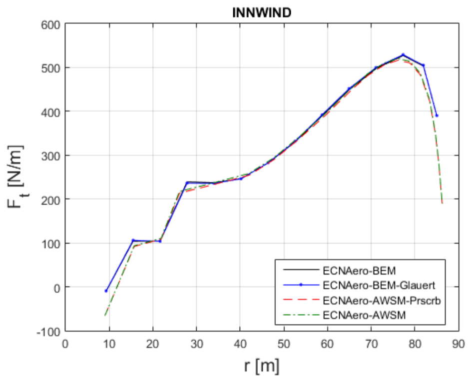

(a) *INNWIND turbine.*

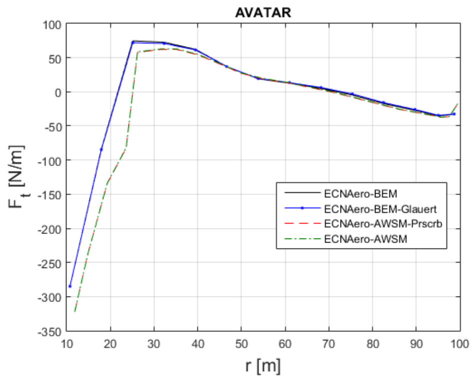

(b) *AVATAR turbine.*

Figure B.13: *Azimuth average tangential force vs. radial position for the INNWIND and AVATAR turbine.*

When analyzing the tangential force at the mid-section of the blade over a rotor revolution, it can be observed that the advancing and retreating effects are dominant. This results in the fact that the tangential force is about twice as high for the INNWIND turbine in case the blade is pointing upwards (advancing), compared to when it is pointing downwards (retreating). For the AVATAR turbine, this effect even means that the tangential force becomes negative in case the blade is pointing downwards. In this case, the torque of the rotor will be produced by the normal force, which has a component in the rotor plane due to the twist angle and AoA.

When comparing the results of the two yaw models, it can be observed that the yaw model of ECN estimates a larger tangential force in the downstream part of the rotor plane and a smaller tangential force in the upstream part of the rotor plane compared to the results from the Glauert yaw model. The results from AWSM are in between the results of the two yaw models.

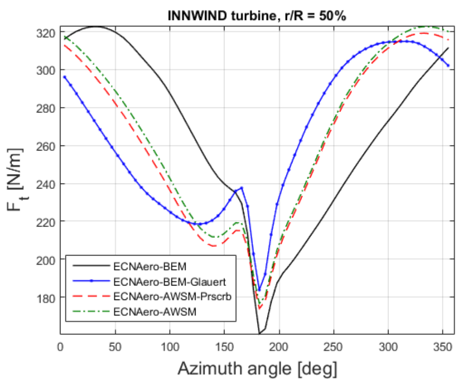

(a) *INNWIND turbine.*

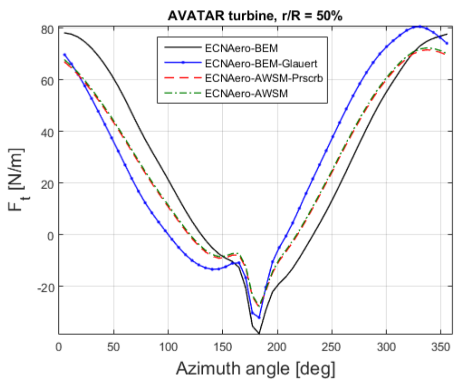

(b) *AVATAR turbine.*

Figure B.14: *Tangential force vs. azimuth position at radial position of* 50% *of blade length.*

When comparing the tangential force at the tip of the blade (Fig. B.15), it can be found that the skewed wake effects become more important, especially in the downstream part of the rotor plane for the INNWIND turbine. The differences between AWSM and BEM are found to be a lot smaller for the AVATAR turbine, which is expected since the blade operates at a low AoA, at which the tangential force is mainly influenced by the drag force, which is found to be rather constant at low AoA.

Again, it seems that the Glauert yaw model seems to capture the decrease in tangential force due the skewed wake better than ECN's yaw model for the downstream part of the rotor plane.

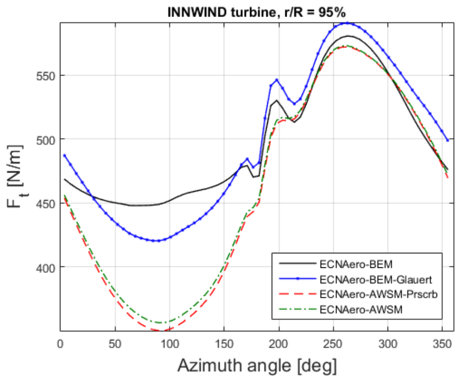

(a) *INNWIND turbine.*

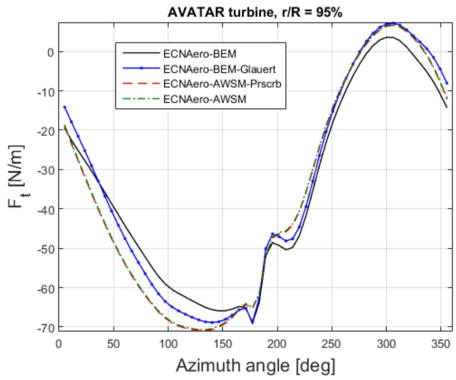

(b) *AVATAR turbine.*

Figure B.15: *Tangential force vs. azimuth position at radial position of* 95% *of blade length.*

B.2.5 Blade Root Bending Moment

In order to see how the differences that were found on a blade sectional level affect the total loads on the blades; the flapwise, edgewise and torsional blade root bending moment are compared in this section.

In Fig. B.16, M_x is shown for both turbines. An excellent agreement is found between the codes for both turbines. When looking carefully, it can be observed that BEM calculates a slightly larger amplitude ($\approx 1-2\%$), whereas the mean value seems to be spot on. This can be explained by the fact that the M_x is mainly determined by the gravity loading.

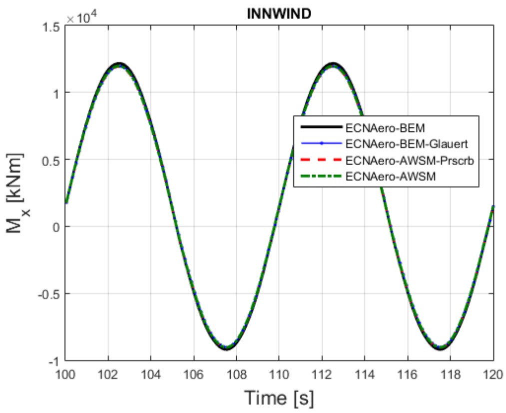

(a) *INNWIND turbine.*

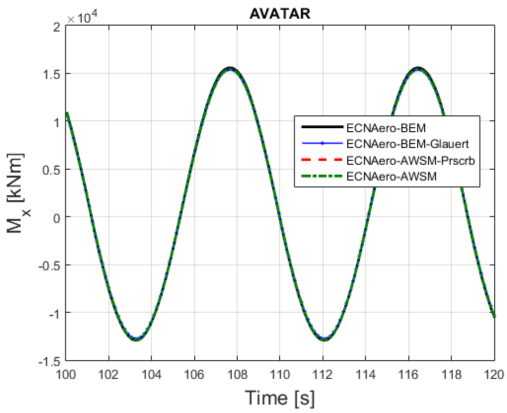

(b) *AVATAR turbine.*

Figure B.16: *Edgewise blade root bending moment as a function of time.*

In Fig. B.17, the M_y is compared for both turbines as function of time. The sudden dip observed in the plots occurs at the point where the blade passes the tower. Overall, an excellent agreement is observed between the two wake configurations of AWSM for both turbines. Furthermore, it can be observed that the mean value of M_y agrees well between all codes for both turbines.

For the INNWIND turbine, it seems that AWSM calculates a lower fluctuation in loads and the Glauert model seems to calculate the highest fluctuations in loads.When looking at the AVATAR turbine, it can be observed that again the Glauert model calculates the largest load fluctuations. However, this time the yaw model of ECN calculates the lowest amount of fluctuations. This result could have a large influence on the fatigue loads.

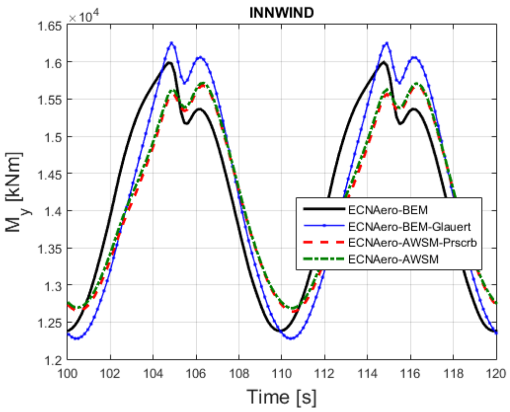

(a) *INNWIND turbine.* (b) *AVATAR turbine.*

Figure B.17: *Flapwise blade root bending moment as a function of time.*

In Fig. B.18, M_z is shown for both turbines. For M_z similar results have been obtained as for M_x. A good agreement has been found between the codes for both turbines. Again, it can be seen that BEM calculates a slightly larger amplitude, whereas the mean value seems to agree very well.

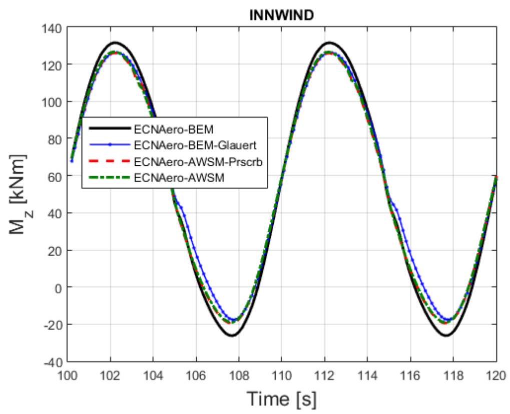

(a) *INNWIND turbine.* (b) *AVATAR turbine.*

Figure B.18: *Torsional blade root bending moment as a function of time.*

Power Spectral Density In order to further investigate the differences that were found for M_y, the power spectral density (PSD) is analyzed for both turbines. The PSD is obtained from an FFT of the time-series of M_y for the last $50s$ of the simulation in order to get enough samples. For this comparison, also the results from the BEM code with a time-step of $\Delta t = 0.01s$ are shown. With the results from the BEM code with a small time-step the effect of the relatively large time-step used in the other simulation can be determined. This simulation is done with the yaw model of ECN.

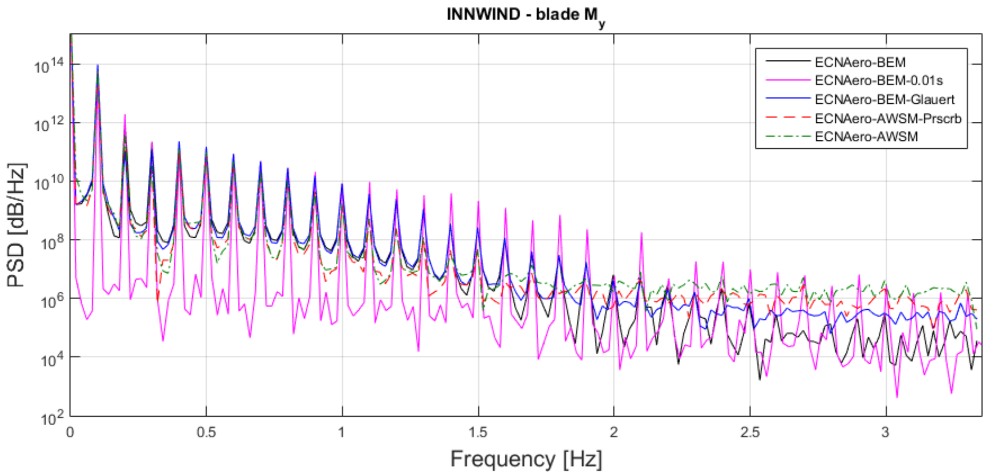

(a) *INNWIND turbine.*

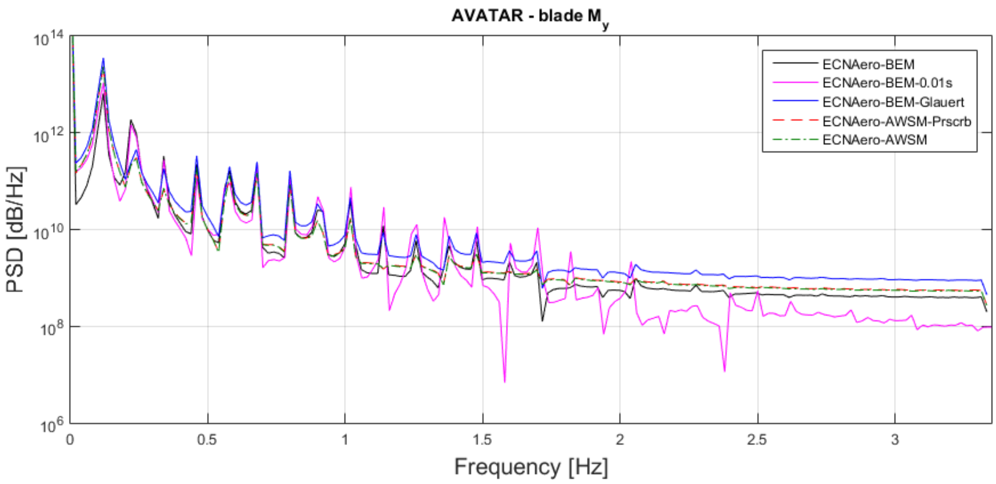

(b) *AVATAR turbine.*

Figure B.19: *Power spectrum density for the blade M_y for the INNWIND and AVATAR turbine.*

In Fig. B.19a, the results are shown for the INNWIND turbine. It can be seen that the results for the low frequencies match reasonably well. The influence of the excitation of 1P, 2P etc. can be identified very well. This is expected to be the case, since the rotor speed does not change during the simulation and the excited frequencies are therefore constant. For frequencies below $f = 1.5Hz$, it can be seen that AWSM usually calculates a lower energy, whereas for higher frequencies AWSM tends to calculate a higher energy and the differences between BEM and AWSM become larger. It can be observed that the results for the Glauert yaw model match better with the results obtained by AWSM.

When comparing the results for the BEM code with the varying time step (ECN yaw model), it can be seen that the simulation with the small time has lower energy for the frequencies that are plotted ($0 \leq f \leq 3.33Hz$). This is the case, since the largest frequencies that can be obtained from an FFT are $f = 1/(2\Delta t)$, which is equal to $f = 3.33Hz$ for the simulation with a time step of $0.15s$. For the case with a small time-step, the maximum frequency is $50Hz$ and the energy is also stored in the higher frequencies. For the frequencies that are multiple of the rotor frequency, it can be seen that the calculated energy matches very well between the simulations with the different time-steps. Also, the energy at the higher frequencies match reasonably well, from which is can be concluded that the simplification of increasing the time-step does not significantly influence the spectrum of the blade loads.

In Fig. B.19b, the PSD of M_y is shown for the AVATAR turbine. From this figure, it can be seen that there is a much better agreement between AWSM and BEM, also compared to the simulation with a smaller time step. It is expected that this is because the AVATAR turbine operates at a low angle of attack, which means that there is no significant influence due to steady and dynamic stall effects and the calculation becomes better predictable.

B.2.6 Blade Tip Deflection

In this section the flapwise blade deformation is discussed. In Fig. B.20, the flapwise blade deformation (δ_x) near the tip (95% blade span) is shown as function of time. It can be found that the results for δ_x are very similar to the results of the flapwise blade moment, as shown in Fig. B.17. Again, a very good agreement has been obtained in terms of mean value between all codes for both turbines.

For the INNWIND turbine, it is found that the fluctuation in flapwise blade deflection are largest for the BEM codes, where the maximum tip deflection is about 15% larger when calculated with the Glauert yaw model. Similar as to the results from the blade M_y, the fluctuations with ECN's yaw model are the smallest for the AVATAR turbine, whereas the Glauert model calculates the largest tip deflections.

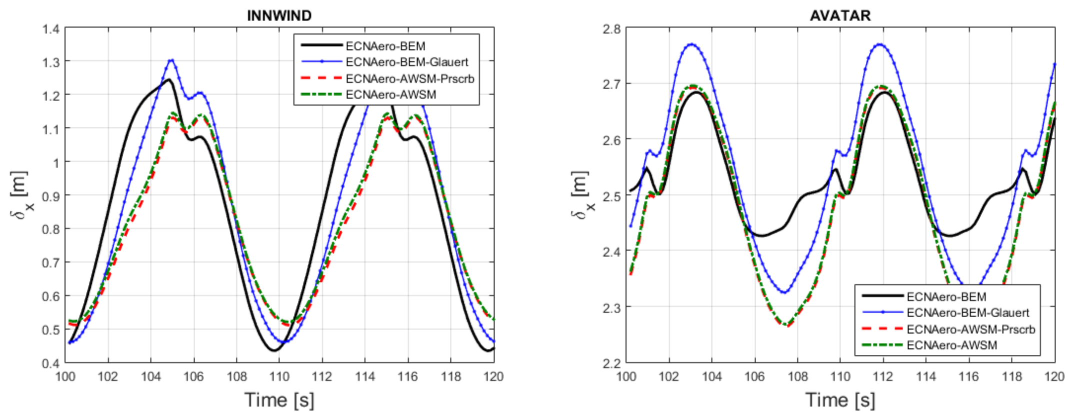

(a) *INNWIND turbine.* (b) *AVATAR turbine.*

Figure B.20: *Blade tip deflection as a function of time for the INNWIND and AVATAR turbine.*

B.2.7 Axial Force

In this section the axial force produced by the complete rotor is analyzed. In Fig. B.21, F_{ax} is shown as function of time for the last $10s$ of the simulation for both turbines. It can be seen that the axial force of the INNWIND turbine is larger, even though the rotor area for this turbine is smaller, which is the results of the higher induction at which this turbine operates.

From Fig. B.21a, it can be seen that there is a good agreement between BEM and AWSM for the INNWIND turbine in terms of mean axial force, whereas BEM calculates slightly higher oscillations. The agreement between the two yaw models is found to be very good, as well as the agreement with the free wake configuration of AWSM. It is found that the prescribed wake configuration estimates a slightly lower F_{ax}, whereas the shape is very similar to the results of the free wake simulation.

When looking at the results for the AVATAR turbine, larger differences are observed between BEM and AWSM. BEM seems to calculate both a higher mean and a higher fluctuation over time. The results between the two wake configurations of AWSM agree very well, as well as the results between the two yaw models in the BEM code.

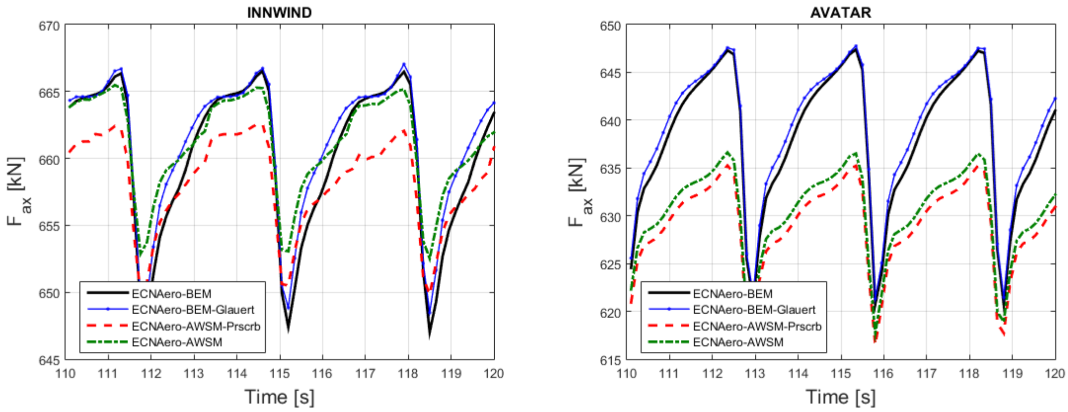

(a) *INNWIND turbine.* (b) *AVATAR turbine.*

Figure B.21: *Axial force as a function of time for the INNWIND and AVATAR turbine.*

B.2.8 Power

The second global parameter that is compared is the aerodynamic power produced by the turbine. In Fig. B.22, the power is shown as a function of time for both turbines.

For the INNWIND turbine, a very good agreement is found between the two yaw models in the BEM code. It can be seen that AWSM calculates a lower power, especially with the prescribed wake configuration. However, the maximum differences are only in the order of $2-3\%$.

Similar to the results for the axial force, the differences between BEM and AWSM are largest for the AVATAR turbine, whereas the differences between the two wake configurations are smaller for this turbine. The maximum differences in power are in the order of 4%. The results of the two yaw models has been found to agree well.

B.2.9 Tower Loads

As a final comparison, the loads on the tower are evaluated. In this section the side-side (M_x), fore-aft (M_y) and torsional (M_z) tower bottom moment has been analyzed.

In Fig. B.23, M_x is shown as function of time for both turbines. For the INNWIND turbine, it can be observed that the results do not show a perfectly cyclic behavior. It is found that the Glauert model calculates a significantly lower moment, compared to the other results. The agreement between the BEM code with ECN's yaw model and AWSM is found to be very good. For the AVATAR turbine, the results from the BEM code with Glauert's yaw model agree better with the results from AWSM, where ECN's yaw model calculates a higher moment.

In Fig. B.24, M_y is shown as a function of time for both turbines. When looking at the results for the INNWIND turbine, it can be seen that AWSM seems to calculate a slightly higher M_y compared to BEM, whereas the amplitude of the fluctuations seems to match very well. Interesting

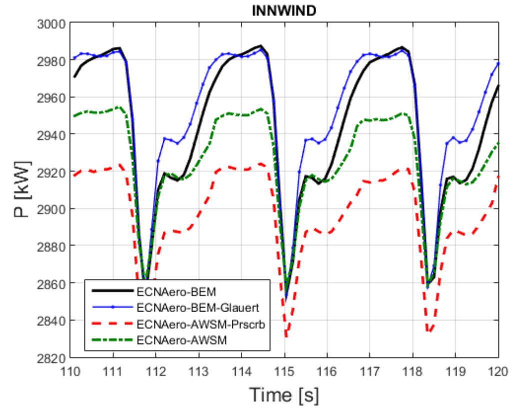

(a) *INNWIND turbine.*

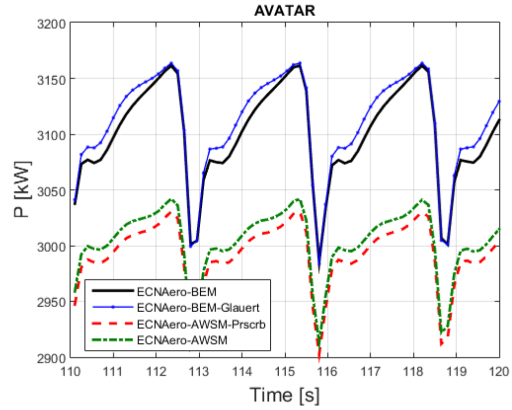

(b) *AVATAR turbine.*

Figure B.22: *Power as a function of time for the INNWIND and AVATAR turbine.*

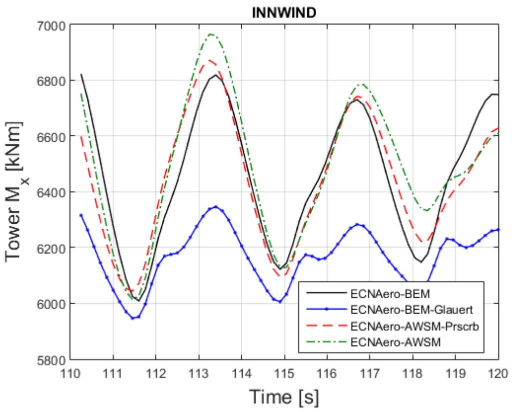

(a) *INNWIND turbine.*

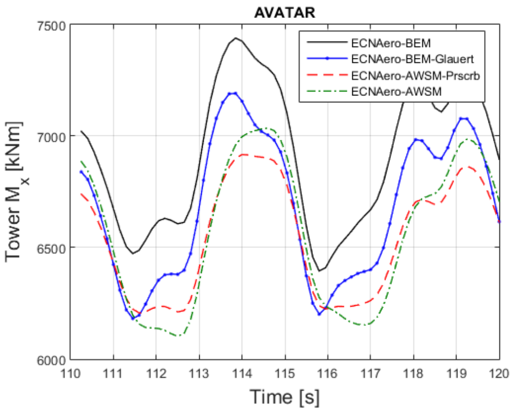

(b) *INNWIND turbine.*

Figure B.23: *Tower side-side moment as a function of time for the INNWIND and AVATAR turbine.*

to observe is that the BEM code with the Glauert model calculates the largest loads when the blade passes the tower, whereas the other codes calculate the maximum load about $1s$ later. For the AVATAR turbine, BEM calculates a larger M_y compared to AWSM. Furthermore, it can be observed that BEM code with ECN's yaw model calculates a larger amplitude of the fluctuation compared to the other three considered simulations. The agreement between the two wake configurations of AWSM has found to be good.

The last tower load that is considered is the torsional moment, M_z, which is plotted against time in Fig. B.25. Interesting to see from this figure is that for the INNWIND turbine the results from the BEM code with ECN's yaw model are very different from the other results. Furthermore, the results from the Glauert model are surprisingly close to the results from both wake configurations of AWSM. For the AVATAR turbine, the same observations can be made, although the results from the Glauert model seem to be lower than for AWSM. The results should be further investigated in order to see where the differences in tower M_x and M_z come from.

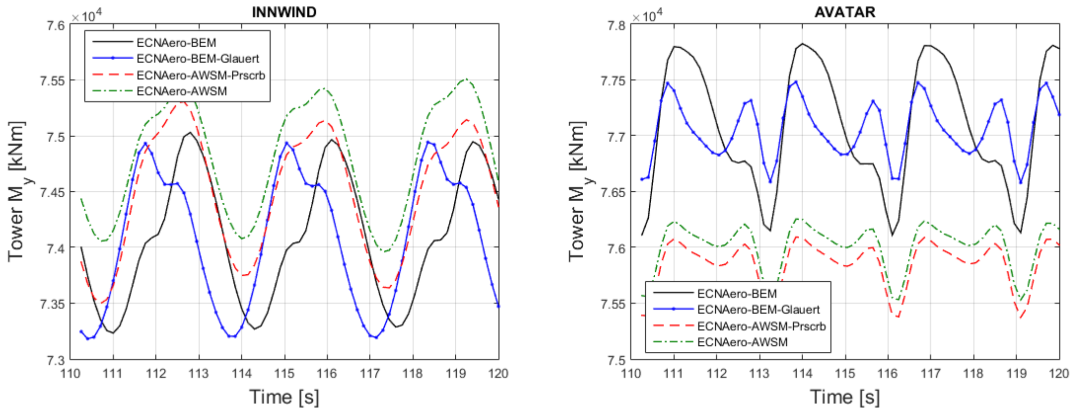

(a) *INNWIND turbine.* (b) *INNWIND turbine.*

Figure B.24: *Tower fore-aft moment as a function of time for the INNWIND and AVATAR turbine.*

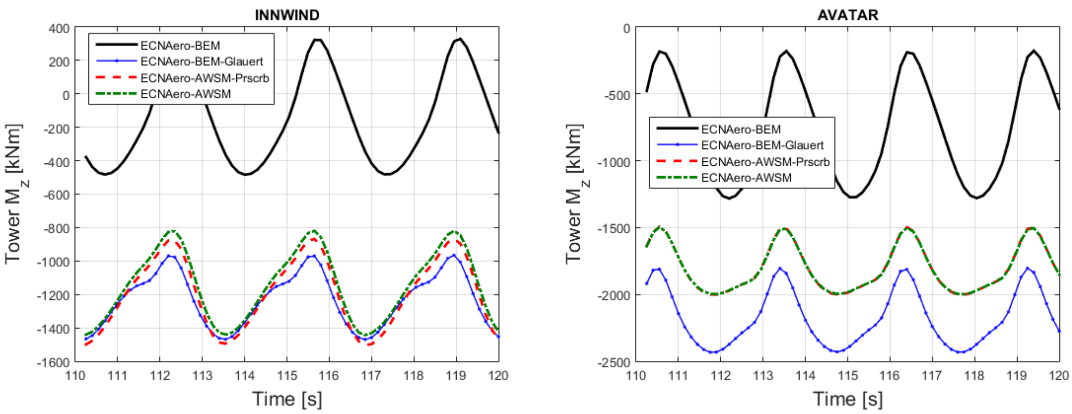

(a) *AVATAR turbine.* (b) *AVATAR turbine.*

Figure B.25: *Tower torsional moment as a function of time for the INNWIND and AVATAR turbine.*

Appendix C

Half Wake

C.1 Case Set-Up

Similar to the test cases of axial and yawed inflow, a time step of $\Delta t = 0.15s$ is used in order to keep the CPU time of AWSM limited. Since the BEM simulations for the half wake case have already been completed for the AVATAR project deliverable, the operational conditions from this test case have been used for the simulation of AWSM as well. This means that the rotor speed is kept constant at 5.75 rpm and the pitch angle is kept constant at $0°$.

C.1.1 Wake Settings AWSM

For this test case, a prescribed (hybrid) and a free wake configuration have been used for the simulations with AWSM. The total wake length is set to three rotor diameters, as was found to be long enough for the solution to not significantly change anymore. This has been done by using calculating the points required for a wake length of 3 rotor diameters for the part of the rotor that is not in the wake and add 25% wake points to compensate for the lower wake velocity at the part of the rotor plane that is in the wake. The total amount of streamwise wake points is determined by the wake length, time step and average convection speed right behind the rotor speed, i.e. $U = U_\infty(1 - \overline{a})$. The amount of streamwise wake points is the same for both wake configurations of AWSM.

For the free wake configuration, the first two rotor diameters of wake length is filled with free wake points (i.e. 2/3 of the complete wake). For the remaining part of the wake, the induced velocity is constant, as is described in Fig. 4.5 (PRSCRBWAKE = 0).

For the prescribed wake configuration, usually only the first rotor revolution of the wake is simulated by free wake points, which is about 20% of the free wake configuration. For the remaining part of the wake, the induced velocity is reduced according to BEM theory. However, it was found that there are significant differences between the prescribed and free wake configuration if only one rotor revolution of free wake points is used (i.e. 70 points), which results in large differences in induced velocity. Therefore, additional simulations have been run with a varying amount of free wake points for the prescribed wake configuration of AWSM. Simulations have been run with 0, 1, 2, 3 and 5 rotor revolutions of free wake points and the results have been compared. An overview of the settings and the CPU time of simulations is shown in Table C.1. It can be seen that increasing the amount of free wake points is the main contributor to the CPU time.

Table C.1: Overview of wake settings for the half wake case.

Wake prescription	n_{total}	n_{free}	CPU time [hr]
Yes (option 1)	778	0	1.14
Yes	778	70	39.87
Yes	778	140	69.32
Yes	778	210	86.18
Yes	778	350	162.60
No (option 0)	778	415	213.18

It has been found that adding free wake points to the prescribed wake configuration, reduced the differences in wake geometry between the prescribed and free wake configuration of AWSM. Besides the wake geometry, also some output parameters are compared from the simulation with varying free wake points. In Table C.2, the results for the blade M_y are shown. The data is presented as an absolute and relative difference to the results from the free wake configuration, for both the mean and standard deviation of M_y. It can be seen that especially the standard deviation of M_y changes a lot with adding more free wake points. From this comparison, it is concluded that 210 free wake points (3 rotor revolutions) is a good trade-off in terms of reducing CPU time and remaining accuracy.

Table C.2: Overview of the results for blade M_y between BEM and various wake options for AWSM.

	$\overline{M_y}$ [$\cdot 10^4 kNm$]	$\Delta\overline{M_y}$ [%]	σ_{M_y} [$\cdot 10^3 kNm$]	$\Delta\sigma_{M_y}$ [%]
BEM	1.1869	-4.51	2.6309	+32.93
AWSM-prscrb-0rev	1.2116	-2.53	2.2305	+12.70
AWSM-prscrb-1rev	1.1935	-3.98	2.1152	+6.87
AWSM-prscrb-2rev	1.2059	-2.99	2.0230	+2.22
AWSM-prscrb-3rev	1.2134	-2.39	1.9764	-0.14
AWSM-prscrb-5rev	1.2367	-0.51	1.9706	-0.43
AWSM-free	1.2431		1.9792	

In Fig. C.1, the first rotor revolution of wake points is plotted for the free wake and the prescribed wake with 1 and 3 rotor revolutions of free wake points respectively. From this figure, it can be seen that in the part of the rotor plane that is in the wake (upper part in the figure), the wake points are scattered, indicating a difference in induced velocity. It should be considered that for the first rotor revolution of wake points, the induced velocity is calculated by the influence of each wake point, indicating that the scatter in wake point positions is caused by the wake points more than one rotor revolution away from the rotor. When comparing the results from the prescribed wake with 210 free wake points, the wake geometry matches much better with the free wake configuration. The results in this report will be presented for the prescribed wake configuration with both 70 and 210 free wake points.

In Fig. C.2, the complete wake of the prescribed and free wake configuration of AWSM is shown. From this figure it can be seen that the part of the rotor plane that is in the wake (top part in the figure), creates much lower vorticity, as is expected due to the lower wind speed. It can also be seen that there are significant differences in the wake geometry. Interesting to see is that the wake is skewed due to the imbalance of the incoming wind speed and that the prescribed and free wake configuration calculate a different direction in which the wake is skewed. It is found that these differences decrease rapidly when the amount of free wake points is increased for the prescribed wake configuration.

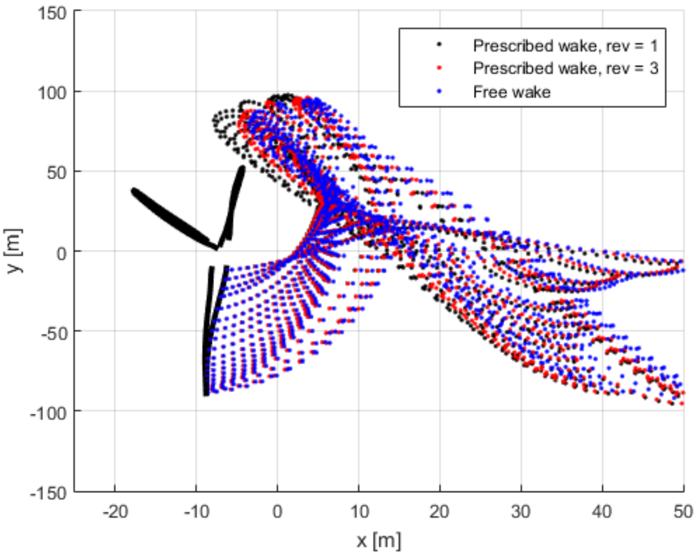

Figure C.1: *Comparison of the wake for various wake configurations.*

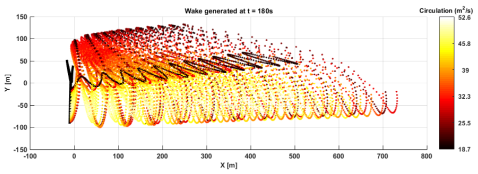

(a) *Prescribed wake,* $n_{free} = 70$.

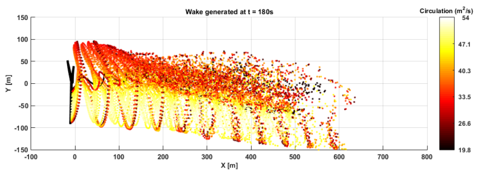

(b) *Free wake,* $n_{free} = 415$.

Figure C.2: *Top view of the wake for the INNWIND turbine in half wake*

C.1.2 Computational Set-up

Most of the important settings for this test case are presented in Section 5.3.1 More details of the computational set-up can be found in Table C.3. Important to note is that all degrees of freedom for the blade are taken into account. Furthermore, the generator runs at constant speed and the controller and pitch actions are turned off. The dynamic stall model that is implemented for the calculations is the Snel model, first order. However, it is expected that this is only used for the root section of the blade, where the angles of attack are above stall.

Table C.3: Overview of simulation settings for the half wake case.

Case	Half Wake
Solver	Phatas-Aero
Subiteration settings	3 (Aerodynamic call at 1 and ≥ 9)
Simulation time (s)	180
Time step (s)	0.15
Blade torsion	ON
Flapping flag	ON
Lagging flag	ON
Dynamic stall	Snel (1st order)
Gearbox support	OFF
Controller	OFF
Generator model	Constant speed
Pitch flag	OFF
Shaft torsion	OFF
Pitch angles (deg)	0.0
Wind speed (m/s)	8
Wind File	Provided

C.2 Comparison of the Results

In this section the results for the half wake case are discussed. For this test case, the most interesting part is to compare the blade aerodynamics when the blade is in the wake compared to when the blade is not in the wake. This will be done by comparing the axial induced velocity, angle of attack and normal and tangential force as function of radial position and as function of azimuth angle at fixed radial locations. Furthermore, the blade loads and tip deflection will be compared. Finally, also the influence on the axial force, power and tower loads will be assessed.

The results will be presented for BEM and AWSM. For the vortex wake code, three different wake configurations are compared, being the prescribed wake with one and three rotor revolution of free wake points, as well as the free wake configuration.

C.2.1 Axial Induced Velocity

The axial induced velocity is expected to change significantly depending if it is in the wake or not. This changing induction over the blade azimuth positions is expected to cause differences between the various codes that have been used. In this section the azimuth averaged $u_{i,ax}$ is analyzed as function of radial position, as well as the induced velocity as function of azimuth position at fixed radial positions.

In Fig. C.3, $u_{i,ax}$ is averaged over a full revolution and plotted against the radial position of the blade. From this figure it can be seen that BEM calculates a larger average $u_{i,ax}$ in the mid-section of the blade, whereas the opposite is true in the tip of the blade. The largest differences are found between BEM and the free wake configuration of AWSM, with differences up to 25% in the mid-section of the blade, which is high considering that the values are already averaged. Furthermore, significant differences are found between the various wake configurations of AWSM, where the free wake configuration calculates the lowest $u_{i,ax}$.

In Fig. C.4, the axial induced velocity is plotted against azimuth angle for the radial positions of $50, 70$ and 95% of the blade span. From the results at $r/R = 50$ and 70%, it can be seen that BEM calculates a rather constant $u_{i,ax}$ over the rotor revolution, whereas AWSM calculates very high fluctuations, with an induction of $\approx 40\%$ when the blade is in the wake compared to when

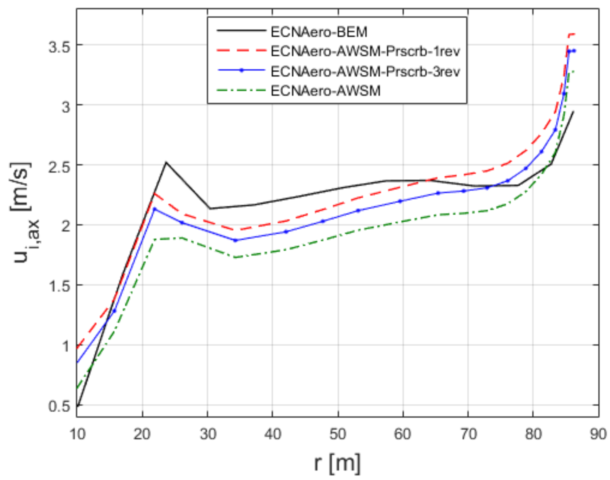

Figure C.3: *Azimuth averaged axial induced velocity vs. radial position.*

the blade is not in the wake. For the three wake configurations of AWSM a good agreement is found in terms of amplitude, although the mean $u_{i,ax}$ seems to decrease when more free wake points are shed in the wake. Near the tip of the blade, at $r/R = 95\%$, large differences have been found between the codes. It can be observed that the lowest induction is observed when the blade is in the wake, i.e. around 270°, as expected. The differences in induction between the wake configurations of AWSM are expected to be due to the large difference in wake geometry, where the wake vortex points in the wake are further from the rotor plane when the amount of free wake points are increased.

C.2.2 Angle of Attack

In this section the angle of attack (AoA) at various radial stations is analyzed. In Fig. C.5, the AoA is averaged of a full revolution and plotted against blade radial position. From this figure it can be observed that BEM calculates a lower AoA compared to AWSM. The difference between BEM and AWSM is $\approx 1°$ for the mid-section of the blade, whereas the agreement seems to be better near the tip of the blade. When comparing the results to the axial induced velocity, it can be observed that the codes that calculate a higher induced velocity calculate a lower AoA and vice versa.

In Fig. C.6, the AoA is shown as function of azimuth angle at three different radial positions along the blade. Compared to the results of $u_{i,ax}$, a much better agreement is found between the codes for the AoA. When looking at the results at $r/R = 50\%$, it can be observed that BEM calculates a larger amplitude in the variation of AoA. This is mainly caused by the fact that BEM calculates a much lower AoA when the blade is in the wake $(2 - 3°$ lower). The agreement is much better when the blade is not in the wake, although there are still significant differences observed between the models. At $r/R = 70\%$, the same observations can be made, although it should be noted that the differences between BEM and AWSM are decreased in the whole range of azimuth positions. Finally, the results near the tip at $r/R = 95\%$ are compared. It can be seen that there is a much better agreement between the codes, especially when the blade is in the wake. However, the same observations can be made near the tip of the blade, where BEM calculates a higher variation in AoA and lower AoA when the blade is in the wake.

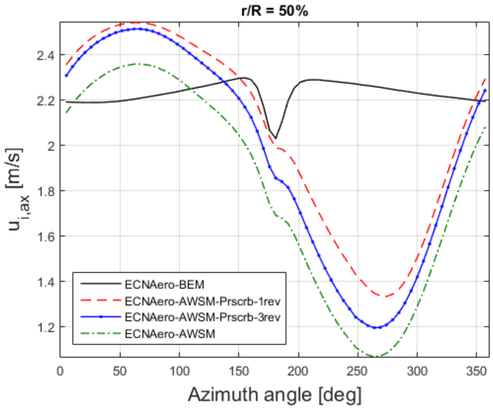

(a) $r/R = 50\%$.

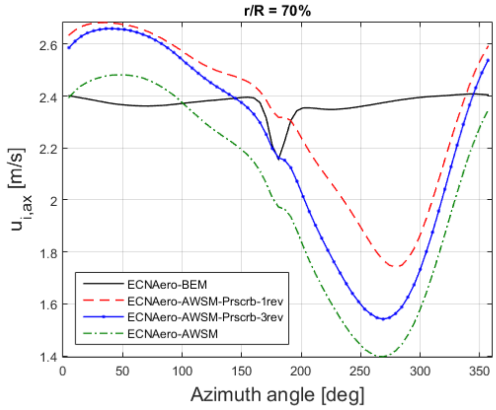

(b) $r/R = 70\%$.

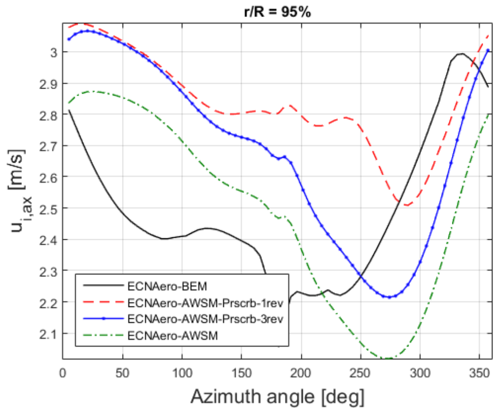

(c) $r/R = 95\%$.

Figure C.4: *Axial induced velocity vs. azimuth angle at different radial positions.*

C.2.3 Normal Force

In Fig. C.7, the azimuth averaged normal force is shown as function of radial position. From the figure, it can be seen that AWSM calculates a larger normal force, as was also observed in the uniform inflow and extreme yaw test case. It can be seen that the normal force distribution follows the trend of the angle of attack, where BEM calculates the lowest value and for AWSM the normal force is increased when the amount of free wake points is increased. At the tip of the blade the difference in AoA was found to be $\approx 0.5°$. However, for the normal force the difference at the tip of the blade is found to be almost a factor of 2, which is expected to be due to the fact that BEM uses the Prandtl correction to model the tip vortex, whereas AWSM models this effect intrinsically. However, it should be noted that this large difference is only observed in a very small section of the blade and it is therefore expected that this would not drastically affect the results.

In Fig. C.8, the normal force is plotted against azimuth angle for three radial positions. From this figure it can be observed that there is a fair agreement between the three wake configurations of AWSM. The fluctuations over a rotor revolution are similar, although it can be observed that the free wake configuration calculates a slightly higher normal force over the complete rotor revolution at all considered radial positions.

In Fig. C.8a, the results are shown at $r/R = 50\%$. From this figure, it can be seen that there is a fair agreement when the blade is not in the wake. It can also be observed that BEM calculates a lower normal force when the blade is in the wake. The differences with the free wake configuration

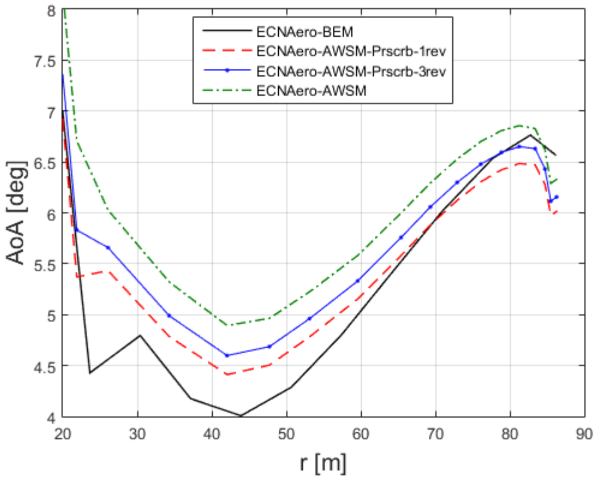

Figure C.5: *Azimuth averaged angle of attack vs. radial position.*

is a factor of 2 at an azimuth angle of 270°, which is when the blade is fully in the wake in horizontal position.

At a radial position of $r/R = 70\%$, it can be observed that the relative differences between BEM and AWSM become smaller, although the absolute differences are still similar. Again, the agreement for the first half rotor revolution is reasonable.

Near the tip of the blade, at $r/R = 95\%$, a different observation can be made. It can be seen that now the largest differences occur when the blade is not in the wake, where BEM calculates a larger normal force. For the azimuth angles when the blade is in the wake, there is a fair agreement found between the codes. However, this could also be caused by the fact that the mean normal force is increased more near the tip for BEM than for AWSM, which was also found in Fig. C.8. In general, it can be concluded that BEM calculates a larger amplitude of the variation over the rotor revolution and that the largest differences are found in the mid-section of the blade.

C.2.4 Tangential Force

In Fig. C.9, the azimuth averaged tangential force can be found as function of radial position. The results from the tangential force agree very well with the results from the normal force. It can be seen that BEM calculates a lower tangential force of the mid-section of the blade and is increasing more rapidly towards the tip of the blade compared to the results from AWSM. Again, it can be observed that the free wake configuration calculates the largest normal force, followed by the prescribed wake configuration with three rotor revolutions of free wake points. At the tip of the blade it is observed that the difference between BEM and AWSM is around a factor of 2, as was also found for the normal force.

In order to inspect how the tangential force varies over the rotor revolution, the tangential force is plotted as function of azimuth angle in Fig. C.10 at three different radial positions. The results for the tangential force as function of azimuth position are found to be similar to the results obtained for the normal force.

At $r/R = 50\%$, it can be seen that BEM overestimates the tangential force in the first half rotor revolution (not in the wake) and underestimates the tangential force in the second half rotor revolution (in the wake), when compared to the results from AWSM. At $r/R = 70\%$, a similar observation can be made, although it can be seen that the results between the codes match better,

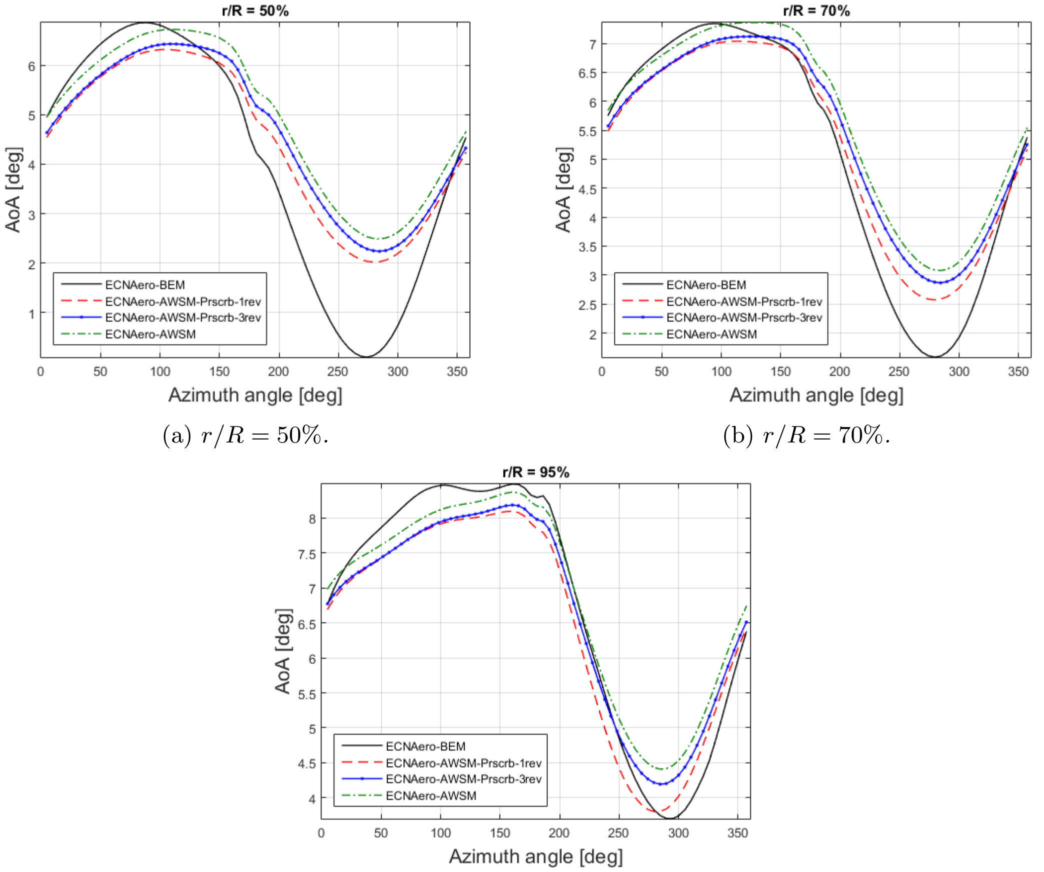

(a) $r/R = 50\%$.

(b) $r/R = 70\%$.

(c) $r/R = 95\%$.

Figure C.6: *Angle of attack vs. azimuth angle at different radial positions.*

as was also found for the axial induced velocity, the AoA and the normal force. In the tip-section of the blade, it can be found that the differences are largest when the blade is not in the wake, which was also found for the normal force. Again, this could be explained by the fact that the mean tangential force increases more rapidly towards the tip of the blade for BEM, resulting in the fact that the mean value near the tip is larger for BEM, from which it looks like the results match better in case the blade is not in the wake. However, it is expected that the differences are largest when the blade is in the wake, since the inflow velocity changes over time in this part of the rotor plane.

C.2.5 Blade Root Bending Moment

In order to see how the differences in local aerodynamic parameters affect the blade loads, the blade root bending moment around the three blade axis is analyzed. In Fig. C.11, the blade root bending moment is shown as function of azimuth angle.

For the blade M_x, it is found that there is an excellent agreement between the codes. Similar to the uniform inflow and extreme yaw case, it is found that the amplitude of the variation of M_x over the rotor revolution is larger for BEM.

For the blade M_y, larger differences have been found. It can be seen that there is a fair agreement if the blade is in the first half rotor revolution, i.e. not in the wake. In case the blade is in the

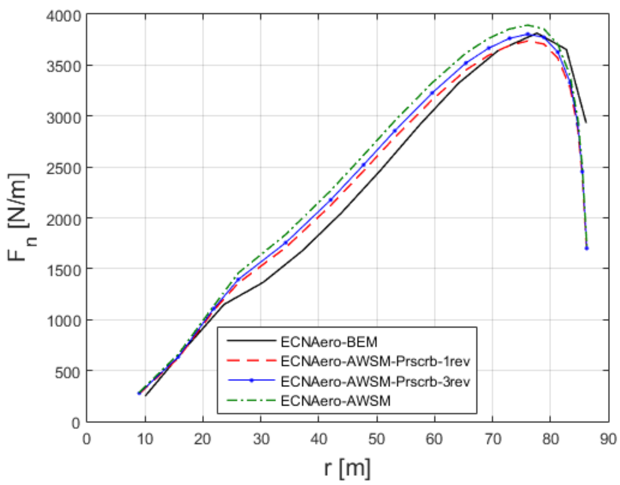

Figure C.7: *Azimuth averaged normal force vs. radial position.*

wake, M_y is found to be $\approx 25\%$ larger for the free wake configuration of AWSM compared to BEM, which could have significant results on the fatigue loads. Furthermore, it can be seen that there are significant differences between AWSM-Prscrb-1rev and the free wake configuration. With this result in mind, it is advised to increase the amount of free wake points for the prescribed wake configuration in case of a half wake simulation. For the blade torsional moment, M_z, it is found that there is an excellent agreement in case the blade is not in the wake. In case the blade is in the wake, the differences between BEM and AWSM are $\approx 10\%$ of the amplitude of the variation over the rotor revolution. Again, it is found that BEM calculates the largest amplitude of the variation of a full rotor revolution.

In order to further investigate the differences in the blade loads, the power spectral density (PSD) of the blade M_y is compared for the different codes. Since the simulation takes a long time to converge for AWSM, only the last $20s$ of the $180s$ of simulation time have been used to create the PSD. In order to compare the results between BEM and AWSM, also the results for BEM are taken for the last $20s$. Therefore, some detail in the figure is missing. It can be seen that there is an excellent agreement between BEM and AWSM for the lower frequencies. However, for frequencies above $f = 0.3Hz$, the differences become larger. This means that the 1P, 2P and 3P excitation is capture quite well between the two codes, whereas for higher frequencies the differences between the codes become larger. Furthermore, it can be seen that the largest energy is contained at the 1P and 2P frequencies, for which there is a good agreement between the codes.

Since the rotor speed is constant, there is a good agreement in the frequencies at which there is high energy, i.e. frequencies that are a multiple of the rotor frequency. However, the frequencies at which the PSD is created do not coincide exactly with a multiple of the rotor frequency, resulting in the fact that the actual peak is not obtained. Due to the coarse time step, the maximum frequency that can be calculated for the PSD is $3.35Hz$.

To investigate the influence of the large time-step, also a simulation with a time-step of $0.01s$ is performed with BEM. Due to the small time step, frequencies up to $50Hz$ are obtained in the PSD. It can be seen that the small time step is better in capturing the effects of higher frequencies. This results in the fact that it even resolves the excitation of the frequencies larger than $1Hz$, which are less well resolved by the simulation with the coarse time step. It should be noted that this is only possible in case of a constant rotor speed, since these high frequencies would otherwise be spread over the spectrum, due to a varying rotor speed. However, it does show that the simulation with a large time step misses the influence of the higher frequencies, although the energy level at these higher frequencies is limited.

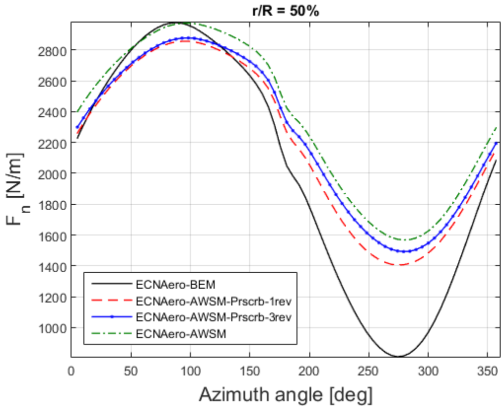

(a) $r/R = 50\%$.

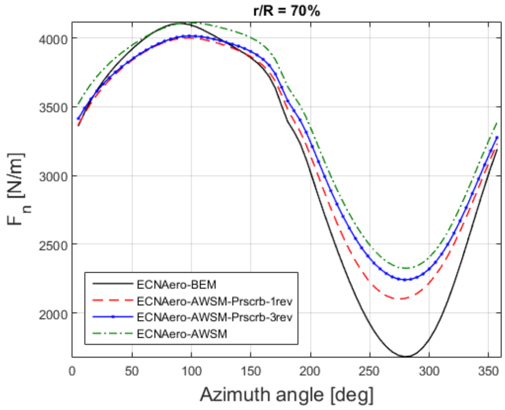

(b) $r/R = 70\%$.

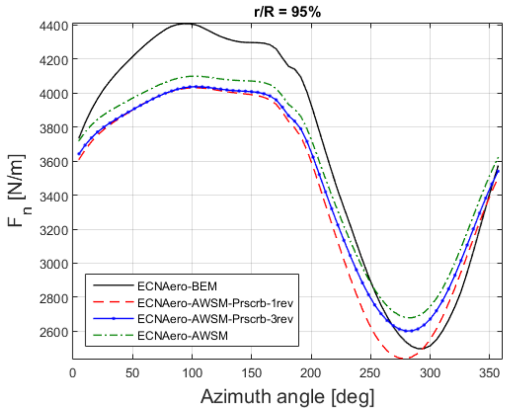

(c) $r/R = 95\%$.

Figure C.8: *Normal force vs. azimuth angle at different radial positions.*

C.2.6 Blade Tip Deflection

In Fig. C.13, the flapwise blade deflection δ_x at $r/R = 95\%$ is shown as function of azimuth angle. As expected, δ_x follows the shape of the blade M_y, since this is the load responsible for the flapwise deflection. It can be seen that the blade fluctuates around a deflection of $0m$, although it should be noted that this deflection is relative to the rotor plane. Since the INNWIND turbine has a prebend of $3.151m$ at the tip, the blade is actually deflecting $\approx 3.1m$ on average during a rotor revolution. Similar to the results found for the blade M_y, there is a good agreement if the blade is not in the wake. Furthermore, it can be observed that BEM calculates a larger fluctuation around the mean, as was found for all blade loads and local aerodynamic parameters so far. In case the blade is in the wake, it is found that the maximum differences are in the order of $0.4m$.

C.2.7 Axial Force

The axial force produced by the rotor is shown in Fig. C.14a for the last $10s$ of the simulation. It can be seen that there is quite a large scatter between the results of F_{ax}, although it should be noted that the maximum difference is found to be 6%, between BEM and AWSM (free wake). It can be observed that BEM calculates a much larger dip in F_{ax} compared to AWSM, which is consistent with the results of the axial induced velocity, where BEM also calculates a large dip due to the tower passage. When comparing the results between the different wake configurations

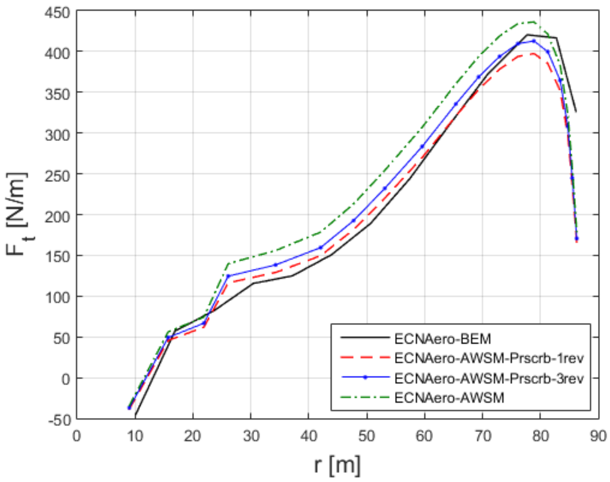

Figure C.9: *Azimuth averaged tangential force vs. radial position.*

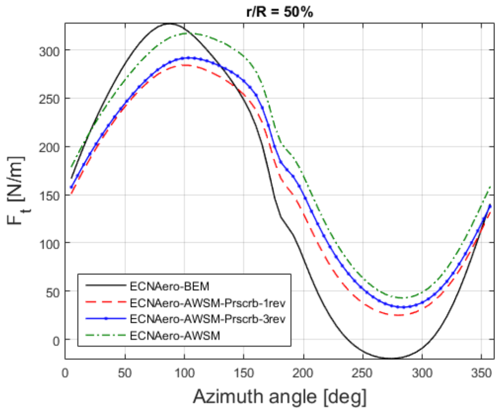

(a) $r/R = 50\%$.

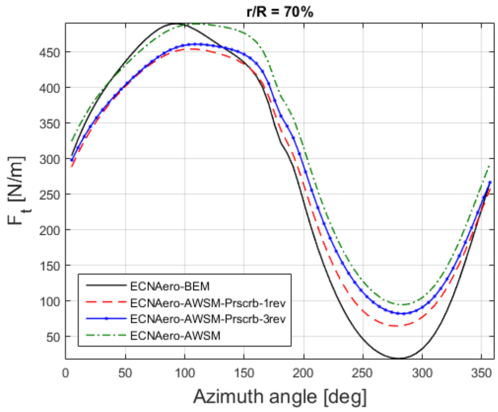

(b) $r/R = 70\%$.

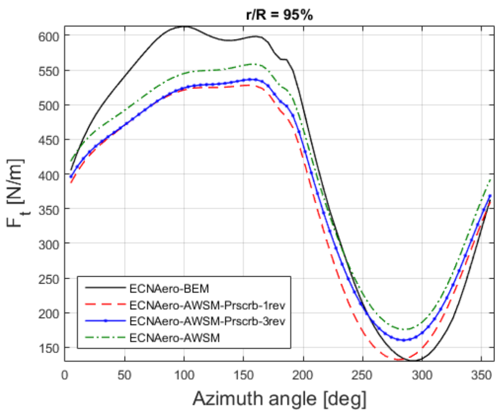

(c) $r/R = 95\%$.

Figure C.10: *Tangential force vs. azimuth angle at different radial positions.*

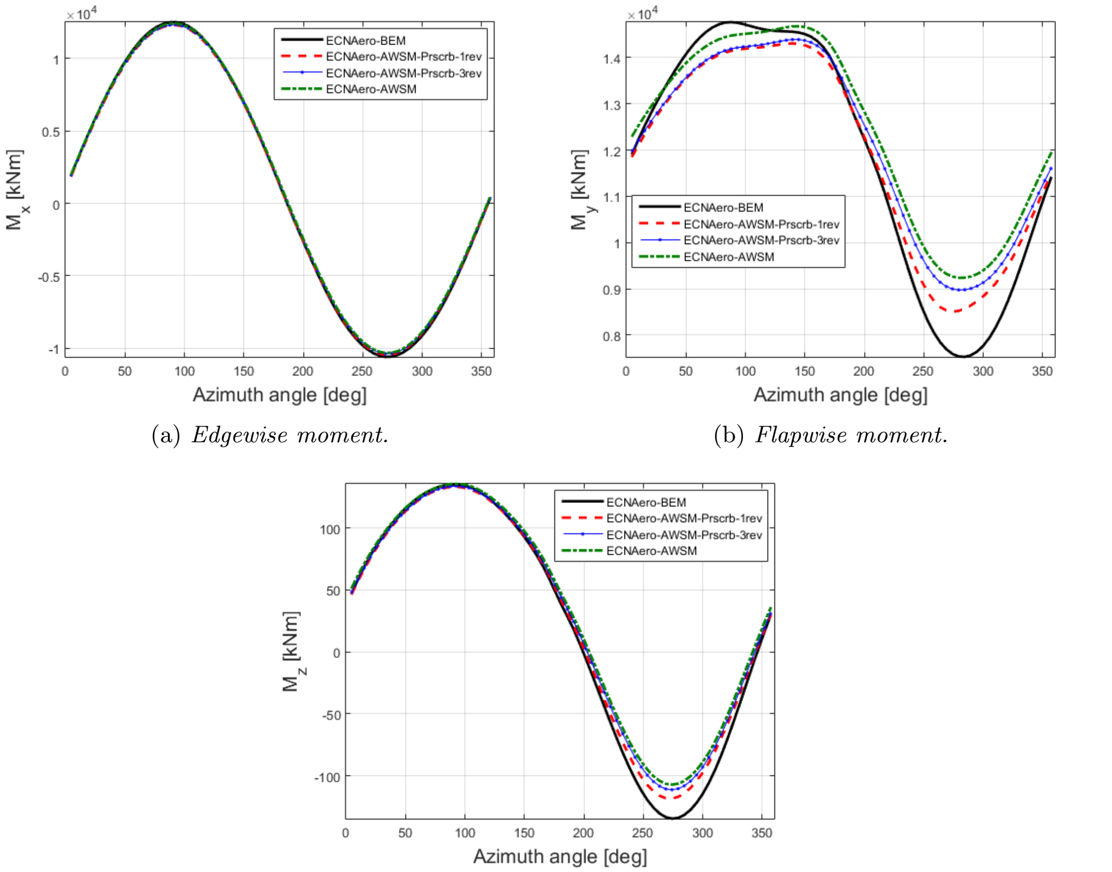

(a) *Edgewise moment.*

(b) *Flapwise moment.*

(c) *Torsional moment.*

Figure C.11: *Blade root bending moment vs. azimuth angle.*

of AWSM, it can be observed that AWSM-Prscrb-1rev shows a smaller variation of F_{ax} compared to the other two wake configurations.

C.2.8 Power

Similar to F_{ax}, the aerodynamic power is plotted against time in Fig. C.14b. From this figure it can be seen that there is a larger scatter in terms of mean value for power compared to F_{ax}, although the amplitude of the fluctuations seem to match better. Interesting to see is that the largest differences are found between AWSM-Prscrb-1rev and the free wake configuration ($\approx 13\%$). It can be observed that the free wake configuration of AWSM calculates a significantly larger power compared to the other codes. From this figure, the importance of the wake configuration settings for AWSM is underlined, since even the difference between the 210 and and 415 wake points still gives a difference of more than 5% in terms of power.

C.2.9 Tower Loads

In order to see how the loads produced by the rotor affect the loads on the support structure, the tower loads are compared in terms of moments around the three axis of the tower.

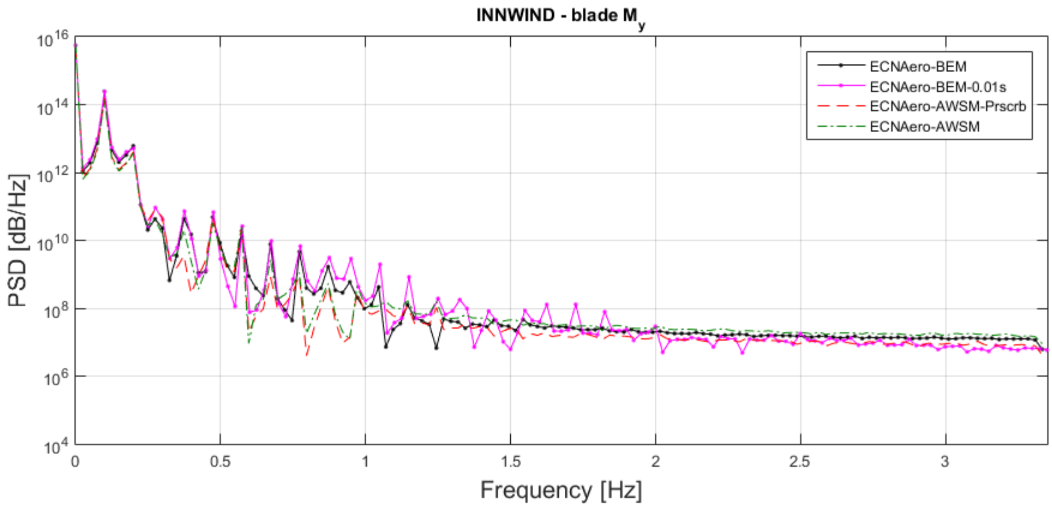

Figure C.12: *Power spectral density of the blade M_y.*

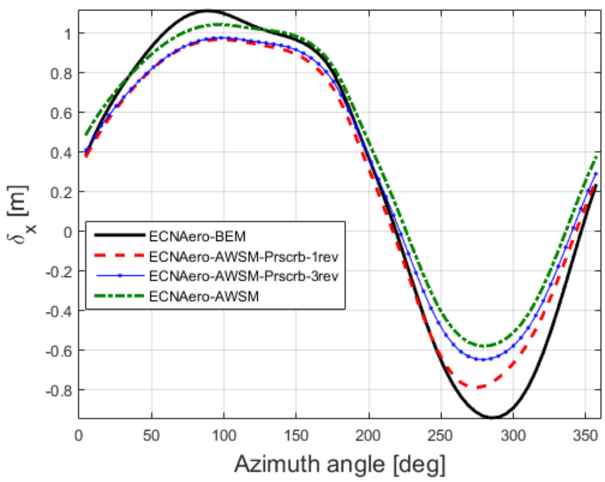

Figure C.13: *Flapwise blade deflection at $r/R = 95\%$ vs. radial position.*

In Fig. C.15a, the tower M_x is plotted as function of time. It can be seen that there is a reasonable agreement between the codes. It is observed that BEM calculates the largest amplitude of the fluctuations over time, as well as the largest mean value. The difference in mean and fluctuating part results in the fact that there is a rather large difference in $M_{x,max}$ between BEM and AWSM - prescribed wake ($\approx 20\%$). Interesting to see is that the results from the free wake configuration are in between the results from BEM and the prescribed wake configurations, whereas for most parameters it is found to give either the highest or lowest values. Furthermore, it can be seen that there is an excellent agreement between the two prescribed wake configurations for M_x, both in mean and fluctuating values.

In Fig. C.15b, the tower M_y is plotted as function of time. From this figure it can be observed that there is a reasonable agreement between the codes with maximum differences in the order of 10%. Again, BEM calculates the largest amplitude in fluctuations, although the mean value is lower compared to AWSM. For the various wake configurations, a good agreement is found in terms of the amplitude, whereas the differences in mean value are around 5% between the prescribed and free wake configuration.

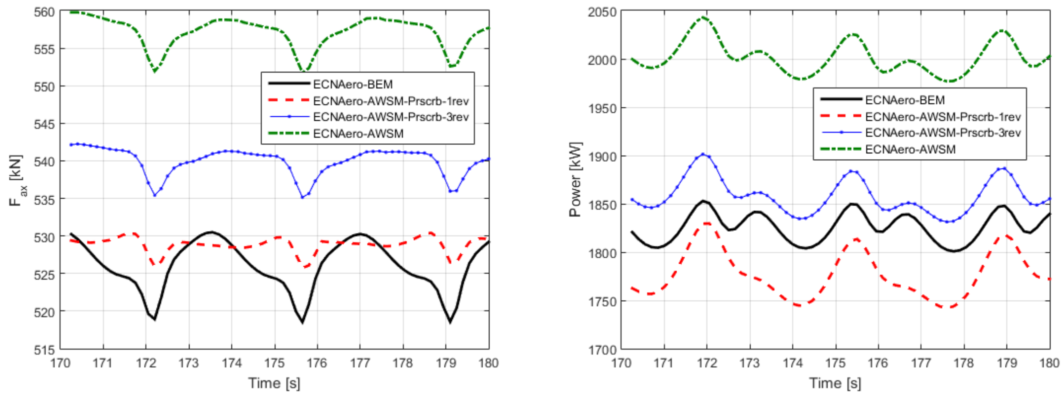

(a) *Axial force.* (b) *Aerodynamic power.*

Figure C.14: *Axial force and power vs. time for the last* 10*s of simulation time.*

In Fig. C.15c, the tower M_z is plotted as function of time. This torsional moment is caused by the difference in inflow velocity between the two sides of the rotor plane. It can be seen that there is an excellent agreement between AWSM-Prscrb-3rev and the free wake configuration. The results from AWSM-Prscrb-1rev are $\approx 10\%$ larger, whereas the results from BEM are $\approx 50\%$ larger. This can be explained by the fact that there are large differences found in the normal force for the blade in the wake between BEM and AWSM. Considering the fact that M_z is created by an imbalance between the forces on the two sides of the rotor plane, the higher M_z found by BEM is caused by the lower normal force calculated when the blade is in the wake compared to AWSM, resulting in a large imbalance in normal force between the two side of the rotor plane.

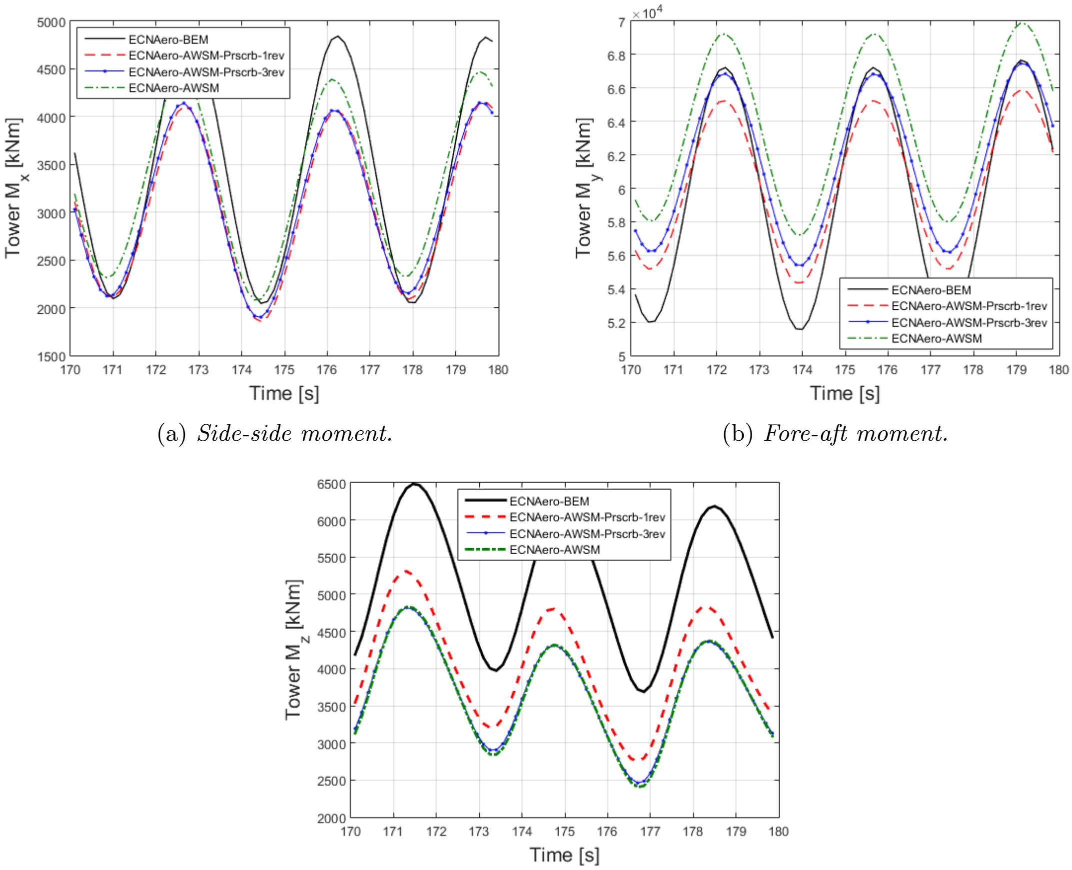

(a) *Side-side moment.*

(b) *Fore-aft moment.*

(c) *Torsional moment.*

Figure C.15: *Tower bottom moment vs. time for the last* 10*s of simulation time.*

Appendix D

Extreme Wind Shear

D.1 Case Set-Up

Similar to the previous test cases, a time step of $\Delta t = 0.15s$ is chosen for the simulations with AWSM, as well as for the simulations with BEM in order to be able to compare the results. As a deliverable for the AVATAR project, the BEM simulations for this test case have already been completed, from which the operational conditions have been taken. This means that the rotor speed is kept constant at $8.095rpm$ and the pitch angle is kept constant to $0°$.

D.1.1 Wake Settings AWSM

For this test case, a prescribed (hybrid) and a free wake configuration is used for the simulations with AWSM. The default wake length of three rotor diameters of wake points is used. The amount of wake points have been determined by the wake length for the mid-section of the blade, where the wind speed is $9.4m/s$. In order to make sure the wake is long enough for the lower part of the wake, where the wind speed is lower due to shear, an additional 25% of wake points is added.

For the free wake configuration, the first two rotor diameters of wake length is filled with free wake points (i.e. 2/3 of the complete wake). For the remaining part of the wake, the induced velocity is constant, as is described in Fig. 4.5 (PRSCRBWAKE = 0). For the prescribed wake configuration, the first rotor revolution of the wake is simulated by free wake points, which is about 20% of the free wake configuration. For the remaining part of the wake, the wake velocity of the vortex points is reduced according to BEM theory.

In Fig. D.1, the side view of the wake is shown for the two wake configurations as described above. The wake is shown at the end of the transient at $t = 132s$, since at this time-step the transient is visible in the wake. It can be observed that there is a very good agreement between the prescribed and free wake configuration for the first two rotor revolution of wake points behind the rotor. It can be seen that the wake points in the lower part of the rotor plane are at approximately the same position for two consecutive rotor revolution, which is expected since the inflow velocity in the lower part of the rotor plane during the transient is close to $0m/s$, as was found in Fig. 5.2b.

It can be observed that the prescribed wake configuration shows a rather steady wake convection for the complete wake, whereas for the free wake configuration the influence of the induced velocity due to the wake points themselves can be observed by a chaotic wake geometry. Furthermore, it can be observed that the for free wake configuration, the wake seems to follow the uptilt angle of 8°, whereas for the prescribed wake configuration this effect is not noticeable. This could be due to the implementation of the wake velocity of the prescribed wake configuration.

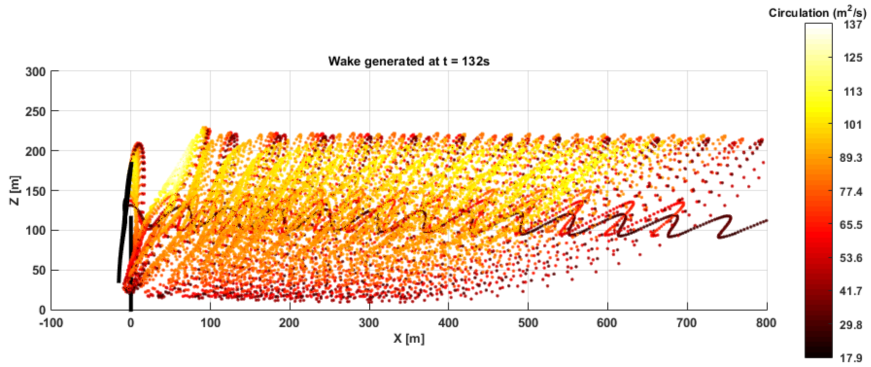

(a) *Prescribed wake configuration.*

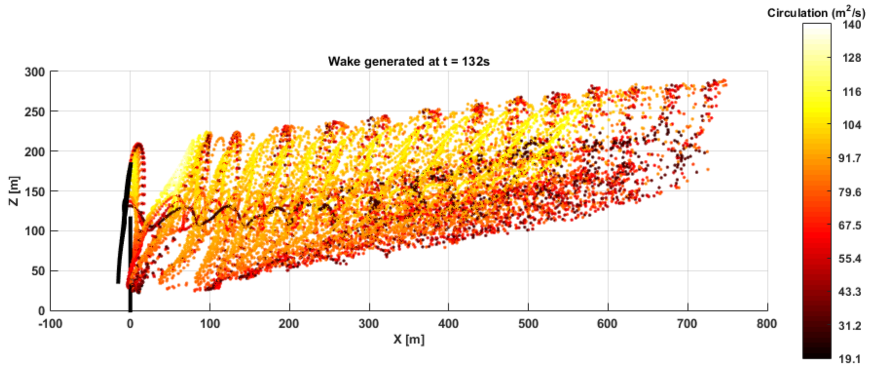

(b) *Free wake configuration.*

Figure D.1: *Side view of the wake for the INNWIND turbine at the end of an extreme wind shear transient.*

D.1.2 Computational Set-up

Most of the important settings for the computational set-up for the extreme wind shear test case are presented in Section 5.4.1. More details of the computational set-up can be found in Table D.1. Important to note is that all degrees of freedom for the blade are taken into account. Furthermore, the generator runs at constant speed and the controller and pitch actions are turned off. The dynamic stall model that is implemented for the calculations is the Snel model, first order. However, it is expected that this is only used for the root section of the blade, where the angles of attack are above stall.

D.1.3 Codes used for Comparison

The extreme wind shear test case is a deliverable for the AVATAR project and hence other partners in the project have contributed with the results from their respective wind turbine analysis tools. These results can be used as a comparison of the results obtained by PhatasAero. In order to

Table D.1: *Overview of simulation settings for the extreme wind shear case.*

Case	Extreme Wind Shear
Solver	Phatas-Aero
Subiteration settings	3 (Aerodynamic call at 1 and $\geq$ 9)
Simulation time (s)	140
Time step (s)	0.15
Blade torsion	ON
Flapping flag	ON
Lagging flag	ON
Dynamic stall	Snel (1st order)
Gearbox support	OFF
Controller	OFF
Generator model	Constant speed
Pitch flag	OFF
Shaft torsion	OFF
Pitch angles (deg)	0.0
Rotor speed (rpm)	8.095
Wind speed (m/s)	9.4
Wind File	Provided

compare the results, the simulations have to be done for the same turbine, at the same wind speed and with the same azimuth position of the blade when the transient starts. Unfortunately, not all partners have delivered results for the INNWIND turbine at $9.4m/s$ with an azimuth angle of 180° at the time of the transient.

It is found that DTU and NTUA have delivered results for the exact same conditions and can therefore be used for comparison. In the following sections, the numerical tools from both partners is briefly discussed.

HAWC2

HAWC2 is an aero-servo-elastic tool developed by DTU Wind Energy [50]. The structural part is based on a multi-body formulation, consisting of linear Timoshenko beam elements, where nonlinear effects (rotation and deformation) are taken into account by coupling constraints.

The aerodynamic part is modeled by a BEM formulation, comparable to an actuator disk model. The BEM equation is calculated locally in grid points over the rotor plane, rather than on each annular element, which is common in BEM codes. A dynamic inflow sub-model is added, which is a filter derived by simulations with a numerical actuator disc. A model for skewed inflow is added, based on the Glauert model. Finally, a dynamic stall model is added, based on the Beddoes-Leishmann model, including effects of shed vorticity and stall separation lag.

hGAST

hGAST is a hydro-servo-aero-elastic code with a modular form to allow changing separate models [50]. The structural part is modeled by Timoshenko beam elements, similar to HAWC2.

For the aerodynamic part, there is the option for a BEM and a panel code with a free wake model. For the BEM model, the standard engineering models have been added, like dynamic inflow (based on ONERA), root and tip losses, 3D correction for airfoil polars and a correction for yaw misalignment.

The free wake model is a combination of a panel representation for the solid surfaces (blades) and a vortex particle approximation for the wake. For the EWS case, the vortex particles emitted by the blades keep the wind velocity component, which is calculated at the time of their release, from which the transient is transferred into the wake.

D.2 Comparison of the Results

In this section, the results from BEM and AWSM are compared, which are obtained by running the extreme wind shear case with PhatasAero. With this comparison, differences in the modeling of the wind shear transient can be compared between the two aerodynamic models. In the next section, the results will also be compared to data from other partners. However, these datasets are run with different structural models and different operational conditions and the comparison will be more qualitatively and focused on observing trends or discrepancies between the models.

For the comparison between BEM and AWSM, first the axial induced velocity, angle of attack and normal/tangential force are plotted as function of time at various radial positions. Secondly, the blade loads and flapwise deformation are compared. Thirdly, the rotor performance is compared by means of the axial force and aerodynamic power. Finally, the tower loads are compared between the models to see how the difference in aerodynamic modeling results in differences in the tower bottom moments.

D.2.1 Axial Induced Velocity

In Fig. D.2, the axial induced velocity is plotted as function of time at the radial positions of 50% and 95% of the blade span. The transient shear starts at $t = 120s$ and continues until $t = 132s$. Interesting to see is that in the mid-section of the blade, the induced velocity is almost constant during the complete time period for BEM. The exception is the dip that occurs every $7s$, which is the influence of the presence of the tower. It seems that the shear does not have a significant influence on the calculation of $u_{i,ax}$ for BEM. A slight increase of $u_{i,ax}$ is observed due to the transient, although this is very limited compared to the results from AWSM. The results from AWSM show large variations in $u_{i,ax}$ over time and the response due to the shear results in a significant increase in $u_{i,ax}$. Furthermore, it can be seen that the results are quickly restored to the original cyclic behavior with a small increase in $u_{i,ax}$, which is due to the influence of the 'old' vortex point in the wake. Finally, it is observed that the prescribed wake configuration calculates $\approx 10\%$ higher $u_{i,ax}$ over the complete time period compared to the free wake configuration.

At $r/R = 95\%$, it can be seen that the variation of $u_{i,ax}$ agrees better between BEM and AWSM, although the results from BEM show significantly lower fluctuations. At $t = 124s$, it can be observed that BEM calculates a local minimum of $u_{i,ax}$, whereas AWSM calculates an local maximum. This is the points where the blade is in upward position and the incoming wind speed is the largest ($\approx 18m/s$ near the tip). The fact that BEM does not calculate this large increase of $u_{i,ax}$ between the lower and upper part of the rotor plane, indicates that BEM calculates the influence of wind shear on the induced velocity different compared to AWSM. At $t = 127s$, a sudden increase in $u_{i,ax}$ is observed for AWSM. This can be explained by the fact that the blade is in downward position and the wind speed becomes close to zero during the transient. This means that for AWSM, the vortex points pile up in this area and consequently calculating a much larger induction. One rotor revolution further, at $t \approx 134s$, these wake points have convected downstream and this sudden increase in $u_{i,ax}$ is no longer observed.

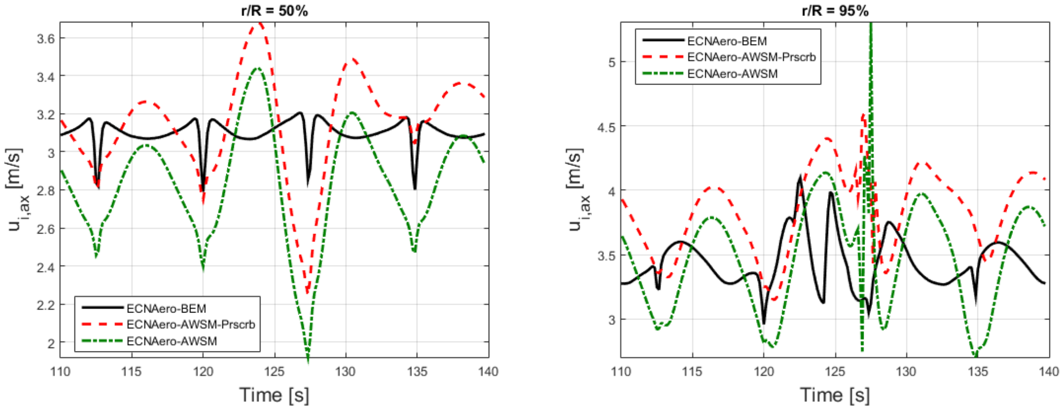

(a) $r/R = 50\%$. (b) $r/R = 95\%$.

Figure D.2: *Axial induced velocity as function of time.*

D.2.2 Angle of Attack

In Fig. D.3, the AoA is plotted as function of time at radial positions of $r/R = 50\%$ and 95%. From this figure it can be observed that there is a much better agreement between BEM and AWSM for the AoA compared to $u_{i,ax}$. It is found that there is a reasonable agreement in terms of the mean value of AoA at both radial positions for BEM and AWSM. However, it should be noted that a difference of only 0.5° can already result in significant differences in aerodynamic forces.

At $r/R = 50\%$, it can be seen that BEM calculates a larger fluctuation over the complete time period (normal shear and transient), as was also found the axial inflow, yawed inflow and half wake test case. At $r/R = 95\%$, the same observation can be made, although there is a difference at $t = 127s$, where the AoA is lower for AWSM. This can be explained by the fact that the tip of the blade is in downward position, where the vortex points from the previous revolution are still close to the rotor plane, due to the low incoming wind speed as a results of the transient shear. The effect of accumulation of wake points is not modeled by BEM. For both radial positions, it is observed that the free wake configuration calculates a slightly higher AoA over the complete time period, although the trend is similar to the prescribed wake configuration.

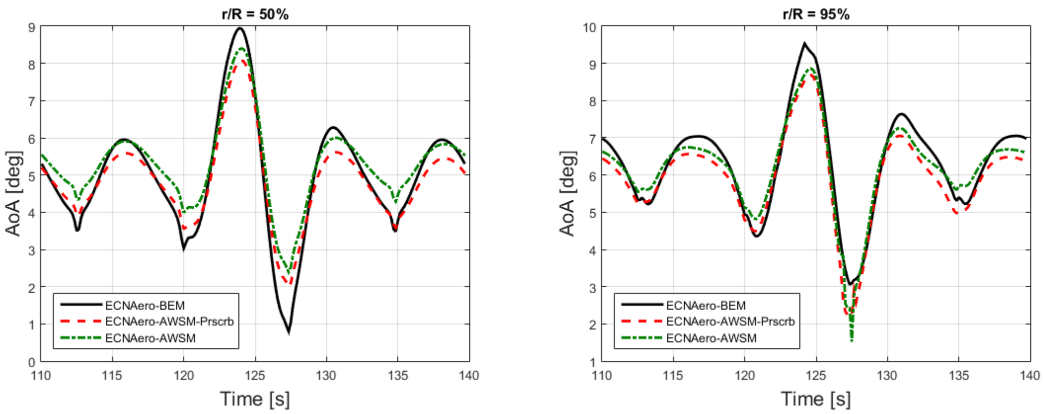

(a) $r/R = 50\%$. (b) $r/R = 95\%$.

Figure D.3: *Angle of attack as function of time.*

D.2.3 Normal Force

In Fig. D.4, the normal force per length is plotted as function of time for radial positions of $r/R = 50\%$ and 95%. The results for the normal force are very similar to the results from the AoA, although there are some differences noticeable.

In the mid-section of the blade it is found that BEM calculates a lower mean value of the normal force compared to AWSM, a result that has also been observed for the axial inflow, yawed inflow and half wake case. At the tip of the blade, the opposite is true, as has also been confirmed with other test cases.

Similar to the results from the AoA, BEM calculates the largest fluctuations over time for both radial positions. The results for $r/R = 95\%$ at $t = 127s$ show that the accumulation of wake points in the lower part of the rotor plane results in an additional decrease in normal force for AWSM compared to the results for BEM, which does not taken this effect into account.

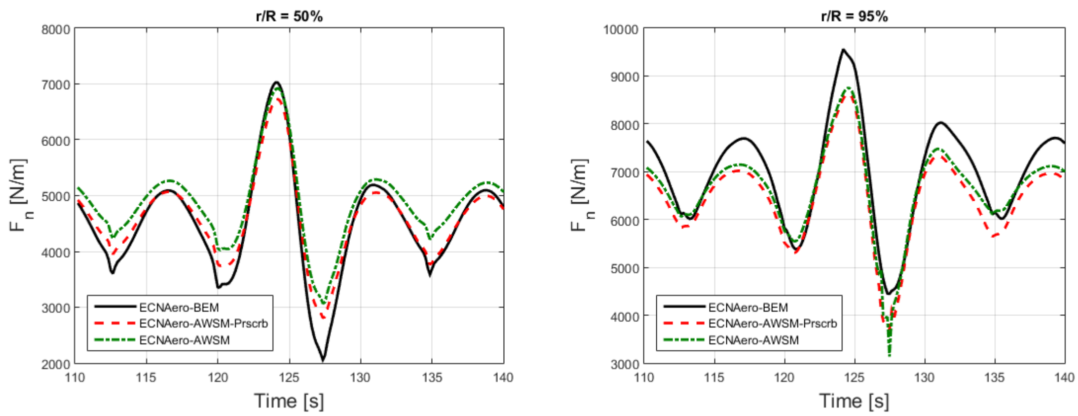

(a) $r/R = 50\%$. (b) $r/R = 95\%$.

Figure D.4: *Normal force as function of time.*

D.2.4 Tangential Force

In Fig. D.5, the tangential force per unit length is shown as function of time at two radial positions. The results for the tangential force are similar to the results found for the normal force, although one difference is found. It can be observed that the transient shear has a larger impact on the tangential force than on the normal force. At $r/R = 50\%$, it is observed that the peak tangential force during the transient is about 2.5 times higher than the peak during a full rotor revolution with normal shear, whereas this is only 40% for the normal force. This effect is also observed at the tip of the blade, although the relative difference is lower.

D.2.5 Blade Root Bending Moment

From a comparison of the local aerodynamics, it is found that BEM does not take all effects into account for the calculation of $u_{i,ax}$ and that BEM calculates a larger fluctuation of the AoA and normal/tangential force over time. In this part, the effect of these differences on the blade loads will be assessed. The blade root bending moment around the three axis of the blade will be compared for BEM and AWSM.

In Fig. D.6, the blade moments are shown as function of time. For the blade edgewise moment in Fig. D.6a, there is an excellent agreement between the codes. It should be noted that this moment

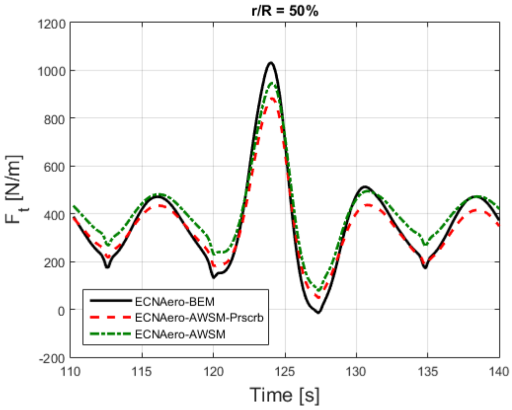

(a) $r/R = 50\%$.

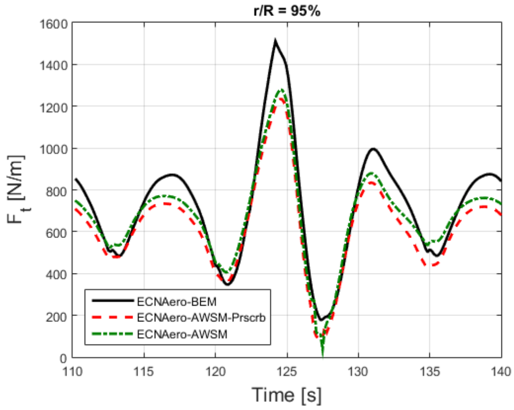

(b) $r/R = 95\%$.

Figure D.5: *Tangential force as function of time.*

is mainly created by the gravity force, which is equal for all codes, hence the good agreement. However, it can be observed that BEM calculates a slightly larger variation over time. The effect of the transient shear has very little effect on M_x.

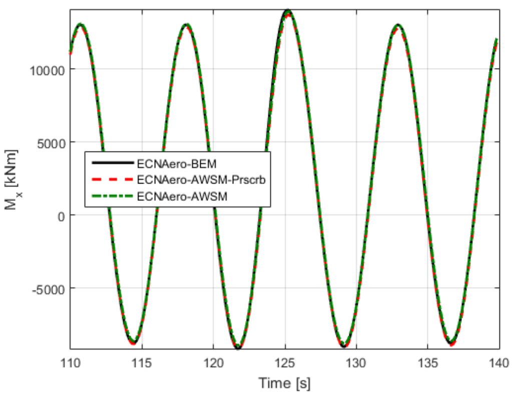

(a) *Edgewise moment.*

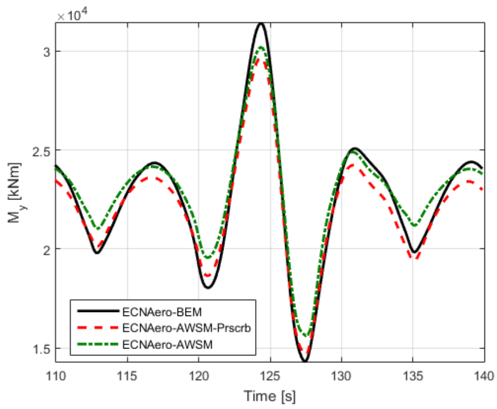

(b) *Flapwise moment.*

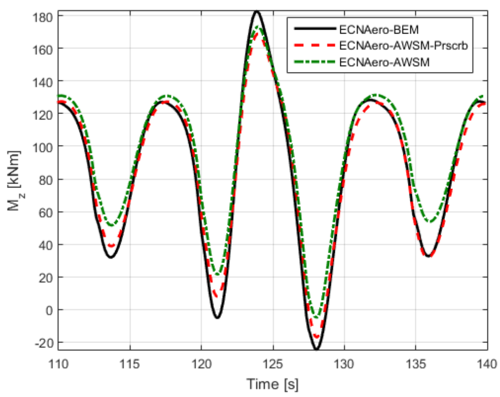

(c) *Torsional moment.*

Figure D.6: *Blade root bending moment vs. azimuth angle.*

In Fig. D.6b, the flapwise moment M_y is shown as function of time. It can be seen that there is a good agreement in terms of mean value for M_y between the codes. Similar to the results from the local aerodynamics, BEM calculates a larger amplitude of the variations and hence a larger maximum and lower minimum value due to the transient. This could have significant implication on the fatigue damage due to this test case. Similar to the results from the local aerodynamics, the free wake configuration results in higher loads, although the differences are only $\approx 5\%$.

The results for the blade torsional moment M_z are shown in Fig. D.6c. It can be seen that there is a good agreement for the peaks of M_z, which is when the blade is in upper part of the rotor plane and the wind speed changes less with height. The largest differences in M_z are observed half a revolution later, when the blade points downwards and the values for M_z are at a minimum. It can be observed that BEM calculates the largest amplitude of the variation over time compared to AWSM, which was also found for the other blade moments. Interesting to see is that the results from the BEM code agree quite well with the results from the prescribed wake configuration of AWSM.

D.2.6 Blade Tip Deflection

The flapwise blade deflection δ_x at $r/R = 95\%$ is shown as function of time in Fig. D.7. From this figure, it can be observed that δ_x follows the trend of the blade M_y. It can be seen that BEM calculates the largest variation in blade deflection over time. Similar to the blade loads, there is a very good agreement in terms of the calculation of the response to the wind shear transient, especially the second half of the transient, where the wind speed variation decrease to the normal shear level, between $t = 126s$ and $132s$.

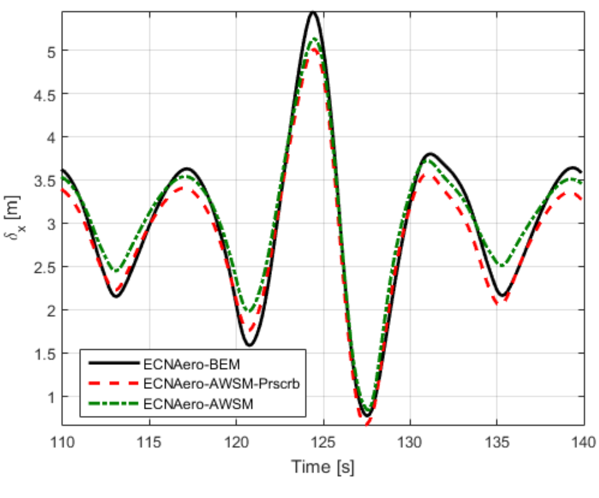

Figure D.7: *Flapwise blade deflection at $r/R = 95\%$ vs. time.*

D.2.7 Rotor Performance

In this section the rotor performance is compared in terms of the total axial force F_{ax} and aerodynamic power P produced by the rotor. In Fig. D.8, F_{ax} and P are shown as function of time. It can be seen that both parameters have a cyclic behavior until $t = 120s$ (start of the transient) and seem to restore to this cyclic behavior very quickly after $t = 132s$ (end of the transient), although the mean value is slightly changed.

From Fig. D.8a, it can be seen that there are significant differences between the two wake configurations of AWSM, where the free wake configuration calculates a 4% higher F_{ax} compared to the prescribed wake configuration. This difference becomes larger after the transient wind shear has passed. Interesting to see is that the result from the BEM code is between the results of the two wake configurations of AWSM. For the response to the transient, it is found that the two wake configurations of AWSM calculate a similar increase and decrease in F_{ax} during the transient period, whereas BEM calculates a higher increase for in F_{ax} for the second part of the transient.

In Fig. D.8b, the results are shown for P. A similar observation can be made regarding the differences between the two wake configurations and BEM, compared to the results for F_{ax}. However, the differences in power are much larger. The difference between the two wake configurations of AWSM is $\approx$ 10% before the transient wind shear and $\approx$ 15% after the transient wind shear. It might be interesting to see what happens when the amount of free wake points is increased to three rotor revolutions, similar to the half wake case. The results for the BEM case are in between the results of the two wake configurations of AWSM, although BEM calculates a larger power increase due to the transient, similar as for the axial force.

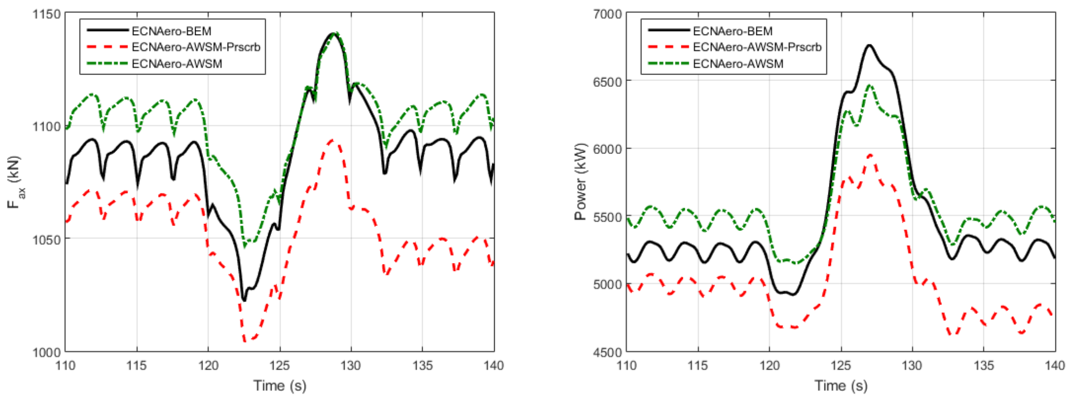

(a) *Axial force.* (b) *Aerodynamic power.*

Figure D.8: *Axial force and aerodynamic power vs. time for the INNWIND turbine under extreme wind shear transient.*

D.2.8 Tower Loads

In this section the tower loads are compared between the results of the different codes. The tower bottom moment around the three axis of the tower are analyzed. In Fig. D.9, the tower moments are shown as function of time.

For the tower side-side moment M_x, it can be seen that there is a good agreement between the codes before the transient wind shear hits the turbine (i.e. $t \leq 120s$). During the transient period, the results from the two wake configurations match very well, whereas the results from the BEM code calculate a larger increase in tower M_x. After the transient has passed the tower ($t \geq 132s$), the influence of the wind shear can still be observed for the results from AWSM, whereas this influence is not observed in the result from the BEM code. The sudden dip in tower M_x at $\approx 127s$ can be explained by the fact that the rotor orientation is such that the gravity of one blade act in the center of the rotor, whereas the gravity of the other two blades act at an equal lateral distance from the tower center, canceling out the effect of gravity on the tower M_x.

For the tower M_y, a good agreement is found between the codes. It can be seen that the results from the BEM code match well with the results from the free wake configuration, whereas the prescribed wake configuration calculates a lower tower M_y. However, it should be noted that the differences are only $\approx 3\%$, which is small for a tower load, where there are a lot uncertainties from the calculation of all forces and deformation in the rotor. It can be observed that BEM calculates the largest increase in tower M_y due to the transient, as was also observed for the tower M_x.

Finally, the tower M_z is compared in Fig. D.9c. From this figure, it can be seen that there is an excellent agreement between the two wake configuration of AWSM, whereas the results from BEM show a larger tower M_z for the complete time period. It can be observed that the transient wind shear has a large impact on the tower M_z, since the maximum value during the transient is approximately 5 times higher compared to the maximum value before the wind shear transient.

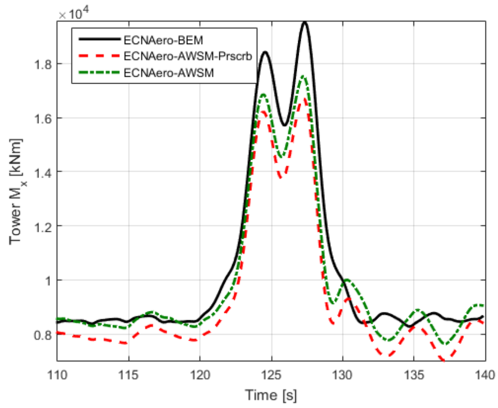

(a) *Side-side moment.*

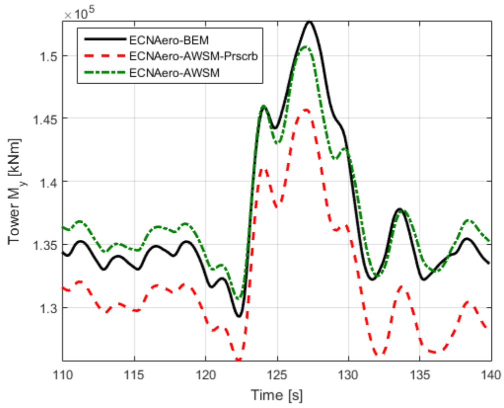

(b) *Fore-aft moment.*

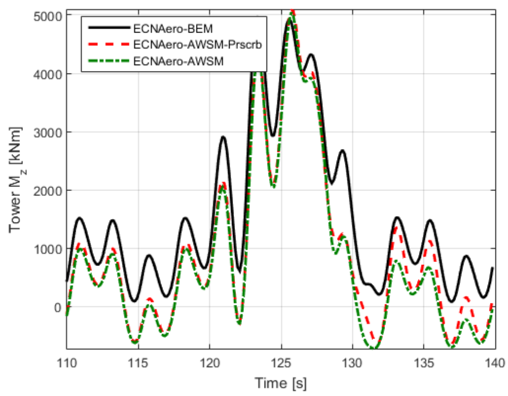

(c) *Torsional moment.*

Figure D.9: *Tower bottom moment vs. time for the INNWIND turbine under extreme wind shear transient.*

D.3 Cross Comparison AVATAR project

In this section the results from PhatasAero are compared to the results from HAWC2 and hGAST for the extreme wind shear case. All results in this section are presented as function of time, where $t = 0s$ is the start of the transient. This is done since not all partners have presented data from before the transient.

The output parameters that are compared are similar to the parameters that are compared for the previous section. Only difference is the normal and tangential force, for which no comparison data was available. Instead, the normal and tangential force coefficient have been compared.

D.3.1 Axial Induced Velocity

In Fig. D.10, the axial induced velocity is compared as function of time at two radial positions. It should be noted that the induced velocity results from the panel code of NTUA were not available and are therefore not present in the figure.

At $r/R = 50\%$, it can be seen that the BEM code of NTUA gives similar results in terms of fluctuations compared to the BEM code from ECN. The results from HAWC2 give a larger variation of induced velocity over time, which is more comparable to the results obtained from AWSM. The large dip in induced velocity due to the tower for ECNAero-BEM is not observed by the other BEM models. This is an indication that the dip in induced velocity due to the tower is overestimated by the model in ECN's BEM model. From the comparison of the other test cases, it was also observed that ECN's BEM code calculates a much larger dip in induced velocity due to the tower compared to AWSM.

At $r/R = 95\%$, it can be observed that the BEM models from NTUA and DTU both calculate a large increase in induced velocity, as was also observed with AWSM. This effect is caused by the low wind speed during the transient wind shear, causing the vorticity in the wake to accumulate in the lower part of the rotor plane, where the blade passes at $t \approx 7s$. It should be noted that the azimuth position at which the peak induced velocity takes place is not the same between the models. This can be argued by the fact that the peak $u_{i,ax}$ does not take place at the same time, although there are only small differences in rotor speed. As was found before, the BEM code from ECN does not take this effect into account for the induction. Furthermore, it can be observed that for AWSM, this increase in induced velocity happens at a very small time-period, whereas the BEM codes of hGAST and HAWC2 calculate a peak that lasts much longer.

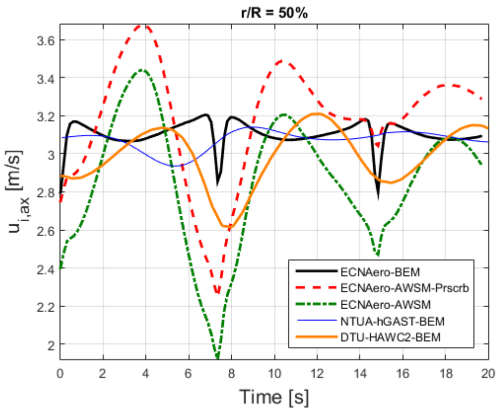

(a) $r/R = 50\%$.

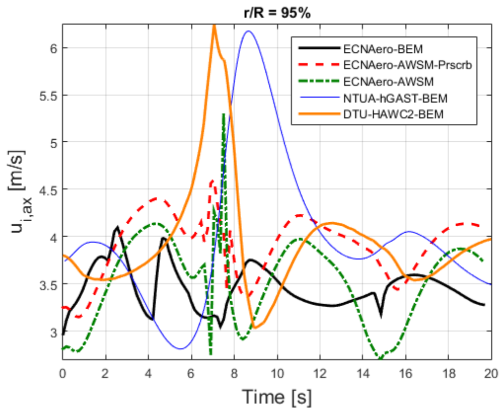

(b) $r/R = 95\%$.

Figure D.10: *Axial induction factor as function of time.*

D.3.2 Angle of Attack

In Fig. D.11, the AoA is compared at $r/R = 50\%$ and 95%. For the results in the mid-section of the blade, it can be seen that AoA at the beginning of the transient ranges between 4° and 5.5°, which is caused by differences in both operational conditions (rotor speed, pitch angle), as well as differences in modeling. In order to distinguish the differences due to the modeling, the increase of AoA due to the transient can be compared, as well as amplitude of the variation in AoA after the transient. It is found that the results form ECN-BEM and HAWC2 show the largest variation of AoA during the transient. Surprisingly, when comparing the results between the BEM and vortex model of hGAST, the results from the vortex model give the largest fluctuations. This result contradicts the observation made between BEM and AWSM, where BEM usually calculates a conservative (i.e. higher) amplitude.

At $r/R = 95\%$, it is found that again the BEM codes calculate the highest increase in AoA due to the transient. However, the largest differences are observed when the blade is in downward position at $t \approx 7s$. This could be explained by the fact that the incoming wind speed is close to zero, which means that the relative wind speed for the blade section is dominated by the rotor speed, resulting in a very low AoA. After the transient has passed, the results between the codes agree better again. When comparing the results between the three vortex code, it can be found that there is a very good agreement during the transient in terms of response.

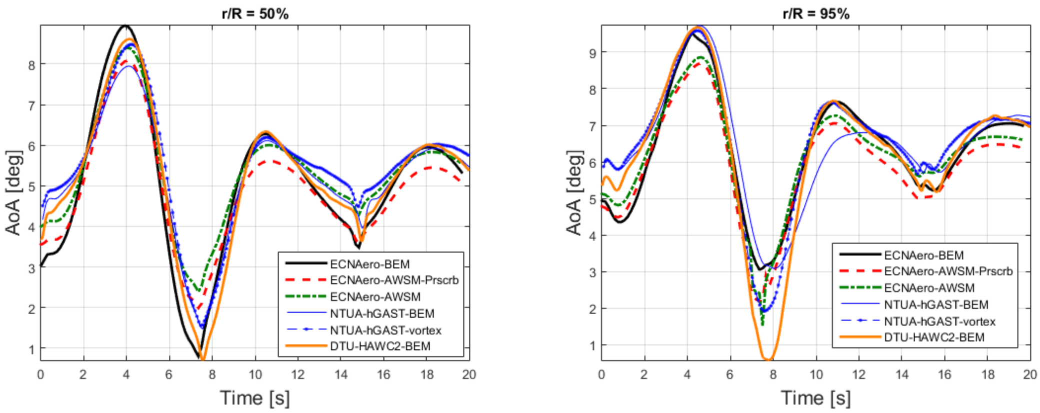

(a) $r/R = 50\%$. (b) $r/R = 95\%$.

Figure D.11: *Angle of attack as function of time.*

D.3.3 Normal Force Coefficient

Since the result files from the other partners did not contain the normal force, the normal force coefficient c_n is compared instead. Since AWSM does not calculate c_n, this is calculated in the following manner:

$$c_n = c_l \cos(\alpha) + c_d \sin(\alpha) \tag{D.1}$$

In Fig D.12, c_n is shown as function of time for two radial positions. It can be seen that there is a good agreement between the codes, which is expected, since the normal coefficient is based only on the AoA, for which a good agreement was found and all codes use the same airfoil polars. Again, it observed that BEM calculates a large amplitude of the variation compared to AWSM.

D.3.4 Tangential Force Coefficient

Similar to the normal force, the tangential force is also not available for the comparison data, hence the tangential force coefficient c_t is compared. c_t is obtained by the following equation:

$$c_t = c_l \sin(\alpha) - c_d \cos(\alpha) \tag{D.2}$$

In Fig. D.13, c_t is shown as function of time. It can be seen that the results from the BEM codes HAWC2 and hGAST show a larger c_t in the mid-section of the blade and a lower c_t in the tip of the blade, compared to the other results. It should be noted that small differences in

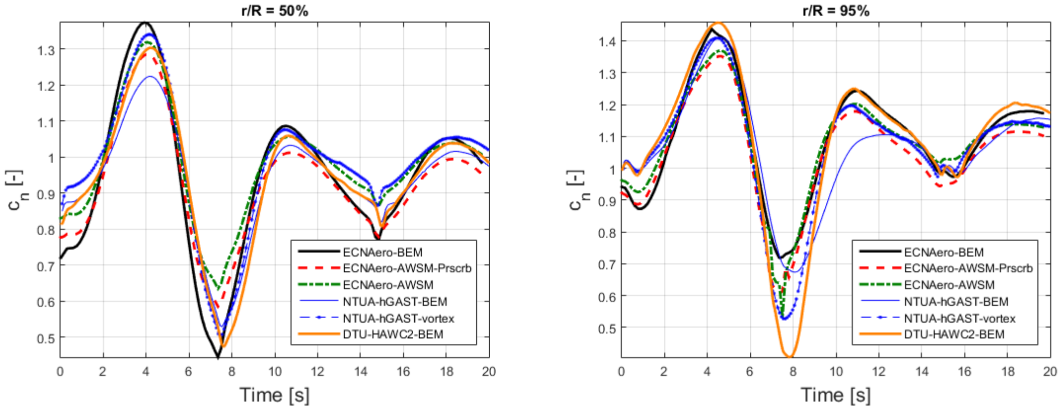

(a) $r/R = 50\%$. (b) $r/R = 95\%$.

Figure D.12: *Normal force coefficient as function of time.*

AoA could lead to significant differences in c_t, since c_l increase faster than c_d at low AoA and the contribution of the lift on the normal force increases as well due to geometrical reasons. However, the differences in AoA are much smaller than the differences in c_t. This gives reasonable doubt that it might be due to different modeling of the 3D effects of the airfoil polar.

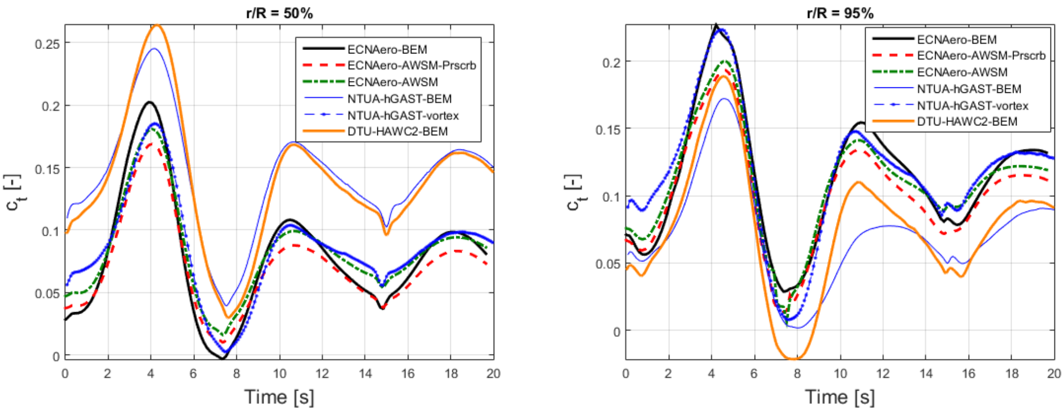

(a) $r/R = 50\%$. (b) $r/R = 95\%$.

Figure D.13: *Tangential force coefficient as function of time.*

D.3.5 Blade Root Bending Moment

In Fig. D.14, the blade root bending moment around the three axis of the blade are compared. For the blade M_x, it can be seen that there is an excellent agreement between the codes, which is expected since the gravity force is the main contributor to M_x, which is constant for all codes.

More interesting is M_y in Fig. D.14b. In this figure it can be seen that the results from ECNAero show a smoother response to the transient, compared to the results from the other codes. This could be explained by the coarse time step, resulting in the fact that the blade aerodynamics is only updated every $0.15s$, whereas the other codes use a smaller time step. Furthermore, it can be observed that the largest increase due to the transient is observed by the BEM codes from ECN and DTU, whereas the BEM code from NTUA shows the lowest peak in M_y. It is found that there is a good agreement for the peak value of M_y between the vortex codes. The largest differences are observed after one rotor revolution of the start of the transient, at $t \approx 127s$. This could be explained by large decrease in wind speed during the transient, which reaches its maximum shear at $t = 126s$. When the transient is passed, it is observed that again the BEM codes from ECN and DTU show the largest amplitude of fluctuations, whereas the BEM code from NTUA shows the smallest variation.

Finally, the results for the blade M_z is compared in Fig. D.14c. It can be observed that the response of M_z lags the transient by $\approx 1s$, which is equal to an azimuth angle difference of $\approx 20°$. This effect is observed by all codes, for which a good agreement is found for the time lag. It can also be found that results from ECNAero seem to respond different to the transient for the first two seconds, compared to the results from HAWC2 and hGAST. This is probably caused by the coarse time step, resulting in a smoother curve for ECNAero. When comparing the peak M_z due to the transient, it can be observed that the results from ECNAero show the largest increase. Interesting to see is that the BEM and vortex code from hGAST show a very good agreement. The results from HAWC2 seem to be in the middle of ECNAero and hGAST. When comparing the results at $t \approx 8s$, it can be observed that the results from HAWC2 show the lowest minimum. Interesting to see is that the vortex code of hGAST shows a lower minimum compared to the BEM code. When the transient has passed, the results from hGAST seem to agree well and predict a smaller M_z compared to the results from HAWC2 and ECNAero.

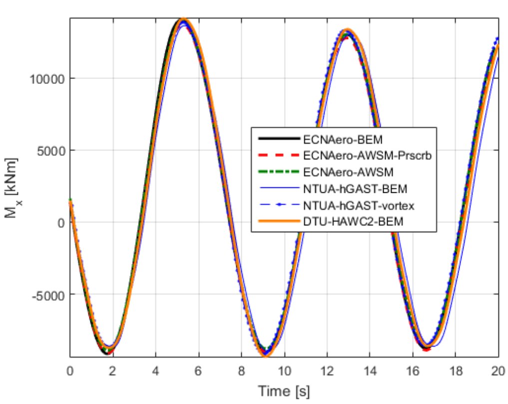

(a) *Edgewise moment.*

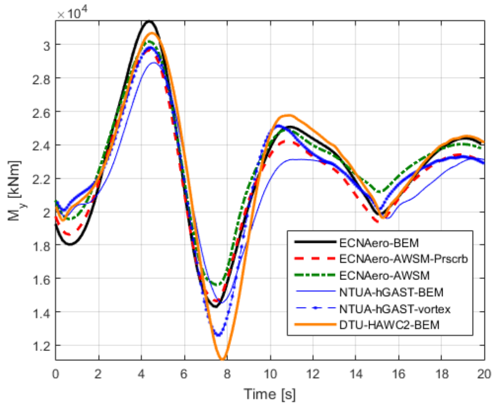

(b) *Flapwise moment.*

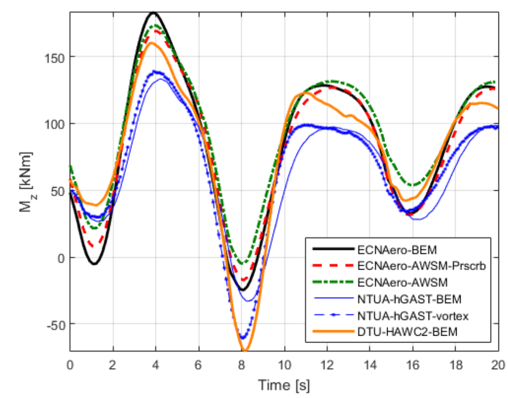

(c) *Torsional moment.*

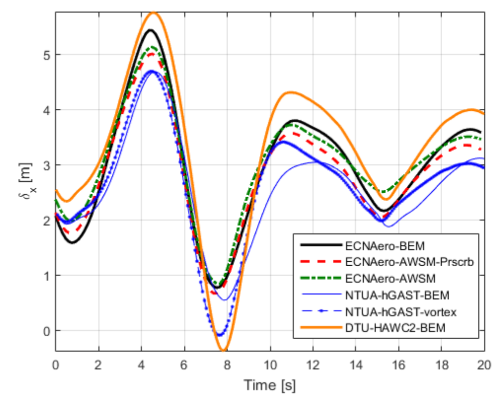

(d) *Flapwise blade deflection at $r/R = 95\%$.*

Figure D.14: *Blade root bending moment and tip deflection vs. time.*

D.3.6 Blade Tip Deflection

The flapwise blade deflection at $r/R = 95\%$ is compared in Fig. D.14d. Since δ_x is mainly caused by the blade M_y, the response of δ_x to the transient is similar to M_y. It should be noted that the definition of δ_x is interpreted differently by the different partners in the project, where ECNAero and HAWC2 define δ_x as the distance from the undeformed blade position, whereas hGAST defined δ_x relative to the rotor plane. The difference is the flapwise pre-bend, which is found to be $3.3151m$ for the INNWIND turbine. After deducting this value from the results from hGAST, δ_x can be compared as defined relative to the undeformed blade. This means that the actual blade deformation is $3.3151m$ more.

It should be noted that the structural models for the different codes are fundamentally different, resulting in a different behavior of the blade deflection, even if the loading is the same. Keeping this in mind, it is found that there are larger differences in δ_x, compared to M_y. It is found that the results from NTUA calculate the lowest tip deflection, whereas HAWC2 calculates the largest δ_x. The difference in maximum tip deflection due to the transient is in the order of $1m$. It is found that there are also significant differences in the remaining part of the transient, although the maximum tip deflection is the most important.

D.3.7 Rotor Performance

In this section the rotor performance is compared by means of F_{ax} and P. It should be noted that these output parameters are very dependent on the operations conditions, like the rotor speed and pitch angle. Since the simulations with HAWC2 and hGAST are done with the controller on, these operational conditions are different and might lead to differences in F_{ax} and P.

In Fig. D.15a, the axial force is shown as function of time. Interesting to see is that the results from ECNAero show an increase in F_{ax} of $\approx 100kN$ during the time period of $3s - 9s$ for the three aerodynamic models used. However, this increase of F_{ax} is only $\approx 40kN$ for HAWC2 and is hardly noticeable for the results from hGAST. Furthermore, it is observed that there are significant differences in the mean value for F_{ax} between the codes, up to $\approx 10\%$. This might also be explained by the fact that the rotor speed and pitch angles are adjusted to the transient for the results by HAWC2 and hGAST, since they have run the simulations with the controller on.

In Fig. D.15b, the aerodynamic power is compared as function of time. Similar to the results from F_{ax}, a large scatter in mean values can be observed, which can be attributed to the different modeling methods, as well as the different operational conditions. It can be seen that there is a good agreement in terms of the response to the transient, where every code calculates an increase in power of $\approx 20\%$.

D.3.8 Tower Loads

Finally, the tower loads will be compared between the different codes. In Fig. D.16, the tower bottom moment around the three axis of the turbine are compared. It should be noted that the results for the tower M_x and M_y from HAWC2 are not taken into account, since the output parameters were very different, which is expected to be due to a difference in the definition of the output parameters.

In Fig. D.16a, the tower M_x is shown as function of time. It can be found that there is a good agreement between the results from ECNAero and hGAST. It is observed that the BEM code of hGAST shows large oscillation during the start of the transient, which are not observed by the other codes. Furthermore, the results from the BEM code of hGAST seems to have a phase difference with the results from all other codes, including the vortex model of hGAST. When comparing the oscillation of M_x, it can be found that there is a very good agreement between

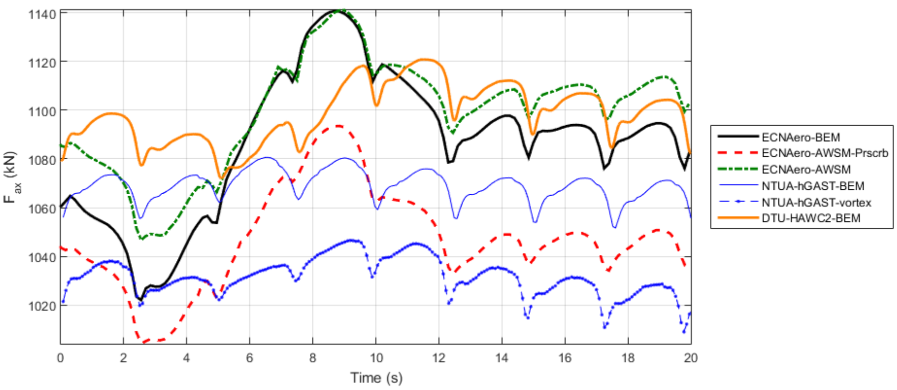

(a) *Axial force.*

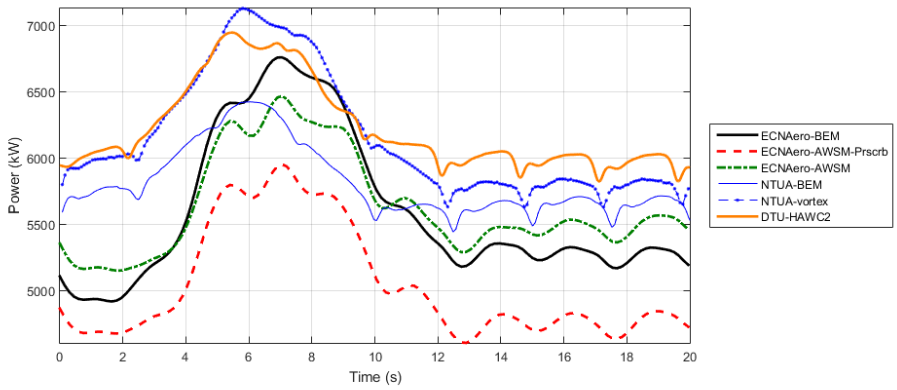

(b) *Aerodynamic power.*

Figure D.15: *Axial force and power vs. time.*

AWSM and hGAST-vortex, whereas the BEM codes either calculate a higher (ECNAero) or lower (hGAST) amplitude.

The tower M_y is shown in Fig. D.16b as function of time. It can be seen that there is a good agreement between ECNAero and hGAST. It can be found that for hGAST, the BEM model shows the smallest increase in M_y due to the transient, whereas the opposite is true for ECNAero. Furthermore, it can be observed that the results from ECNAero show a larger mean value and amplitude of M_y compared to hGAST, although the differences are below 10% in mean value.

For the tower M_z, the results from HAWC2 have been included as well. It can be seen that the results from HAWC2 show the largest peak in M_z, which is about 40% larger than the peak calculated by the other codes. Interesting to see it that the results from the vortex code of hGAST show the lowest values of M_z, whereas usually the BEM code of hGAST shows the lowest values. Furthermore, it can be observed that the high fluctuations during the transient, as found by ECNAero, are smaller for the results from the other codes, especially in the first half of the transient. The high fluctuations are caused by the blades passing the tower. In the second half of the transient, the results from HAWC2 also show large fluctuations, whereas the results from hGAST show a much smaller influence of the blades passing the tower.

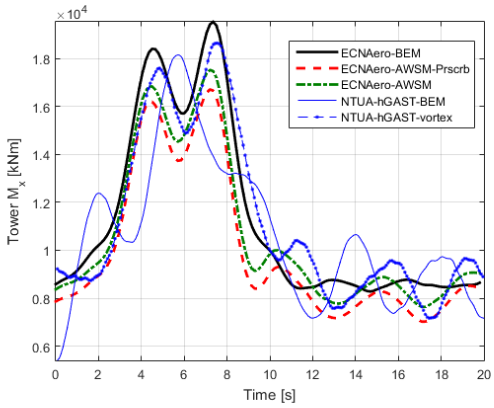

(a) *Side-side moment.*

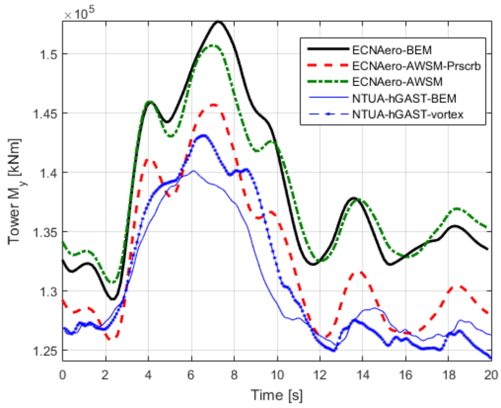

(b) *Fore-aft moment.*

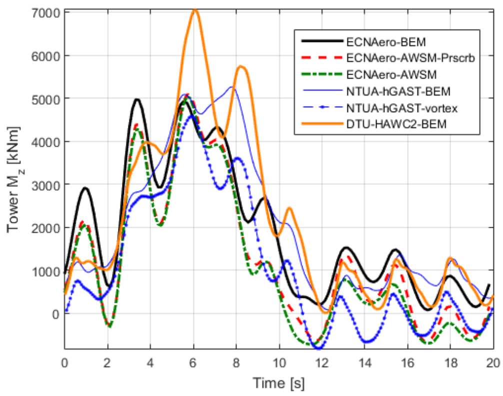

(c) *Torsional moment.*

Figure D.16: *Tower bottom moment vs. time.*

Appendix E

Turbulent Inflow

E.1 Case Set-Up

As described in the report, a time-step of $\Delta t = 0.10s$ is chosen in order to capture the high frequency dynamics involved in a turbulent inflow case, while keeping the CPU time to a reasonable level. The operational conditions for the turbulent inflow case are prescribed by a controller, which prescribes the pitch angle and rotor speed as a function of time for the complete time-period. Since the turbulence test case is run in the partial load regime, the pitch angle is constant throughout the complete time-period and only the rotor speed is varied over time.

The rotor speed settings are determined by running a simulation with the BEM code of Phatas with a time-step of $\Delta t = 0.01s$. The results from this analysis serve as the input for the controller. In Fig. E.1, the rotor speed is plotted against time for the last $20s$ of the simulation. From this figure it can be seen that there are small differences in the actual rotor speed for BEM and AWSM compared to the input rotor speed, as defined by the controller. However, it is found that the difference azimuth position after $150s$ in less than $1°$ between the results of BEM and AWSM, which is considered to be accurate enough in order to do the comparison between BEM and AWSM.

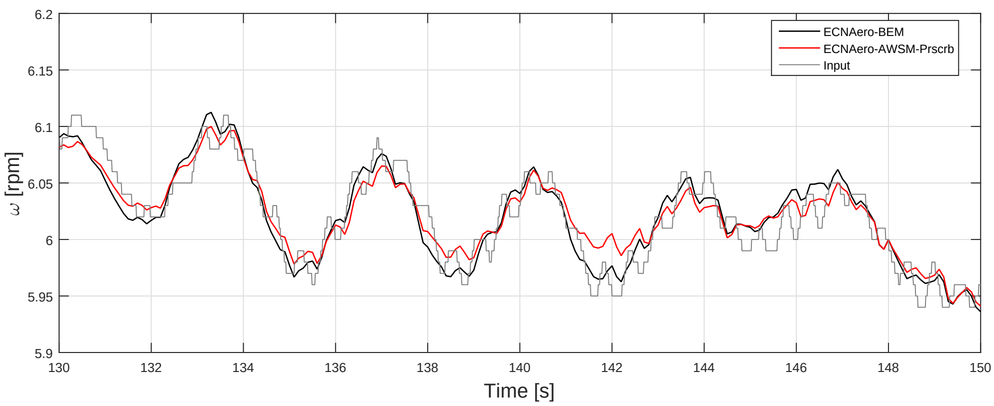

Figure E.1: *Rotor speed of the INNWIND turbine during a turbulent inflow.*

E.1.1 Wake Settings AWSM

For this test case, both a free and prescribed wake configuration are used for the simulations with AWSM. In order to determine the wake settings, first some simulations have been run with only the aerodynamics module, which significantly reduces CPU cost. From these simulations it has been found that a wake length of two rotor diameters is sufficient to accurately capture the dynamics of the turbulent inflow, whereas for a steady inflow three rotor diameters are usually required.

The total amount of wake points has been determined by the average wake velocity, with an induction factor of 0.31 for a wake length of two rotor diameters. In order to capture some of the nearby wake dynamics, the first rotor revolution of the wake is simulated by free wake points for the prescribed wake configuration, which is about 15% of the free wake configuration. For the remaining part of the wake, the wake velocity of the vortex points is reduced according to BEM theory.

In Fig. E.2, the wake that is generated in AWSM during the dynamic inflow is shown. From this figure, it can be seen that the wake geometry is rather chaotic, due to the varying inflow velocity, indicating that the results from previous time-steps still influence the aerodynamic through the presence in the wake. As was discussed in Section 6.5.3, there are significant difference between the free and prescribed wake configuration, where the free wake configuration calculates a lower induction and thus a higher wake velocity.

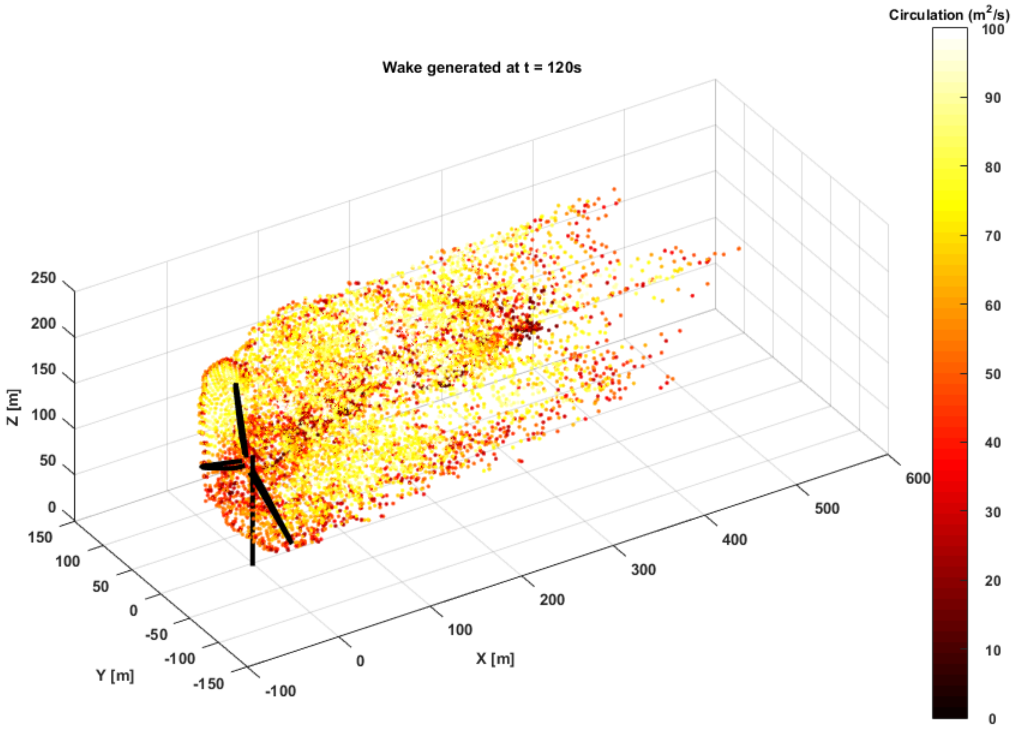

Figure E.2: Visualization of the wake for the INNWIND turbine in a turbulent inflow field.

E.1.2 Computational Set-up

Similar to the other test cases, the important settings for the turbulence test case have been mentioned in the report. The additional settings for the turbulent inflow case are described in

Table E.1. Different than for other test cases, the turbulent inflow case is run with the controller on. However, it should be mentioned that in order to get a proper comparison in terms of azimuth position at the same time, the rotor speed is prescribed for the controller. Furthermore, since the rotor speed is able to adjust to the wind speed, the shaft torsion is modeled as well. This was not the case for the steady inflow case with a fixed rotor speed, since the shaft torque showed unphysical behavior.

Table E.1: *Overview of simulation settings for the turbulent inflow case.*

Case	Turbulent inflow
Solver	Phatas-Aero
Subiteration settings	3 (Aerodynamic call at 1 and $\geq$ 9)
Simulation time (s)	150
Time step (s)	0.10
Blade torsion	ON
Flapping flag	ON
Lagging flag	ON
Dynamic stall	Snel (1st order)
Gearbox support	OFF
Controller	ON (prescribed)
Pitch flag	OFF
Shaft torsion	ON
Pitch angles (deg)	Prescribed
Rotor speed (rpm)	Prescribed
$U_{hub,avg}$ (m/s)	8
Wind File	Provided

E.2 Comparison of the Results

In this section the results from the turbulence test case are compared between BEM and AWSM. First the local blade aerodynamics are compared, by means of the axial induced velocity, angle of attack, normal force and tangential force. Next, the blade root bending moments and blade tip deflection are compared to see how the differences in local aerodynamics affect the loads and deformations of the blade. Next, the rotor performance is compared by comparing the axial force and aerodynamic power. Finally, the tower bottom moments are compared to inspect differences in the loads on the tower.

E.2.1 Axial Induced Velocity

In Fig. E.3, the axial induced velocity is compared between BEM and AWSM at two radial positions along the blade. In the mid-section of the blade it can be seen that the results from BEM show an almost constant $u_{i,ax}$, whereas AWSM shows a large variation. At the tip section of the blade, it can be seen that BEM shows a much more varying induced velocity, which is caused by several engineering corrections, like the Prandtl correction and yaw model. However, the variations in $u_{i,ax}$ are still smaller for BEM compared to AWSM at the tip of the blade.

In order to get a better insight in the fluctuating part of $u_{i,ax}$, the results between BEM and AWSM are compared in the frequency domain. The frequency domain analysis is done by computing the PSD of $u_{i,ax}$ for the time-period between $100s$ and $150s$. The PSD of $u_{i,ax}$ is shown in Fig. E.4 at 50% and 95% of the blade span for the frequencies up until $1Hz$.

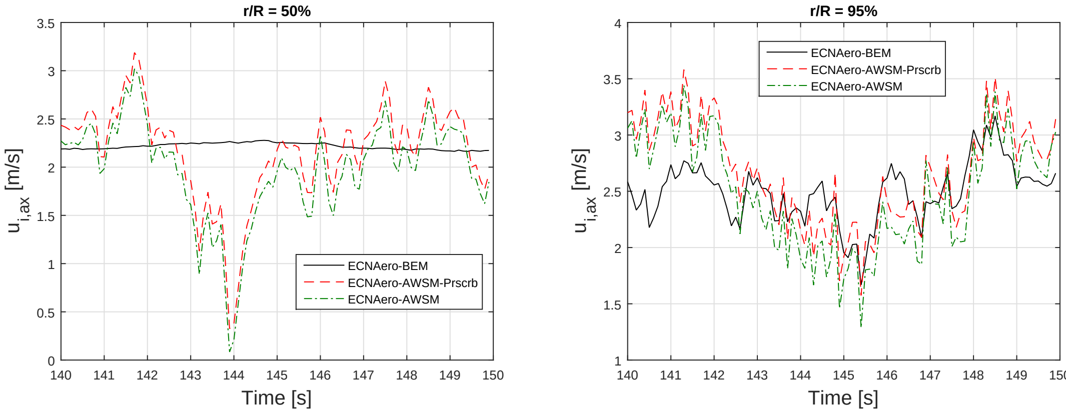

(a) $r/R = 50\%$.
(b) $r/R = 95\%$.

Figure E.3: *Axial induced velocity vs. time for the INNWIND turbine in a turbulent inflow.*

When comparing the results of the induced velocity in the mid-section of the blade, it can be seen that the results from AWSM show a much larger energy over the complete range of frequencies, indicating a larger fluctuation, since the mean values were found to be similar between BEM and AWSM. Interesting to observe is that the results from BEM show a very small increase in energy near the 1P frequency ($f \approx 0.1Hz$), whereas AWSM shows a large peak near the 1P, 2P and 3P frequency. At the tip-section of the blade, it can be seen that there is a much better agreement between BEM and AWSM. Interesting to observe is that at the tip-section of the blade, both BEM and AWSM have an energy peak near the 1P, 2P and 3P frequency, where AWSM shows the largest energy for the 1P frequency. For frequencies above 5P, it can be seen that some differences start to occur between the two wake configurations of AWSM. However, the effect of this difference is rather small due to the lower energy in this frequency region.

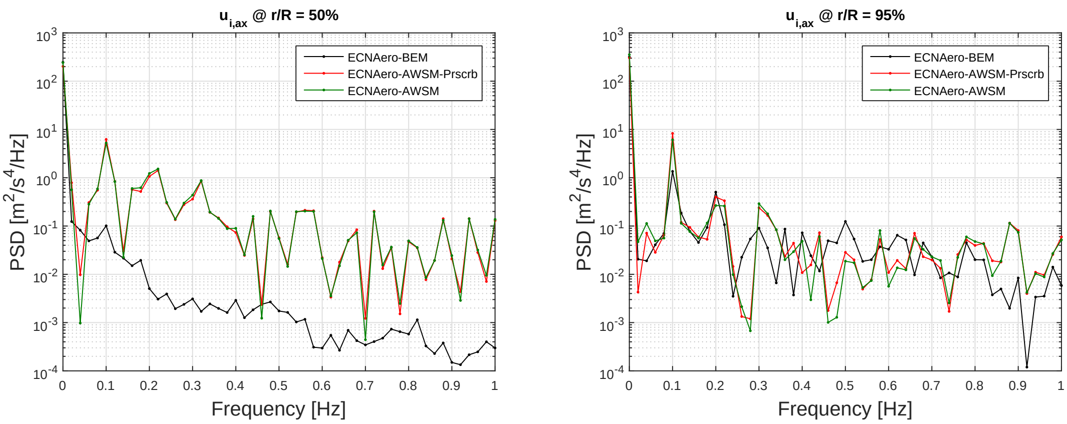

(a) $r/R = 50\%$.
(b) $r/R = 95\%$.

Figure E.4: *Comparison of the power spectral density of the axial induced velocity.*

In order to get a better insight in the mean and fluctuating part of the induced velocity over the complete blade length, the mean and standard deviation values are calculated at every 5% (from $20 - 95\%$) of the blade radial position. In Fig. E.5, the statistics are plotted as function of the the radial position for the time period between $100s$ and $150s$. From this figure, it can be seen that there is a good agreement between BEM and AWSM-Prscrb for the mean value of $u_{i,ax}$ over the mid-section of the blade, although bigger differences are obtained in the root- and tip-section of the blade. Interesting to observed that the results from the free wake configuration show a much lower mean $u_{i,ax}$. This might be explained by the fact that the wake velocity in the prescribed wake configuration is based on BEM theory, resulting in a better agreement for the induced velocity with BEM.

When looking at the standard deviation, it can be observed that AWSM calculates a five times higher variation in $u_{i,ax}$ until approximately $r/R = 70\%$. After this points, the standard deviation for BEM increases towards the value of AWSM, but remains significantly lower. It is expected that this increase in standard deviation is a results of the influence of the Prandtl tip correction, which is applied on a local level and its influence increases towards the tip of the blade. Interesting to observe is that there is an excellent agreement for the standard deviation value for the two wake configurations, especially considering the differences in the mean value.

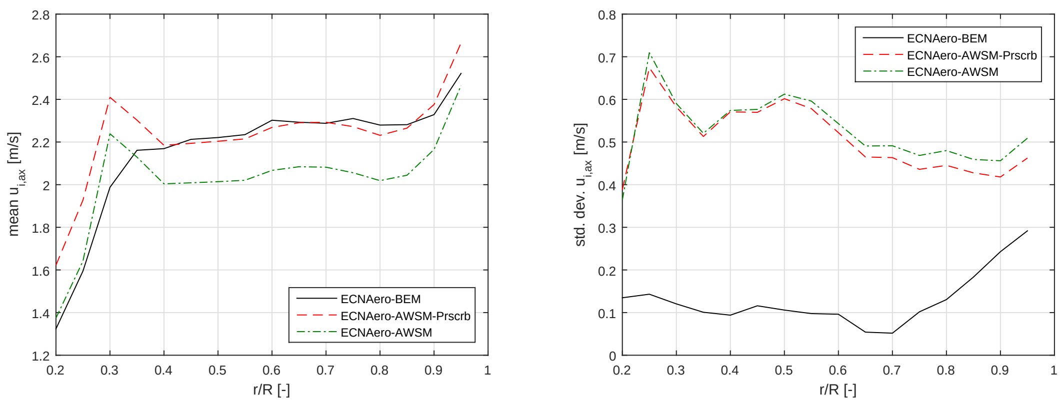

(a) *Mean values.* (b) *Standard deviation values.*

Figure E.5: *Statistics of the axial induced velocity for the INNWIND turbine for a* 50*s turbulent inflow.*

E.2.2 Angle of Attack

For the AoA, a similar analysis is done as for $u_{i,ax}$. In Fig. E.6, the AoA is shown as a function of time at the mid- and tip-section of the blade. It can be observed that there is a good agreement between BEM and AWSM in terms of the mean values, although it can be observed that the AoA for BEM seems to fluctuate more. This can be explained by the fact that there is a smaller variation in $u_{i,ax}$ for BEM. Important to note is that a small difference in AoA could results in large differences in loads. Furthermore, it can be seen that the free wake configuration shows a slightly higher AoA, which is explained by the lower $u_{i,ax}$.

In Fig. E.7, the AoA is shown in the frequency domain for mid- and tip-section of the blade. It can be observed that the results for the AoA from BEM show a larger energy for the complete frequency spectrum compared to AWSM. This is expected, since the induced velocity is more constant in the mid-section of the blade, whereas the incoming wind velocity and rotor speed is the same. Near the tip of the blade, there is an good agreement between BEM and AWSM for the AoA. When comparing the results from the two wake configurations of AWSM, a good agreement is found, indicating that the two methods are similar in terms of the fluctuations and energy distribution over the frequencies.

In order to quantify the differences between BEM and AWSM over the complete blade length, the mean and standard deviation values of AoA are obtained from a time-period of 50s. In Fig. E.8a, the mean AoA is plotted as function of the radial position along the blade. From this figure, it can be seen that BEM calculates a larger AoA in the root and tip section and a lower AoA in the

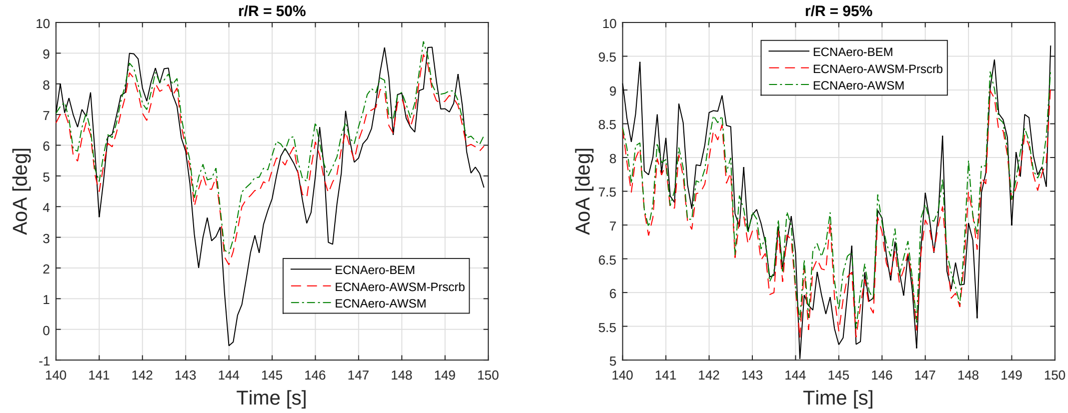

(a) $r/R = 50\%$. (b) $r/R = 95\%$.

Figure E.6: *Comparison of the angle of attack for the INNWIND turbine in a turbulent inflow.*

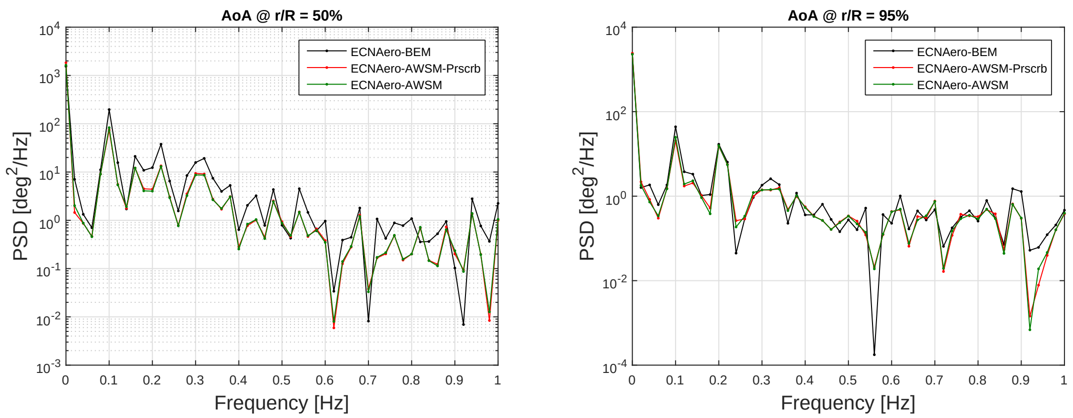

(a) $r/R = 50\%$. (b) $r/R = 95\%$.

Figure E.7: *Comparison of the power spectral density of the angle of attack.*

mid-section compared to AWSM-Prscrb. This results is the exact opposite of the trend that was found for $u_{i,ax}$ in Fig. E.5a. This results is expected, since a higher induced velocity results in a lower AoA, in case all other conditions are similar. The results from the two wake configuration of AWSM show a good agreement in terms of the trend, although it is observed that the free wake configuration shows a larger AoA over the complete blade length.

The standard deviation values of the AoA are shown in Fig. E.8b. From this figure, it can be seen that BEM calculates a higher fluctuation of AoA along the complete blade length. The differences between BEM and AWSM are $\approx 50\%$ in the mid-section of the blade and $\approx 15\%$ in the tip-section. Again, a good agreement is found between the two wake configurations of AWSM for the fluctuating part.

E.2.3 Normal Force

In Fig. E.9, the normal force is shown as function of time at the mid- and tip-section of the blade. Similar to the AoA, a good agreement is observed in terms of mean value, although BEM seems to calculate a higher amplitude of the variation over time. This effects seems to be smaller in the tip-section of the blade, compared to the mid-section. Interesting to observe is that there is a

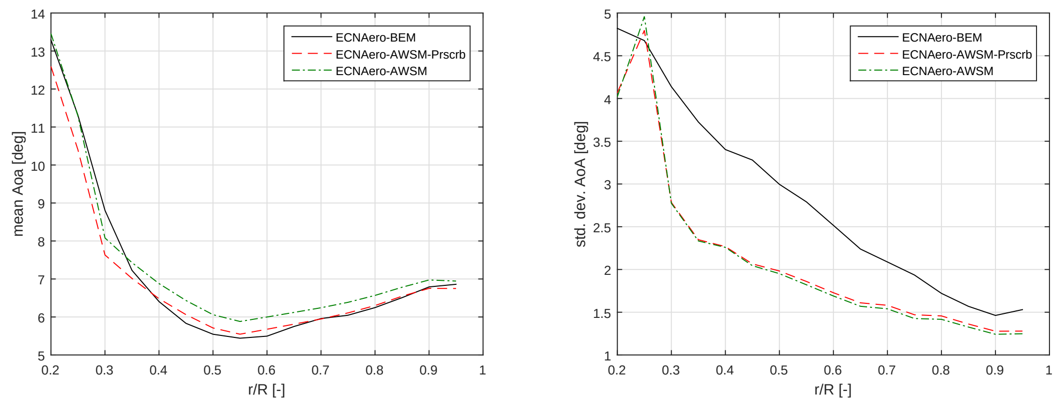

(a) *Mean values.* (b) *Standard deviation values.*

Figure E.8: *Statistics of the angle of attack for the INNWIND turbine for a 50s turbulent inflow.*

good agreement between the two wake configurations of AWSM, despite the significant difference in $u_{i,ax}$.

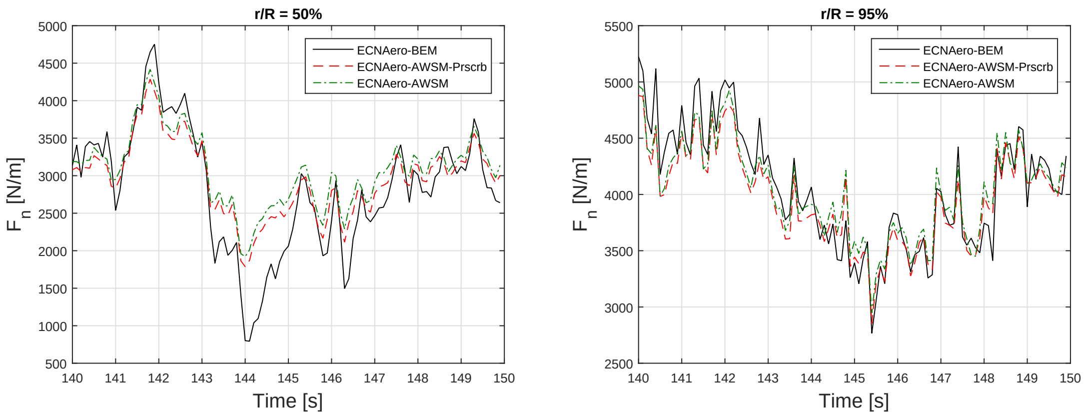

(a) $r/R = 50\%$. (b) $r/R = 95\%$.

Figure E.9: *Comparison of the normal force for the INNWIND turbine in a turbulent inflow.*

The mean and standard deviation values of the normal force are plotted as function of the blade radial position in Fig. E.10. It can be observed that there is a good agreement between BEM and AWSM-Prscrb in terms of the distribution of the mean normal force during the complete time-period. In the mid-section of the blade, it can be observed that AWSM calculates a slightly higher normal force ($2-3\%$ higher), which might be caused by the effect of the shed vortices in the mid-section of the blade. The results from the free wake configuration of AWSM show a significantly higher mean F_n over the complete blade length of approximately 5%.

When comparing the standard deviation between BEM and AWSM, it can be seen that BEM calculates $\approx 50\%$ higher F_n in the mid-section of the blade and the differences become smaller towards the root and tip. This result is similar to the observation that was made for the AoA. Again, an excellent agreement is found for the standard deviation values between the two wake configurations of AWSM.

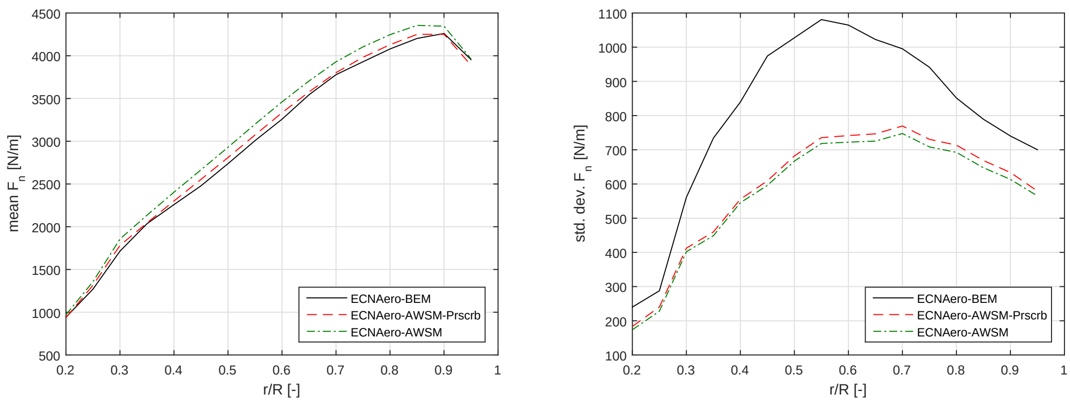

(a) *Mean values.* (b) *Standard deviation values.*

Figure E.10: *Statistics of the normal force for the INNWIND turbine for a* 50s *turbulent inflow.*

E.2.4 Tangential Force

The time-series of the tangential force is shown in Fig. E.11 at the mid- and tip-section of the blade. From this figure, it can be seen that there is a good agreement between BEM and AWSM in terms of the mean value, although it can be observed that BEM seems to calculate a larger fluctuation over time at both radial position. This is a similar observation as was made for the AoA and normal force.

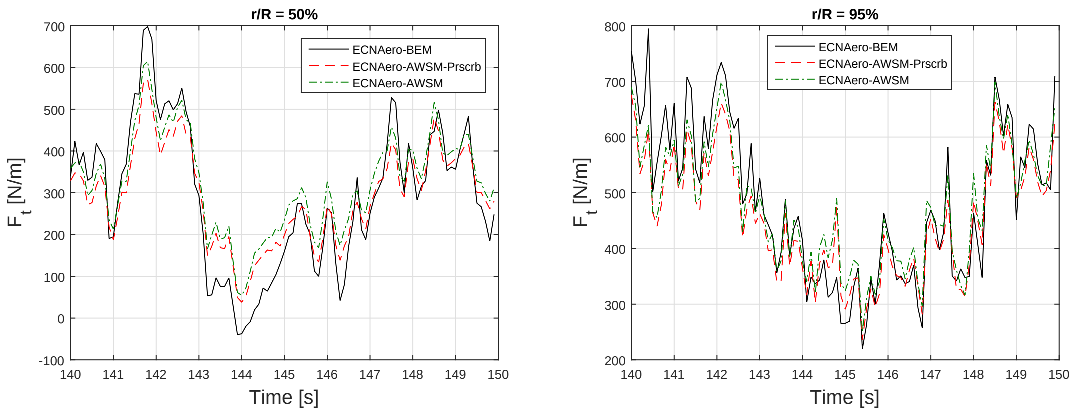

(a) $r/R = 50\%$. (b) $r/R = 95\%$.

Figure E.11: *Comparison of the tangential force for the INNWIND turbine in a turbulent inflow.*

The statistics of the time-series described above are shown in Fig. E.12. From this figure, it can be seen that BEM calculates a higher mean tangential force between $r/R = 30\%$ and 80% compared to AWSM-Prscrb. Due to this higher mean F_t, the results from BEM show an increased torque, which results in a 4.4% higher aerodynamic power for BEM compared to AWSM. It can be seen that the results from the free wake configuration show an even larger mean F_t, resulting in a 7.6% higher power compared to the prescribed wake configuration. This is a significant difference in terms of the calculation of the aerodynamic power of the turbine, which is an important parameter to evaluate the revenue from the wind turbine. Therefore, it is important that the difference between the two wake configurations is further investigated.

When inspecting the standard deviation values, it can be observed that BEM shows a larger fluctuation over the complete blade length. This result is in agreement with the observations that were made for the AoA and F_n. Again, a good agreement is found between the two wake configurations.

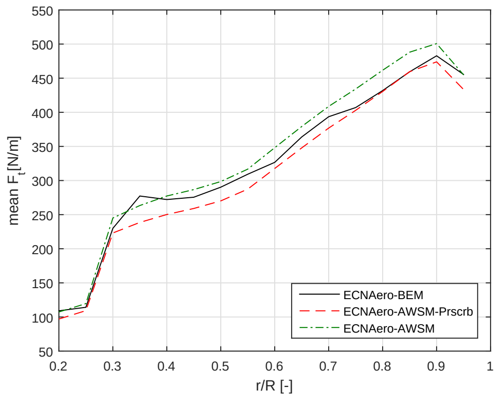

(a) *Mean values.*

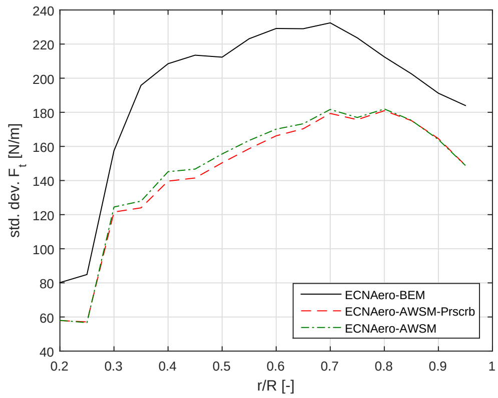

(b) *Standard deviation values.*

Figure E.12: *Statistics of the tangential force for the INNWIND turbine for a* 50*s turbulent inflow.*

E.2.5 Blade Root Bending Moments

In this section the blade root bending moment around the three axis of the blade are compared. In Fig. E.13, the blade M_x, M_y and M_z are plotted as function of time for BEM and AWSM. The aerodynamic contribution to M_x is small compared to gravitational forces.

For the blade M_x, it can be seen that there is an excellent agreement between BEM and AWSM. This is caused by the fact that M_x is mainly determined by the gravity force, which results in a 1P cyclic variation of M_x.

For the blade M_y, a generally good agreement is found between BEM and AWSM in terms of the mean value. It can be seen that the free wake configuration of AWSM shows a slightly larger mean value compared to the prescribed wake. For the fluctuating part, it can be observed that BEM usually calculates higher variation of M_y over time, which results in a higher ultimate load, as well as higher fatigue loads.

The blade M_z shows a similar behavior compared to M_x, which is expected since M_z is also mainly influenced by the gravity force, due to the offset between the blade and the rotor plane. When comparing the extreme values during the time-period, it can be observed that BEM calculates a slightly higher load amplitude, resulting in a higher ultimate and fatigue load. In terms of the mean values, there is a good agreement between BEM and AWSM, whereas the free wake configuration seems to calculate a slightly higher mean value.

In Fig. E.14, the PSD of the blade M_y is shown. From this figure, it can be seen that BEM shows a larger energy for the 1P, 2P and 3P frequency. From this result, it can be concluded that BEM shows a larger variation in the blade M_y, especially for the lower (forcing) frequencies, which contain the most energy in the spectrum. This increased fluctuation of M_y obtained by BEM results in an increased DEQL (fatigue) load of the blades, which is found to be 26% and 32% higher compared to the prescribed and free wake configruation of AWSM respectively, for the selected time-period ($T : 100 - 150s$).

This difference in the DEQL is caused by the difference in the area below the PSD curve for the blade M_y. It can be seen that largest differences occur for the first three rotor frequencies. At

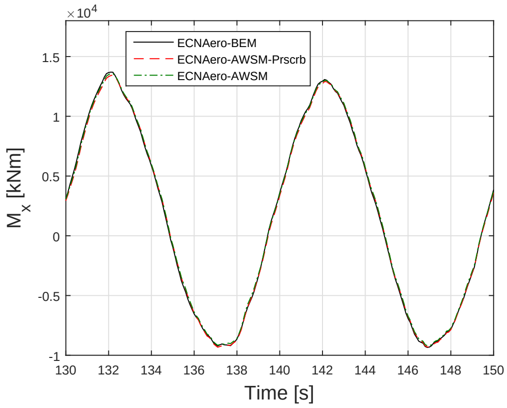

(a) *Edgewise.*

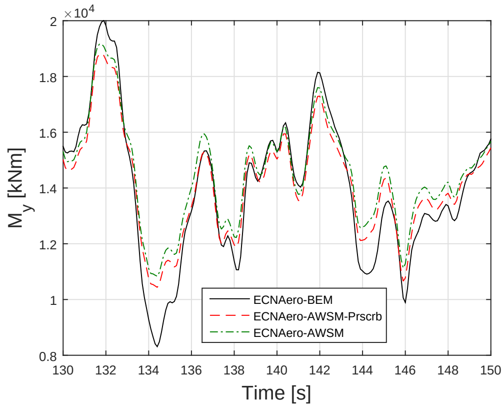

(b) *Flapwise.*

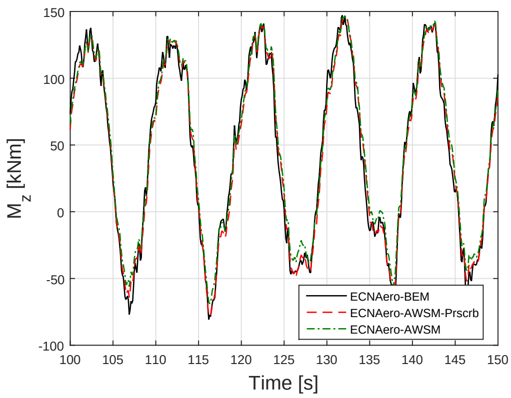

(c) *Torsional.*

Figure E.13: *Comparison of the blade root bending moment for the INNWIND turbine in a turbulent inflow.*

these energy peaks, the difference in energy between BEM and AWSM is in the order of 50%, although the logarithmic scale might suggest a reasonable agreement.

E.2.6 Blade Deflection

The blade deformation at $r/R = 95\%$ is shown as function of time in Fig. E.15. The same structural model is used for BEM and AWSM and the differences are therefore a result of the aerodynamic modeling only. However, there might be differences in the response to a deformed blade between BEM and AWSM. From the figure, it can be seen that there is a good agreement between BEM and AWSM, which is expected since a good agreement was found for the blade M_y. Similar as for the blade loads, BEM calculates a larger variation for the blade deflection. This results in a maximum blade deflection of $2.34m$ for BEM and $2.07m$ and $2.16m$ for the prescribed and free wake configuration of AWSM. When comparing the differences between the results of the two wake configurations, it can be seen that there is a good agreement in terms of the variation, whereas the free wake configuration shows a slightly higher mean blade deflection.

However, the tip deflection is most important when the blade is passing the tower, due to the tower clearance. For azimuth angles around 180°, the blade deflection is found to be much smaller and the agreement between BEM and AWSM is found to be better, in an absolute sense.

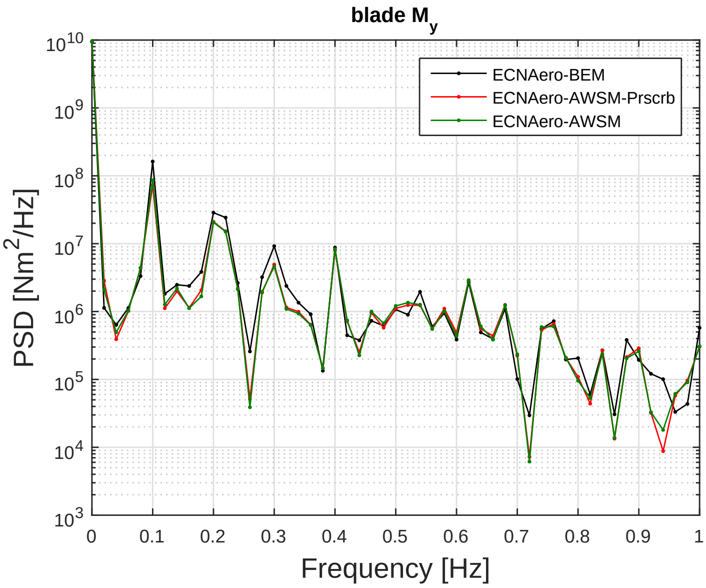

Figure E.14: *Comparison of the power spectral density of the blade M_y.*

E.2.7 Rotor Performance

In order to compare how BEM and AWSM take the influence of a turbulent wind field into account on the rotor performance, the axial force and power are compared. In order to account for the inertia of the rotor, a dynamic inflow model is implemented which affects the axial momentum equation. In Fig. E.16a, F_{ax} is plotted as function of time. In this figure, also the results form a BEM simulation without the dynamic inflow model are presented, to see how the dynamic inflow model affects the results in BEM for a turbulent wind field. It can be seen that the results from BEM show a smaller variation in axial force, due to the dynamic inflow model, which results in a better agreement between BEM and AWSM. The results from AWSM show a smaller variation of axial force, which might be a result of the dynamic inflow behavior which is modeled intrinsically, although it might also be caused by the lower variation of AoA that has been observed for AWSM. When comparing the results from the two wake configurations of AWSM, it can be seen that the free wake configuration shows a much higher mean value of F_{ax}.

In Fig. E.16b, the power is compared between BEM and AWSM. Again, the BEM results are presented with and without dynamic inflow model. From the figure, it can be seen that the inclusion of the dynamic inflow model results in a much better agreement between BEM and AWSM, although it is observed that AWSM still shows a smaller variation of power over time. Similar to the results of F_{ax}, it is unclear whether this is caused by an underprediction of the dynamic inflow behavior or by the lower variation of AoA found by BEM, which is caused by the inclusion of the variation of $u_{i,ax}$ over the azimuth blade position. The difference in mean value between the various model are caused by the difference in F_t, as discussed in Section E.2.4. When comparing the two wake configurations of AWSM, it can be seen that indeed the free wake configuration seems to calculate a larger mean power over the complete time-series.

E.2.8 Tower Loads

In this section, the loads on the tower are compared between BEM and AWSM. In Fig. E.17, the tower bottom yawing moments M_x, M_y and M_z are plotted as function of time. For the tower

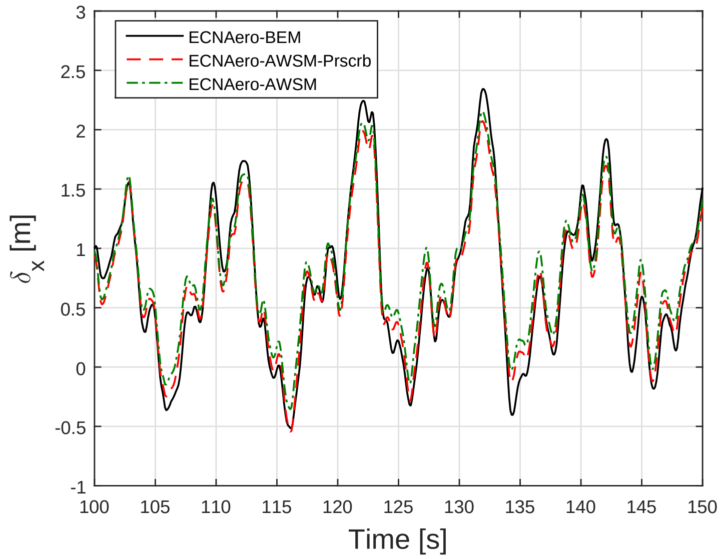

Figure E.15: *Blade deflection at $r/R = 95\%$ for the INNWIND turbine in a turbulent inflow.*

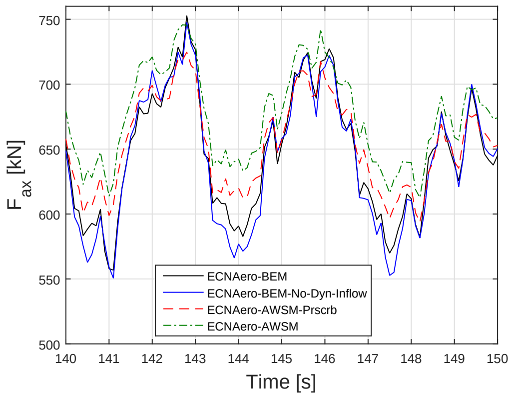

(a) *Axial Force*

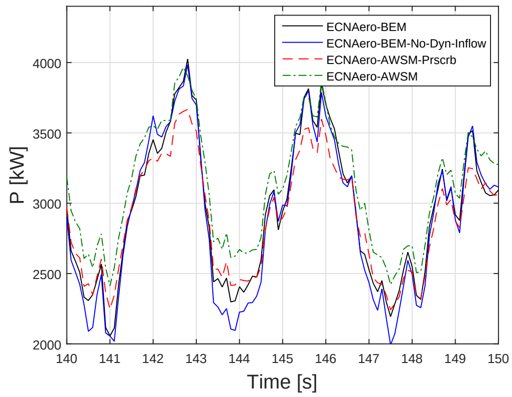

(b) *Power.*

Figure E.16: *Comparison of the rotor performance for the INNWIND turbine in a turbulent inflow.*

M_x, it can be seen that there is a good agreement in the trend, although it can be observed that BEM calculates a larger load amplitude, with the exception of one cycle around $t = 105s$.

In Fig. E.17b, the tower fore-aft moment is plotted as function of time. From this figure, it can be seen that again there is a good agreement between BEM and AWSM. In general, it can be observed that the results from BEM show a larger variation of M_y. This is expected, since the same behavior if found for F_{ax}, which caused the fore-aft moment. Furthermore, it can be seen that the free wake results show a slightly higher mean value of M_z.

Finally, the tower M_z is shown in Fig. E.17c, for which the same observation can be made as for the tower M_x and M_y, where BEM calculates a higher load amplitude. In general, these observations will result in a larger fatigue load for simulations with BEM, which makes BEM a more conservative model.

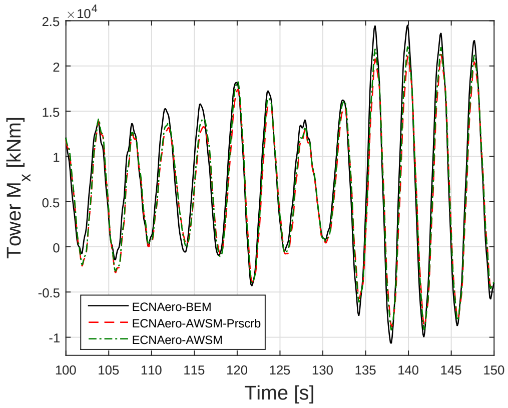

(a) *Side-side moment.*

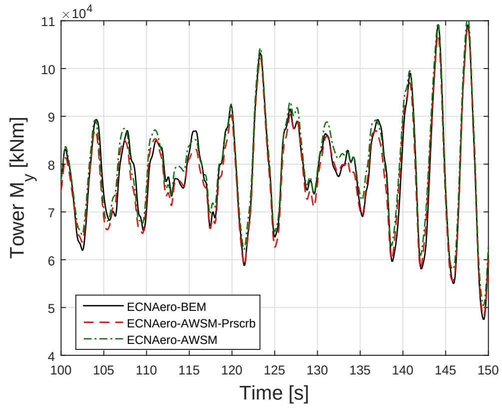

(b) *Fore-aft moment.*

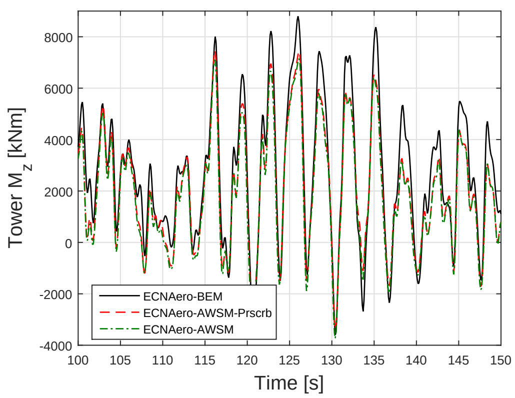

(c) *Torsional torsional.*

Figure E.17: *Comparison of the tower bottom bending moment for the INNWIND turbine in a turbulent inflow.*

Appendix F

Pitch Step

In this appendix, the results from four different pitch step experiments from the New MEXICO experiment are shown and compared to the results from simulations with BEM and AWSM. First the results for the response of the blade sectional loads are compared for 1146, for which the largest overshoot in aerodynamic forces was observed and is considered the most interesting case for comparison. Next, the blade loads for runs 1147, 1152 and 1153 are compared.

F.1 Comparison of the Sectional Load Response

In this section, the response to the pitch step is compared in terms of the scaled F_n and F_t. This will be done for all five blade positions at which the experimental data is gathered. Since each run consists of two pitch steps, both responses will be compared. In this way it can also be assessed whether there is a difference in response when the aerodynamic force increases or decreases.

F.1.1 Results at 25% blade span

The first location that is considered is the location at 25% blade span, which is the location closest to the root. In Fig. F.1, the response to the pitch steps is shown for the scaled F_n. It can be seen that the experimental results show a large fluctuation of the normal force over time, whereas the results from both BEM and AWSM do not show this behavior. This variation is found to be a 1P influence and might be caused by both the tower effect as well as the blade deformation. Although this fluctuation seems to be large on the scaled axis, the absolute value of the fluctuations is rather small, since the total F_n in the root section is small.

When comparing the response to the first pitch step, it can be seen that there is a large overshoot of the normal force in the experimental data. Interesting to see is that it takes around $3s$ for the experimental data to converge to a steady cyclic behavior, which is 21 rotor revolutions. After approximately 8 rotor revolutions, F_n drops below the steady value for a pitch angle of $5°$, after which another 13 rotor revolution are required to reach the steady value. This behavior of the solution to reach a value below the steady value is not observed for both the results form BEM and AWSM. When comparing the experimental results to the results from the simulations, it can be observed that the solution from BEM seems to reach the steady value after approximately 3 rotor revolutions, whereas AWSM requires more than 10 rotor revolutions. This indicates that AWSM calculates a longer influence of the dynamic inflow as a response to the pitch step.

For the second pitch step, it can be seen that F_n does not drop below the steady value for the experimental data. It can be seen that both the experimental data and the solution from AWSM require more than $3s$ (21 rotor revolutions) to reach a steady value and have a very similar exponential decay of F_n over time. Again, the results from BEM show a very fast recover from the pitch step, where the steady state solution seems to be reached within $1s$.

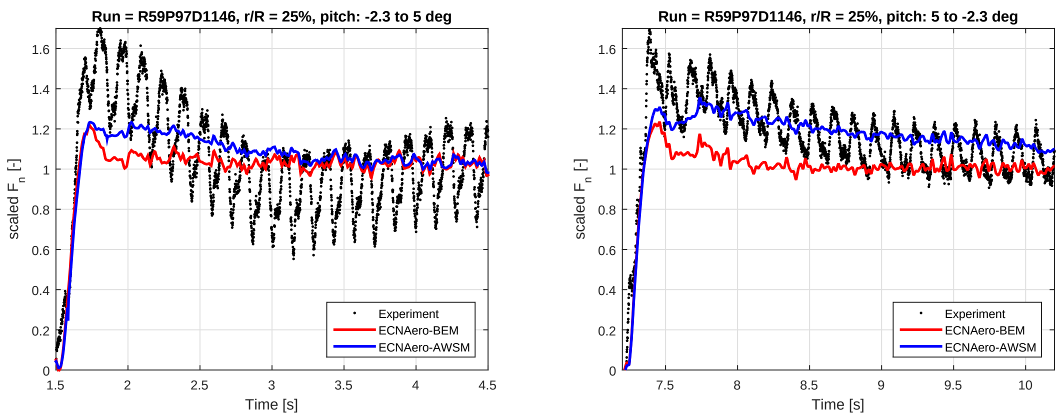

(a) $\theta : -2.3^\circ$ *to* 5°.

(b) $\theta : 5^\circ$ *to* -2.3°.

Figure F.1: *Comparison of the scaled normal force during the pitch step of run 1146 at* $r/R = 25\%$.

In Fig. F.2, the results for F_t are shown at 25% blade span. From this figure, it can be seen that there is a much smaller variation of F_t over time for the experimental data, as was found for F_n. From the experimental results, it can be seen that the solution seem to have a smaller overshoot and a faster recover when the pitch angle is increased, as is shown for the first pitch action. During this pitch action the total aerodynamic force is decreased. For the second pitch action, the pitch angle is decreased and the total force is increased. During this pitch angle, a larger overshoot in F_t is shown and the solution takes longer to reach the steady value. This effect is well modeled by AWSM, whereas it can be observed that BEM shows a very fast recover from the pitch step, indicating a smaller influence of the dynamic inflow effect.

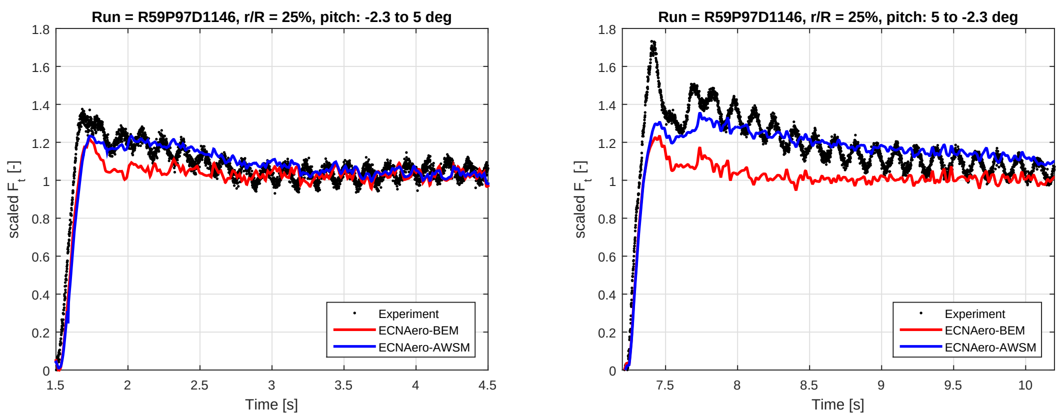

(a) $\theta : -2.3^\circ$ *to* 5°.

(b) $\theta : 5^\circ$ *to* -2.3°.

Figure F.2: *Comparison of the scaled tangential force during the pitch step of run 1146 at* $r/R = 25\%$.

F.1.2 Results at 35% blade span

In Fig. F.3, the response to the scaled F_n is shown at 35% blade span. From this figure, it can be seen that the experiment shows a larger overshoot during the first pitch step, whereas a very good agreement of the initial response is found for the second pitch step. In terms of dynamic inflow, it can be seen that the results from BEM only show the influence of the pitch step for a short time-period, whereas AWSM takes much longer to reach the steady value after the pitch step. The response in the experimental data seems to be in between the results of BEM and AWSM at 35% blade span.

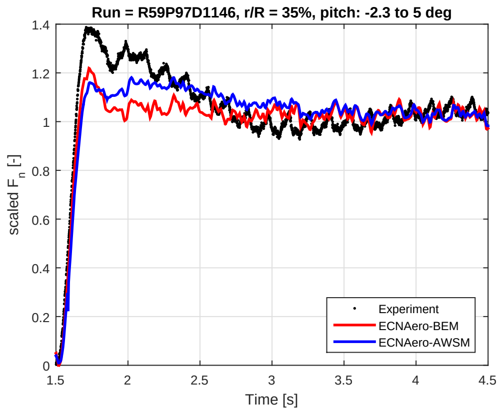

(a) $\theta : -2.3^\circ$ *to* 5°.

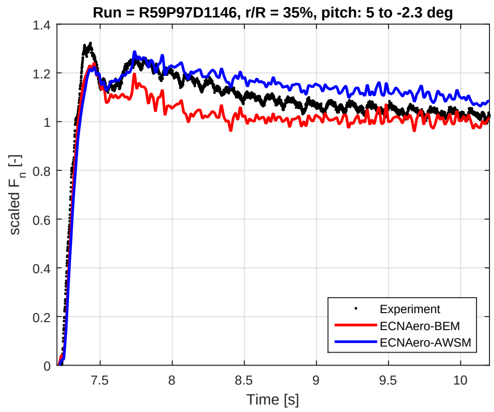

(b) $\theta : 5^\circ$ *to* -2.3°.

Figure F.3: *Comparison of the scaled normal force during the pitch step of run 1146 at* $r/R = 35\%$.

For the tangential force, it can be seen that there is hardly any overshoot during the first pitch step, whereas there is large overshoot during the second pitch step. For the first pitch step, the experimental results seem to agree better with the results from BEM, although it should be noted that this is the case since the experiment does not show any overshoot, whereas the results from BEM and AWSM do show an overshoot. During the second pitch step, it can be seen that BEM and AWSM underestimate the overshoot of F_t. Again, it can be seen that the results from BEM seem to quickly reach the steady state value, whereas the results from AWSM require a much longer period to converge. Again, the experimental results are in between in terms of dynamic inflow.

F.1.3 Results at 60% blade span

In the mid-section of the blade, at 60% span, the response on F_n is shown in Fig. F.5. From this figure, it can be seen that there is a good agreement in the overshoot in F_n between the experiment and the results from BEM for both pitch steps during this run. For the first pitch step, it can be seen that the results from BEM seem to quickly reach the steady value, whereas the results form the experiment require more rotor revolutions to adjust to the new situation. The results from AWSM show an even longer time-period to adjust to the new pitch angle. For the second pitch step, it can be seen that the results between the experiment and BEM seem to agree well in terms of dynamic inflow, whereas the results from AWSM require a longer time to reach the steady value.

For F_t at 60% blade span, it can be seen that there is a large difference in the response between the two pitch steps for the experimental results. For the first pitch step, it can be seen that the results from the experiment do not show an overshoot, whereas the results from BEM and AWSM do show an overshoot. Again, from the simulation with BEM, F_t is quickly recovered to the steady

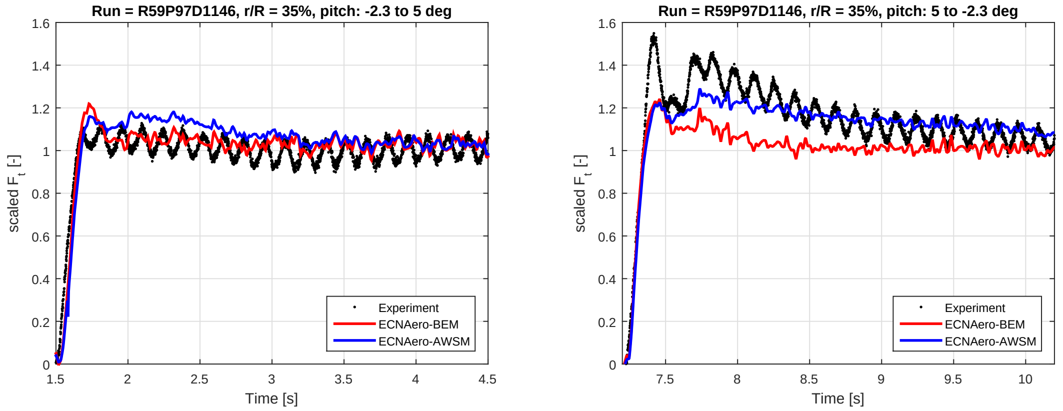

(a) $\theta : -2.3^\circ$ *to* 5°. (b) $\theta : 5^\circ$ *to* -2.3°.

Figure F.4: *Comparison of the scaled tangential force during the pitch step of run 1146 at* $r/R = 35\%$.

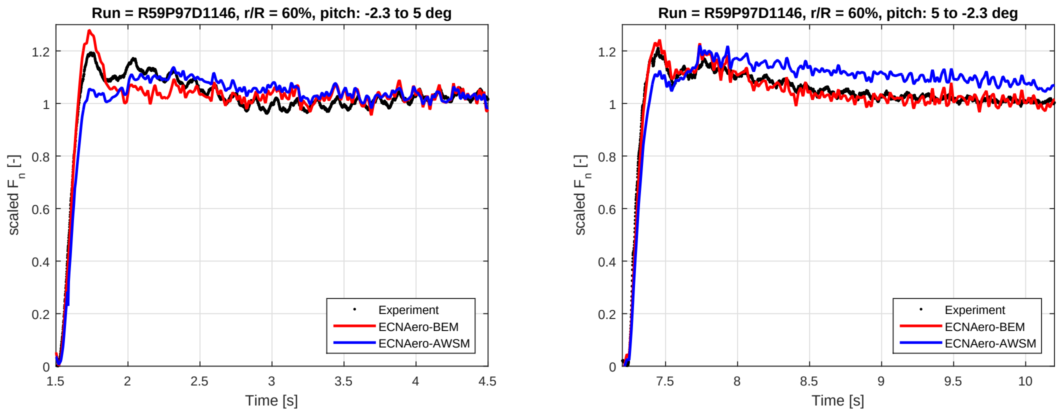

(a) $\theta : -2.3^\circ$ *to* 5°. (b) $\theta : 5^\circ$ *to* -2.3°.

Figure F.5: *Comparison of the scaled normal force during the pitch step of run 1146 at* $r/R = 60\%$.

value. AWSM shows a longer time-period to reach the steady value, similar to the results from the experiment. For the second pitch step, it can be seen that the experimental data shows a larger overshoot of F_t, after which the solution seems to slowly approach the steady value after approximately 20 rotor revolutions. The results from AWSM seem to require a similar period to reach the steady value, whereas the results from BEM reach the steady value much faster.

F.1.4 Results at 82% blade span

The response of F_n to the pitch step at 82% blade span can be found in Fig. F.7. In this figure, it can be seen that there is a very good agreement between AWSM and the experiment for the initial part of the response for both pitch steps. The results from BEM seem to underestimate the increase of F_n compared to the experimental data. When comparing the convergence towards the steady value of F_n after the pitch steps, it can be seen that BEM shows a much shorter time to reach a steady value compared to AWSM. The results from the experiment show a convergence time in between the results from BEM and AWSM.

In Fig. F.8, the results for F_t are shown for both pitch steps. For both pitch steps, it can be seen that the experiment shows a much larger overshoot compared to the results from both BEM and

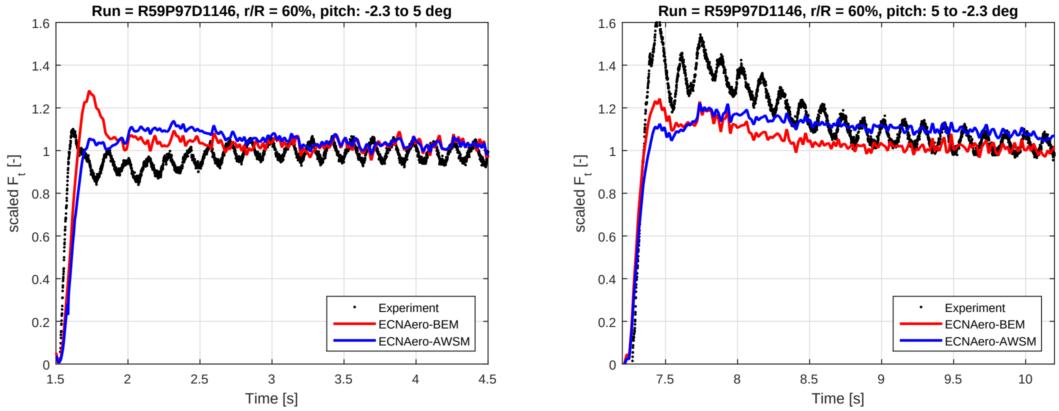

(a) $\theta : -2.3^\circ$ *to* 5°. (b) $\theta : 5^\circ$ *to* -2.3°.

Figure F.6: *Comparison of the scaled tangential force during the pitch step of run 1146 at* $r/R = 60\%$.

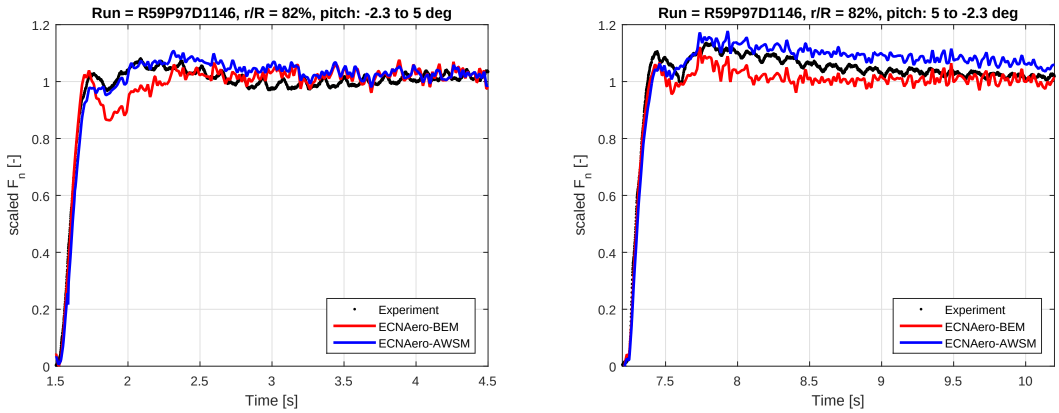

(a) $\theta : -2.3^\circ$ *to* 5°. (b) $\theta : 5^\circ$ *to* -2.3°.

Figure F.7: *Comparison of the scaled normal force during the pitch step of run 1146 at* $r/R = 82\%$.

AWSM. From Fig. F.8a, it can be seen that the results from AWSM take longer to respond to the pitch step compared to the results from BEM. The overshoot of F_t in the results from AWSM also occurs later, when the results from the experiment are already approaching a steady value. For the second pitch step, it can be seen that there is a good agreement in terms of the response time between the experiment and AWSM. The results from BEM seem to reach the steady value much quicker.

F.1.5 Results at 92% blade span

Finally, the results in the tip-region are compared for F_n. From this comparison, it can be seen that BEM seems to underestimate the increase in F_n during the initial part of the response for both pitch steps. The results from AWSM seem to agree much better with the experimental data, although it seems that the effect of the pitch step has a longer effect on the results for AWSM.

The tangential force shows an interesting behavior in the tip region, as can be seen in Fig. F.10. For the first pitch step, it seems that the results from the experiment reach the steady value in approximately one rotor revolution after the pitch angle has reached its final value after the pitch step. The results from both BEM and AWSM require a longer response time, where the

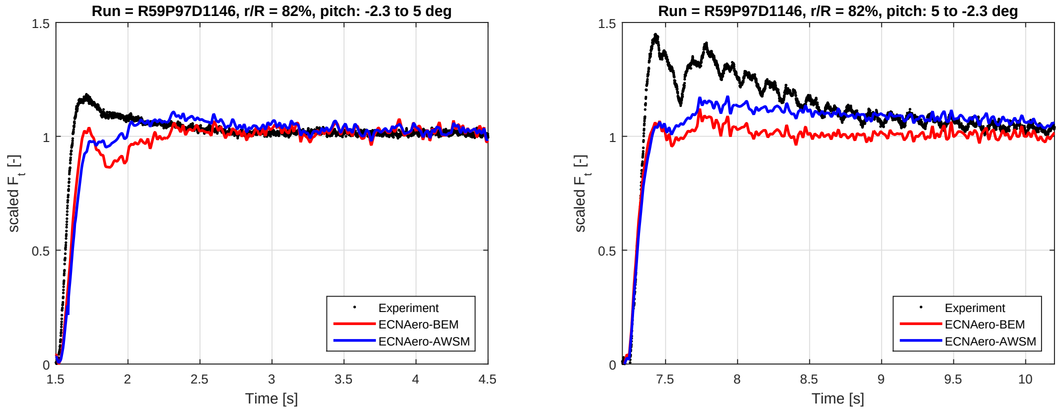

(a) $\theta : -2.3^\circ$ *to* 5°.
(b) $\theta : 5^\circ$ *to* -2.3°.

Figure F.8: *Comparison of the scaled tangential force during the pitch step of run 1146 at* $r/R = 82\%$.

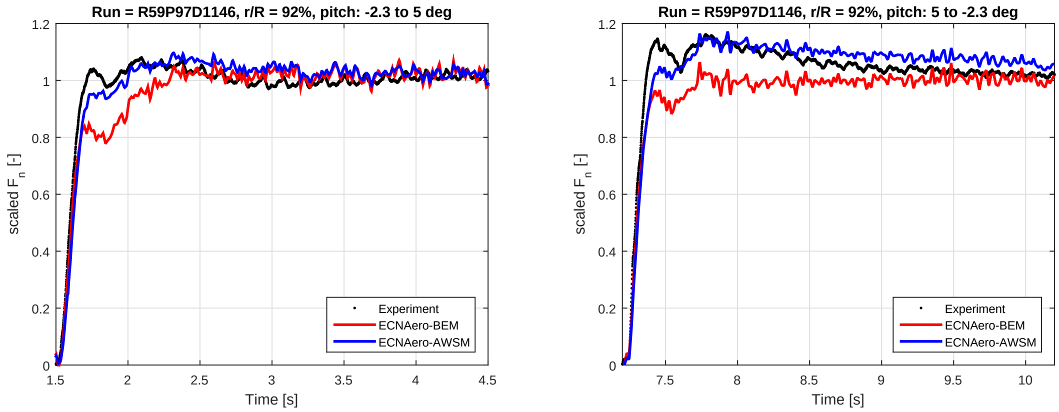

(a) $\theta : -2.3^\circ$ *to* 5°.
(b) $\theta : 5^\circ$ *to* -2.3°.

Figure F.9: *Comparison of the scaled normal force during the pitch step of run 1146 at* $r/R = 92\%$.

results from BEM show a much smaller initial peak. For the second pitch step, the results from the experiment show a large overshoot in F_t. Due to this large overshoot, a large time-period is required to reach the steady value of F_t. This result is in good agreement with the observation made for AWSM, whereas the results from BEM seem to reach the steady value much faster.

F.2 Blade Root Bending Moments

In this section the blade root bending moments M_x and M_y are presented for runs 1147, 1152 and 1153. In the main body of the thesis, the exact definition of M_x and M_y is defined as well as the results for experiment run 1146 of the New MEXICO experiment. This experiment is performed at a tip speed ratio of $\lambda \approx 10$, resulting in a turbulent wake state (TWS) when the pitch angle is $\theta = -2.3^\circ$. In order to see how the results from BEM and AWSM compare to the experimental results for normal operational conditions, the blade loads in run 1147 are compared, which are performed at a lower λ. Furthermore, M_x and M_y for runs 1152 and 1153 are compared, where the rotor speed is lower and the pitch action is faster relative to the rotational velocity of the blades.

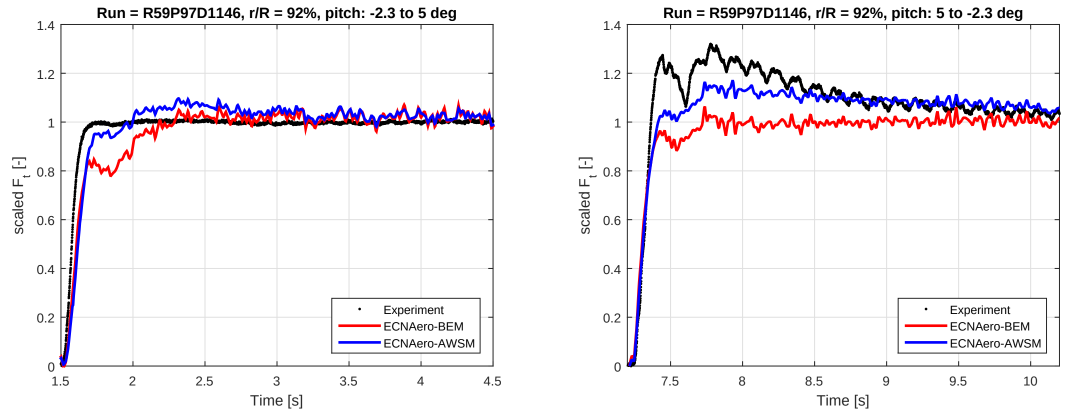

(a) $\theta : -2.3^\circ$ *to* 5°. (b) $\theta : 5^\circ$ *to* -2.3°.

Figure F.10: *Comparison of the scaled tangential force during the pitch step of run 1146 at* $r/R = 92\%$.

F.2.1 Run 1147

In run 1147 of the New MEXICO experiment, the wind velocity is increased from $9.97 m/s$ to $15.19 m/s$ compared to run 1146, while keeping the rotor speed the same (425.1 rpm). This results in a decrease in the tip speed ratio to 6.6, which is the design conditions for the New MEXICO turbine model. During this run, the turbine will not operate in a TWS. From this experiment it is interesting to see if there are differences with the results from run 1146, where the rotor does operate in a TWS.

In Fig. F.11, the results for M_x and M_y are plotted as function of time. From this figure, it can be seen that there is hardly an overshoot in M_x and M_y for both pitch steps noticeable. In general, a good agreement is found in the blade loads between BEM, AWSM and the experiment. It can be seen that there is a better agreement when the loads are lower (lower induction), especially for M_y.

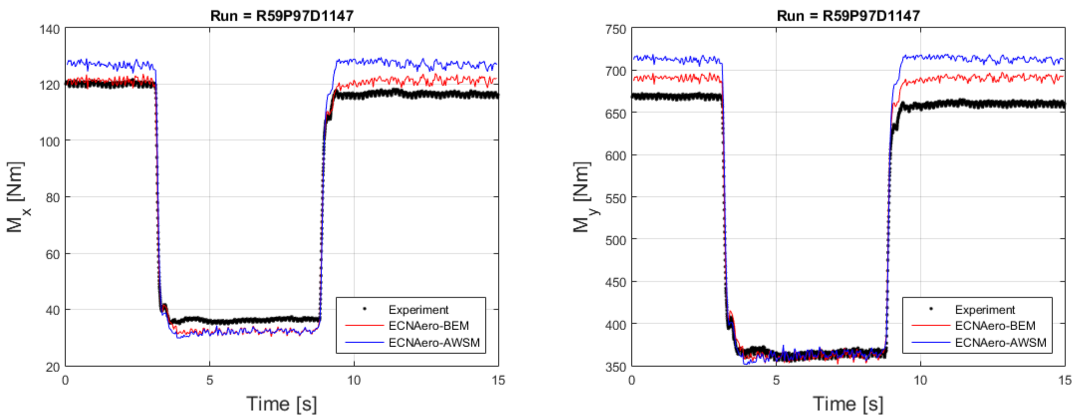

(a) *Edgewise moment.* (b) *Flapwise moment.*

Figure F.11: *Comparison of the blade root bending moments during the pitch step of run 1147.*

In order to compare the response of M_y, the results are scaled to assess the relative difference in the loads. In Fig. F.12, $\tilde{M}_y$ is shown as function of time during both pitch steps. From this figure, it can be seen that there is no significant overshoot during both pitch steps. Also, there is a very good agreement in terms of the response between BEM, AWSM and the experiment. It can be seen that the response can be divided in three parts. First $\tilde{M}_y$ is increased due to the changing pitch angle. Then the loads are decreased, which might be attributed to the fact that the accelerated or decelerated flow around the airfoil is shed in the wake. During the last part, M_y increasing again to reach the steady value of the new pitch angle. An excellent agreement is found in the development of $\tilde{M}_y$ during the pitch step, as well as the time to reach the steady value.

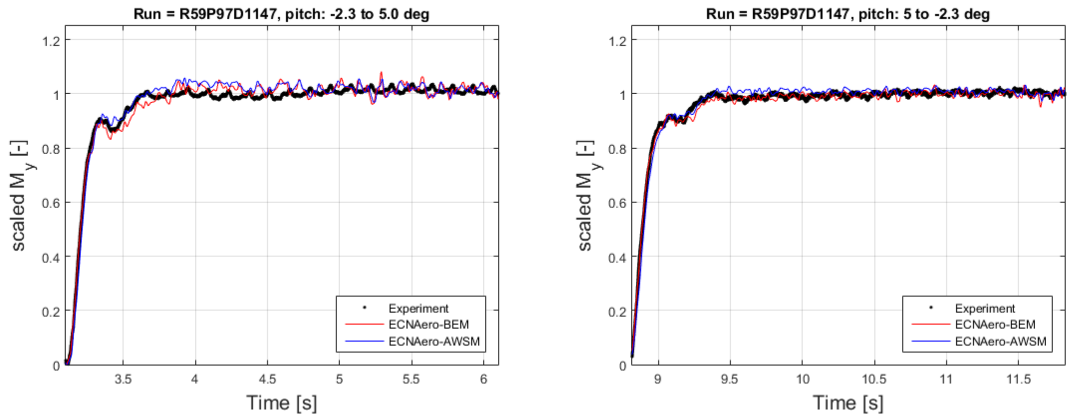

(a) $-2.3°$ *to* $5°$. (b) $5°$ *to* $-2.3°$.

Figure F.12: *Comparison of the scaled flapwise blade root bending moments during the pitch step of run 1147.*

F.2.2 Run 1152

In run 1152 of the New MEXICO experiment, the wind velocity is decreased from $9.97m/s$ to $7.68m/s$ and the rotor speed is decreased from 425.1 rpm to 324.9 rpm compared to run 1146. This is done in order to keep the tip speed ratio constant, but increasing the pitch speed relative to the rotational velocity of the blade.

In Fig. F.13, the results for M_x and M_y are shown as function of time. From figure, it can be seen that there is a significant overshoot in the loads, as was also found for the results in run 1146. The results of BEM, AWSM and the experimental data show a very similar agreement as was found for run 1146. Again, a good agreement is found between BEM and AWSM for M_x and M_y is found when the loads are low ($\theta = 5°$). When the loads are higher ($\theta = -2.3°$), it can be seen that AWSM calculates a higher load compared to BEM, where the experimental results fall in between.

The results for $\tilde{M}_y$ during both pitch steps are shown in Fig. F.14. From this figure, it can be seen that there is an almost identical response as was found from the results in run 1146 of the New MEXICO experiment. It can be seen that there is a very good agreement between the results from BEM, AWSM and the experiment for the initial response to the pitch step change. However, it can be seen that BEM seems to arrive at the steady state value for the new pitch step much faster compared to the experimental results, which indicates an underestimation of the dynamic inflow effect. On the other hand, it can be seen that the influence of dynamic inflow seems to have a longer lasting effect on the results for AWSM compared to the experiment, indicating an overestimation of the dynamic inflow effect. This can be explained by the long wake length of AWSM in this experiment.

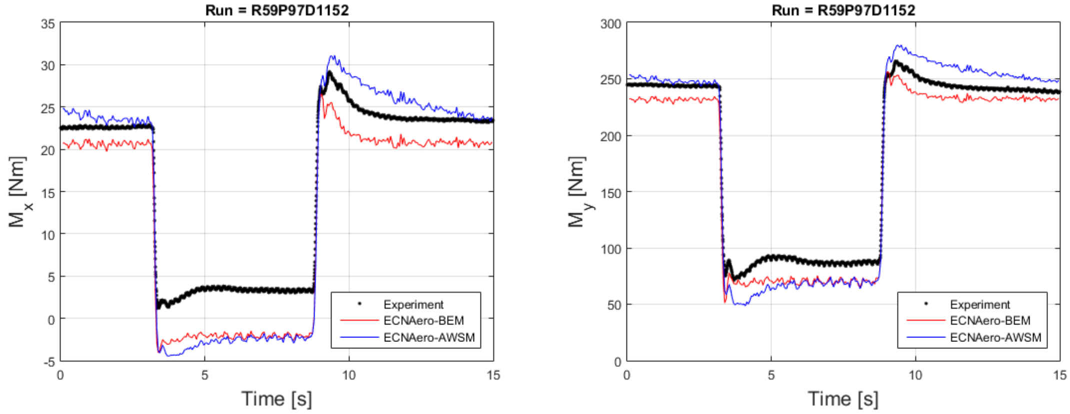

(a) *Edgewise moment.* (b) *Flapwise moment.*

Figure F.13: *Comparison of the blade root bending moments during the pitch step of run 1152.*

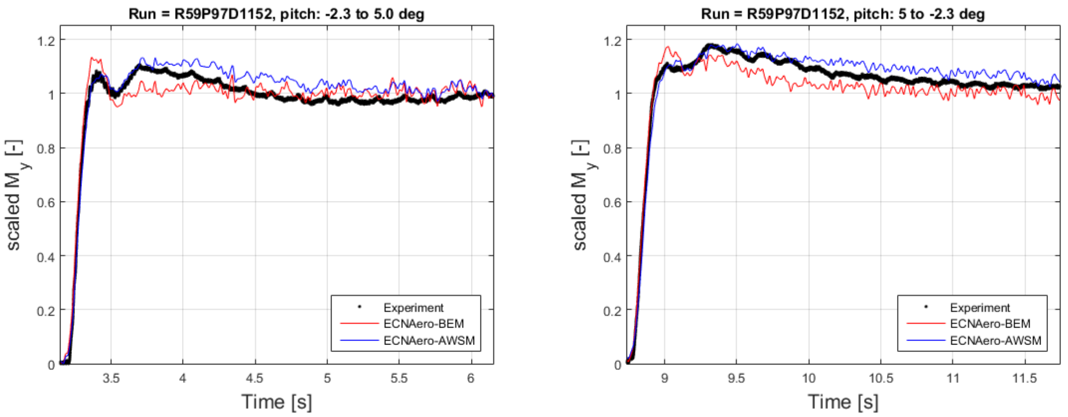

(a) $-2.3°$ *to* $5°$. (b) $5°$ *to* $-2.3°$.

Figure F.14: *Comparison of the scaled flapwise blade root bending moments during the pitch step of run 1152.*

F.2.3 Run 1153

The final experiment that is considered for the pitch step case is run 1153 from the New MEXICO experiment. In this run, the wind speed is set to $11.57m/s$ and the rotor speed to 324.9 rpm. This results in a tip speed ratio of 6.614, which is similar to run 1147. Therefore, it is expected that similar results are obtained as for this run.

In Fig. F.15, the results for M_x and M_y are shown for run 1153. From this figure, it can be seen that there the results are very similar to the results from run 1147, although the mean value of M_x and M_y are smaller, due to the lower effective velocity (lower wind and rotor speed).

The results of $\tilde{M_y}$ for both pitch steps for run 1153 are shown in Fig. F.16. From this figure, it can be seen that there is an excellent agreement found between BEM, AWSM and the experiment. This results was also found in run 1153. From these results it can be concluded that there is not a very significant difference found by the increased pitch speed due to the lower rotor speed for run 1152 and 1153, compared to run 1146 and 1147.

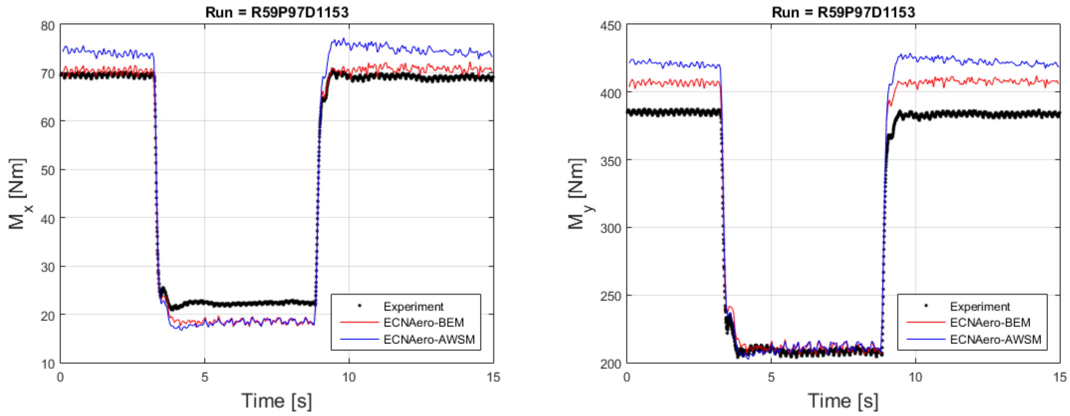

(a) *Edgewise moment.* (b) *Flapwise moment.*

Figure F.15: *Comparison of the blade root bending moments during the pitch step of run 1153.*

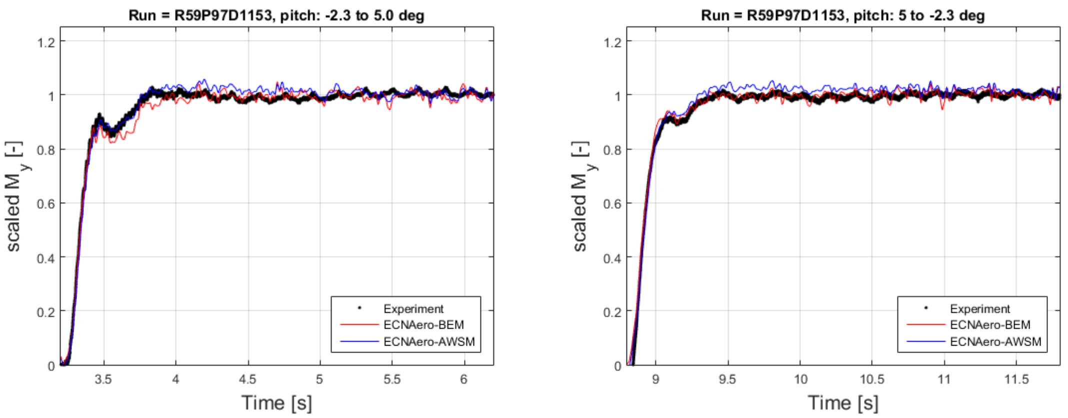

(a) $-2.3°$ *to* $5°$. (b) $5°$ *to* $-2.3°$.

Figure F.16: *Comparison of the scaled flapwise blade root bending moments during the pitch step of run 1153.*